Next generation neural activity models: Bridging the gap between mesoscopic and microscopic brain scales

Áine Byrne

May 2017

Abstract

Neural mass and neural field models have been actively used since the 1970s to model the coarse grained activity of large populations of neurons and synapses. They have proven especially useful in understanding brain rhythms. However, although motivated by neurobiological considerations, they are phenomenological in nature, and cannot hope to recreate some of the rich repertoire of responses seen in real neuronal tissue. In this thesis we consider the θ-neuron model that has recently been shown to possess an exact mean-field description for smooth non-pulsatile interactions, and show that the inclusion of a more realistic synapse model leads to a mean-field model, that has many of the features of a neural mass model, coupled to a further dynamical equation that describes the evolution of network synchrony.

We have carried out extensive analysis on the model for both a single and a two population system. Importantly, unlike its phenomenological counterpart this *next generation neural mass model* is an exact macroscopic description of the underlying microscopic spiking neurodynamics, and is therefore a natural candidate for use in large scale human brain simulations. Using our reduced model, we replicate a human MEG power spectrogram to demonstrate that the model is capable of reproducing transitions from high amplitude to low amplitude signals, which are believed to be caused by changes in the synchrony of the underlying neuronal populations.

We then shift our focus to a spatially extended model and construct a *next generation neural field model*. Using both Turing instability analysis and numerical continuation techniques we explore the existence and stability of spatio-temporal patterns in the system. In particular, we show that this new model can support states above and beyond those seen in a standard neural field model.

Acknowledgements

Firstly, I would like to thank my supervisor, Prof. Stephen Coombes, who has been a constant source of support and encouragement over the past 3 and a half years. You have shown me the joys of academic research and for that I will be forever grateful. To my co-supervisor, Dr. Theo Kypraios, I apologise for the lack of statistics that this project presented. Thank you for continuing to show such interest, even so. Thank you also to Dr. Daniele Avitabile, who never turned me away from his door when I needed help with my numerics.

To the MEG group at the Sir Peter Mansfield Imaging Centre (SPMIC), thank you for all of the useful discussions on brain imaging and for taking the time to teach me how to use the MEG. In particular, I would like to extend my gratitude to Dr. Matthew Brookes and Dr. Prejaas Tewarie for providing me with interesting projects to work on.

I am grateful to my examiners Prof. Peter Ashwin and Dr. Reuben O'Dea for a very pleasant viva and for their useful and insightful comments.

I feel it is necessary to thank my family for putting up with me. Your belief in me has never faltered. This, combined with your love and support has always motivated me to push on when life got me down.

To Kenneth, thank you for always being there when I needed someone to talk to and for never failing to keep me entertained.

Last but not least, I would like to acknowledge my friends. To the friends I have made in Nottingham, thank you for keeping me sane over the course of my PhD and ensuring that I did not let my studies take over my life entirely. To my friends in Dublin, thank you for giving me an abundance of reasons to not stay away from home for too long.

Contents

Chapter 1

Introduction

"If the human brain were simple enough for us to understand it, we would be too simple to understand it"

- Ken Hill

Over the past century, the field of theoretical neuroscience has provided a window into the brain. Despite the immense complexity of the brain, theoretical modelling has allowed for major advances to be made towards understanding behaviour, conciousness and disease. An early example of this is the work of Hodgkin and Huxley, who modelled the generation and propagation of action potentials in the giant squid axon using differential equations. Discoveries such as this one can only be made possible through close collaboration between experimentalists and theoreticians, to combine clinical observation with carefully designed mathematical models.

This thesis focuses on the development of new modelling approaches for use in brain imaging studies, with a particular emphasis on magnetoencephalography (MEG). Through extensive discussions with colleagues at the Sir Peter Mansfield Magnetic Imaging Centre (SPMIC) we identified the need for a new type of neural population model, to help us better understand the transitions from high amplitude to low amplitude signals seen in electrophysiological recordings of the brain. In particular, we

are interested in investigating these modulations in the beta band (13–30 Hz). These transitions from high amplitude to low amplitude, and vice versa, are believed to be caused by a change in the synchrony of underlying neuronal population.

Neural field models are typically used to describe brain dynamics at the mesoscopic scale (large populations of neurons). However, as these models entirely neglect the within-population synchrony, one is forced to investigate these changes in synchrony through simulations of a large network of spiking neurons. As large-scale simulations are notoriously difficult to gain insight from, we sought to develop an alternative modelling approach, which would act to bridge the gap between these large-scale simulations and the coarse-grained neural mass modelling approach. Using newly established mean field reduction techniques we develop *next generation neural activity models* which can account for changes in the population synchrony.

An overview of both the biology and the mathematical techniques used in this thesis is covered in Chapter 2. We first review the structure of the brain and its ability to generate oscillations. We then provide an overview of brain imaging techniques, with a particular emphasis on MEG. The latter half of the chapter concerns itself with the development of mathematical models of neural activity, at both the microscopic single neuron level and the mesoscopic mean field level.

Chapter 3 introduces our *next generation neural mass model*, and describes the reduction of a network of θ-neurons to an equivalent low dimensional system. This chapter also includes an extensive bifurcation analysis of both the single and the two population model.

In Chapter 4 we consider how our new model can be applied to MEG data. We look at movement induced changes in beta band activity, known as movement related beta decrease (MRBD) and post movement beta rebound (PMBR). We use the model to gain insight into the mechanisms behind these phenomena. Lastly, we show that by switching to a two hemisphere model (comprising of two identical populations) we

get a better fit with the data.

The focus then shifts to a spatially extended model. In Chapter 5 we show that the reduction techniques presented in Chapter 3 still hold for a network of spatially distributed θ-neurons. This allows us to construct our *next generation neural field model*. The spatially extended system is then analysed in one and two spatial dimensions using Turing instability analysis.

In Chapter 6 we consider a further exploration of the model presented in Chapter 5, and its ability to create patterns. We use numerical machinery to perform parameter continuations, to explore the behaviour of both the global Turing patterns away from bifurcation and local patterns, such as travelling fronts.

This thesis concludes with a discussion on the main findings of the work presented here and possible future projects and extensions.

Glossary

Below is a list of the common abbreviations used in this thesis:

EEG	electroencephalography
ERD	event-related desynchronisation
ERS	event-related synchronisation
GABA	gamma aminobutyric acid
MEG	magnetoencephalography
MRBD	movement related beta decrease
OA	Ott-Antonsen ansatz
PING	pyramidal-interneuron network gamma
PMBR	post movement beta rebound
PSP	post synaptic potential
QIF	quadratic integrate-and-fire

Chapter 2

Background

2.1 Neurons and brain structure

The brain is primarily made up of *neurons* and *glia*. There are roughly 10^{11} neurons in the human brain. They consist of three distinct parts: the dendrites, the soma and the axon, see Figure 2.1.1. Dendrites enable neurons to communicate with each other; branching out from the soma, they connect to the axons of other neurons, allowing signals to be passed between the two neurons. Dendrites guide *post synaptic potentials*

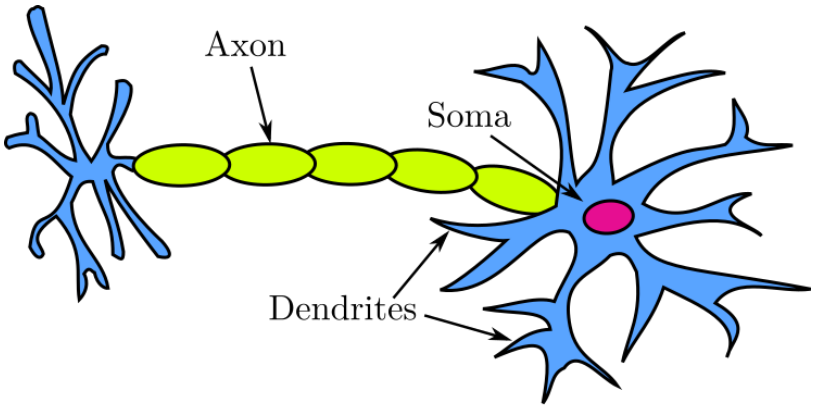

Figure 2.1.1. Diagram of a neuron: Schematic illustrating the 3 main components of a neuron: the dendrites, the soma and the axon

into the soma, which processes these inputs and may subsequently fire an *action potential*. An action potential is a short burst of electrical activity, of magnitude ~ 100 mV, lasting less than 1 ms. These bursts of electrical activity are transmitted through the axon to the *synapse*, the junction between the axon of one neuron (*presynaptic*) and the dendrite of another neuron (*postsynaptic*). On average axons branch roughly 10^3 times, hence there are roughly 10^{14} synapses in the human brain.

The concentration of ions differs between the interior of the neuron (intracellular) and its surrounding (extracellular) medium. This leads to a potential difference across the neuron, called the *membrane potential*. When the neuron is at rest, i.e. receiving no inputs, we say that the membrane potential is at *resting potential* (typically around 65 mV). Ion channels, which are responsible for allowing ions to flow in and out of the cell, can increase or decrease the membrane potential by allowing positively/negatively charged ions to either enter or leave the cell. Each ion channel has an associated *synaptic reversal potential*. This electrical potential corresponds to the value of the membrane potential for which there is no net flow of that ion across the membrane.

At a synapse the presynaptic neuron releases a chemical known as a *neurotransmitter*, which binds to the chemical receptors of the postsynaptic neuron and opens the ion channels. This allows the ions to flow in or out of the cell. This process can have either an excitatory (depolarising) or an inhibitory (hyperpolarising) effect on the postsynaptic neuron depending on the characteristics of the synapse. Excitatory post-synaptic potentials (EPSPs) occur when the membrane potential of the cells is raised as a result of positivity charged ions, such as sodium (Na^+), flowing into the cell or negatively charged ions, such as chloride (Cl^-), flowing out of the cell. Inhibitory post-synaptic potentials (IPSPs), on the other hand, occur when the membrane potential of the cells is lowered as a result of negatively charged ions flowing into the cell, or positively charged cells flowing out of the cell.

When the membrane potential is increased above the neuron's *threshold potential*,

the neuron can produce an *action potential*, which travels along the axon to the synapse restarting the whole process. EPSPs increase the membrane potential, driving the neuron closer to threshold level and increasing the probability of the neuron firing an action potential. IPSPs have the opposite effect, forcing the neuron further away from the threshold level and decreasing the likelihood of a firing event. There are many different types of neurons, which are all notably distinct and have a wide variety of morphologies, functions and electrical responses. However, all neurons send and receive action potentials, either chemically or electrically.

Glia, derived from the Greek for glue, support and hold the neurons together. These cells also provide a number of other functions such as delivering nutrients and oxygen to neurons as well as taking away dead cells and mopping up glutamate and other toxins. It is believed that there are roughly ten times as many glia cells than neurons [55]. However, in this thesis will ignore the presence of glia and focus solely on neurons.

2.2 Brain rhythms

Ever since the first recordings of the human electropherogram by Hans Beregr in 1924 [17], electrophysiological brain recordings of large populations of neurons have been shown to be dominated by oscillations. These oscillations are thought to be driven by both the dynamics of the individual neurons and by the interactions between neurons. When a neuron receives an input it produces oscillations in the form of rhythmic action potentials, as well as the oscillations of its membrane potential. Hence, a neural populations can be thought of as a system of oscillators, where the observed rhythms are due to the synchronised activity of the individual neurons. This type of activity is usually the result of feedback connections within the population. When large populations of neurons synchronise in this way, we can observe these

oscillations at the scalp level. The power and the frequency of these oscillations can be measured using brain imaging techniques, such as magnetoencephalography (MEG) and electroencephalography (EEG), see §2.3 for more details on brain imaging techniques.

Classically brain rhythms have been divided into 5 functionally distinct bands; delta, theta, alpha, beta, gamma. Each frequency band is associated with different actions and functions [36, 164].

- **Delta *0.5–3.5 Hz*:** the predominant frequency in deep sleep, associated with learning and the brain's reward system [119].
- **Theta *4–7 Hz*:** thought to play a role in working memory and is of particular interest in place cell studies (for spatial navigation) [93].
- **Alpha *8–12 Hz*:** the most prominent and widely studied brain rhythm, responsible for the disengagement of task-irrelevant brain areas, working memory and short term memory retention [62].
- **Beta *13–30 Hz*:** originally discovered in the motor cortex, thought to be responsible for motor initiation and termination but not execution [57].
- **Gamma *>30 Hz*:** responsible for a wide range of processes, such as attention, movement preparation, memory formation and multisensory and sensorimotor integration [147].

More recently functionally distinct sub-bands have been reported within the classical beta and gamma bands [102].

As well as being functionally distinct, different brain rhythms can be localised to specific areas of brain. This was shown by Jasper and Andrews [91, 92] when they demonstrated that the beta rhythm present in the vicinity of the primary motor cortex and the primary somatosensory cortex was not affected by the presentation of a weak

visual stimulus which suppressed the alpha rhythm, recorded from the occipital lobe (the portion of the brain responsible for vision).

2.3 Brain imaging

When brain areas synchronise and fire action potentials simultaneously, coherent synaptic currents are generated. These currents can be measured and examined using techniques such as EEG and MEG. As the electrical current of a single neuron is very small, these techniques rely on the synchronous activity of thousands of neurons. One of the main complications of EEG is that brain activity is measured non-invasively at scalp level and the skull spatially distorts the electric fields as they pass through, which impedes source localisation.

In accordance with Maxwell's laws, an alternating electrical current $\mathbf{E}$ generates a magnetic field $\mathbf{B}$, as follows:

$$\nabla \times \mathbf{E} = -\frac{\partial \mathbf{B}}{\partial t}. \tag{2.3.1}$$

Magnetic fields are less susceptible to interference from the skull, hence it has become increasingly popular in recent years to measure the magnetic field using MEG instead of the electric field and use (2.3.1) to infer the corresponding electric field. MEG is yet to overtake EEG in terms of popularity as it has a number of shortcomings. First, the magnetic fields produced in the brain are very small, hence MEG detectors must be extremely sensitive. In order to obtain this sensitivity MEG employs superconducting quantum interference devices (SQUIDs) to successfully measure the magnetic field, see §2.3.1. Second, MEG detectors are very expensive as SQUIDS require liquid helium to keep them below their required operating temperature of 3 K. Not only is liquid helium becoming more and more scarce, the shielding required makes MEG up to 100 times more expensive than EEG. Lastly, there is the inverse function problem; it is mathematically impossible to determine the location of the currents as there is no

unique solution to (2.3.1). Instead we must estimate the most likely location of the sources, see §2.3.4.

2.3.1 Superconducting quantum interference device

Invented in the 1960s, the SQUID is a highly sensitive magnetometer which can measure magnetic fields as small as 10^{-16} Tesla. This is achieved by exploiting the superconducting phenomenon known as *Cooper Pairs*. As fermions, electrons must obey Pauli's exclusion principle, which states that two identical fermions cannot occupy the same quantum state. However, at low temperatures, sub 30K, two electrons may bind together to form a Cooper pair, which, as a boson, is no longer restricted by Pauli's exclusion principle. Hence any number of pairs can exist in the same quantum state [53, 13].

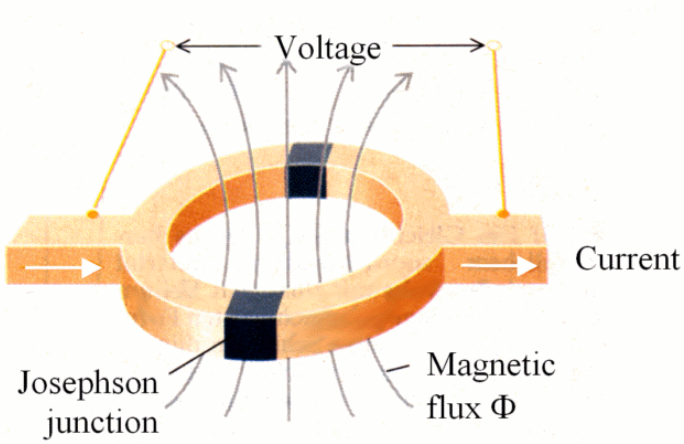

Figure 2.3.1. SQUID: The superconducting quantum interference device, a highly important element of the MEG detectors for accurately measuring small changes in the magnetic field. Figure reproduced from [1].

The SQUID is a superconducting loop consisting of two superconductors separated by thin insulating layers which form Josephson junctions, see Fig. 2.3.1. The Cooper pairs can tunnel quantum mechanically through the Josephson junction, provided the wavefunctions describing the Cooper pairs on either side of the junction differ in phase.

As a result current can pass through the superconducting loop, and the magnitude of the current is dependent on the phase difference across the junction, which is in turn related to the magnetic flux passing through the loop. The current in fact oscillates with the applied magnetic flux, and by measuring the frequency of these oscillations one can measure the magnetic flux of the applied magnetic field [30].

The first MEG recording was performed by David Cohen in 1968, using a copper induction coil as his detector [42]. Meanwhile in the Ford Research Labs James Zimmerman and his team were working on creating SQUID devices for MEG [171]. In 1972 Cohen became the first man to record MEG signals using a SQUID device [43]. Cohen used a single SQUID detector to measure the magnetic field at a number of different locations on the subject's scalp. In the 1980s, the use of arrays of sensors which could cover larger areas became the standard. Now MEG arrays are pre-set in the MEG helmet which covers the majority of the head. These helmets usually contain up to 300 sensors.

2.3.2 Background noise and gradiometer

Even with the ability to make such precise measurements one must overcome the issue of interference. The Earth's magnetic field is roughly 10^8 times larger than the fields produced by the brain. Computers, cars and mobile phones are also a major problem. In order to overcome this problem MEG scanners are placed inside magnetically shielded rooms.

Inside the shielded room the subject's body can still cause interference. *Gradiometers* are used to reduce this interference by measuring the spatial gradient of the magnetic field rather than the magnitude alone. Standard gradiometers consist of oppositely wound coils, placed at different distances from the head. As the magnetic field decays rapidly with distance this makes for a better measurement of the magnetic field, significantly reducing the signal-to-noise ratio.

2.3.3 Optically-pumped magnetometers

An emerging technology known as *optically-pumped magnetometers* (OPMs) or *atomic magnetometers* could be set to replace SQUIDs in MEG scanners [100]. This cutting edge technology being developed for MEG at SPMIC is likely to make MEG more pervasive in brain imaging. These devices are also capable of detecting magnetic fields as small as 10^{-16} T and do not require extensive shielding or liquid helium for cooling. Another benefit of OPMs is that they can be placed directly on to the scalp, like EEG recording devices. This significantly reduces the signal-to-noise ratio, and may even render the use of gradiometers in MEG obsolete. These devices exploit a quantum property known as spin to measure an applied magnetic field. Spin is the intrinsic angular momentum of a particle/nucleus.

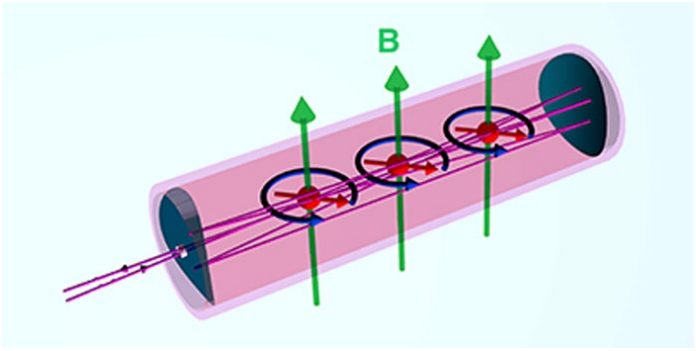

Figure 2.3.2. Optically-pumped magnetometer: Schematic of an OPM. The pump laser aligns the spins and then the applied magnetic field (green) changes the orientation of these spins. The probe laser (purple) is applied to measure the change in spin orientation. Figure reproduced from [148].

An OPM cell contains high pressure alkali vapour, which is formed by heating a small amount of alkali metal to its boiling point inside the glass cell. A *pump laser* is applied to the vapour, aligning the spins of the electrons inside the cell. Applying an external magnetic field will shift the collective orientation of the electron spins, which alters the index of refraction of the gas. Now applying a linearly polarised *probe laser* through the gas allows one to measure the extent of the shift in spin orientation,

by measuring the polarisation of the laser beam after it passes through the alkali gas. This shift can the be related back to the strength and orientation of the applied magnetic field [145].

2.3.4 Inverse function problem

The most challenging problem for MEG is that even after the magnetic fields have been successfully recorded it is mathematically impossible the turn this data into an exact 3D current density map, as the inverse problem of (2.3.1) does not have a unique solution. Various methods exist to approximate a solution of (2.3.1), each of which uses their own set of a priori assumptions. The most popular of these methods, which is used in the SPMIC, is beamforming [31]. This method assumes the currents in the brain can be modelled as current dipoles (a reasonable assumption given the nature of ionic currents which typically travel in reasonably straight lines) and that temporal patterns of electrical activity are not the same in two spatially separate brain regions. Beamforming uses weighted sums of the MEG sensor measurements to obtain a record of the electrical activity at a particular location, over the course of the experiment. The weighting factors are calculated to ensure that the signals originating from the location of interest are preserved, while the signals originating from any other location (either inside or outside the brain) are suppressed [30, 160]. A common strategy used for reconstructing spatio-temporal source activities is to assume an equivalent current dipole model [146], a model of the magnetic field that would have formed had we placed a dipolar current at the area of interest [143]. Spectrograms which show the observed power at different frequencies over the course of an experiment (known as *time-frequency spectrograms*) can be computed for single brain regions by applying the beamforming method to the location of interest. If we wish to build a 3D image of the changes in electrical activity across the brain we simply repeat the process at multiple locations [30].

2.4 Conductance based single neuron models

There currently exists a plethora of single neuron models for describing the spiking dynamics of cortical cells. These models are typically divided into two classes; type I and type II. The distinction between the two classes stems from differences in their excitability. This distinction was first introduced by Hodgkin in 1948 [83], and was later classified in more detail by Ermentrout [63]. The onset of firing in Type I neurons occurs through a saddle node bifurcation on the invariant circle (SNIC). However, in type II neurons firing can be brought on by a subcritical Hopf bifurcation, a supercritical Hopf bifurcation, or a saddle node bifurcation outside the invariant circle [138]. This corresponds to differences in their characteristic frequency-current 'f-I' curves, as shown in Fig. 2.4.1. The onset of firing occurs at *zero freqenucy* for type I neurons, and at a *non-zero* frequency for type II neurons. Hence, type II neurons can fire at arbitrarily low frequencies in response to constant current injection. This

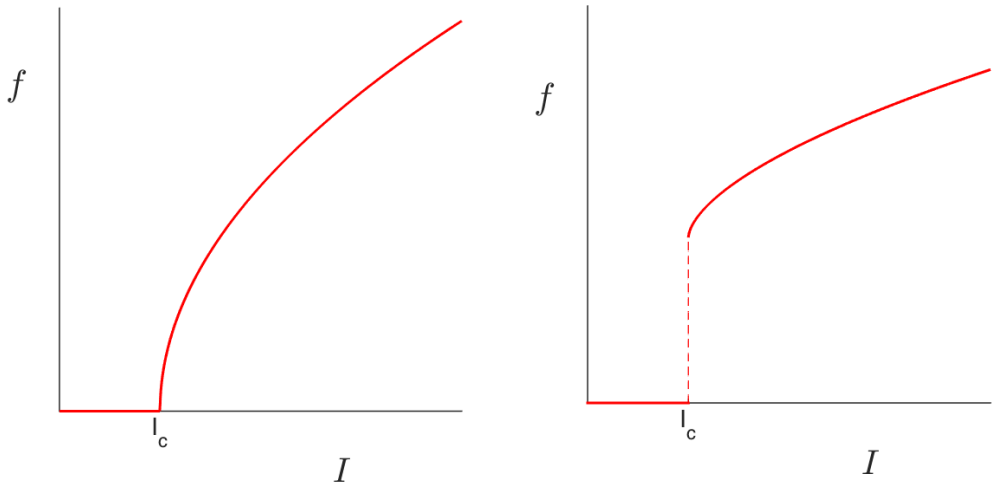

Figure 2.4.1. Type I versus Type II: Both figures show the oscillation frequency as a function of the input current I. When the current is increased past the critical current I_c the system starts to oscillate. For type I neurons (left) the oscillations start at the so called *zero frequency*, and the 'f-I' curve is continuous. For the type II neuron the oscillations start at an non-zero frequency, hence, the 'f-I' curve is discontinuous.

results in a continuous 'f-I' curve for type I neurons and a discontinuous 'f-I' curve for type II neurons. In both cases the critical current I_c is defined as the minimum external current needed to induce oscillations in the system.

2.4.1 Hodgkin-Huxley

In the early 1950s, Alan L. Hodgkin and Andrew F. Huxley carried out an extensive series of experiments on the giant squid axon. They used these results to develop a model which described the creation and propagation of action potential [84]. The original model incorporated three types ion channels; a sodium channel, a potassium channel and leakage channel. The leakage channel accounts for the other channels which are not described by the model. Hodgkin and Huxley used circuit dynamics to write the total current through the membrane I as

$$I = C_m \frac{\mathrm{d}V}{\mathrm{d}t} = g_K(V - V_K) + g_{Na}(V - V_{Na}) + g_l(V - V_l), \tag{2.4.1}$$

where C_m is the membrane capacitance, V is the membrane potential, g_i is the conductance of the ion channel denoted by i and V_i is the corresponding synaptic reversal potential. The leak conductance g_l is assumed to be constant, as it represents the passive flow of ions through ungated channels. The reversal potential of this channel V_l was found to be similar to the reversal potential of the potassium channel V_K, as nongated channels are permeable to potassium ions. The potassium and sodium channels open and close and as such g_K and g_{Na} change in time. Using voltage clamps and current blockers, Hodgkin and Huxley successfully modelled these conductances in terms of gating variables which we now interpret as the probability of the channel being open or closed. Figure 2.4.2 shows the behaviour of the model when the input current I is less than the critical current I_c, roughly equal to the critical current and larger than the critical current.

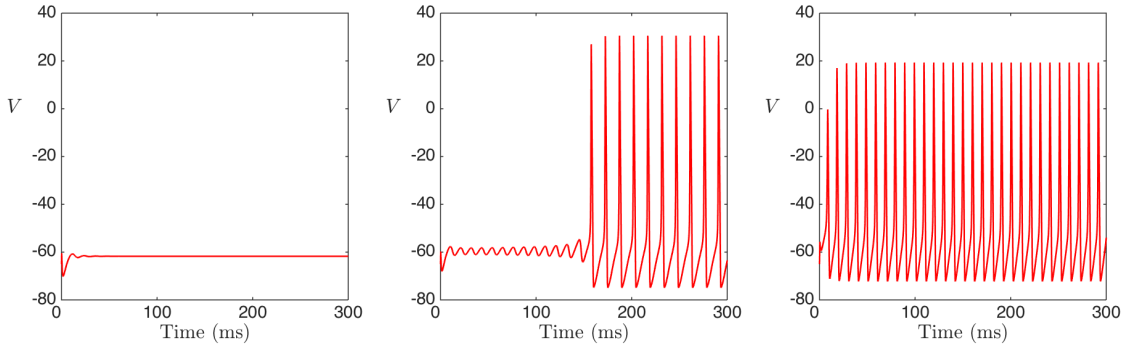

Figure 2.4.2. Hodgkin-Huxley dynamics: Plots of the membrane potential V in the Hodgkin-Huxley model (2.4.1) for a range of different input currents I. In the first plot $I < I_c$ so the input does not generate rhythmic firing activity. In the middle plot $I \simeq I_c$, and we see the emergence of rhythmic firing activity at a non-zero frequency. In the final plot $I > I_c$, hence, we see a rhythmic firing activity at a higher frequency and lower amplitude.

The Hodgkin-Huxley model built the foundations for more detailed biophysical neuron models. These extensions include, but are not limited to, other ion channels [44], stochasticity [71] and more complicated dendrite and axon geometries [103]. Notably, the Human Brain Project is attempting to reconstruct the morphologies of neurons and their dendritic trees, and have successfully reconstructed and simulated a population of roughly 31,000 Hodgkin-Huxley type neurons with 13 ion channels [120]. The Hodgkin-Huxely model has also been used as a starting point for the derivation of simplified neuron models. See [137] for a review of the Hodgkin-Huxley model and its adaptations.

2.4.2 Quadratic integrate-and-fire

The quadratic integrate-and-fire (QIF) model was designed by Latham *et al.* [112] explicity to understand the generation of low firing rate activity in the cortex. This simple spiking model describes the evolution of the neuronal voltage v, with an ordinary differential equation and a reset condition that corresponds to a firing event. When

the voltage reaches a set threshold value v_{th}, the voltage resets to the reset value v_{reset}. For a single neuron the voltage evolution is given by the following equations:

$$\begin{aligned} \frac{\mathrm{d}}{\mathrm{d}t}v(t) &= v(t)^2 + \eta, \\ v(t_{s-}) &= v_{th}, \\ v(t_{s+}) &= v_{reset}, \end{aligned} \tag{2.4.2}$$

where η is the background drive/external input and t_s is the spike time of the neuron. When $\eta > 0$ the QIF model exhibits spiking behaviour, as seen in Fig. 2.4.3a. The QIF model is a type I model so the onset of spiking occurs through a SNIC bifurcation and starts at zero frequency, as can be seen in Fig. 2.4.3b. The frequency of oscillation is given by $2\sqrt{\eta}$.

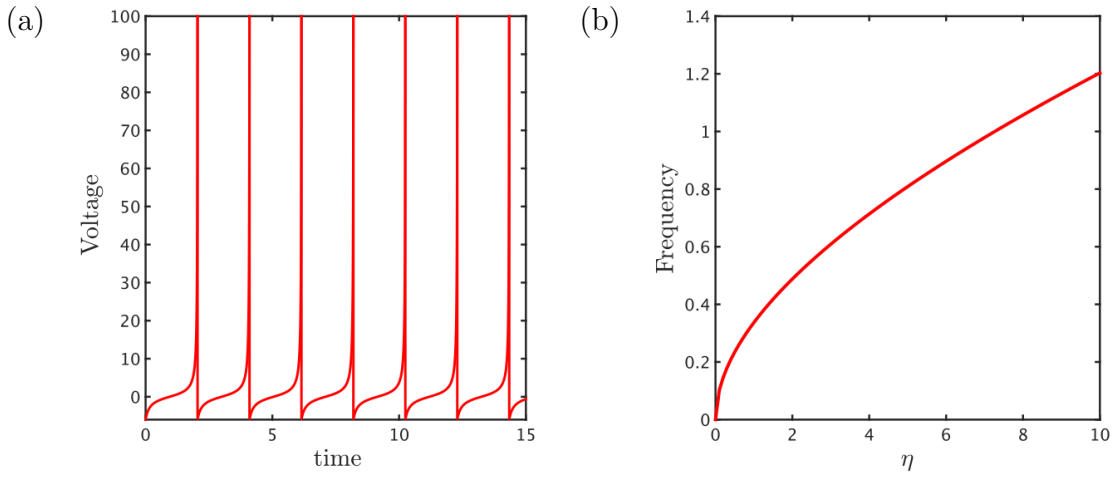

Figure 2.4.3. Quadratic integrate-and-fire model: Results for a simulation of a quadratic integrate-and-fire neuron, given by (2.4.2). (a) Voltage trace for $\eta = 2$, $v_{reset} = -6$mV, $v_{th} = 100$mV, showing the evolution of the voltage over time. (b) Frequency of oscillation as a function of the external drive η, it can be seen that the frequency is given by $2\sqrt{\eta}$.

2.4.3 Theta neuron

The θ-neuron model or Ermentrout-Kopell canonical model is now widely known throughout computational neuroscience as a parsimonious model for capturing the firing and response properties of a cortical cell [68]. It is described by a purely one dimensional dynamical system evolving on a circle according to

$$\frac{\mathrm{d}}{\mathrm{d}t}\theta = (1-\cos\theta) + (1+\cos\theta)\eta, \qquad \theta \in [-\pi, \pi), \tag{2.4.3}$$

where, as in §2.4.2, η represents a constant background drive.

For $\eta < 0$ the θ-neuron supports a pair of equilibria $\theta_\pm$, with $\theta_+ < 0$ and $\theta_- > 0$, and no equilibria for $\eta > 0$. In the former case the equilibria at θ_+ is stable and the one at θ_- unstable. In neurophysiological terms, the unstable fixed point at θ_- is a threshold for the neuron model. Any initial conditions with $\theta \in (\theta_+, \theta_-)$ will be attracted to the stable equilibrium, while initial data with $\theta > \theta_-$ will make a large excursion around the circle before returning to the rest state. For $\eta > 0$ the θ-neuron oscillates with frequency $2\sqrt{\eta}$. When $\eta = 0$ the θ-neuron is poised at a SNIC

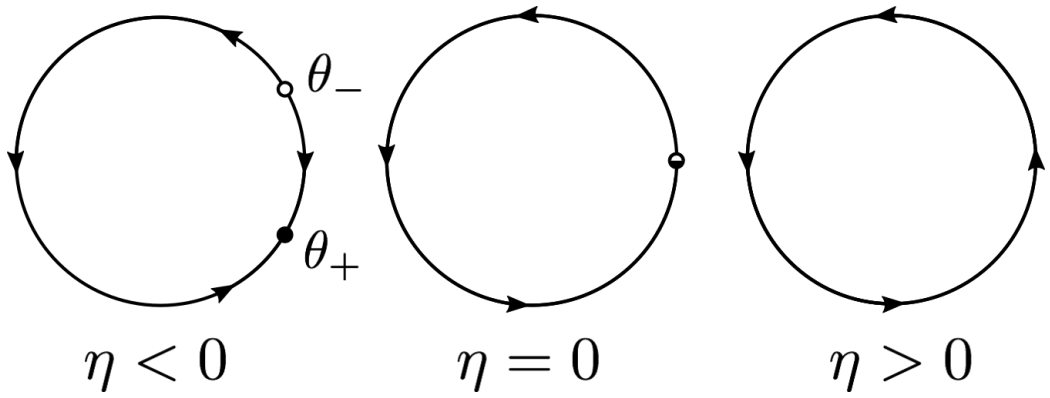

Figure 2.4.4. Theta neuron dynamics: The leftmost figure shows the system when $\eta < 0$,in this case there are two fixed points $\theta_\pm$, one of which is stable θ_+ while the other is unstable θ_-. The middle figure shows the saddle-node on an invariant circle bifurcation at $\eta = 0$, when θ_+ and θ_- collide. The last figure shows the behaviour of the system for $\eta > 0$; here no fixed points exist and the system oscillates counter-clockwise.

bifurcation. A network of θ-neurons can be described with the introduction of an index $i = 1, \ldots, N$ and the replacement $\eta \to \eta_i + I_i$, where I_i describes the synaptic input current to neuron i.

The θ-neuron model is formally equivalent to the QIF model in the limit $v_{reset} \to -\infty$ and $v_{th} \to +\infty$, under the transformation $v_i = \tan(\theta_i/2)$ (so that $\cos\theta_i = (1 - v_i^2)/(1 + v_i^2)$ and $\sin\theta_i = 2v_i/(1 + v_i^2)$). As $\lim_{v\to\infty}(2\tan^{-1} v) = \pi$, the neuron is said to 'spike' when $\theta = \pi$.

2.5 Kuramoto model

The Kuramoto model is another phase oscillator model which is often used to describe synchrony. The model describes the evolution of phases $\theta_i = \theta_i(t)$ of N coupled oscillators:

$$\frac{\mathrm{d}}{\mathrm{d}t}\theta_i = \omega_i + \frac{K}{N}\sum_{j=1}^{N}\sin(\theta_j - \theta_i), \qquad i = 1, \ldots, N, \tag{2.5.1}$$

where ω_i are the intrinsic natural frequencies and K is the coupling strength [104].

The synchrony of the population can be described by the *Kuramoto order parameter*, which is defined as

$$z(t) = R(t)e^{i\Psi(t)} = \frac{1}{N}\sum_{j}^{N} e^{i\theta_j(t)}. \tag{2.5.2}$$

Here R is the coherence and Ψ is the average phase. If a population is perfectly synchronised $R = 1$, conversely, if the system is perfectly asynchronised then $R = 0$.

These systems can be imagined on a unit disk in the complex plane, where the oscillators move around the edge of the disk and the Kuramoto order parameter lives within the disk. Figure 2.5.1 shows a snapshot of a simulation of 50 phase oscillators, the angular position of the coloured dots represent the phases of the individual oscillators and the black circle represents the Kuramoto order parameter, where its angular position is the average phase of the population Ψ and the distance

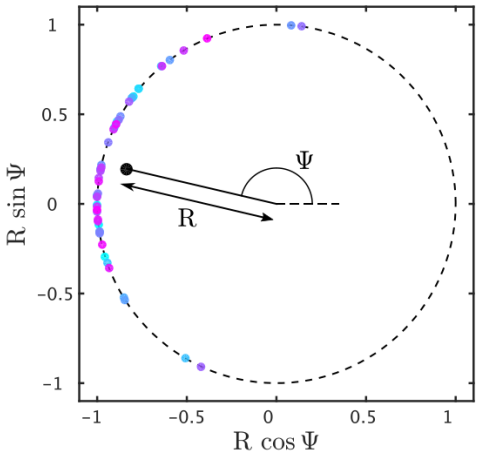

Figure 2.5.1. Kuaramoto model: Snapshot of a simulation of 50 Kuramoto oscillators, described by (2.5.1), with coupling strength $K = 6$, where the intrinsic frequencies ω_i were drawn from a Lorentzian distribution with centre π and width π.

from the centre is the coherence R.

If the intrinsic frequencies ω_i are chosen from a Lorentzian distribution, the coherence of the network obeys the following equation in the large N limit:

$$R = \sqrt{1 - \frac{2\Delta}{K}}, \tag{2.5.3}$$

where Δ is the width at half maximum of the Lorentzian distribution [104].

2.6 Neural mass modelling

It is widely believed that the main information processing power of the brain stems from the synchronous behaviour of large populations of neurons, and as measurable brain rhythms are generated by such activity it is impractical to model these oscillations with large networks of interacting single neuron models. In 1972 Hugh R. Wilson and Jack D. Cowan proposed that cortical dynamics could be studied through the

analysis of the mean field dynamics, rather than studying the underlying stocastic spiking processes themselves [165]. They successfully showed that this allowed them to employ phase plane methods to analyse the system, as well as allowing them to construct numerical solutions. This class of modelling later became known as *neural mass modelling*, a method which uses low dimensional models to describe the coarse grained activity of large populations of neurons and synapses. They are typically cast as systems of ordinary differential equations (ODEs) and in their modern incarnations are exemplified by variants of the two dimensional Wilson-Cowan model. This is a simple model which tracks the activity of an excitatory population of neurons coupled to an inhibitory population of neurons. Augmenting such models to include more realistic forms of synaptic and network interaction has proved especially successful in providing fits to neuroimaging data.

Historically one of the first examples in this area is the Zetterberg model for the EEG rhythm [169]. This minimal model of a cortical column is based on previous ideas developed by Lopes da Silva and colleagues [115, 116] and is built from three interacting neural mass models. The first neural mass represents a population of pyramidal cells, the second a population of excitatory interneurons, and the third a population of inhibitory interneurons. This model will be examined in more detail in §2.6.3. Another well known neural mass model is that of Liley [114], which pays particular attention to the role of synaptic reversal potentials; see [56] for a discussion of this model within the context of Freeman's ideas on the importance of chaos for cognition and perception [72]. As well as proving useful for understanding EEG rhythms ranging from delta through to gamma [152], neural mass models have been used to describe brain resonance phenomena [153], resting brain state activity [58] and are very popular in the neuroimaging community. In this latter instance they are often used for model driven fusion of multiple neuroimaging modalities, such as EEG and functional magnetic resonance imaging (fMRI) [158], as well as to augment the

dynamic causal modelling framework for understanding how event-related responses result from the dynamics of coupled neural populations [123]. Moreover, they are now an integral part of the Virtual Brain project that aims to deliver the first open simulation of the human brain based on individual large-scale connectivity [142], as well as play a key role in the neuro-computational modelling of neurological and psychiatric disorders [21]. This latter work is especially viable since neural mass models can incorporate accurate descriptions of synaptic processing, typically in the form of a synaptic response function that is driven by firing *rate* rather than by the arrival times of individual action potentials. This is precisely what we will discuss in the next section.

2.6.1 Framework of neural mass models

Neural mass models generate brain rhythms using the notion of population firing rates, aiming to side-step the need for large scale simulations of more realistic networks of spiking neurons. However, both approaches often make use of the same level of description for synaptic processing, in a manner that we shall now clarify.

As stated in §2.1, presynaptic firing results in the release of neurotransmitters at a synapse which causes a change in the membrane conductance of the post-synaptic neuron. This post-synaptic current may be written as $I = g(v_{\text{syn}} - v)$, where v is the voltage of the post-synaptic neuron, v_{syn} is the membrane reversal potential and g is a conductance. As was the case in the Hodgkin-Huxley model, see §2.4.1, the conductance is proportional to the probability that a synaptic receptor channel is in an open conducting state. This probability depends on the presence and concentration of neurotransmitter released by the presynaptic neuron. If the post-synaptic current I is positive (negative) we say that the synapse is excitatory (inhibitory). The effect of some synapses can be described with a function that fits the shape of the post-synaptic response due to the arrival of action potential at the pre-synaptic release site. A

post-synaptic conductance change $g(t)$ would then be given by $g(t) = \kappa s(t - T)$ for $t \geq T$, where T is the arrival time of a pre-synaptic action potential, $s(t)$ fits the shape of a realistic post-synaptic conductance, and κ the coupling strength.

For fast pulsatile interactions we may set $s(t) = \delta(t)$, where δ is a Dirac-delta function. For a more realistic form, describing a normalised post synaptic potential (PSP) with an exponential decay, we may set $s(t) = \alpha \mathrm{e}^{-\alpha t}\Theta(t)$, whilst for a more general PSP with both a rise and fall time we would set $s(t) = (1/\alpha_1 - 1/\alpha_2)^{-1}[\alpha_1 \mathrm{e}^{-\alpha_1 t} - \alpha_2 \mathrm{e}^{-\alpha_2 t}]\Theta(t)$. Here $\Theta(t)$ is a Heaviside step function included to enforce causality, and the parameters α, $\alpha_{1,2}$ are decay rates. The conductance change arising from a train of action potentials, with firing times T^m, is given by

$$g(t) = \kappa \sum_{m \in \mathbb{Z}} s(t - T^m). \tag{2.6.1}$$

If s is the Green's function of a linear differential operator Q, such that $Qs = \delta$, then we may write (2.6.1) in the equivalent form

$$Qg = \kappa \sum_{m \in \mathbb{Z}} \delta(t - T^m). \tag{2.6.2}$$

Table 2.6.1 shows list of commonly used synaptic filters s and their corresponding differential operators Q. From this point forward we will work with the choice $s(t) = \alpha^2 t \mathrm{e}^{-\alpha t}\Theta(t)$, describing the so-called α-function. This can be obtained from the difference of exponentials form described above in the limit $\alpha_{1,2} \to \alpha$, so that the corresponding differential operator Q is

$$Q = \left(1 + \frac{1}{\alpha}\frac{\mathrm{d}}{\mathrm{d}t}\right)^2. \tag{2.6.3}$$

In many neural population models it is assumed that the interactions are mediated by firing rates rather than action potentials (spikes) *per se*. To see how this might

Table 2.6.1. Synaptic filtering: Examples of differential operators and their corresponding temporal filters. The first example shows pulsatile coupling, where no synaptic filtering has been applied to the incoming spike. The second type of filter shown is an exponentially decaying function, which accounts for the slow decay of the instantaneous pulse. It does not however account for the time it take a synapse to process the incoming action potential, increasing instantaneously to the maximum value as soon as the spike arrives. The last example takes into account this synaptic processing delay, increasing smoothly to its peak value and then decaying exponentially back to zero. Note that $\Theta(t)$ represents the Heaviside function.

	$s(t)$	Q
Pulsatile	$\delta(t)$	1
Slow decay	$\alpha \mathrm{e}^{-\alpha t}\Theta(t)$	$\left(1+\frac{1}{\alpha}\frac{\mathrm{d}}{\mathrm{d}t}\right)$
Processing delay	$\left(\frac{1}{\alpha_1}-\frac{1}{\alpha_2}\right)^{-1}\left[\alpha_1 \mathrm{e}^{-\alpha_1 t}-\alpha_2 \mathrm{e}^{-\alpha_2 t}\right]\Theta(t)$	$\left(1+\frac{1}{\alpha_1}\frac{\mathrm{d}}{\mathrm{d}t}\right)\left(1+\frac{1}{\alpha_2}\frac{\mathrm{d}}{\mathrm{d}t}\right)$

arise we perform a short-time average of (2.6.2) over some time-scale τ and assume that s is sufficiently *slow* so that $\langle Qg\rangle_t$ is approximately constant, where

$$\langle x\rangle_t = \frac{1}{\tau}\int_{t-\tau}^{t} x(t')\mathrm{d}t', \tag{2.6.4}$$

then we have that $Qg = \kappa f$, where f is the instantaneous firing rate (number of spikes per unit time). For a single neuron (real or synthetic) experiencing a constant drive it is natural to assume that this firing rate is a function of the drive alone. If we assume that a neuron spends most of its time close to rest such that $v_{\mathrm{syn}} - v \approx v_{\mathrm{syn}}$, and absorb a factor v_{syn} into κ, then for synaptically interacting neurons this drive is directly proportional to the conductance state of the presynaptic neuron. Thus for a single population of identically and globally coupled neurons operating synchronously we are led naturally to equations like:

$$Qg = \kappa f(g). \tag{2.6.5}$$

A common choice for the *population* firing rate function is the sigmoid

$$f(g) = \frac{f_0}{1 + \mathrm{e}^{-r(g-g_0)}}, \tag{2.6.6}$$

which saturates to f_0 for large g. This functional form, with threshold g_0 and steepness parameter r, is not derived from a biophysical model, rather it is seen as a physiologically consistent choice. Figure 2.6.1 shows the typical shape of the firing rate function (2.6.6). The extension to multiple interacting populations is straightforward, and the popular Jansen-Rit model [89] (which is covered in § 2.6.3), provides a classic example of such a generalisation.

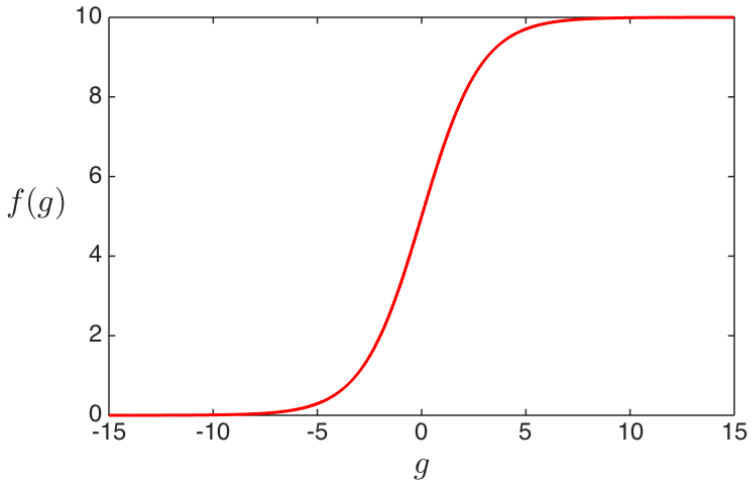

Figure 2.6.1. Sigmoidal firing rate function: Plot of the firing rate function given by (2.6.6) for $f_0 = 10$, $g_0 = 0$ and $r = 0.7$.

2.6.2 Wilson-Cowan model

Hugh R. Wilson and Jack D. Cowan were pioneers in the field of neural mass modelling. Together they developed the beautifully simple Wilson-Cowan model [165], which describes the evolution in time of the mean activity of a population of excitatory neurons (E) and a population of the inhibitory neurons (I). The pair later augmented

the original model to include a spatial component. This type of model is now known as a neural field model. We will explore neural field models in Chapter 5. Here, we will only consider the spatially clamped case.

The mean activity of the populations E/I is the proportion of cells firing in the corresponding populations. The behaviour of the system depends upon the interactions between the excitatory and inhibitory populations, as well as their self-interaction. Each population receives excitatory (inhibitory) input from itself, with coupling strength w_{EE} (w_{II}), and inhibitory (excitatory) feedback from the other population, with coupling strength w_{EI} (w_{IE}), as well as an external input P_E (P_I), see Figure 2.6.2. The model takes the following form

$$Q_E E = f(w_{EE}E + w_{EI}I + P_E), \tag{2.6.7}$$

$$Q_I I = f(w_{IE}E + w_{II}I + P_I), \tag{2.6.8}$$

where f is the sigmoidal firing rate given by (2.6.6) and Q_i is the linear first order differential operator

$$Q_i = \left(1 + \frac{1}{\alpha_i}\frac{\mathrm{d}}{\mathrm{dt}}\right), \tag{2.6.9}$$

for $i = \{E, I\}$.

Figure 2.6.3 shows a two parameter bifurcation diagram in P_E and P_I. The saddle node bifurcation curves are depicted using solid lines and the Hopf bifurcation with dashed lines. The saddle node curves collide at cusp bifurcations at $P_E \simeq -3$, $P_I \simeq -5$ and at $P_E \simeq 3$, $P_I \simeq -7$. We also observe 4 *Takens-Bodagnov* bifurcations, when the Hopf curves collides with the saddle node curves. The system has three fixed points in the area enclosed by these curves, and one elsewhere. In the area enclosed by the Hopf curves the system oscillates. This simple model has been used time and time again as the starting point for developing more complicated and biologically realistic models, see [59] for a short review.

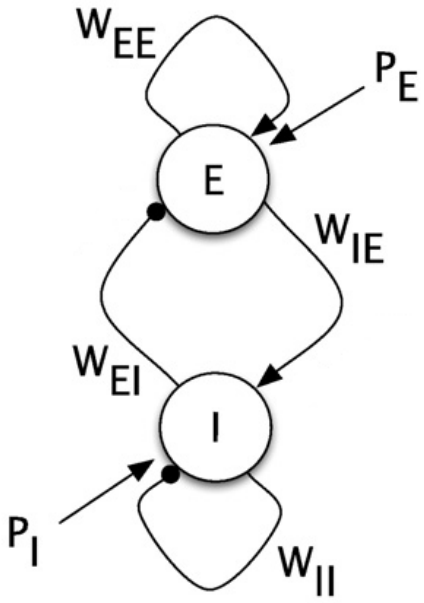

Figure 2.6.2. Schematic diagram of the Wilson-Cowan model: Diagram showing the interactions between the two neural populations in the Wilson-Cowan model; excitatory (E) and inhibitory(I)

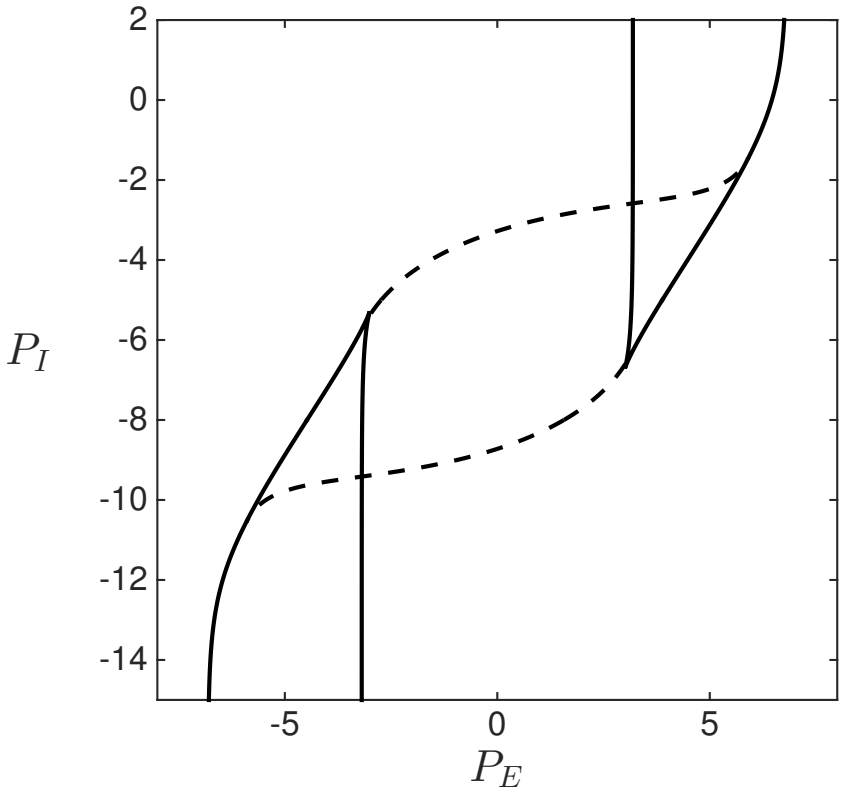

Figure 2.6.3. Bifurcation diagram for the Wilson-Cowan model: Two parameter bifurcation continuation of the external input currents P_E and P_I for the Wilson-Cowan model, as described by (2.6.7)–(2.6.8). The solid black curves represent saddle-node bifurcations and the dashed lines Hopf curves. The system has three fixed points in the areas under the lower saddle node curve and above the upper saddle node curve, and one fixed point elsewhere. Oscillatory behaviour exists in the parameter regime between the two Hopf curves. Note the existence of 2 types of co-dimension 2 bifurcations, we observe cusp bifurcations when the saddle node curves collide and Takens-Bodagnov bifurcations when the Hopf curve collides with the saddle node curve. Parameters values: $w_{EE} = -w_{EI} = w_{IE} = 10$, $w_{II} = 2$

2.6.3 Jansen-Rit model

As discussed above, the Zetterberg model was one of the first augmentations of the Wilson-Cowan model. The Zetterberg model is now more widely known as the Jansen-Rit model, due to Ben H. Jansen and Vincent G. Rit's success in using the model to better understand epileptic seizures [89]. The model consists of 3 interacting neural masses, a population of pyramidal cells (P), a population of excitatory interneurons (E) and a population of inhibitory interneurons (I). The model takes the following form

$$Q_E g_P = \kappa_P f(g_E - g_I), \tag{2.6.10}$$

$$Q_E g_E = \kappa_E f(w_E g_P) + A, \tag{2.6.11}$$

$$Q_I g_I = \kappa_I f(w_I g_P), \tag{2.6.12}$$

where Q_a is given by (2.6.3) under the replacement $\alpha \to \alpha_a$, and κ_a, w_a are connectivity constants which account for the density of synaptic connections between the

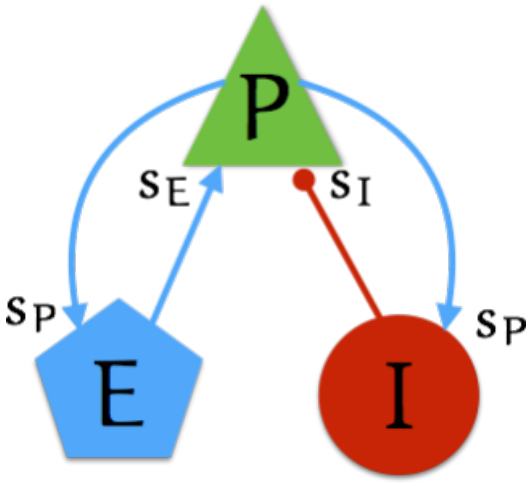

Figure 2.6.4. Schematic diagram of the Jansen-Rit model: Diagram showing the interactions between the pyramidal neurons (P), the excitatory interneurons (E) and the inhibitory interneurons (I) for the Jansen-Rit model.

populations, and A is the external input. A schematic diagram of the model is shown in Fig. 2.6.4.

As the Jansen-Rit model was developed for modelling epileptic seizures, it is important that it can support both low amplitude and high amplitude oscillations at alpha frequency. Figure 2.6.5 shows a one parameter continuation of the external input A. Solid (dashed) black lines represent stable (unstable) fixed points and green (blue) circles represent stable (unstable) limit cycles. Noteworthy is the range $A \simeq 3 - -5$, where there are two mutually stable limit cycles. If the system is in one of these oscillating states a perturbation may drive the system to the other limit cycle. This transition corresponds to an epileptic seizure if the system is perturbed from the low amplitude state to the high amplitude state.

A two parameter bifurcation of the Jansen Rit model is shown in Fig. 2.6.6. The red curve represents the continuation of the saddle-node bifurcation and the blue the Hopf bifurcation. For both a high amplitude and low amplitude oscillatory state to coexist, as in Fig. 2.6.5, κ_P must lie in the range of values between roughly 0.0315 and 0.0335, for which the system has 3 Hopf bifurcations, which is a very small range. Hence, small changes in κ_P could result in large changes to the behaviour of the system. One can imagine that the healthy brain state lies either above or below this range of κ_P values for which there are 3 Hopf bifurcations. The system only has one periodic orbit outside this region and hence, if the system were perturbed it would still return to this state.

Despite its usefulness in describing certain large scale brain rhythms, especially the alpha rhythm ($8 - -13$ Hz), it suffers the same deficiencies as all other neural mass models, namely it cannot track the level of synchrony *within* a neuronal population.

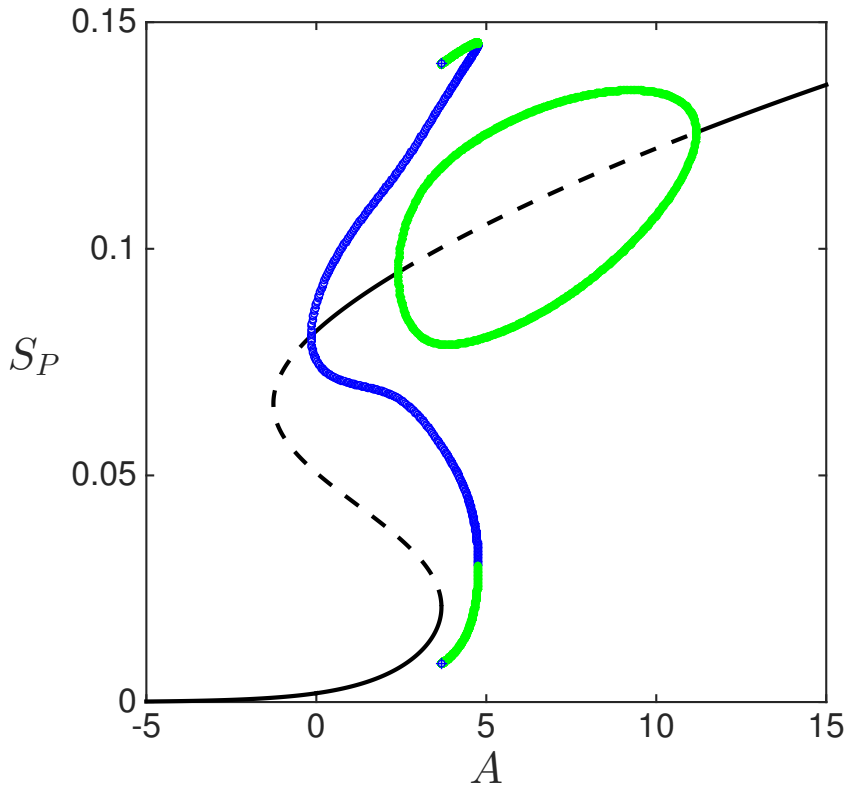

Figure 2.6.5. One parameter bifurcation diagram for the Jansen-Rit model: One parameter continuation of the fixed points of (2.6.10)–(2.6.12) in the external drive A. Solid black lines: stable fixed points; dashed black lines: unstable fixed points; green circles: stable oscillations; blue circles: unstable oscillations. Importantly there exists a range of parameter values ($A \simeq 3.5 - -5$) where both low amplitude and high amplitude oscillations exist and are stable. Parameter values: $\kappa_P = 0.0325$, $\kappa_E = 3.5$, $\kappa_I = 14.7$, $w_1 = 135$, $w_2 = 34.2$, $\alpha_E = 100$, $\alpha_I = 50$, $\nu = 5$, $r = 0.56$, $\theta = 6$.

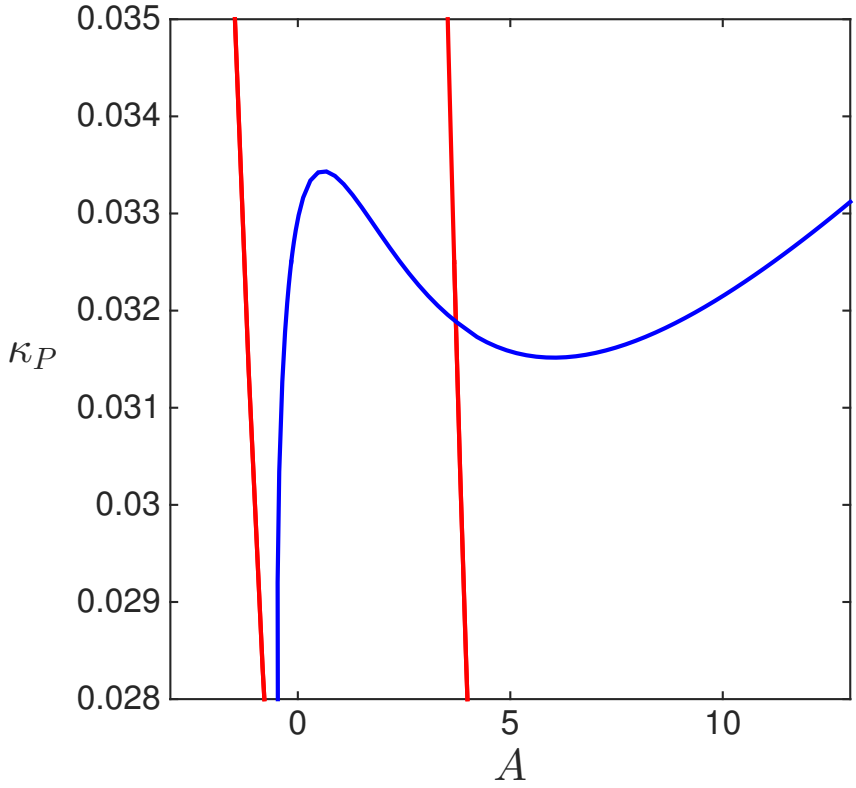

Figure 2.6.6. Two parameter bifurcation diagram for the Jansen-Rit model: Two parameter continuation of the fixed points of (2.6.10)–(2.6.12), in the external drive A and the inhibitory coupling strength κ_P. Red: saddle-node bifurcation; blue: Hopf bifurcations. Note that there are three Hopf bifurcations for only a small range of κ_P values, hence small changes in κ_P would result in large changes to the behaviour of the system, in particular the destruction of the multiple stable periodic orbits. Parameter values as in Fig. 2.6.2.

2.6.4 Downfalls of neural mass modelling

It is important to remember that at heart all neural mass models to date are essentially phenomenological, with state variables that track coarse grained measures of the average membrane potential, population firing rate or synaptic activity. At best they are expected to provide appropriate levels of description for many thousands of near identical interconnected neurons with a preference to operate in *synchrony*. This latter assumption is especially important for the generation of a sufficiently strong physiological signal that can be detected non-invasively. The variation of synchrony within a neuronal population is believed to underlie the decrease or increase of power seen in given EEG frequency bands. The former phenomenon is called event-related desynchronisation (ERD), and the latter, event-related synchronisation (ERS) [130]. Unfortunately the assumption of synchrony within neural mass models means that they cannot hope to describe ERD and ERS, at least not at the single population level. Rather, this sets a natural challenge for the next generation of neural mass models. It is precisely this issue that we deal with in this thesis.

Chapter 3

Next generation neural mass models I: Derivation and analysis

As discussed in Chapter 2, although neural mass models are motivated by neurobiological considerations they are phenomenological in nature. The state variables in these models track coarse grained measures of the average membrane potential, population firing rate or synaptic activity, and are used to provide a description for many thousands of near identical interconnected neurons operating in a near synchronous regime. In Chapter 2, we briefly introduced the phenomena known as event-related desynchronisation (ERD) and event-related synchronisation (ERS), which correspond to decreases and increases of power for the different frequency bands. We stated that these phenomena are believed to be the result of variations in the synchrony of the underlying neuronal populations. Hence, they cannot be explained using standard neural mass models, and as such we wish to develop alternative modelling approaches which can account for these changes in within-population synchrony.

As a starting point to move beyond the current neural mass models we draw inspiration from the physics of self-organised networks. The observation of macroscopic coherent states in large networks of coupled spiking neuron models has inspired a

search for equivalent low-dimensional dynamical descriptions, see [8] for a recent review of oscillatory network dynamics in neuroscience. However, although the mathematical step from microscopic to macroscopic dynamics has proved elusive for the majority of spiking models, the Ott-Antonsen (OA) ansatz [126] has provided a very useful tool in making this step for a specific case of spiking model. The OA ansatz was originally developed to construct solutions of the Kuramoto model on a reduced invariant manifold [105]. The key assumption of the ansatz is that the distribution of phases is unimodal, and hence, the ansatz is well suited to describing systems that dynamically evolve between an incoherent asynchronous state and a partially synchronised state, which is often the case in systems with interactions that are prescribed by harmonic functions. Unfortunately, it is not capable of describing cluster states; states in which the neurons form multiple groups with distinct phases. Many people have tried to extend the OA ansatz to describe cluster states, as well as other types of systems, but a general theory is yet to be found [149].

Recent work by Luke *et al.* has shown that the θ-neuron model is amenable to such a reduction for smooth non-pulsatile coupling [117]. A similar approach was taken by Montbrió *et al.*, using a formally equivalent Lorentzian ansatz to reduce a network of QIF neurons [122]. Laing extended this work to include gap junctions and first order synapses [109]. The work in this chapter shows how we can augment these approaches to incorporate a biologically realistic form of synaptic coupling which has been commonly adopted within current neural mass models. In this way we arrive at the first instance of a *next generation neural mass model*, with a derived (as opposed to postulated) population firing rate that directly depends upon the within population synchrony.

In this chapter we shall introduce the quadratic integrate-and-fire model, with a realistic form of synaptic coupling. We then transform to the θ-neuron framework and show how the OA ansatz can be applied to describe the system on a reduced

invariant manifold. The latter half of this chapter focuses on the bifurcation structure of this model for both a single population and a two population model. This analysis highlights the large window of parameter space in which stable oscillations exist and the exotic bifurcation structure of the two population model. A condensed account of this work can be found in [48].

3.1 Model description

We consider a network of N QIF neurons, which can be described as follows:

$$\frac{\mathrm{d}}{\mathrm{d}t}v_i = \eta_i + v_i^2 + I_i, \qquad i = 1, \ldots, N. \tag{3.1.1}$$

This equation can be obtained from (2.4.2), under the replacement $v \to v_i$ and $\eta \to \eta_i + I_i$. The synaptic current is chosen to be,

$$I_i = g(t)(v_{\mathrm{syn}} - v_i), \tag{3.1.2}$$

where $g(t)$ represents a common time-dependent synaptic conductance, which arises from global coupling.

The synapse is modelled as a second order synapse,

$$g(t) = \frac{\kappa}{N}\sum_{j=1}^{N}\sum_{m\in\mathbb{Z}} s(t - t_j^m), \tag{3.1.3}$$

where κ is the coupling strength, t_j^m is the mth firing time of the jth neuron and s is the synaptic filter $s(t) = \alpha^2 t\mathrm{e}^{-\alpha t}\Theta(t)$. As discussed in §2.6.1 this choice of synaptic filter allows us to write (3.1.3) as

$$Qg(t) = \frac{\kappa}{N}\sum_{j=1}^{N}\sum_{m\in\mathbb{Z}} \delta(t - t_j^m), \tag{3.1.4}$$

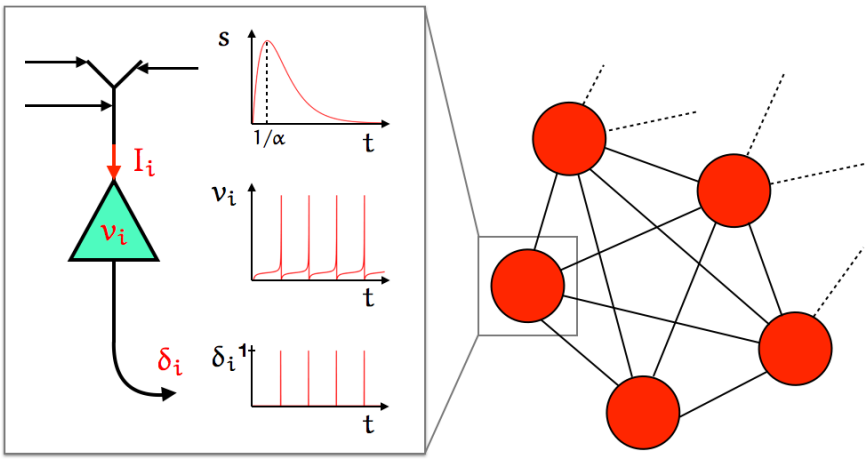

Figure 3.1.1. QIF neural network: The diagram on the right shows an all-to-all coupled network. The zoom on the left shows each of the components of (3.1.1), (3.1.3) and (3.1.4). The top plot of the zoomed section shows the shape of the synaptic filter for the case that $s(t)$ is an α-function: $s(t) = \alpha^2 t e^{-\alpha t}\Theta(t)$, where α^{-1} is the *time-to-peak*. I_i is the total synaptic current that enters the cell body and v_i is the voltage of the cell which oscillates as shown in the middle plot. The corresponding output spike train is given by a sequence of Dirac-delta functions $\delta_i = \sum_{m\in\mathbb{Z}} \delta(t - T_i^m)$, as illustrated in the bottom plot.

where

$$Q = \left(1 + \frac{1}{\alpha}\frac{\mathrm{d}}{\mathrm{d}t}\right)^2. \tag{3.1.5}$$

Figure 3.1.1 shows a network schematic, and the behaviour of each of the components in the model.

In the following we shall draw the background drives η_i from a Lorentzian distribution $L(\eta)$ with

$$L(\eta) = \frac{1}{\pi}\frac{\Delta}{(\eta - \eta_0)^2 + \Delta^2}, \tag{3.1.6}$$

where η_0 is the centre of the distribution and Δ the full width at half maximum. The significance of this choice will be made apparent later.

As shown in Fig. 3.1.2, for a model with predominantly inhibitory connections, we see patterns of coherent spiking. As we have assumed all-to-all coupling, the degree of coherence is mainly controlled by Δ, the degree of heterogeneity of the constant

current drives η_i. The numerical scheme used for these simulations is described in Appendix A.1. In this figure we also track the evolution of two macroscopic order parameters, the instantaneous firing rate r,

$$r(t) = \frac{1}{N}\sum_{j=1}^{N}\sum_{m\in\mathbb{Z}}\delta(t-t_j^m), \tag{3.1.7}$$

and the average membrane potential V,

$$V(t) = \frac{1}{N}\sum_{j=1}^{N} v_j(t). \tag{3.1.8}$$

For large N both of the order parameters r and V show a smooth temporal variation. In the case of complete synchrony we would expect these mean field signals to show a periodic temporal variation, essentially following a trajectory reminiscent of a single QIF neuron receiving periodic drive, whilst for an asynchronously firing population these mean field signals would be constant in time (modulo finite size fluctuations). To quantify the degree of coherence (or phase-locking) within an oscillatory population it is convenient to use the Kuramoto order parameter (2.5.2). However, it is first necessary to recast the model in terms of *phase* variables.

As discussed in §2.4.3 the link between the QIF neuron and the θ-neuron is well known, and as such it is natural to introduce the phase variable $\theta_i \in [-\pi, \pi)$ according to $v_i = \tan(\theta_i/2)$, with reset conditions $v_i(t_{s+}) = \infty$ and $v_i(t_{s-}) = -\infty$. In this case we arrive at the θ-neuron network

$$\frac{\mathrm{d}}{\mathrm{d}t}\theta_i = (1-\cos\theta_i) + (1+\cos\theta_i)(\eta_i + g(t)v_{\mathrm{syn}}) - g(t)\sin\theta_i, \tag{3.1.9}$$

$$Qg = 2\frac{\kappa}{N}\sum_{j=1}^{N} P(\theta_j). \tag{3.1.10}$$

Here $P(\theta) = \delta(\theta-\pi)$ and is periodically extended such that $P(\theta) = P(\theta+2\pi)$, and we

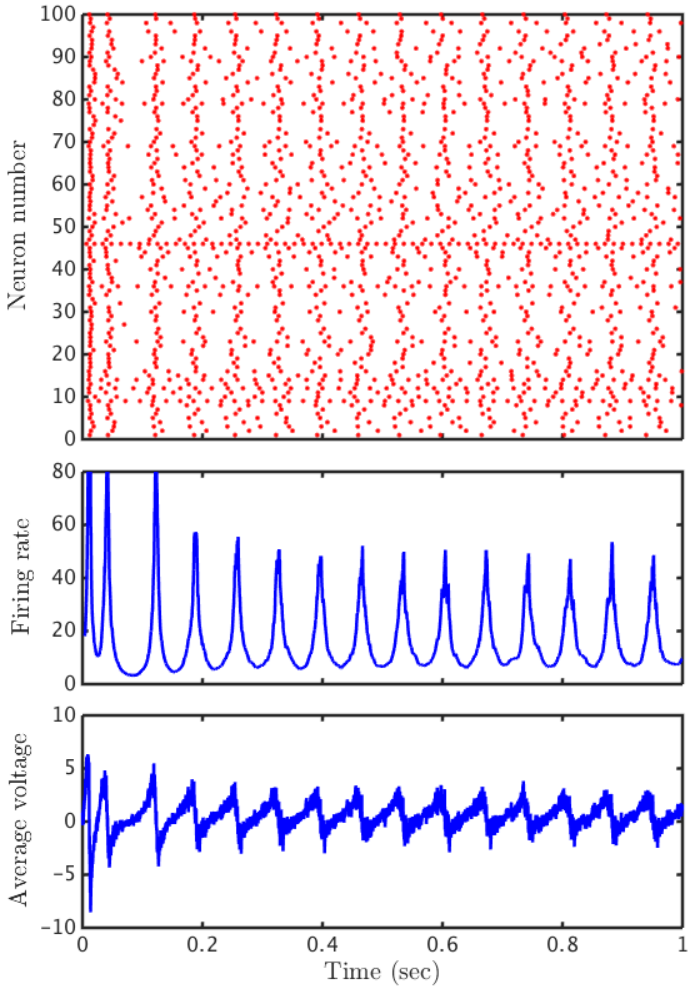

Figure 3.1.2. QIF dynamics: The top plot shows a raster depicting the spike times for a sample of size 100 in a network of 500 QIF neurons, given by (3.1.1)–(3.1.6). The lower plots show the mean field variables: the firing rate r and the average voltage V. Parameter values are chosen such that the system exhibits partial synchrony; $\eta_0 = 20$, $\Delta = 0.5$, $v_{\text{syn}} = -10$, $\kappa = 3.14$, $\alpha = 0.95$.

have used the result that $\delta(t-t_j^m) = |\dot{\theta}_j(t_j^m)|\delta(\theta_j(t)-\pi)$ (this corresponds to a simple change of variables). We will only consider the case that θ_j increases through π (so that spikes are only generated on the upswing of the corresponding voltage variable).

As well as naturally providing a phase variable the θ-neuron network is more straightforward to simulate as the model has continuous trajectories on an N-torus (and there is no need to handle the discontinuous reset conditions). As was the case for the Kuramoto model, it is possible to describe the system of phase oscillators in terms of the Kuramoto order parameter, which is defined by (2.5.2). We reiterate that if the population is perfectly synchronised then $R = 1$ and similarly if it is perfectly asyncronous then $R = 0$. In Fig. 3.1.3 we show a sequence of snapshots of the Kuramoto order parameter for the dynamics shown in Fig. 3.1.2, as well as the time evolution of R and Ψ. Much as the order parameters (r, V) vary smoothly with time (for large N) so does the pair (R, Ψ). The numerical scheme used to compute these figures is described in Appendix A.2.

Figure 3.1.4 illustrates the type of network evolution that can be generated with different values of synchrony. Here we show the distribution of phases for different values of the network coherence as well as the average network current. As one would expect, a highly synchronous regime produces a pulse-like periodic signal. Whereas in the partially synchronous regime the synaptic current is smoother, yet still periodic. When the system is completely asynchronous the observed synaptic current is constant, as all of the neurons fire asynchronously.

3.2 Ott-Antonsen reduction

In the limit $N \to \infty$ the state of the network at time t can be described by a continuous probability distribution function $\rho(\eta, \theta, t)$. Where $\rho(\eta, \theta, t)\mathrm{d}\theta$ corresponds to the fraction of oscillators with phase between θ and $\theta + \mathrm{d}\theta$ and constant background

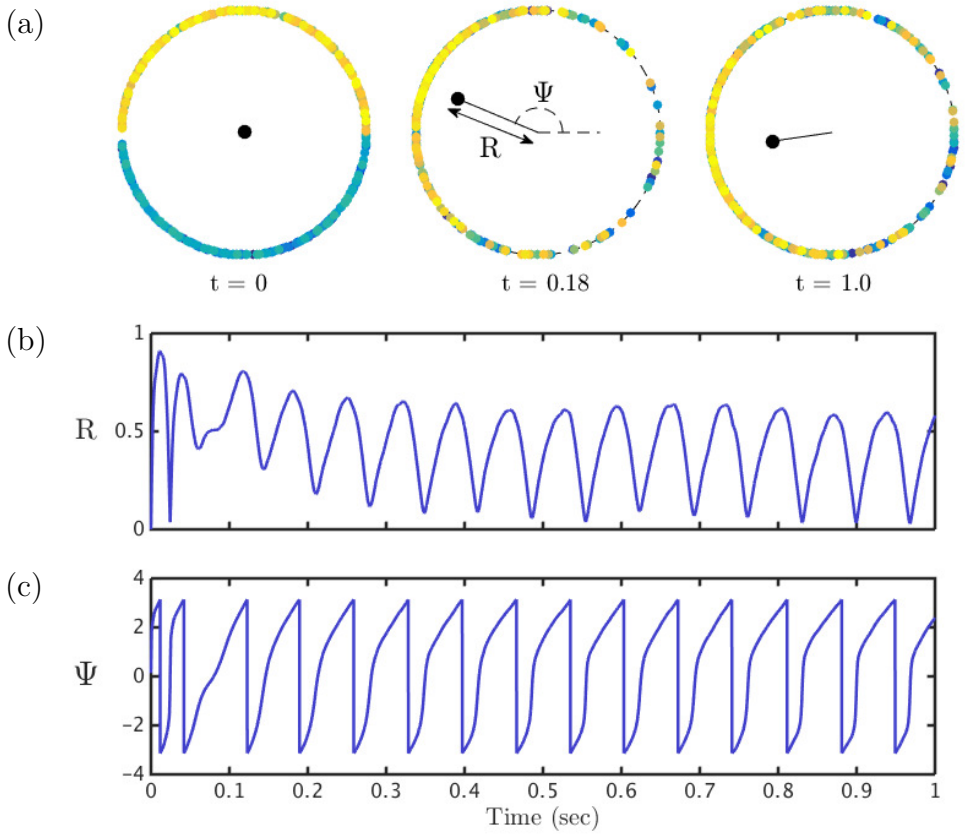

Figure 3.1.3. Results for a network of θ-neurons (3.1.9)–(3.1.10)**:** (a) The top set of plots show the phases of the individual neurons, represented by the coloured dots, at three different values of time t. The phase of each neuron is the angular position of the coloured dot. The black dot in the centre represents the Kuramoto order parameter $z = Re^{i\Psi}$. In the left most plot the system is asynchronous and as such $z \simeq 0$. The middle plot illustrates that the length from the centre of the disk to the black dot represents the population synchrony R, and the average phase Ψ, is represented by the angular position of the black dot. The right plot shows the system at a later point in time. (b) A time series of the population synchrony R. (c) The evolution of the average phase Ψ as functions of time. One observes that both the population synchrony and average phase continuously oscillate. Parameter values as in Fig. 3.1.2.

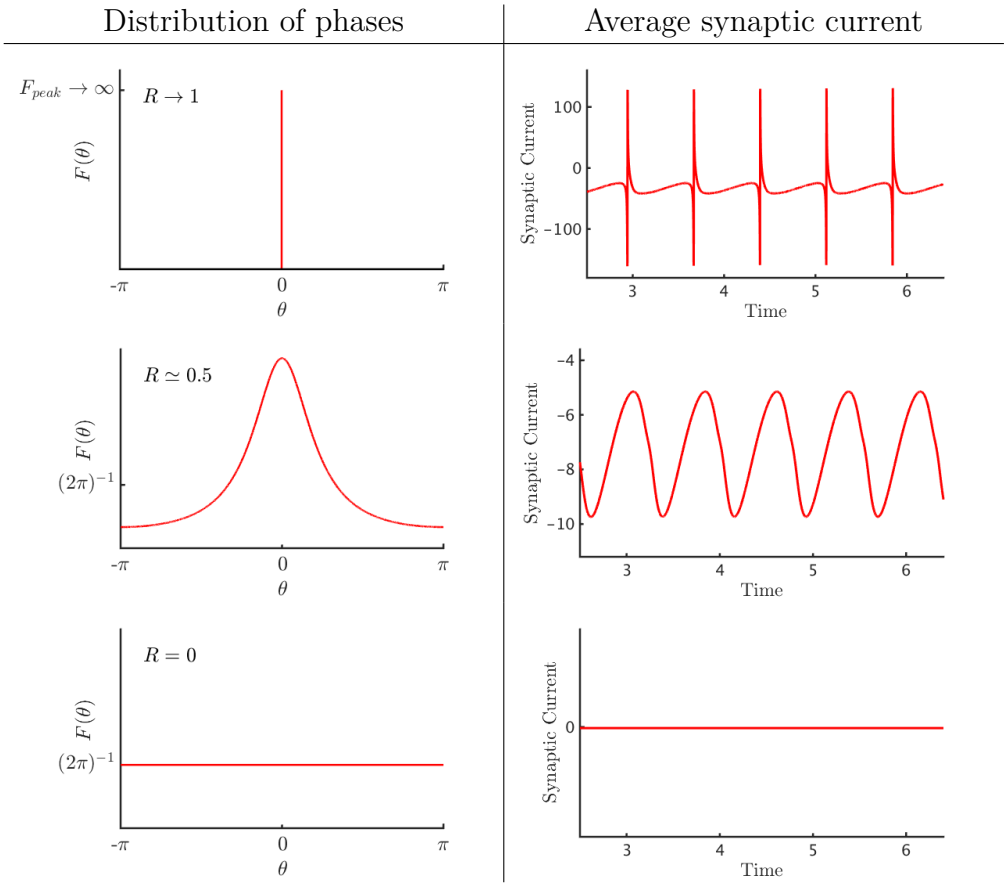

Figure 3.1.4. Distribution of phases: Figure illustrating the distribution of phases $F(\theta)$ in the large N limit and the average synaptic current for different values of the population coherence R. For simplicity we have fixed the choice of time so that $\Psi(t) = 0$. When the population is completely synchronous ($R = 1$) all of the neurons have the same phase and, as a result, all of the neurons fire together such that $F(\theta) = \delta(\theta)$ and the average synaptic current is very *spiky*. In the regime where $R \simeq 0.5$ the phases are more distributed. Although a dominant phase can be clearly identified (by the peak value), not all neurons have this phase. The OA ansatz gives the shape of the distribution in the form $F(\theta) = (2\pi)^{-1}(1-|z|^2)/(|e^{i\theta} - z|^2)$. This spread in the phase distribution acts to smooth out the spikes in the average synaptic current to create a smooth oscillatory signal. When the population of neurons is completely asynchronous ($R = 0$) there is no dominant phase and every phase is equally probable such that $F(\theta) = 1/(2\pi)$. In this case all of the neurons fire at different times as their phases are uniformly distributed which yields a constant synaptic current. Note that the peak in the distribution of phases move as the system evolves in time, with a velocity $\dot{\Psi}$.

drive η at time t. The probability density function $\rho(\eta, \theta, t)$ satisfies the following continuity equation (arising from the conservation of oscillators):

$$\frac{\partial \rho}{\partial t} + \frac{\partial}{\partial \theta}(\rho v_\theta) = 0, \tag{3.2.1}$$

where v_θ is a given realisation of $\dot{\theta}$ given by (3.1.9) (remembering that η is a random variable),

$$v_\theta = (1 - \cos\theta) + (1 + \cos\theta)(\eta + g v_{\text{syn}}) - g \sin\theta. \tag{3.2.2}$$

The global drive to the network, given by the right hand side of (3.1.10), can be constructed as

$$\lim_{N\to\infty} \frac{1}{N} \sum_{j=1}^{N} P(\theta_j) = \int_0^{2\pi} \mathrm{d}\theta \int_{-\infty}^{\infty} \mathrm{d}\eta \rho(\eta, \theta, t) P(\theta). \tag{3.2.3}$$

Hence, the evolution of the synaptic conductance g is given by

$$Qg = \frac{\kappa}{\pi} \sum_{m\in\mathbb{Z}} \int_0^{2\pi} \mathrm{d}\theta \int_{-\infty}^{\infty} \mathrm{d}\eta \rho(\eta, \theta, t) \mathrm{e}^{im(\theta-\pi)}, \tag{3.2.4}$$

where we have used the result that $2\pi P(\theta) = \sum_{m\in\mathbb{Z}} \mathrm{e}^{im(\theta-\pi)}$. The formula for v_θ may be written conveniently in terms of $\mathrm{e}^{\pm i\theta}$ as

$$v_\theta = \beta \mathrm{e}^{i\theta} + \gamma + \overline{\beta} \mathrm{e}^{-i\theta}, \tag{3.2.5}$$

where $\beta = ((\eta - 1) + v_{\text{syn}} g + ig)/2$ and $\gamma = (\eta + 1) + v_{\text{syn}} g$, and $\overline{\beta}$ denotes the complex conjugate of β.

Here we make use of the OA ansatz by assuming that $\rho(\eta, \theta, t)$ has the product structure

$$\rho(\eta, \theta, t) = L(\eta) F(\eta, \theta, t), \tag{3.2.6}$$

where $L(\eta)$ is the Lorentzian distribution defined by (3.1.6). This separation, which is necessary for the reduction, can be viewed as a convenient factorisation. Since $F(\eta, \theta, t)$ should be 2π periodic in θ it can be written as a Fourier series:

$$F(\eta, \theta, t) = \frac{1}{2\pi}\left[1 + \left\{\sum_{n=1}^{\infty} F_n(\eta, t)\mathrm{e}^{in\theta} + \mathrm{cc}\right\}\right], \tag{3.2.7}$$

where cc denotes complex conjugate. The insight in [126] was to restrict the Fourier coefficients such that $F_n(\eta, t) = a(\eta, t)^n$, where $|a(\eta, t)| \leq 1$ to avoid divergence of the series. There is also a further requirement that $a(\eta, t)$ can be analytically continued from real η into the complex η-plane, that this continuation has no singularities in the lower half η-plane, and that $|a(\eta, t)| \to 0$ as $\mathrm{Im}\,\eta \to -\infty$. If we now substitute (3.2.5) into the continuity equation (3.2.1), use the OA ansatz, and balance terms in $\mathrm{e}^{i\theta}$ we obtain an evolution equation for $a(\eta, t)$ as

$$\frac{\partial}{\partial t}a + ia^2\beta + ia\gamma + i\overline{\beta} = 0. \tag{3.2.8}$$

It is now convenient to introduce the continuum Kuramoto order parameter

$$z(t) = \int_0^{2\pi} \mathrm{d}\theta \int_{-\infty}^{\infty} \mathrm{d}\eta \rho(\eta, \theta, t)\mathrm{e}^{i\theta}, \tag{3.2.9}$$

where $|z| \leq 1$. Substituting both (3.2.6) and (3.2.7) into (3.2.9), and performing the integral over θ we find

$$\overline{z}(t) = \int_{-\infty}^{\infty} \mathrm{d}\eta L(\eta) a(\eta, t). \tag{3.2.10}$$

Here, we have made use of the orthogonality properties of $\mathrm{e}^{i\theta}$, namely $\int_0^{2\pi} \mathrm{e}^{ip\theta}\mathrm{e}^{iq\theta}\mathrm{d}\theta = 2\pi\delta_{p,-q}$, where δ_{ij} is the Kronecker delta function. By noting that the Lorentzian (3.1.6) has simple poles at $\eta_\pm = \eta_0 \pm i\Delta$, we may use contour integration to evaluate the integral in (3.2.10) along a large semi-circle contour in the lower half η-plane. This yields the result $\overline{z}(t) = a(\eta_-, t)$. It is important to highlight the significance of the

choice of distribution for the background drives η_i. This step in the reduction can only be completed if the distribution contains a simple pole in the lower half η-plane. Here, we have chosen a Lorentzian distribution but any distribution which satisfies this criteria can be used. Using similar techniques to evaluate (3.2.4), we find that the mean field dynamics of the synaptic conductance g can be written as

$$Qg = \kappa f(z), \tag{3.2.11}$$

where

$$\begin{aligned} f(z) &= \frac{1}{\pi}\left[1 + \left\{\sum_{m=1}^{\infty}(-1)^m z^m + \text{cc}\right\}\right] \\ &= \frac{1}{\pi}\frac{1-|z|^2}{1+z+\overline{z}+|z|^2}. \end{aligned} \tag{3.2.12}$$

where $|z| < 1$.

It is illuminating to express f as function of W using (3.2.18) from which we find

$$f(W) = \frac{1}{\pi}\frac{W+\overline{W}}{2} = r. \tag{3.2.13}$$

This demonstrates that $f(z)$ is indeed the firing rate of the population, driving the global synaptic current. Figure 3.2.1 shows f as a function of z. As expected f takes its highest value when $z \simeq \mathrm{e}^{i\pi}$, corresponding to high synchrony where all of the neurons fire and reset at the same time. To obtain the dynamics for z we note that $\overline{z}(t) = a(\eta_-, t)$, substitute this into (3.2.8), and take the complex conjugate which yields,

$$\frac{\mathrm{d}z}{\mathrm{d}t} = -i\frac{(z-1)^2}{2} + \frac{(z+1)^2}{2}(-\Delta + i\eta_0 + v_{\text{syn}}g) - \frac{z^2-1}{2}g. \tag{3.2.14}$$

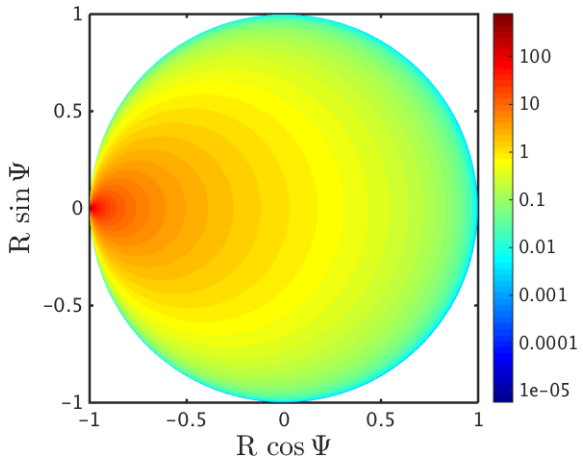

Figure 3.2.1. Firing rate dynamics: Density plot showing the firing rate f (3.2.12) as a function of the complex number $z = Re^{i\Psi}$. Firing is highest near $z = e^{i\pi}$, which corresponds to highly synchronous behaviour where all of the phases of the neurons go through π simultaneously.

It is convenient to separate (3.2.14) as $\mathrm{d}z/\mathrm{d}t = \mathcal{F}(z;\eta_0,\Delta) + \mathcal{G}(z,g;v_{\mathrm{syn}})$, where

$$\mathcal{F}(z;\eta_0,\Delta) = -i\frac{(z-1)^2}{2} + \frac{(z+1)^2}{2}\left[-\Delta + i\eta_0\right], \tag{3.2.15}$$

$$\mathcal{G}(z,g;v_{\mathrm{syn}}) = i\frac{(z+1)^2}{2}v_{\mathrm{syn}}g - \frac{z^2-1}{2}g. \tag{3.2.16}$$

As a reminder to the reader Δ is the heterogeneity parameter which is defined as the width of the Lorentzian distribution, η_0 is the mean of the background drive which is the centre of the Lorentzian distribution and v_{syn} is the synaptic reversal potential. Here we interpret (3.2.15) as describing the intrinsic population dynamics and (3.2.16) the dynamics induced by synaptic coupling. Thus the form of the mean field model is precisely that of a standard neural mass model discussed in §2.6, and given by (2.6.5). Importantly the firing rate f is a derived quantity that is a real function of the complex Kuramoto order parameter for synchrony. This in turn is described by a

complex ODE with parameters from the underlying microscopic model.

Figure 3.2.2 shows results for a simulation of 500 θ-neurons (red) and a simulation of the reduced mean field model (blue). It is strikingly clear that the two simulations agree very well. If the size of the population in the large scale simulations is reduced then one can begin to see finite size fluctuations as expected. Remarkably, the mean field equations provide a good fit for the dynamics of a θ-neuron network with a population size as small as 10. The finite size effects are apparent, but the underlying behaviour is visible and still matches the mean field dynamics. The macroscopic order parameters (r, V) in the reduced mean field model are plotted in Fig. 3.2.3. As expected, they behave similarly to the corresponding order parameters for the large scale simulations plotted in Fig. 3.1.2. Likewise, the mean field representation of (R, Ψ), plotted in Fig. 3.2.4, agree extremely well with those shown in Fig. 3.1.3. The mean field simulations can easily be performed using MATLAB's built in ODE solvers.

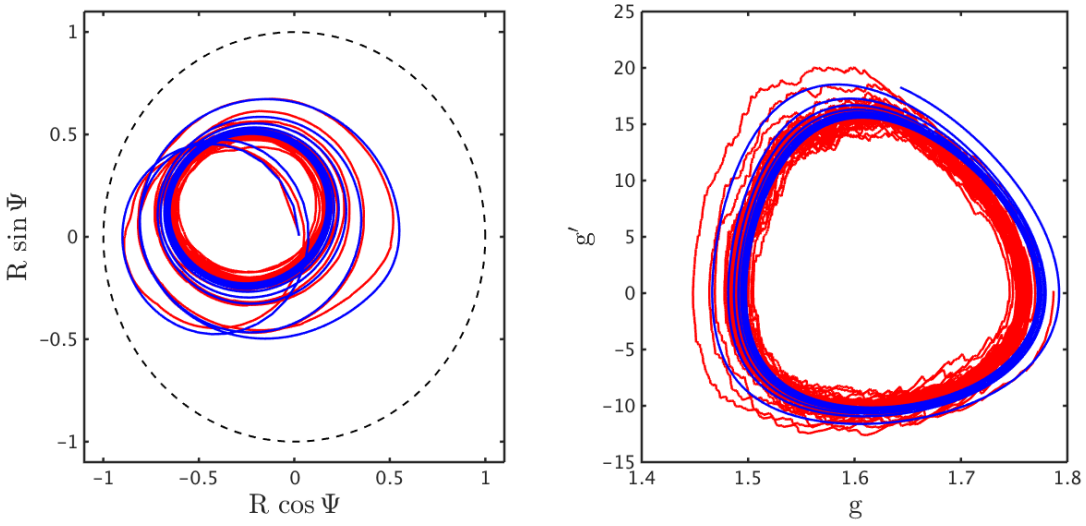

Figure 3.2.2. Validity of reduction: Comparison between the reduced mean field network (3.2.15)–(3.2.16) (blue) and simulation a network of 500 θ-neurons (3.1.9)–(3.1.10) (red). Phase plane for the Kuramoto order parameter $z = Re^{i\Psi}$ is shown on the left and the phase plane for the synaptic conductance g is shown on the right. Parameter values as in Fig. 3.1.2.

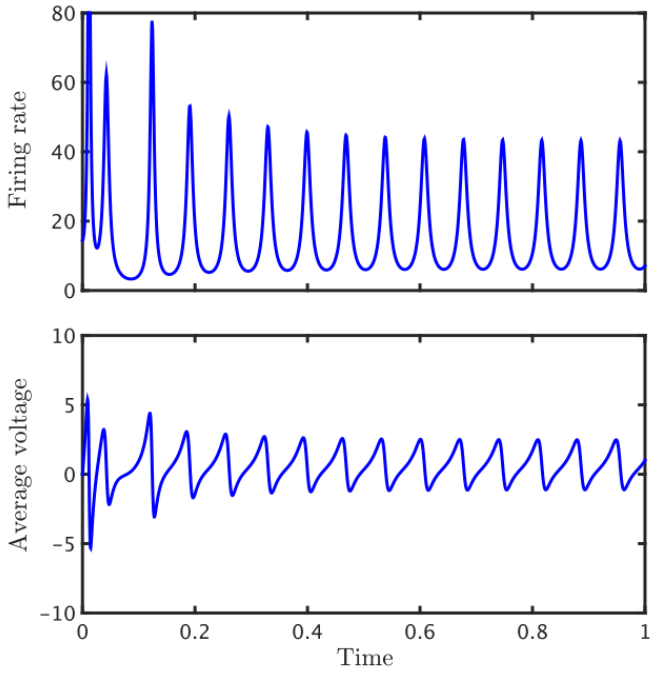

Figure 3.2.3. Mean field reduction for a QIF network: Time series for the mean field variable $W = \pi r + iV$, where r is the population firing rate and V is the average voltage. Comparing these plots to the corresponding plots for a 500 neuron simulation in Fig. 3.1.2 it is clear to see that they agree well. The finite size fluctuation for V are quite apparent when comparing the results for the large scale simulation to those of the reduced mean field model. However, the overall behaviour is similar. Parameters as in Fig. 3.1.2.

Interestingly, Montbrió *et al.* have recently shown that a similar reduction exists for a network of QIF neurons. Using a Lorentzian distribution as their ansatz for the distribution of membrane potentials v_i, they have found an alternative continuity equation which describes the system in terms of the population firing rate r and the average membrane potential V. More importantly they also provided a mechanism for transforming between order parameters in the phase and the voltage descriptions with the use of a conformal transformation [122]. The key observation made by Montbrió *et al.* was to note that the Lorentzian distribution represents the Poisson distribution on the half-plane and the OA ansatz corresponds to the the Poisson distribution on

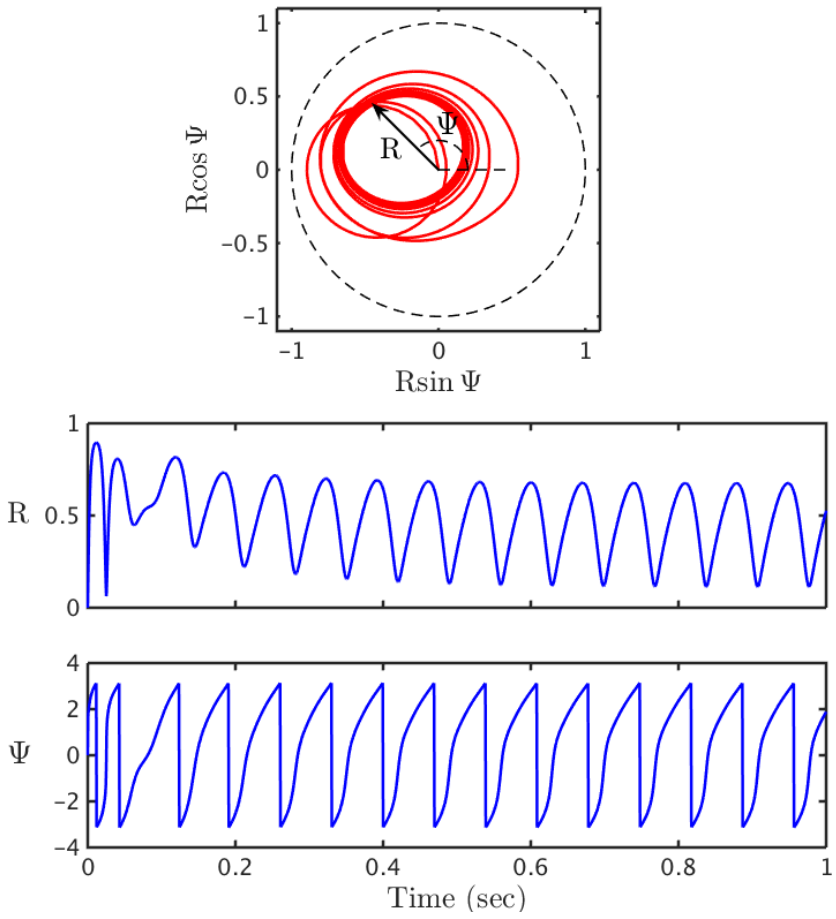

Figure 3.2.4. Mean field dynamics of the θ-neuron network (3.2.15)–(3.2.16)**:** Phase plane of the Kuramoto order parameter z, showing $R(t)$ andn$\Psi(t)$, as well as a time series for both R and Ψ. Once again the plots match very well with the corresponding plots for the simulation of 500 θ-neurons in Fig. 3.1.3. Interestingly even the initial behaviour is well matched. Parameters as in Fig. 3.1.3.

the unit disk, and hence, it is easy to establish a conformal mapping between the two representations. If we introduce the complex order parameter for the voltage description as

$$W = \pi r + iV, \tag{3.2.17}$$

then the conformal transformation is given as

$$W = \frac{1 - \overline{z}}{1 + \overline{z}}, \tag{3.2.18}$$

where $\overline{z}$ denotes the complex conjugate of z. We refer the reader to [122] for a more thorough description of the Lorentzian reduction, used by Montbrió *et al.*.

3.3 Next generation neural mass model: analysis

The mean field model derived in §3.2 is a natural candidate for a next generation neural mass model. It generalises the form of the phenomenological neural mass model whilst maintaining contact with biological reality in that it preserves the notion of both population firing rate *and* synchrony. Note that a similar model has recently been discussed by Laing [110], although here the focus was on smooth (non-pulsatile) interactions and a first order synapse model (namely $Q = (1 + \alpha^{-1}\mathrm{d}/\mathrm{d}t)$) with no provision for synaptic reversal potentials. In mathematical terms we are now faced with understanding the dynamics of a coupled system of ODEs given by

$$Qg = \kappa f(z), \tag{3.3.1}$$

$$\frac{\mathrm{d}z}{\mathrm{d}t} = \mathcal{F}(z; \eta_0, \Delta) + \mathcal{G}(z, g; v_{\mathrm{syn}}), \tag{3.3.2}$$

with f, $\mathcal{F}$ and $\mathcal{G}$ given by (3.2.12), (3.2.15) and (3.2.16) respectively, and Q a linear differential operator given by (3.1.5). One practical way to assess the emergent behaviour of the model under parameter variation is through numerical bifurcation analysis. We now pursue this for (3.3.1) and (3.3.2) as well as for its natural extension to cover two interacting populations.

3.3.1 Single population

We first consider the case of a predominantly inhibitory population. Using XPPAUT [66] we find that for a wide range of system parameters it is possible to find a Hopf bifurcation of a steady state to a periodic orbit under parameter variation of η_0 (controlling the mean value of the background drive). Figure 3.3.1 shows such a bifurcation diagram. It can be seen that a stable periodic orbit exists for η_0 roughly between 0 and 90. It is also possible to find a Hopf bifurcation in a predominantly excitatory population, provided we have sufficiently fast synapses $\alpha \gtrsim 2.5$. In the case of a predominantly excitatory population we also have a series of saddle-node bifurcations. Figure 3.3.2 shows a one parameter continuation in η_0, illustrating that the Hopf bifurcation is subcritical in this case. A two parameter continuation was computed in the mean background drive η_0 and the synaptic reversal potential v_{syn} to trace both the Hopf and the saddle-node bifurcations, see Fig. 3.3.3. It can be seen that the saddle-node bifurcation only exists for positive v_{syn} (excitatory coupling) and negative η_0 (inhibitory background drive). The switch from sub- to super-critical behaviour appears to happen at $v_{\text{syn}} \simeq 0$, when the coupling changes from being excitatory dominated to inhibitory dominated.

To illustrate the large region of parameter space that can support oscillations we show a two parameter continuation of the Hopf bifurcation in Δ and η_0 (the parameters which control the shape of the Lorentzian distribution (3.1.6)), for several values of the coupling strength κ and reversal potential v_{syn}, see Fig. 3.3.4. The

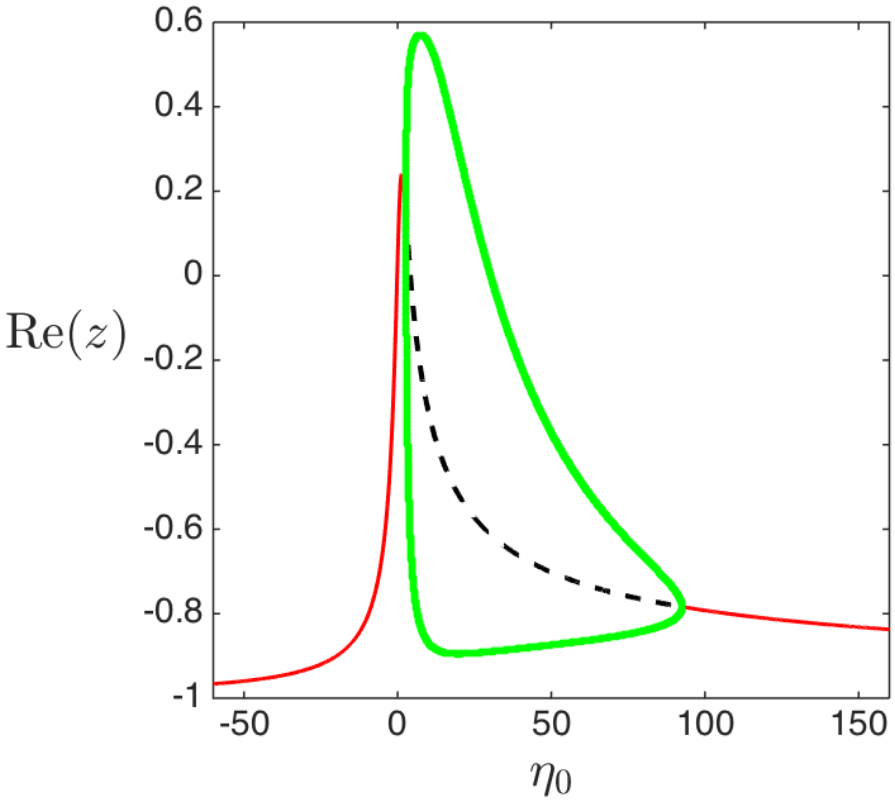

Figure 3.3.1. Bifurcation diagram for an inhibition dominated network: One parameter continuation in the mean background drive η_0, for the mean field model described by (3.2.15)–(3.2.16) with negative value of the synaptic reversal potential v_{syn} (predominantly inhibitory synapses). For $\eta_0 \leq 0$ there exists a stable fixed point (solid red line). At $\eta_0 \simeq 0$ the fixed point goes unstable (dashed black line) at a Hopf bifurcation and we see the emergence of periodic solutions. The solid green curve shows the minimum and maximum of the periodic orbit. These periodic solutions are destroyed at a second Hopf bifurcation at $\eta_0 \simeq 90$. Parameter values: $\Delta = 0.5$, $v_{\text{syn}} = -10$, $\kappa = 1$, $\alpha = 3$.

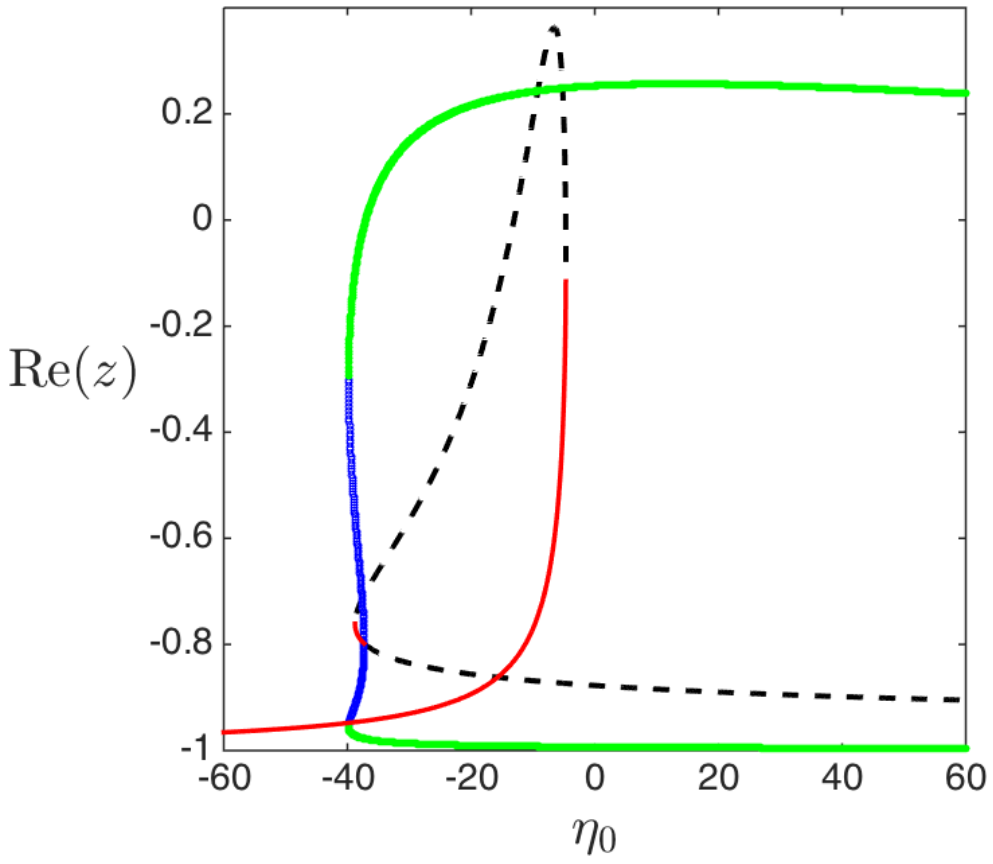

Figure 3.3.2. Bifurcation diagram for an excitation dominated network: One parameter continuation in the mean background drive η_0, for the mean field model described by (3.2.15)–(3.2.16) with a positive value of the synaptic reversal potential v_{syn} (predominantly excitatory synapses). For $\eta_0 \leq -40$ there exists a stable fixed point (solid red line). At $\eta_0 \simeq -40$ there is a saddle-node of periodic orbits bifurcation, where we see the emergence of both stable (green) and unstable (blue) limit cycles. As η_0 is increased further we see a saddle-node bifurcation, and hence the creation of another stable fixed point, as well as an unstable fixed point (dashed black). The stable branch then goes unstable at a subcritical Hopf bifurcation which destroys the unstable branch of periodic solutions. As η_0 is increased through roughly 5 there is a second saddle-node bifurcation, which destroys the remaining stable fixed point solution and one of the unstable solutions, leaving a single unstable fixed point and stable periodic solution. Parameter values: $\Delta = 0.5$, $v_{\text{syn}} = 10$, $\kappa = 5$, $\alpha = 3$.

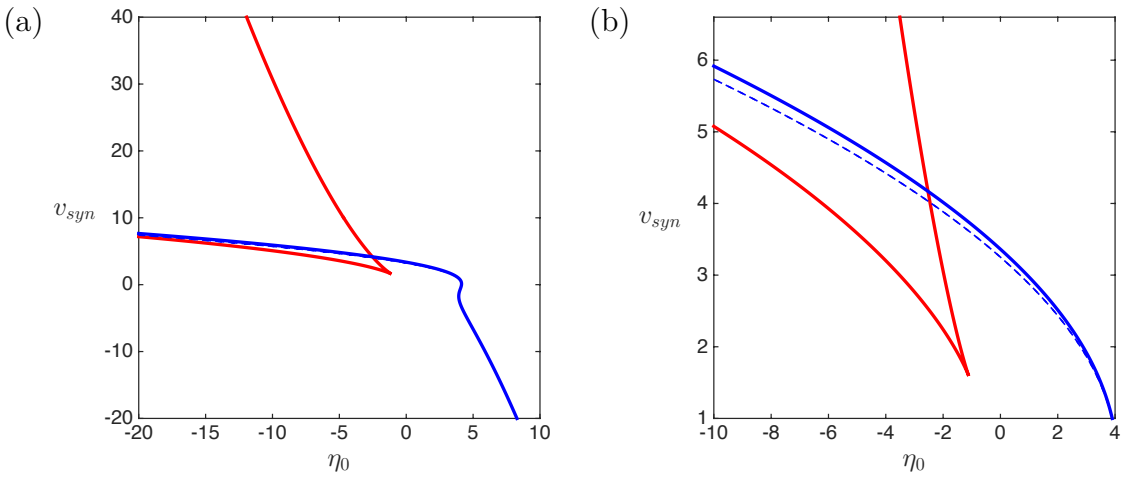

Figure 3.3.3. Two parameter bifurcation diagrams for the mean field model (3.2.15)–(3.2.16)**:** (a) Two parameter continuation in the mean background drive η_0 and the synaptic reversal potential $v_{\rm syn}$, showing the Hopf curve (blue) and the saddle-node curves (red), which meet at a cusp bifurcation at $\eta_0 \approx 1$, $v_{\rm syn} \approx 2$. Oscillatory solutions exist above the Hopf curve, and there are 3 fixed points between the two saddle-node curves. In the region above the Hopf curve and inside the saddle-node curves there exist a limit cycle, a stable solution and two unstable solutions. In the region below the Hopf curve and inside the saddle-node curves there exist two stable solutions and an unstable solution. (b) Zoomed version of plot on the left, to show the saddle-node of periodic orbits (dashed blue). Parameter values as in Fig.3.3.2.

system supports oscillations in the regions below the curves.

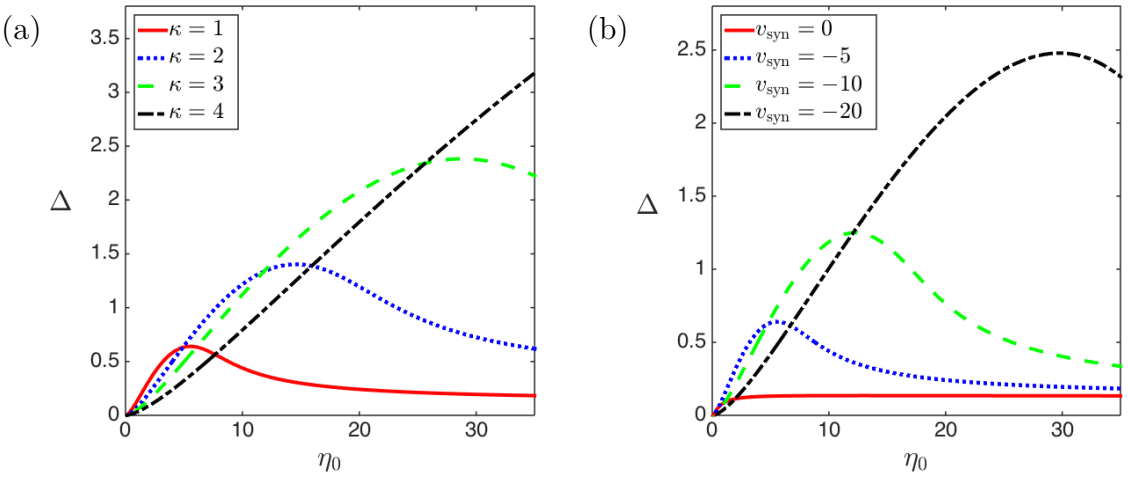

Figure 3.3.4. Two parameter bifurcation diagram for a predominantly inhibitory network: Two parameter continuations of a Hopf bifurcation, for the model (3.2.15)–(3.2.16), in the mean background drive η_0 and the heterogeneity of the background drive Δ, for various values of (a) the coupling strength κ and (b) the synaptic reversal potential v_{syn}. The system oscillates for the parameter values under the curves. Parameter values as in Fig. 3.3.1.

3.3.2 Two populations

Next we consider a two population system, one excitatory dominated and one inhibitory dominated, with reciprocal connections. Introducing the labels E and I for each population then the natural generalisation of (3.3.1) and (3.3.2) is

$$Q_{ab} g_{ab} = \kappa_{ab} f(z_b), \tag{3.3.3}$$

$$\frac{\mathrm{d}z_a}{\mathrm{d}t} = \mathcal{F}_a(z_a) + \sum_b \mathcal{G}_b(z_a, g_{ab}), \tag{3.3.4}$$

where $a, b \in \{E, I\}$. Here, Q_{ab} is obtained from (2.6.3) under the replacement $\alpha \to \alpha_{ab}$, $\mathcal{F}_a(z_a) = \mathcal{F}(z_a; \eta_0^a, \Delta^a)$ and $\mathcal{G}_b(z_a, g_{ab}) = \mathcal{G}(z_a, g_{ab}; v_{\text{syn}}^{ab})$. The set up of the

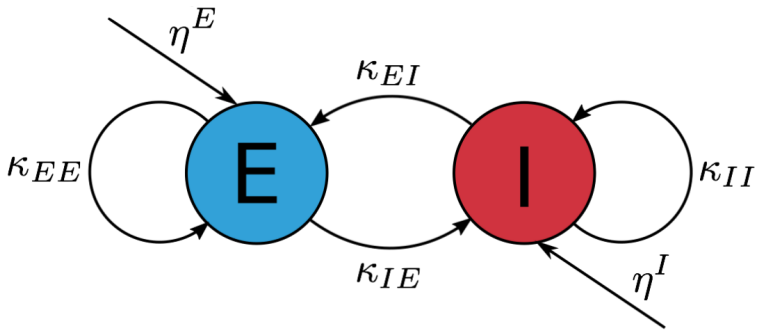

Figure 3.3.5. Set up of two population network: Schematic of the two population system, illustrating each of the connections and associated parameters.

two population system is shown in Fig. 3.3.5. The system now consists of 12 ODES, there is one second order equation for each synaptic connection (namely (3.3.3)), of which there are 4, and a complex ODE describing the Kuramoto order parameter for each of the populations (namely (3.3.4)). The system of equations (3.3.4) generalises those recently presented by Laing [110]. Here, we extend his model to include synaptic

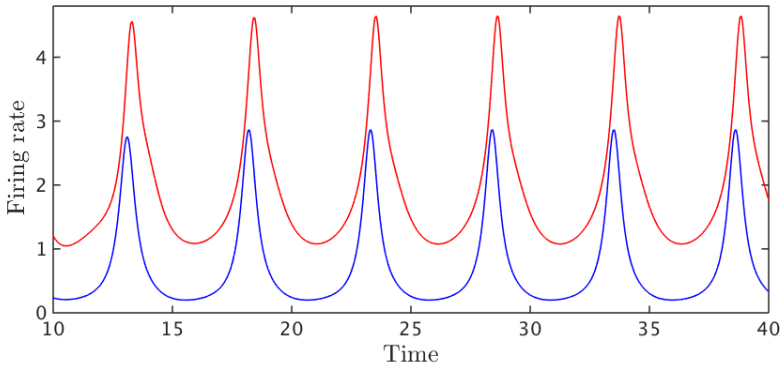

Figure 3.3.6. PING rhythm in two population network: Evolution of the firing rate of the excitatory (blue) and inhibitory (red) populations for network defined by (3.3.4)–(3.3.3). It can be seen that the two populations oscillate at the same frequency, but that the inhibitory population lags slightly behind. Parameters values: $\alpha_{EI} = 0.8$, $\alpha_{IE} = 10$, $\kappa_{EI} = 0.5$, $\kappa_{IE} = 0.65$, $v_{\text{syn}}^{EI} = -10$, $v_{\text{syn}}^{IE} = 10$, $\eta_0^E = 10$, $\eta_0^I = 0$, $\Delta^E = \Delta^I = 0.5$, $\kappa_{EE} = \kappa_{II} = 0$.

reversal potentials and self coupling. Our model also includes a more biologically

realistic form of synaptic coupling. The model presented by Laing assumed a smooth non-pulsatile interaction term with first order synaptic processing. Whereas our model assumes pulsatile interactions with second order synaptic processing. Laing highlighted the ability of his model to produce a so-called pyramidal-interneuronal network gamma (PING) rhythm [24]. The PING rhythm corresponds to oscillatory behaviour involving the interplay of an excitatory population of pyramidal neurons and an inhibitory population of interneurons, whereby the excitatory population synchronises the inhibitory population, causing them to fire at the same frequency, but with a slight lag. We found that our augmented network can also support the PING rhythm (in the absence of self-coupling), which can be seen in Fig. 3.3.6.

There are a number of mechanisms which can destroy the PING rhythm. Using bifurcation theory, we will show how our model satisfies the criteria for a PING rhythm laid out in [24, 25], namely when the synaptic connections between the two populations are too weak or the external drive into the inhibitory population is too strong we do not see the PING rhythm. Figure 3.3.7 shows a one parameter bifurcation digram for the coupling strength between the excitatory and the inhibitory populations κ_{IE}. It can be seen in the bifurcation diagram that periodic behaviour can be destroyed in a supercritical Hopf bifurcation as κ_{IE} is decreased. In Fig. 3.3.8 we show a bifurcation diagram under the variation of κ_{EI}. Again, as the strength of the synaptic connections between the inhibitory and the excitatory populations κ_{EI} is weakened periodic behaviour is destroyed in a supercritical Hopf bifurcation. We test the hypothesis that increasing the external input to the inhibitory population destroys the PING rhythm by varying the mean background drive to the inhibitory population η_0^I, which is shown in Fig. 3.3.10. Increasing η_0^I leads to a supercritical Hopf bifurcation which also terminates the PING rhythm.

To fully explore the two population system we reintroduce the self coupling connections, $\kappa_{EE} \neq 0$, $\kappa_{II} \neq 0$, and carry out a one parameter continuation of the

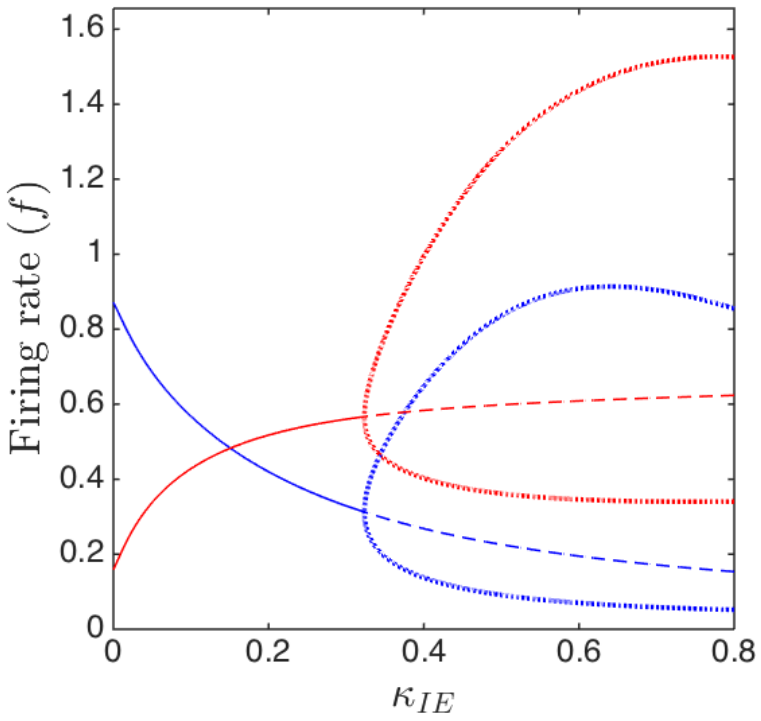

Figure 3.3.7. Bifurcation diagram in κ_{IE} for the two population model: Bifurcation diagram for a reciprocally connected PING network defined by (3.3.4)–(3.3.3) under variation of the strength of the connection from the excitatory population to the inhibitory population κ_{IE}, for both the excitatory (blue) and inhibitory (red) populations. Solid lines: stable; dashed lines: unstable. Circles show maximum and minimum values of $f(z_E)$ and $f(z_I)$ over one period of oscillation when no steady states are stable. Parameters values as in Fig. 3.3.6

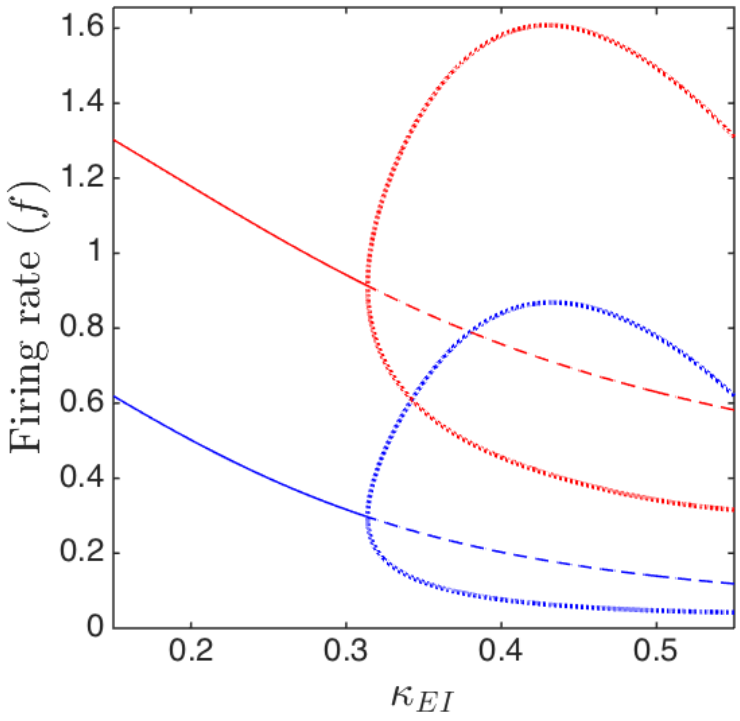

Figure 3.3.8. Continuation in κ_{EI} for the two population model: Corresponding bifurcation diagrams to Fig. 3.3.7 under variation of the strength of the connection from the inhibitory population to the excitatory population κ_{EI}, for both the excitatory (blue) and inhibitory (red) populations. Note that PING rhythms can be terminated by decreasing the strength of coupling to the excitatory population from the inhibitory population. Parameters as in Fig. 3.3.7 with $\kappa_{IE} = 0.9$.

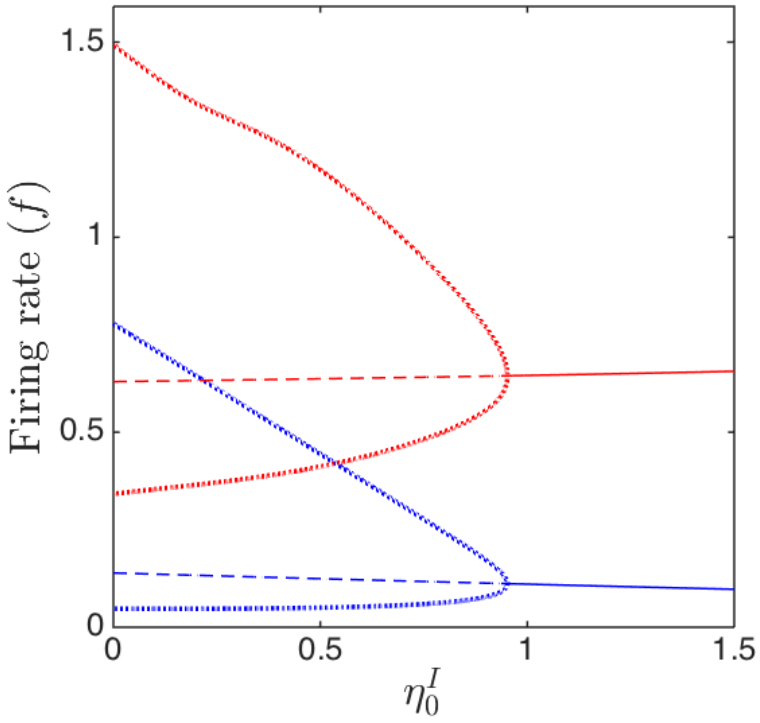

Figure 3.3.9. Bifurcation diagram in η_0^I for the two population model: Corresponding bifurcation diagrams to Fig. 3.3.7 and Fig. 3.3.8 under variation of the mean background drive to the inhibitory population η_0^I, for both the excitatory (blue) and inhibitory (red) populations. Note that PING rhythms can be terminated by increasing the natural frequency of the inhibitory population. Parameters as in Fig. 3.3.7 with $\kappa_{IE} = 0.9$.

mean background drive to the inhibitory population η_0^I, see Fig. 3.3.10. As η_0^I is increased we observe the appearance of oscillatory behaviour through a supercritical Hopf bifurcation, which is destroyed at a second supercritical Hopf bifurcation when η_0^I is increased further. Note the appearance/disappearance of period doubling through two period doubling bifurcations on this branch of periodic solutions. We also observe the appearance and disappearance of an isola of periodic orbits through two saddle

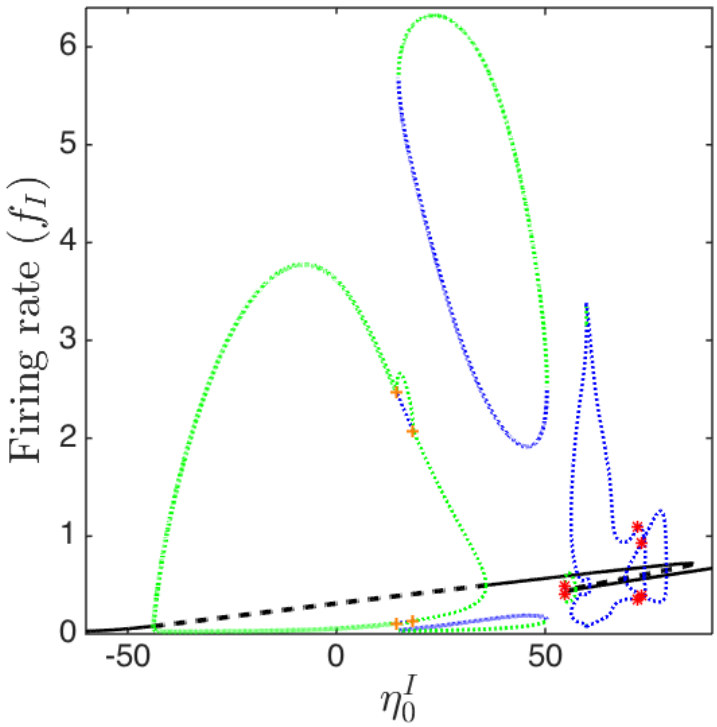

Figure 3.3.10. Continuation in η_0^I of the two population model: Bifurcation diagram, for the model described by (3.3.4)–(3.3.3), in the mean background drive to the inhibitory population η_0^I. It can be clearly seen that the inclusion of self coupling in the twpo population system leads to a rich bifurcation structure. Solid lines: stable; dashed lines: unstable; green (blue) dotted line: stable (unstable) oscillations; orange crosses: period doubling bifurcations; red stars: torus bifurcations. Of particular interest is the appearance/disappearance of an isola at $\eta_0^I \simeq 15 - -50$. Parameters: $\alpha_{EE} = 1$, $\alpha_{EI} = 0.7$, $\alpha_{IE} = 1.4$, $\alpha_{II} = 0.4$,$\kappa_{EE} = 3$, $\kappa_{EI} = 1$, $\kappa_{IE} = 2$, $\kappa_{II} = 1.5$, $v_{\text{syn}}^{EI} = 10$, $v_{\text{syn}}^{IE} = -v_{\text{syn}}^{EI} = 8$, $v_{\text{syn}}^{II} = -12$, $\eta_0^E = 20$, $\Delta^E = \Delta^I = 0.5$.

node bifurcations of periodic orbits. The first saddle node occurs before the second Hopf bifurcation, i.e. there exists two stable periodic orbits for this window of parameter space. Further increasing η_0^I leads to another saddle node bifurcation of periodic orbits, shortly followed by a torus bifurcation and then a saddle-node on invariant circle bifurcation which destroys the unstable branch of the periodic orbit. The stable branch of the periodic orbit is destroyed at a supercritical Hopf bifurcation, as η_0^I is increased further. Along the unstable fixed point branch there are four Hopf bifurcations all of which either create or destroy unstable periodic behaviour. Between the second and third of these bifurcations there are two torus bifurcations, one on each periodic orbit.

Figure 3.3.11 shows the behaviour of the system for $\eta_0^I = -20$ and $\eta_0^I = 25$ respectively. In both cases the excitatory population has two frequencies; the fast gamma rhythm is modulated by the lower frequency, which is synchronised to the inhibitory population oscillations. For $\eta_0^I = 25$, the system follows the orbit created by the isola, and there are two peaks in the (inhibitory) firing rate per period.

3.4 Discussion

We began this chapter with a discussion of the failures of the standard neural mass model, in particular its inability to support the well documented phenomena of ERS and ERD, which set the scene for our *next generation neural mass model*. We introduced a network of θ-neurons, and outlined how the OA ansatz was used to reduce the network to an equivalent fourth order system of equations. The model presented here is very much in the original spirit of neural mass modelling, yet importantly it can be interpreted directly in terms of an underlying spiking model. Moreover, the *derived* structure of the macroscopic equations can be viewed as a modification of the standard neural mass framework whereby the firing rate of the system is now

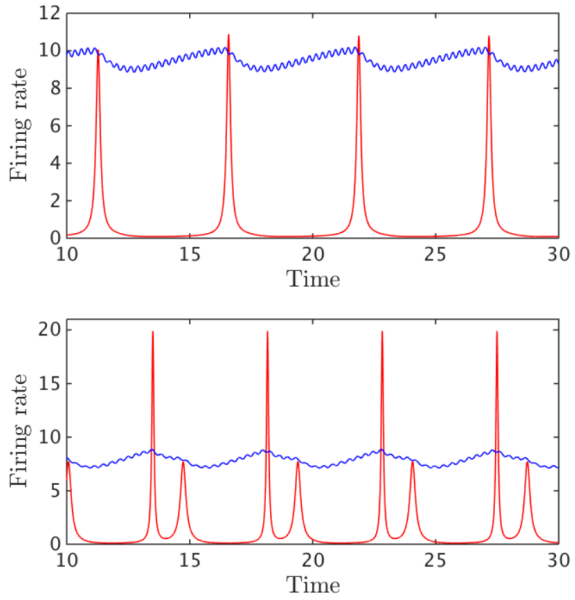

Figure 3.3.11. Behaviour of two population model (3.3.4)–(3.3.3)**:** Firing rate for the excitatory (blue) and inhibitory (red) populations, showing the exotic behaviour that is present when self coupling is reintroduced. Plots corresponds to Fig. 3.3.10 at $\eta_0^I = -20$ (top) and $\eta_0^I = 25$ (bottom). Parameters values as in Fig. 3.3.10.

coupled to the degree of synchrony within a population. Also, the firing rate function in this generalised neural mass model is a derived quantity, rather than the standard sigmoidal function.

An extensive bifurcation analysis was carried out on the single population system, which highlighted the system's preference to oscillate for a large set of parameter values. The two population bifurcation analysis exposed a number of interesting bifurcations, which would be interesting to explore further. In particular, to explore the model as a potential candidate for epilepsy modelling, given that we found areas of parameter space where both low amplitude and high amplitude oscillatory states coexist.

This chapter highlighted the capabilities of the model, but we must also note some of its drawbacks. The network is all-to-all coupled, which many would argue is unrealistic. However, we believe that all-to-all coupling is a reasonable assumption when considering small densely connected areas of cortex. The main failing of this model is its inability to generate cluster states, and other more exotic types of behaviour. Unfortunately we do not have the tools necessary for reducing general spiking neuron models at present. However, advances have been made in this direction, and they are discussed in Chapter 7

In the next chapter we outline the recent success of this model in explaining β-rebound, and discuss other possible applications.

Chapter 4

Next generation neural mass models II: Applications to magnetoencephalography

The model presented in Chapter 3 is an ideal candidate for population-level modelling approaches aimed at understanding *in vivo* brain activity. It takes the form of a generalised neural mass model, while also maintaining biological relevance, as it preserves the notions of both within population synchrony and population firing rate. We believe it will prove particularly useful in understanding event-related desynchronisation (ERD) and event-related synchronisation (ERS), two important phenomenon which standard neural mass models fail to incorporate.

Our focus will be on two special cases of ERD and ERS, movement related beta decrease (MRBD) and post movement beta rebound (PMBR). MRBD and PMBR are beta band modulations, believed to be caused by changes in synchrony within a relatively localised region of motor cortex. To describe these effects we are faced with modelling at a mesoscopic brain scale, with particular emphasis on the changes in synchrony within a population of, say, 10^{6-7} excitatory pyramidal cells and their

associated inhibitory interneurons. A neural mass model would be ideal for this scale, if the question of interest related to rate rather than spike. As such, this problem presents the perfect opportunity to use our *next generation neural mass modelling* approach.

This chapter begins with an introduction to the beta rhythm, followed by a recapitulation of what is already known about MRBD and PMBR. We then discuss the experimental design and results of the median nerve experiment which we carried out as part of this study. The focus then shifts to how the model described in Chapter 3 can be used to describe the MRBD and PMBR. The last section of the chapter concentrates on a two population model and demonstrates how the additional population provide a better fit to the observed time-scales of MRBD and PMBR. The first half of this chapter is set to be published in [35].

4.1 Beta rhythms and β rebound

4.1.1 The beta rhythm

The modelling of brain rhythms is now a well established and vibrant part of computational neuroscience. As discussed in Chapter 2, recordings of large populations of neurons are well known to be dominated by oscillations (rhythmic activity in cell assemblies) across a wide range of temporal scales and scientists have sought to develop large scale models to describe the five main frequency bands: delta, theta, alpha, beta and gamma. Moreover, it has long been known, since the early works of Jasper and Andrews [91, 92], that different brain rhythms can be localised to specific areas of the brain, and that these rhythms are functionally distinct.

Hans Berger was the first to associate the beta rhythm with the motor cortex [18]. He noted that the beta oscillations had a smaller amplitude and higher frequency than the previously seen alpha rhythms. This was later confirmed by Jasper and

Penfield during a recording from the cortical surface of epilepsy patients [90]. They showed that the characteristic resting frequency of the motor cortex is about 25 Hz. However, premotor areas tend to exhibit a lower beta frequency of about 17–22 Hz [136]. Although the beta rhythm has been predominantly studied in relation to sensorimotor behavior, it also plays a role in attention [76] and anxiety [80, 70].

4.1.2 Beta decrease and rebound

In their seminal 1949 paper [90], Jasper and Penfield discovered that the beta rhythms generated in the motor cortex were suppressed during voluntary movement, and lasted for the entirety of the movement, as well as approximately 0.5 seconds after movement termination. This phenomenon later became known as movement related beta decrease (MRBD). MRBD was originally thought to be the consequence of planning and executing movement. Interestingly, in the case of voluntary movements MRBD is seen roughly 1 s before movement initiation. Hence, movement planning must play some role in MRBD. However, as MRBD is also present in tactile movement and for median nerve stimulation [128, 2], this cannot be the entire story. The current belief is that the desynchronisation of beta oscillations is related to neural activation and an increase in processing power [129].

It wasn't until 1994 that Salmelin and Hari [141] discovered the temporary rise in amplitude of the beta oscillations following movement cessation. This increase in power is now known as post-movement beta rebound (PMBR), and can last anywhere between $1 - 10$ seconds [136, 132, 97]. The length of PMBR varies greatly with experimental design and between participants [73]. In general, high amplitude beta oscillations are thought to reflect inhibition [37, 75], a hypothesis supported by quantifiable relationships between beta amplitude and local concentrations of the inhibitory neurotransmitter gamma aminobutyric acid (GABA) [75, 78, 94, 124]. As such, PMBR is thought to reflect the active inhibition of neuronal networks post-

movement [3, 150]. An alternative, but not mutually exclusive hypothesis, which has been proposed by Donner and Siegal, is that the beta signal, in part, represents long range integration across multiple brain regions [60] (see also [98]). Indeed this is a hypothesis supported by some evidence suggesting that large scale distributed network connectivity is mediated by beta oscillations [32, 79, 82].

Multiple papers have employed a large number of carefully controlled experimental paradigms, in humans and animals, to further investigate beta rebound phenomena, see [40, 98] for reviews. It is clear that beta band modulation is robust across subjects, occurring during internally and externally cued movements [130]. However, despite the robust nature of beta task induced decrease and post stimulus rebound, the effect itself is relatively poorly understood. Interestingly, both MRBD and PMBR have been seen in studies where the subject is asked to think about moving, without carrying out the movement [144, 133].

Recent work, reviewed in [32, 33, 140], has begun to show the potential importance of beta band modulation. For example, Fig. 4.1.1 shows two relative time-frequency spectra depicting the changes in neural oscillations in sensorimotor cortex in response to a cued finger movement task. The time-frequency spectrum is extracted from a location of interest in left primary motor cortex. The left hand panel (a) shows the case for healthy individuals. Notice that in the beta band, the MRBD and PMBR are observed clearly. The right hand panel (b) shows the case for patients with schizophrenia. Note the significant reduction in PMBR. Furthermore, this same study showed that the magnitude of the beta rebound correlated significantly with the severity of ongoing symptoms of schizophrenia, thus highlighting direct clinical relevance of the measurement. This is just one example of how beta band oscillations have been identified as a potential biomarker of disease; other examples include Parkinson's disease [156]. In addition, the robustness of MRBD and PMBR has meant that they have also been used in neuroscience applications ranging from brain

computer interfaces [131] to markers of neural plasticity [74, 121].

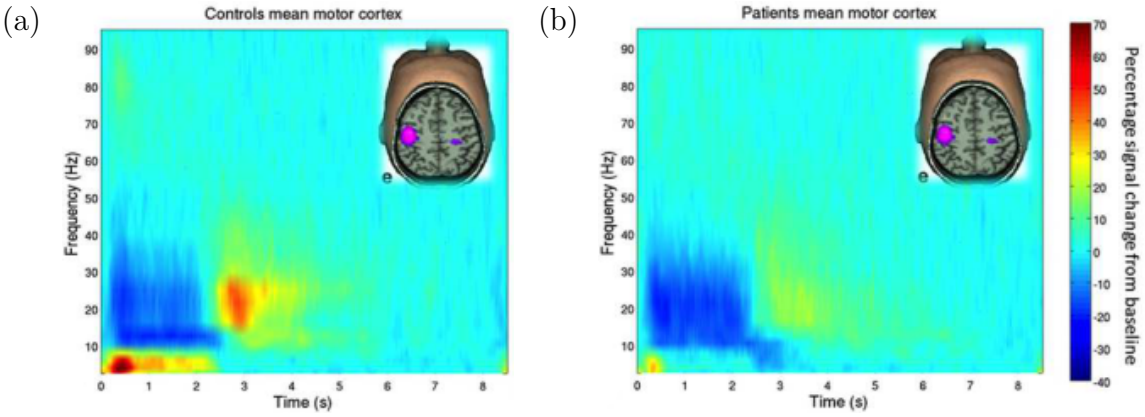

Figure 4.1.1. The beta rebound and its disruption in patients with schizophrenia: (a) Time-frequency spectrograms showing changes in the amplitude of neural oscillations, in contralateral sensorimotor cortex, when subjects execute a 2s finger movement. Note that, in the beta band, a loss in oscillatory power during movement is accompanied by an increase in power on movement cessation. (b) Equivalent time-frequency spectrogram in patients with schizophrenia. Note the significant reduction in the beta rebound. (Figure reproduced with permission from [140].)

It is also noteworthy that the beta band power loss and rebound, whilst commonly thought of as being observable in the sensorimotor cortex, is not a sole property of the sensorimotor system. For example, Fig. 4.1.2 shows instances of observation of very similar phenomena in other cortical areas. Figure 4.1.2a shows time-frequency oscillatory dynamics of a network of brain areas encapsulating the bilateral insular cortex (the area between the temporal and parietal lobes), throughout a cognitive task [113, 33]. The task itself involves presentation of a series of visual stimuli; some stimuli are relevant to the task, others irrelevant. Subjects were asked to respond if the relevant stimuli match some predetermined condition. Note here that only the results for the non-target stimuli are shown (meaning that the subjects did not actually make a response). In the relevant condition, clear beta modulation is observed with a decrease in amplitude followed by a rebound above baseline. Furthermore, this effect was also shown to be abnormal in schizophrenia, again demonstrating its clinical

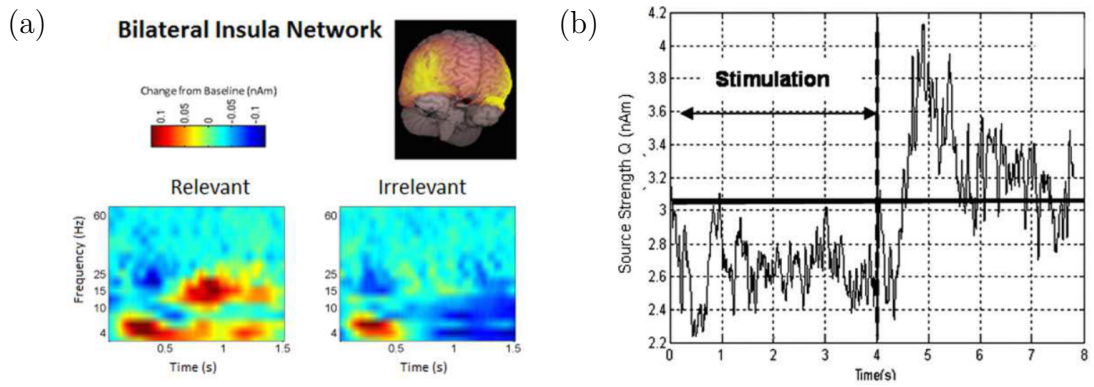

Figure 4.1.2. Task induced beta band decrease and rebound phenomena in other cortical regions: (a) Time-frequency dynamics in a network of brain areas including bilateral insular. The task involved visual stimuli that were relevant and irrelevant to the task. Note the significant reduction and rebound in beta oscillations in the relevant condition. (Reproduced with permission from [113].) (b) Timecourse showing the envelope of beta oscillations in primary visual cortex during passive viewing of a visual grating. Visual stimulation occurred in the 0–4 s window. Note again the task induced power loss and post stimulus rebound. (Figure reproduced with permission from [154].)

relevance. Figure 4.1.2b shows the case for simple sensory stimulation of the visual cortex [154]. Here, subjects were asked to passively view a drifting visual grating; the figure shows the envelope of beta band oscillations throughout the task. Note again the clear structure with a loss in beta amplitude during stimulation and an increase on stimulus cessation. These represent two simple examples which show that the beta band effect is not simply a property of the sensorimotor system, but rather is a ubiquitous effect that is observed robustly across many cortical regions.

The above indicates that stimulus related beta power loss and post stimulus rebound are general observable effects, seen in many cortical areas, during both sensory and cognitive tasks. Further, the perturbation to the post stimulus rebound in disease has been robustly demonstrated. Thus, the generation of new mathematical models from which we can accurately predict task induced beta band dynamics are of much importance.

4.2 Experimental Study

4.2.1 Experimental paradigm and data collection

A somatosensory paradigm was used to demonstrate the robustness of beta band modulation in sensorimotor cortex. Two subjects took part in the study, which was approved by the University of Nottingham Medical School Ethics Committee. The paradigm comprised of electrical stimulation to the subject's left median nerve. This was achieved by locating the subject's median nerve and applying a series of 500 μs duration current pulses to two gold electrodes placed on the subject's wrist. The current was delivered using a Digitimer DS7A constant current stimulator, and the amplitude was increased slowly until a visible movement of the thumb was observed. Each experimental run comprised of a total of 80 pulses delivered with an inter-stimulus-interval (ISI) of 10 s. A single experimental run lasted approximately 13 minutes. Each subject performed the study twice, on two separate days, to assess robustness. Median nerve stimulation was used in order to obtain a clean data set with a controlled paradigm and minimal interference. Experiments which use voluntary movement over median nerve stimulation are far less reproducible, regardless of whether the movement is cued or self-cued [128].

MEG data were captured using the third order synthetic gradiometer configuration of a 275-channel CTF whole-head MEG system (MISL, Port Coquitlam, Canada). The subject was positioned upright, with their head in the MEG helmet, whilst data were recorded at a 600 Hz sampling rate. Three localisation coils were attached to the head as fiducial markers (one above the nose and one slightly on front of each ear) prior to the recording. These markers are used as references, energising these coils at the start and end of data acquisition enables the localisation of the fiducial markers relative to the MEG sensor geometry as well as determination of total head movement. In order to co-register brain anatomy to the MEG sensor array, prior to the MEG recording each

subject's head shape was digitised relative to the fiducial markers using a 3D digitiser (Polhemus IsoTrack, Colchester, VT, USA). Volumetric anatomical MR images were acquired using a 3T MR system (Phillips Achieva, Best, Netherlands) running an MPRAGE sequence (1 mm^3 resolution). Following data acquisition, the head surface was extracted from the anatomical MR image and coregistered (via surface matching) to the digitised head shape for each subject. This allowed complete coregistration of the MEG sensor array geometry to the brain anatomy, thus facilitating subsequent forward and inverse calculations.

4.2.2 Data analysis

First the MEG data were inspected visually (by myself) and any trials containing excessive interference were removed. The first trial in each run was also excluded as the surprise of the first stimulation caused an increase in noise. Data were then analysed using synthetic aperture magnetometry (SAM) [163], a beamforming variant [159, 77, 81, 139, 161] that has been applied successfully in many studies to localise neural oscillatory amplitude changes. Data were first filtered to the beta band (13–30 Hz). Following this the SAM beamformer was applied and the oscillatory amplitude was contrasted between an active and a control time window in order to delineate the spatial signatures of the beta amplitude changes. This allowed us to obtain a spatial area for the generation of spectrograms. The forward model was based upon a multiple local sphere head model and the forward calculation by Sarvas [86, 143].

The data was filtered into different frequency bands, ranging in length from 4 Hz to 10 Hz. In order to compute the average across trials a Hilbert transform was taken. Taking the average across the 80 raw signals would result in a massive loss in information, as the signals' phases differ and hence, would cancel each other out. The average of the Hilbert transformed signals was taken for each frequency band, and the mean baseline activity ($8 - 10$ s) was then subtracted from each, to produce the

relative time-frequency spectrograms.

4.2.3 Experimental results

Figure 4.2.1 shows the relative time-frequency spectrograms for each of the participants on two separate days, where baseline activity has been subtracted. The top line represents participant 1 and the bottom line represents participant 2. Day 1 is shown in the left hand column and Day 2 in the right hand column. For each trial shown there is a $10-20\%$ decrease in power at $t=0$ s, which lasts for approximately 0.5 s, demonstrating MRBD. At $t\simeq 0.5$ s there is a $60-100\%$ increase in power, exemplifying PMBR. Although the comparison between participants shows dissimilarities in the shape and length of PMBR, the maximum strength and timing of both the MRBD and PMBR are comparable. Importantly, the similarity between each participant's time-frequency spectrogram on the two separate days is unmistakable. Although the median nerve stimulation, and subsequent thumb movement, only lasts for a few milliseconds, the evoked response caused by the stimulation lasts significantly longer. This can be seen by examining the bottom left corner of each of the time-frequency spectrograms in Fig. 4.2.1. One can notice an increase in the low frequency activity at $t\simeq 0$ s, which appears to last for roughly $0.3-0.4$ s, corresponding to the transduced median nerve stimulation. Also, noteworthy is the increase in gamma band activity during movement, which is most prominent in participant 1's spectrograms.

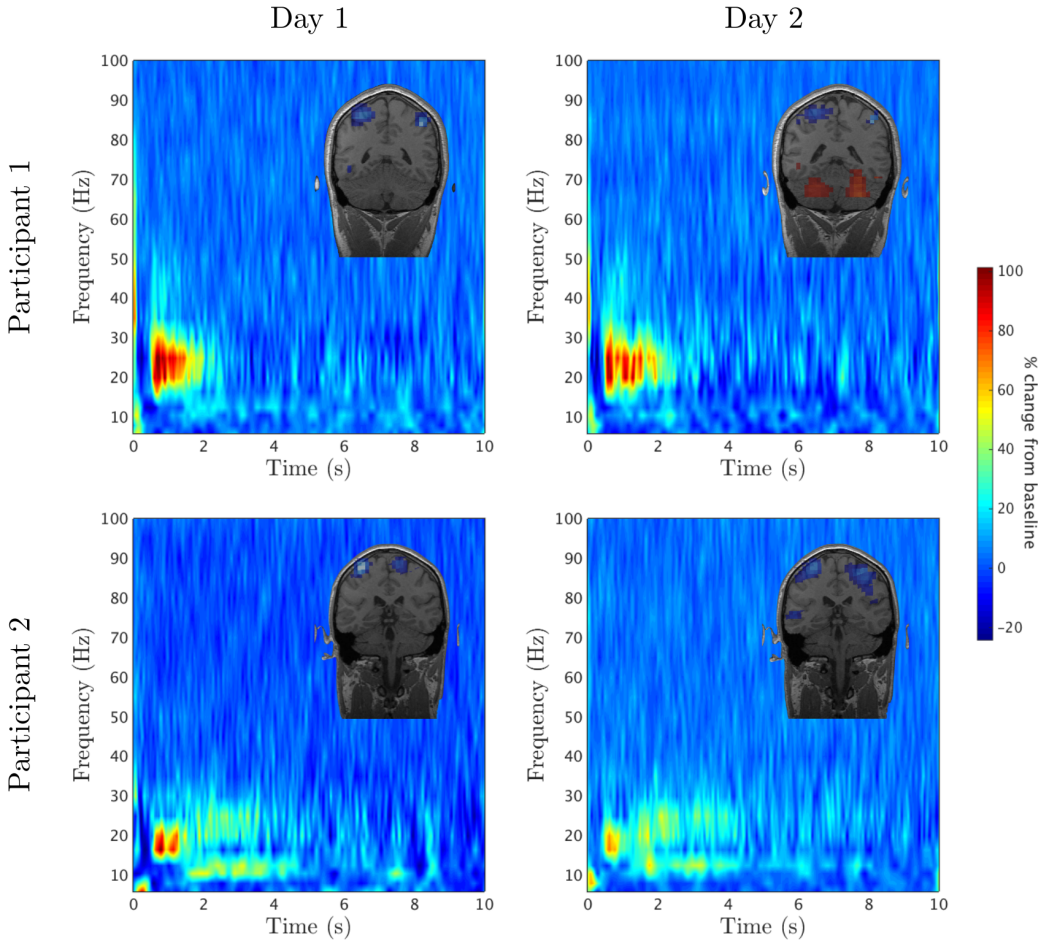

Figure 4.2.1. Robust beta rebound for median nerve stimulation: Time-frequency spectrograms showing the percentage change from baseline of the activity in the motor cortex, for two participants on two separate days. The top row shows the results for participant 1 and the second row represents data from participant 2. Each participant displayed a clear difference in their PMBR. However, the strength and timing of both the MRBD and PMBR are consistent between subjects and trials. PMBR for each participant appears to be strikingly reproducible.

4.3 A mechanistic interpretation of movement induced changes in the beta rhythm

In order to utilise the model presented in Chapter 3 here, we must first alter the model to give it physiological units. This is done by adding a number of terms into (3.1.1),

$$C\frac{\mathrm{d}}{\mathrm{d}t}v_i = \eta_i + \sigma v_i^2 + I_i, \qquad i = 1, \ldots, N, \tag{4.3.1}$$

where C is the capacitance and σ is a proportionality constant, which from now on (without loss of generality) will be set to unity. The reset conditions remain unchanged. Now (4.3.1) describes the evolutions of a current, with units μA. Hence, C has units mF, v_i has units mV, σ has units AV^{-2}, g has units $\mathrm{m}\Omega^{-1}$, and the natural frequency of oscillation for the single neuron is given by $2\sqrt{\eta_i}/C$ Hz. Reducing the model, as described in Chapter 3, we arrive at the following the mean field model:

$$Qg = kf(z), \tag{4.3.2}$$

$$C\frac{\mathrm{d}z}{\mathrm{d}t} = \mathcal{F}(z; \eta_0, \Delta) + \mathcal{G}(z, g; v_{\mathrm{syn}}), \tag{4.3.3}$$

where $k = \kappa/C$ and f, $\mathcal{F}$ and $\mathcal{G}$ are unchanged and given by (3.2.12), (3.2.15) and (3.2.16) respectively.

In §4.2 we demonstrated how an externally cued thumb movement caused a decrease in beta band power, lasting roughly 0.5 s, followed by a $2-4$ s increase in beta band power, typifying MRBD and PMBR, respectively. The median nerve stimulation only lasts 500 μs, however, the evoked response lasts significantly longer. In §4.2 we identified an increase in the low frequency activity immediately after stimulation, which lasted for around $0.3-0.4$ s. We interpret this as the evoked response caused by the median nerve stimulation and base the design of the external drive on this transduced signal, rather than the median nerve stimulation itself. This is a reasonable

assumption as we are modelling a small area of cortex and this is the drive as perceived by this area.

We model the transduced signal as a temporally filtered drive $A = A(t)$, that is received by every neuron in the model. In this case the dynamics of z obey (4.3.3) under the replacement $\eta_0 \to \eta_0 + A$, with

$$Q_D A(t) = \Omega(t), \tag{4.3.4}$$

where Q_D is the differential operator obtained from Q in (3.1.5) under the replacement $\alpha \to \alpha_D$, and $\Omega(t)$ is a rectangular pulse,

$$\Omega(t) = \Pi\Theta(t)\Theta(\tau - t), \tag{4.3.5}$$

where Π is the strength of the drive and Θ is once again the Heaviside function. As the evoked response in the experimental data lasts between 0.3 and 0.4 s, we set $\tau = 0.4$ s.

The parameter values were set such that the system oscillated at beta frequency, in a partially synchronous regime (these parameter values are given in the caption of Fig. 4.3.1). The system was evolved until transients had dropped off and then the stimulus was applied. The time of stimulation was set to be $t = 0$. Figure 4.3.1 shows the phase plane for the Kuramoto order parameter $z = Re^{i\Psi}$, as well as a time series of R, in response to the drive described above. The colours correspond to the different time periods: before drive (blue), during drive (red), after drive (green). The system oscillates in partial synchrony with R oscillating between approximately $0.05 - 0.6$ in the absence of drive. Once the drive is switched on the amplitude of these oscillations decreases and hence the power is also reduced, corresponding to MRBD. Note that the frequency also increases during this period. After the drive is switched off, the level of coherence increases as the value of the order parameter is drawn towards the edge of the unit disk before spiralling back to the original limit cycle. This corresponds to

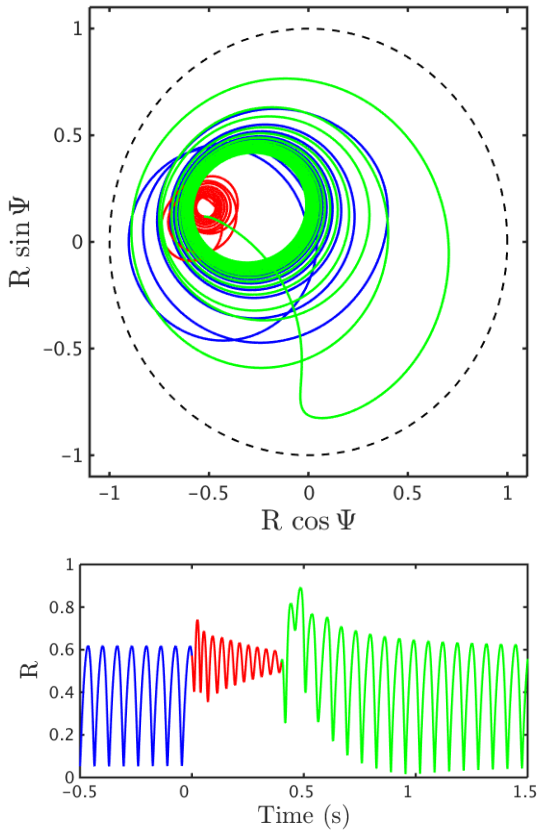

Figure 4.3.1. Response of the system to drive: Plots showing the variation of the Kuramoto order parameter z in the model given by (4.3.2)–(4.3.3), when it is stimulated with a drive described by (4.3.4)–(4.3.5). Top: Phase plane for z, demonstrating the behaviour of the system in response to the drive $A(t)$. The blue curve represents the system before the pulse arrives, as it settles to its non-perturbed dynamics ($t < 0$), the red curve illustrates how the system behaves when the pulse is switched on ($0 < t < \tau$) and the green shows how the system reacts once the drive is switched off ($t > \tau$). Bottom: Time series of the within population synchrony R showing the change in the level of coherence; before (blue), during (red) and after (green) the drive is switched on. The amplitude of the oscillations in R appear significantly reduced while the drive is switched on. Parameter values: $\eta_0 = 21.5$ μA (mean background drive), $\Delta = 0.5$ μA (heterogeneity of background drive), $v_{\text{syn}} = -10$ mV (synaptic reversal potential), $k = 3.14$ (coupling strength), $\alpha^{-1} = 35$ ms (synaptic time constant), $C = 30$ mF (membrane capacitance), $\tau = 0.4$ s (length of drive), $\alpha_D^{-1} = 5.6$ ms (synaptic time constant for drive) and $\Pi = 15$ mA (strength of drive).

PMBR. Importantly the system does not rebound until $t \simeq 0.5$ s as seen in the real data. It should be noted that the stimulus corresponds to roughly 80% of this time

to rebound. However, as the evoked response is present in $60-80\%$ of the 0.5 s of MRBD in the real data we believe that this is a satisfactory result.

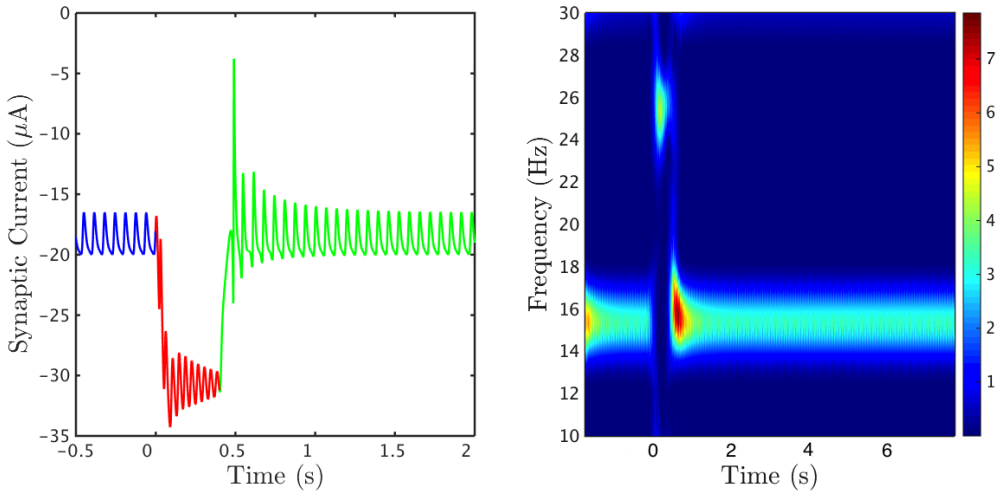

Figure 4.3.2. Response of the synaptic current to drive: Time series and spectrogram of the synaptic current, in the model given by (4.3.2)–(4.3.3), showing the response of the system to the external drive $A(t)$ (4.3.4). The colours in the time series (left) correspond to the different time periods; before drive (blue), during drive (red), after drive (green). Both figures clearly demonstrate the rebound of the system, there is an increase in amplitude (and hence power) at $t \simeq 0.5s$, after the drive was switched on. Parameters values as in Fig. 4.3.1

As MEG measures synaptic current, it is important to examine the effects of the drive on the synaptic current in the model. To do this we must use the transformation (3.2.18) identified by Montbrio *et al.* [122], to determine the average population voltage V and substitute it into the formula for the average synaptic current $I = g(v_{\text{syn}} - V)$. Figure 4.3.2 shows a time series and spectrogram for this current. The time series (left) shows that when the drive is switched on the synaptic current is reduced. However, the neurons are now also receiving a strong excitatory current in the form of the drive. There is a large increase in the amplitude of the oscillations at $t \simeq 0.5$ s, corresponding to PMBR. The extent of the rebound can be seen more clearly in the time-frequency spectrogram (right). The initial increase in amplitude is very large; however, the

percentage increase between $t = 0.5 - 1.5$ s is relatively small. The synaptic current appears to have fully settled back to its pre-drive behaviour by $t \simeq 1$ s, indicating a PMBR of roughly 1 s, which is not as long as the PMBR seen in our experimental data. However, PMBR can last for anywhere between 1 and 10 seconds. An increase in power can also be seen at roughly 26 Hz at $t \simeq 0$ s, corresponding to the increase in frequency during the drive on period. This high-beta activity can be interpreted as the processing of the motor input.

Interestingly, we see a direct correlation between synchrony and synaptic current. The time series in Fig. 4.3.1 (bottom) shows a peak in synchrony at $t \simeq 0.5$ s, just as the time series in Fig. 4.3.2 (left) shows a sharp increase in the amplitude of the synaptic current at $t \simeq 0.5$ s. This increase in amplitude can also be seen in the spectrogram, Fig. 4.3.2 (right). It was found that the strength of the drive Π dictates the extent of the rebound; the greater the strength of the drive, the greater the rebound. However, it also prescribes the frequency of the oscillations during the interval when the drive is switched on. Therefore it is important to find the balance, where we have a prominent PMBR but also a physically realistic frequency during the interval of time when the drive s switched on. As stated in §4.2, there is an increase in gamma band activity during stimulation (Fig. 4.2.1). This is a commonly observed effect in motor tasks, which can also be seen in the time-frequency spectrograms in §4.1.2 (Fig. 4.1.1).

4.4 Two hemisphere model

The current literature suggests that inter-hemispheric connections are important in the production of movement-related modulation of the beta band [97]. It is believed that the interplay between the right and the left hemisphere may be responsible for the overshoot seen in beta rebound. Jurkiewicz *et al.* found that MRBD and PMBR

were present in both hemispheres during a self paced finger tapping exercise [97]. In both cases the strongest response was seen in the contralateral hemisphere [97]. A recent paper by Zaepffel *et al.* found that MRBD was strongest in the contralateral hemisphere in the planning phase, before becoming more bilateral as one approached movement execution [168]. This would also tie in with Donner and Siegal's theory that the beta rhythm represents long range integration across the brain [60].

To test these hypotheses we set up a system of two identical interacting populations of neurons, where one population represents the left motor cortex and the other the right. As the connections between the two populations are long range they must be excitatory. The system of equations take a similar form of those given in §3.3.2,

$$Q_{ab}g_{ab} = k_{ab}f(z_b), \tag{4.4.1}$$

$$C\frac{\mathrm{d}}{\mathrm{d}t}z_a = \mathcal{F}(z_a) + \sum_b \mathcal{G}(z_a, g_{ab}; v_{\mathrm{syn}}^{ab}), \tag{4.4.2}$$

where $a, b \in \{1, 2\}$, $k_{ab} = \kappa_{ab}/C$ and f, $\mathcal{F}$ and $\mathcal{G}$ are given by (3.2.15), (3.2.15) and (3.2.16), respectively. As the two population are identical $k_{11} = k_{22}$, $k_{12} = k_{21}$, $v_{\mathrm{syn}}^{11} = v_{\mathrm{syn}}^{22}$, $v_{\mathrm{syn}}^{12} = v_{\mathrm{syn}}^{21}$, $\alpha_{11} = \alpha_{22}$ and $\alpha_{12} = \alpha_{21}$. We shall label the intra-population connection with aa and the inter-population connections as ab. Note that this model differs from the two population model described in Chapter 3 as the two populations are identical in this case, and this model also contains a capacitance term C.

4.4.1 Bifurcation analysis

First we carried out a bifurcation analysis to assess whether or not the additional population added any interesting dynamics. Figure 4.4.1 shows a one parameter bifurcation of the mean background drive η_0, as a function of the firing rate of population 1, $f_1 = f(z_1)$. It can be seen that there are two oscillatory states, one of which is fully synchronous and the other is a phase locked state. The oscillatory

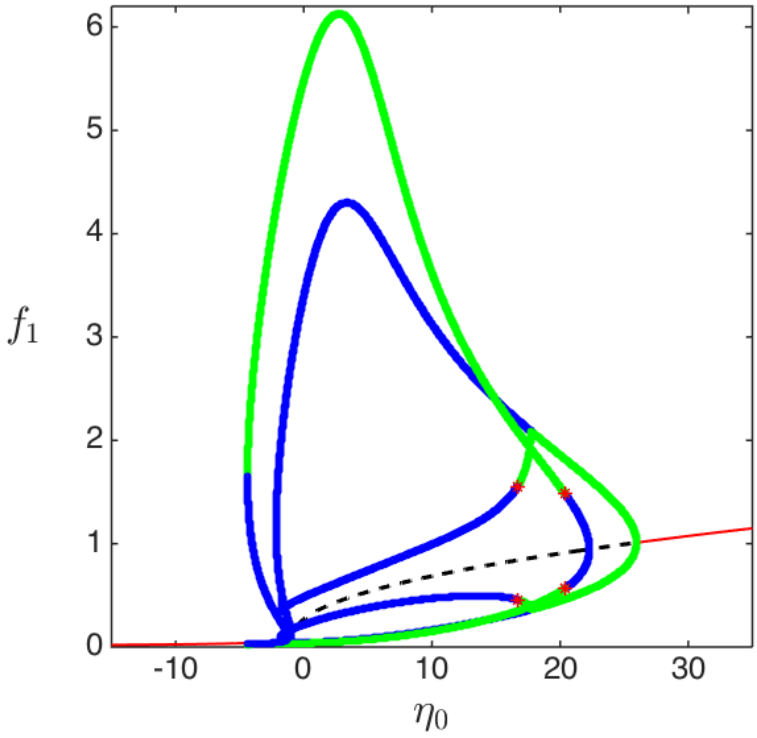

Figure 4.4.1. Bifurcation diagram in η_0 for the two hemisphere model: One parameter bifurcation diagram for the model described by (4.4.1)–(4.4.2), in the mean background drive η_0. Solid red lines: stable fixed point; dashed black lines: unstable fixed point; green (blue) circles: stable (unstable) oscillations; red stars: torus bifurcations. Starting from the right and reducing η_0 the system undergoes a Hopf bifurcation which results in synchronous oscillations forming in the two populations. Decreasing η_0 further sees a second Hopf bifurcation and the creation of unstable oscillations, which are out of phase. This oscillatory state then becomes stable at a torus bifurcation at $\eta_0 \simeq 22$. As η_0 is decreased further the synchronous state bifurcates into two branches, one stable and one unstable. The unstable branch remains synchronous, but we see a loss in synchrony along the stable branch. The stable branch goes unstable at another torus bifurcation at $\eta_0 \simeq 18$. Parameter values: $k_{aa} = 4.5$, $k_{ab} = 5.4$, $v_{\rm syn}^{aa} = -10$ mV, $v_{\rm syn}^{ab} = 10$ mV, $\Delta = 0.5$ μA, $\alpha_{aa}^{-1} = 30$ ms, $\alpha_{ab}^{-1} = 75$ ms, $C = 30$ mF.

activity that ceases as η_0 is increased through roughly 27 μA corresponds to the synchronous solution. This solution is seen in the single population model. The branching of this oscillatory solution is, however, not seen in the single population case, and it corresponds to a symmetry breaking. The unstable branch remains

synchronous, but the stable branch does not. The stable branch then goes unstable at a torus bifurcation. The phase locked solution, which is destroyed as η_0 is increased through about 22 μA, does not exist in the single population model. Here the two populations prescribe the same orbit but are out of phase. This solution becomes stable at another torus bifurcation as η_0 is increased through approximately 20 μA.

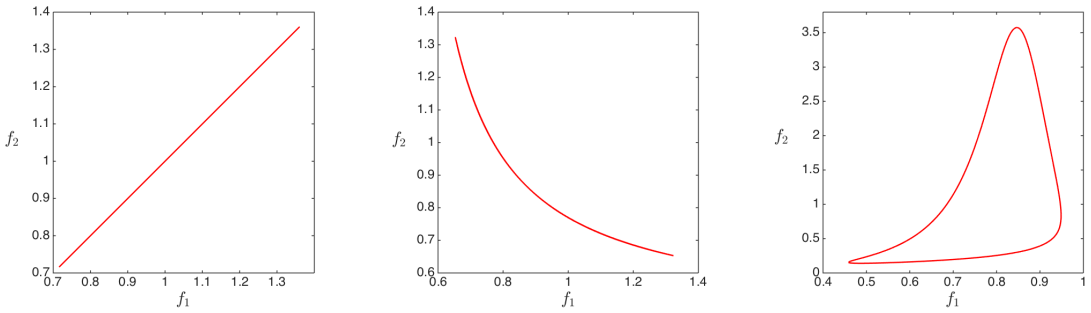

Figure 4.4.2. Examination of inter-hemisphere synchrony: Plots of the firing rate of population 1 (f_1) against the firing rate of population 2 (f_2), showing the different synchronisation regimes, for the model defined by (4.4.1)–(4.4.2). On the left the two populations are fully synchronous ($\eta_0 = 24.54$ μA), in the centre the two populations are phase-locked ($\eta_0 = 21.22$ μA) and in the final plot on the right the populations no longer oscillate in synchrony ($\eta_0 = 9.138$ μA). Parameter values as in Fig. 4.4.1.

Figure 4.4.2 shows the phase planes of the firing rates, f_1 and $f_2 = f(z_2)$, for each of the types of behaviour that the system exhibits. The left plot shows the synchronous solution at $\eta_0 = 24.54$ μA. The centre plot is for the phase-locked solutions at $\eta_0 = 21.22$ μA. The figure on the right shows the non-symmetric solution at $\eta_0 = 9.138$ μA; one can clearly see that the phase plane no longer shows a symmetric solution. This demonstrates that the two populations are no longer operating in synchrony. As further evidence that the second population is behaving differently to the first population we show the bifurcation diagram in η_0 as a function of the firing rate of population 2, f_2, see Fig. 4.4.3. It can be clearly seen that when the branching bifurcation occurs the stable branch takes a different path to the corresponding branch in Fig. 4.4.1.

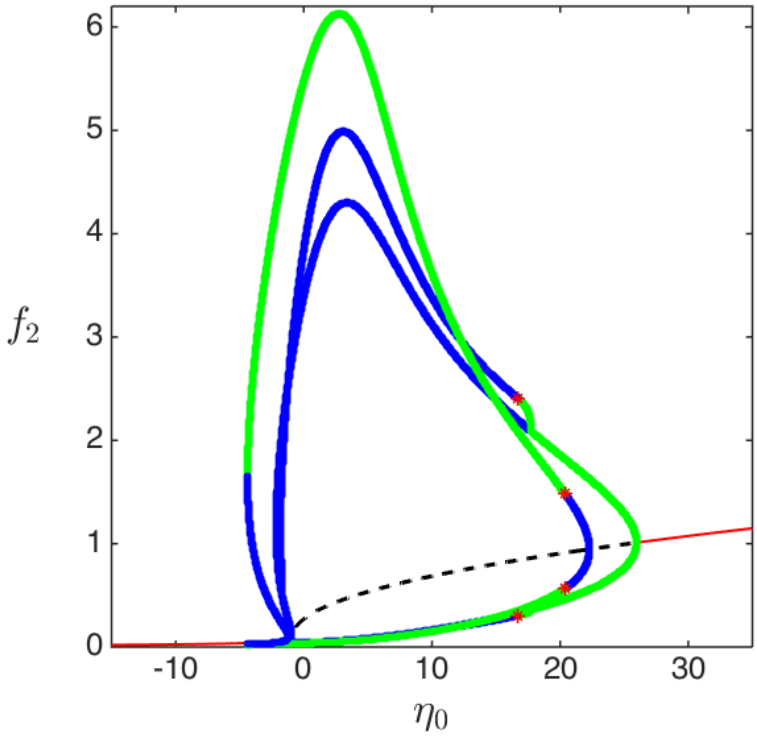

Figure 4.4.3. Bifurcation diagram in η_0 for f_2 for (4.4.1)–(4.4.2)**:** We see a similar diagram to that in Fig. 4.4.1, but for the firing rate of the other population. Note that when the system undergoes the branching bifurcation (at $\eta_0 \simeq 18$ μA) the emergent stable branch takes a different course to the stable branch in Fig. 4.4.1. This shows that the two populations are no longer operating in synchrony, and in fact have different periodic orbits. Parameter values as in Fig. 4.4.1 .

4.4.2 Simulations

We chose our parameter values such that there is multi-stability in the system, namely at least two periodic solutions, as we believe that multi-stability is key for lengthening PMBR. The stimulus, as described in §4.3, was applied to one of the populations (contralateral) once the system had settled to its relative equilibrium behaviour.

The behaviour of the Kuramoto order parameter for each of the populations is shown in Fig. 4.4.4. As before the blue, red and green represent the before, during and after drive intervals, respectively. It is immediately obvious that the extent of the

change in synchrony in the contralateral population is higher than in the ipsilateral population. Also noteworthy is the fact that the magnitude of the overshoot of the order parameter, even in the stimulated population, is significantly smaller than in the single population case. In order to get a better view of how the order parameter is

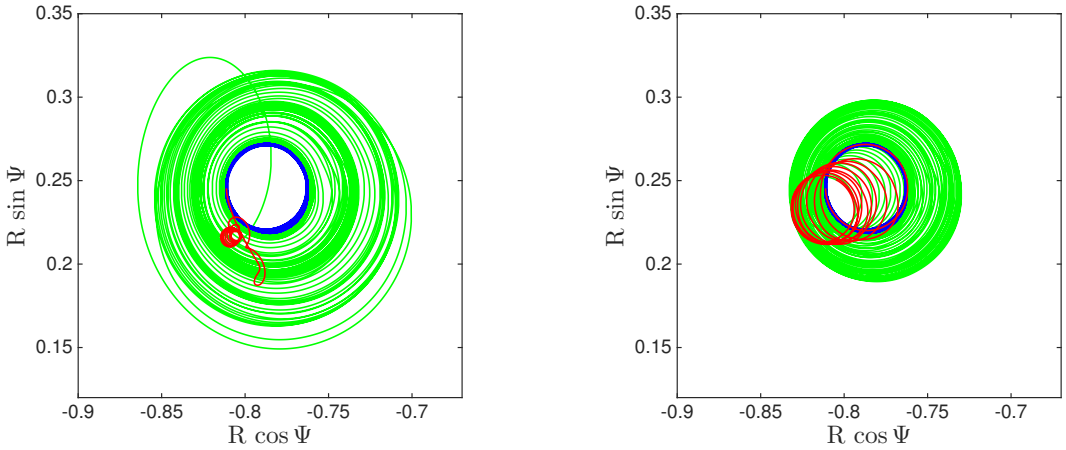

Figure 4.4.4. Rebound in two hemisphere model: Phase planes of the Kuramoto order parameters z_i for the two hemisphere model (4.4.1)–(4.4.2), illustrating how the system reponds when one of the populations receives an input. The Kuramoto order parameter from the stimulated population z_1 is shown on the left and the non-stimulated on the right. Colouring same as in Fig. 4.3.1. Rebound can be seen in both plots, but it is greater in the stimulated population. Parameter values as in Fig. 4.4.1, with $\eta_0 = 23$ μA.

behaving we plotted R as a function of time for each of the populations, see Fig. 4.4.5. The PMBR lasts for over 3 seconds, which is significantly closer to the value observed in our experiments. It can also be seen that the initial increase in amplitude of the oscillations in the driven population is significantly larger. However, both populations appear to oscillate with approximately the same amplitude after roughly 1 second. Close examination of the zoomed in plot in Fig. 4.4.5 reveals that the stimulus knocks the two populations out of phase and that it takes over 1.5 seconds for the populations to re-establish phase synchrony.

As in §4.3 we must also examine the response of the synaptic current to the drive. In this case the synaptic current has two parts, one arising from self coupling and

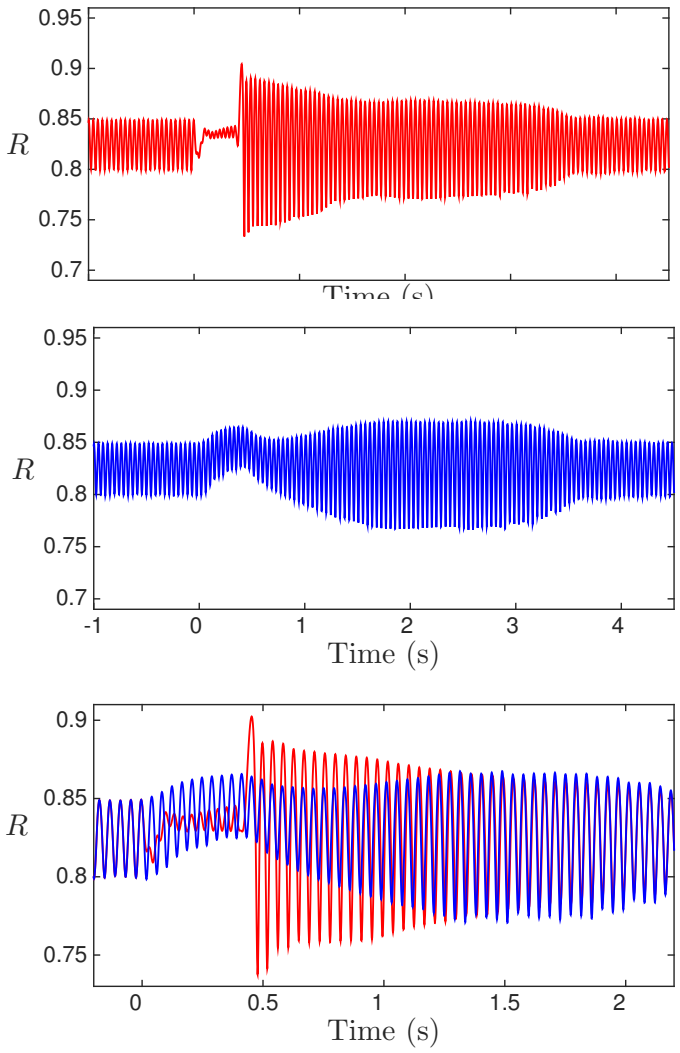

Figure 4.4.5. Response of the within population synchrony for the two hemisphere model: Time series of the within population synchrony R, in the model given by (4.4.1)–(4.4.2), which shows the effect of the stimulus on R lasts for significantly longer than in the single population case. The top two plots illustrate the response of the contralateral (red) and ipsilateral (blue) populations. The bottom plot shows both populations together to illustrate how they desychronise when the drive is applied. Parameter values as in Fig. 4.4.4.

other from the reciprocal coupling, $I_a = g_{aa}(v_{\text{syn}}^{aa} - V_a) + g_{ab}(v_{\text{syn}}^{ab} - V_b)$. Before the drive is applied the two populations are synchronous, hence, $I_1 = I_2$. The application of the stimulus results in a breaking of symmetry and the two currents are no longer

the same, see Fig. 4.4.6. The stimulated population (red) has both a strong MRBD and PMBR, whereas the other population has a weaker response. As seen in the plots of the within population coherence the magnitude of the PMBR appears to be roughly equal in the two populations after approximately 1 second. Figure 4.4.7 shows the time-frequency spectrograms for both I_1 and I_2. These plots confirm that after around $1 - 1.5$ s the magnitude of the PMBR is of a similar magnitude in the two populations. One may note that the high frequency activity, present when the drive is switched on in the single population case, is no longer present. However, this is not the case. We have chosen to only show the $13 - 35$ Hz activity as we are interested in beta band activity, if we look at a larger range of frequency values one can observe high frequency activity at around 45 Hz in the stimulated population when the drive is switched on.

Interestingly, the system's response to drive depends on the initial data; Fig. 4.4.8 shows a sample of these responses. We found the response was dependent upon which state the system was in when the stimulus was applied, as well as the phase of the oscillations. These criterion fit nicely with our current view on beta rebound, which is that for the individual trials we have little to no rebound in some cases, as the brain is in a suboptimal state or at a suboptimal phase in its oscillatory cycle. It is possible that in our experiment the individual trials match each of these types of behaviour and the act of averaging gives us the stereotypical definition of MRBD and PMBR. More investigation would be needed to verify this hypothesis, which could eb carried out using the data set we collected, but we did not have time to carry out this study.

4.5 Discussion

We have shown that the simple mechanistic model presented in Chapter 3 exhibits both MRBD and PMBR. We demonstrated that the transient response of the reduced

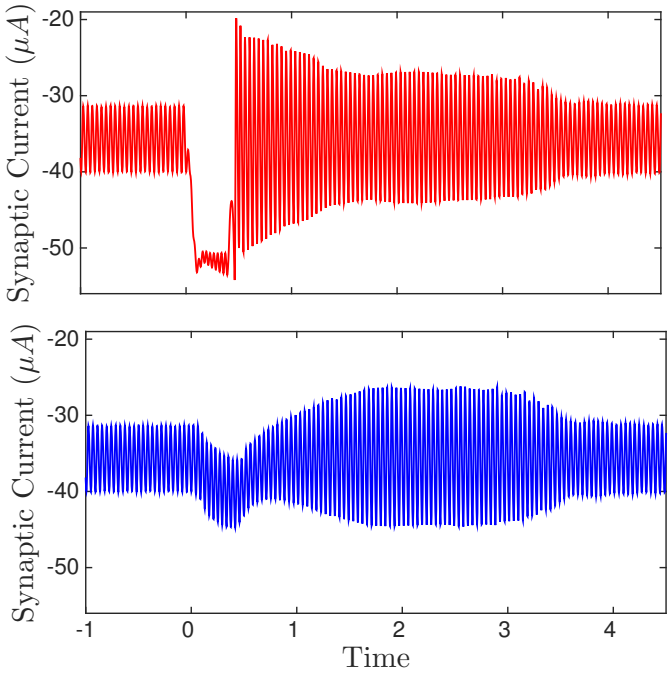

Figure 4.4.6. Effect of the drive on the synaptic currents in the two hemisphere model: Time series of the synaptic current in the two hemisphere model (4.4.1)–(4.4.2), showing both MRBD and PMBR in both of the populations. (Top) Contralateral population, shows strong MRBD and PMBR. (Bottom) Ipsilateral population, the effects are weaker but still notably apparent. Parameter values as in Fig. 4.4.4.

model is sufficiently rich to capture the time scales of both MRBD and PMBR, when it is stimulated whilst operating in the beta frequency range. Importantly, the model parameters can be altered so that the population oscillates at other frequencies, and hence it can be used to explain other ERD/ERS phenomena in the brain. In the case of the single population model, the length of the PMBR was shorter than that seen in our experimental data. However, the model still provided sufficient insight into the two mechanisms, revealing a clear link between the model responses and the changes in within-population coherence. This gives further support to the notion that beta band amplitude changes, and in particular those in MRBD and PMBR, are in fact due to changes in synchrony.

Experimental evidence suggests that the connections between right and left motor

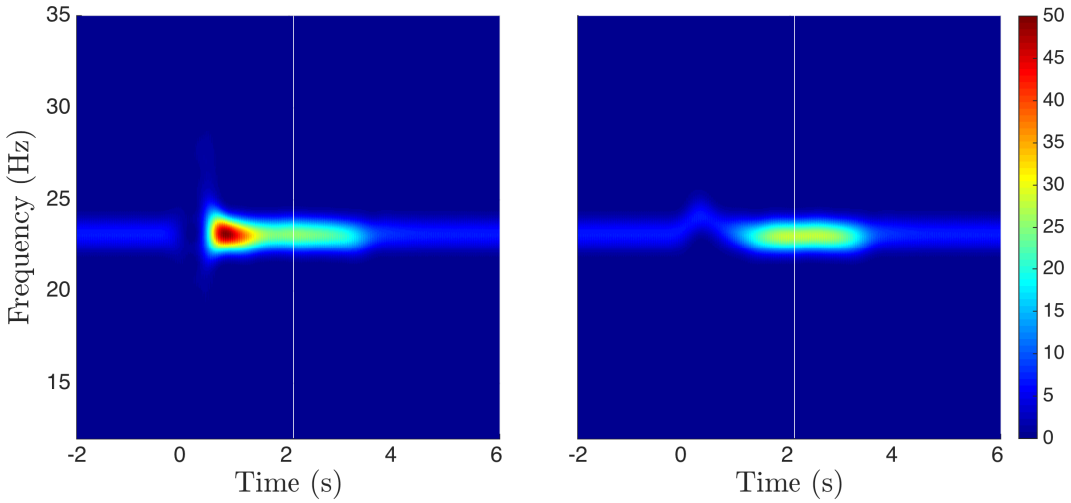

Figure 4.4.7. Spectrograms of the synaptic currents in the two hemisphere model (4.4.1)–(4.4.2)**:** Time-frequency plots for the synaptic current of each of the populations; contralateral (left), ipsilateral (right). This highlights the extent and the length of both MRBD and PMBR in each of the populations. Note that the frequency of oscillation lies within the beta band in both cases. Parameter values as in Fig. 4.4.4.

cortex play an important role in the generation of MRBD and PMBR, as such, we constructed a two hemisphere model. The two hemisphere model provided a richer set of structures within the phase space, such as symmetry breaking and torus bifurcations. Consequently, the two hemisphere model was capable of producing PMBR with a range of different lengths, more consistent with experimental observations. A further study of the data would be required to compare the magnitude of MRBD and PMBR in the ipsilateral hemisphere.

This work presents a number of possible extensions and exciting further research questions. It is also possible that noise may play a constructive role in MRBD and PMBR. Recently, Lai *et al.* demonstrated that the OA ansatz can be extended to perform a mean-field reduction for Kuramoto networks in the presence of noise [106], and this approach could also be used to treat QIF and θ-neuron networks. Other factors that could perhaps lead to a more biologically realistic response include

additional populations, additional synaptic receptors and spatial extension. We will discuss how to spatially extend the model in the next chapter. Other extensions are discussed in more detail in Chapter 7.

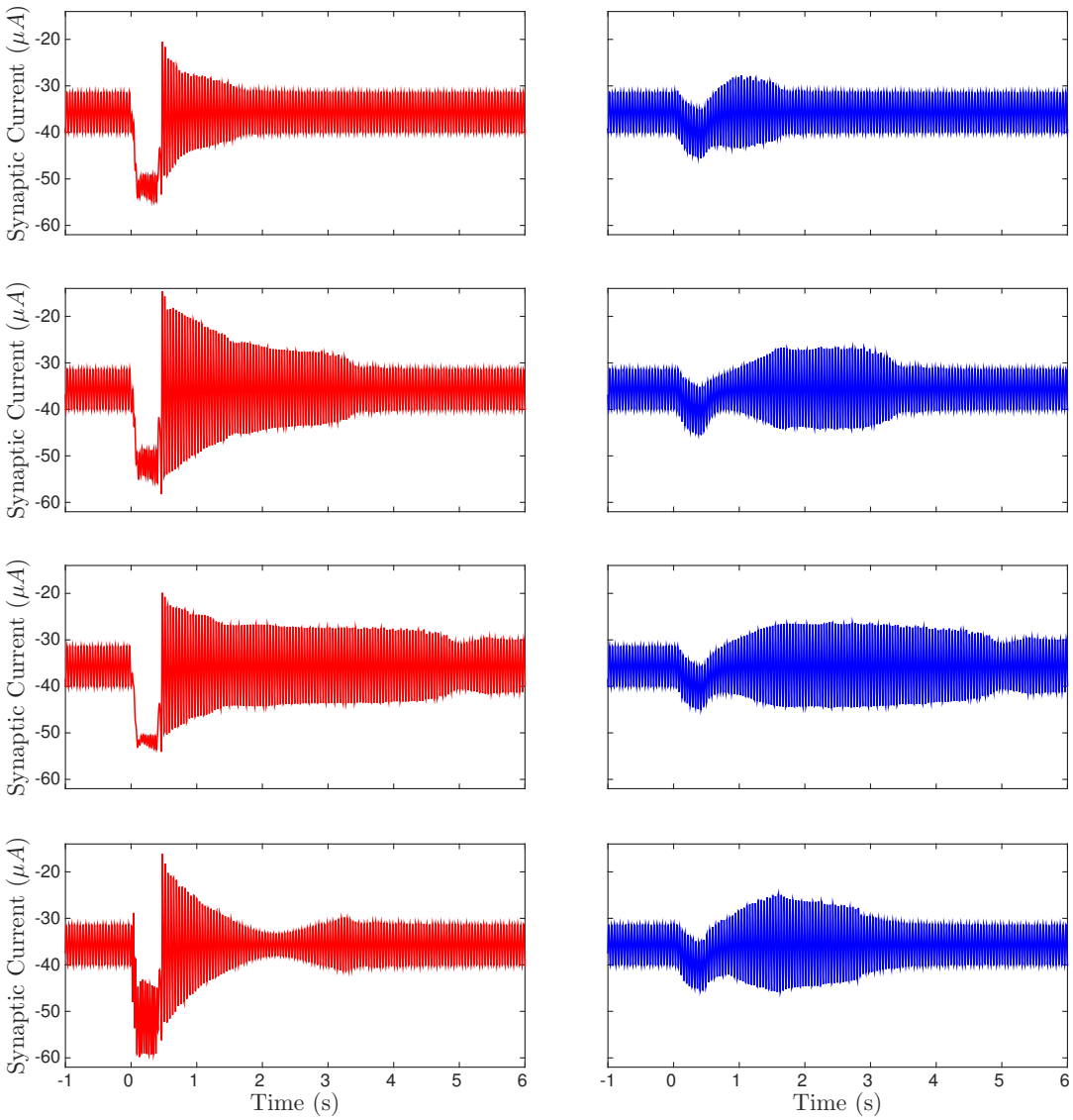

Figure 4.4.8. Different responses to the stimulus for the two hemisphere model: Time series of the synaptic current of each of the populations in (4.4.1)–(4.4.2), showing how the response differs with the choice of initial conditions. The stimulated population is shown on the left (red) and the undriven population on the right (blue). The first row shows a short PMBR, the second row shows an medium length PMBR, the third row illustrates a long PMBR and the last row presents a different type of response. The response in the last row appears to exhibit a short sharp PMBR, followed by some desynchronisation in the contralateral population, while there is only PMBR in the ipsilateral population. Note that the magnitude of the MRBD and PMBR also changes between each of the rows. Parameter values as in Fig. 4.4.4.

Chapter 5

Next generation neural fields I: Analytical calculations for global patterns

The act of passing information between brain regions produces waves of neural activity across the cortex, which are are readily observed using non-invasive techniques such as electroencephalography (EEG) and magnetoencephalography (MEG), as well as in brain slices [65]. Another commonly observed spatial pattern is the so called "bump attractor". This spatially-localised increase in population firing is produced in working memory tasks and the location of the bumps can be linked to the memory location [167]. As point models, neural mass models fail to describe these spatially distributed brain states. It is customary instead to use neural field models to describe wave and bump states in the brain.

This chapter begins with a brief overview of neural field modelling, which reviews the standard approach of neural field models. Section 5.2 provides an introduction to Turing instability analysis, for a one dimensional neural field model with spike frequency adaptation. We then move on to our *next generation neural field model*

by describing how to spatially extend the model presented in Chapter 3. The latter half of the chapter focuses on a Turing instability analysis of our next generation neural field model in both one and two spatial dimensions. In this section we also illustrate the types of patterns that the system can support, by performing numerical simulations.

5.1 Neural field modelling

Neural field models have been shown to mimic many of the phenomena commonly observed in real cortical tissue. They have been particularly successful in describing neurophysiological phenomena, such as EEG/MEG rhythms [170], working memory [111], binocular rivalry [28] and orientation tuning in the visual cortex [14]. They are typically cast as a system of non-local differential equations which describe the spatiotemporal evolution of coarse grained population variables, such as the firing rate of a neuronal population, the average synaptic current, or the mean membrane potential [52].

The first attempt at a neural field model is attributed to Beurle [20]. He built a model to describe the propagation of activation in a given volume of neural tissue. His model was purely excitatory, but, even so, allowed him to examine the propagation of large scale brain activity. It wasn't until the 1970s that Wilson and Cowan [166] extended this model to a two layer system. This model was also an extension of their previous local neural mass model [165], described in Chapter 2. Unlike Beurle, they were interested in spatially localised bump solutions, which were believed to be related to working memory. In his seminal paper, Amari created what is known today as the standard neural field equation [5, 6]. By introducing a Mexican hat type coupling function (local excitation and long range inhibition), he reduced the system to a single equation with a mixture of excitatory and inhibitory connections. This allowed him to

construct explicit solutions for a number of spatial patterns, and assess their stability (at least for a Heaviside firing rate function) [95, 96, 47].

Unlike neural mass models, neural field models are inherently non-local. This leads to the introduction of a weighting function w, which accounts for the interaction between two points in the tissue,

$$f \to w \otimes f, \tag{5.1.1}$$

where f is the population firing rate and $\otimes$ represents a spatial convolution. Neural field models are typically cast as variants of the Amari model,

$$\frac{1}{\alpha}\frac{\partial}{\partial t}u(x,t) = -u(x,t) + \int_{-\infty}^{\infty} \mathrm{d}y w(y) f(u(x-y,t)), \tag{5.1.2}$$

where u represents the activity of the tissue at position x and time t and α is the synaptic time constant. In the case of the Amari model, the firing rate f is chosen to be the Heaviside function, and more generally it is chosen to be a sigmoid. There exist a number of natural extensions to this model to include more biologically realistic features, such as multiple populations/cortical sheets [64, 46], delays [135, 45, 87, 108], adaptation [15, 50, 54, 99], inhomogeneity [49, 11, 26] and dendritic processing [27, 51].

Like their counterparts, neural field models fail to incorporate changes in the underlying synchrony, as they assume that the tissue operates in a near synchronous regime. As such, these models cannot account for the changes in synchrony within spatial patterns. In Chapter 3 we demonstrated that in the absence of a spatial component it is possible to use the OA ansatz to derive an exact mean field model for a network of θ-neurons. In this chapter we will build on this work to construct a *next generation neural field model*.

5.2 Introduction to Turing instability analysis

Neural field equations are typically analysed using linear stability analysis, in particular Turing instability analysis. In 1952, Alan Turing proposed a mechanism for the emergence of patterns in biological systems [157]. Although originally intended for the study of reaction-diffusion equations, Turing's seminal work has been used to analyse many spatially distributed systems. See [118] for an in depth review of pattern formation in biological systems. Here, we are interested in the application of Turing's work to neural field equations. For Mexican hat connections, neural field models with sigmoidal firing rates are well known to support Turing instabilities to spatially patterned states [29, 47]. This was first studied by Wilson and Cowan in 1972 [165], and later by Ermentrout and Cowan, who extended this work to describe visual hallucinations [67].

Using a one dimensional neural field model with linear adaptation as an example, we will describe how the spatially homogeneous steady state can go unstable to global Turing patterns. The inclusion of adaptation ensures that the system can undergo both Turing and Turing-Hopf instabilities. The spike frequency adaptation occurs in the form of an additional ODE, which accounts for the fact that the firing rate of a population of neurons is temporarily reduced after the initial increase which occurs when it is stimulated with an external drive. The system is described as follows,

$$\frac{1}{\alpha}\frac{\partial}{\partial t}u(x,t) = -u(x,t) + (w \otimes f(u))(x,t) - \beta a(x,t), \tag{5.2.1}$$

$$\frac{\partial}{\partial t}a(x,t) = -a(x,t) + u(x,t), \tag{5.2.2}$$

where the spike frequency adaptation a provides negative feedback, and β is the strength of this effect. There exists a spatially homogeneous steady state solution (u^*, a^*), where $u(x,t) = u^*$ and $a(x,t) = a^*$ for all x and t. At steady state $u^* = a^*$

and

$$(1+\beta)u^* = Wf(u^*), \tag{5.2.3}$$

where $W = \int_{\mathbb{R}} \mathrm{d}y w(y)$. For a balanced kernel, the integral W is equal to zero, which fixes the homogeneous steady state as $u^* = a^* = 0$. We will assume a balanced kernel for the rest of this section. We linearise around (u^*, a^*) by letting $u(x,t) \to u^* + \delta u(x,t)$ and $a(x,t) \to a^* + \delta a(x,t)$, with $|\delta u|, |\delta u|, << 1$. If the steady state is stable this perturbation will simply decay. However, we are interested in the case where the steady is unstable state and the perturbation grows in time. The perturbation takes the form $(\delta u(x,t), \delta a(x,t)) = (U, A)\mathrm{e}^{\lambda t}\mathrm{e}^{ikx}$ for some real amplitudes (U, A) where $\lambda \in \mathbb{C}$ is the *growth-rate* and $k \in \mathbb{R}$ is the *wave number*.

Linearising (5.2.1) and (5.2.2) about the fixed point gives

$$\frac{1}{\alpha}\frac{\partial}{\partial t}\delta u(x,t) = -\delta u(x,t) + f'(0)(w \otimes \delta u)(x,t) - \beta \delta a(x,t), \tag{5.2.4}$$

$$\frac{\partial}{\partial t}\delta a(x,t) = \delta u(x,t) - \delta a(x,t). \tag{5.2.5}$$

We now introduce a Fourier transform of the form

$$\widehat{\psi}(k) = \int_{-\infty}^{\infty} \mathrm{e}^{ikx}\psi(x)\mathrm{d}x, \tag{5.2.6}$$

to exploit the fact that $w \otimes \mathrm{e}^{ikx} = \widehat{w}(k)\mathrm{e}^{ikx}$, where $\widehat{w}(k)$ is the Fourier transform of $w(x)$. This allows us to write the system as

$$\frac{\partial}{\partial t}\begin{bmatrix}\delta u \\ \delta a\end{bmatrix} = \begin{pmatrix}-\alpha + \alpha f'(0)\widehat{w}(k) & -\alpha\beta \\ 1 & -1\end{pmatrix}\begin{bmatrix}\delta u \\ \delta a\end{bmatrix} \equiv \mathcal{J}(k)\begin{bmatrix}\delta u \\ \delta a\end{bmatrix}. \tag{5.2.7}$$

The stability of the system is assessed by analysing the characteristic equation $\mathcal{E}(\lambda, k) = 0$, where

$$\mathcal{E}(\lambda, k) \equiv \det(\mathcal{J}(k) - \lambda(k)\mathrm{I}_2), \tag{5.2.8}$$

and I_n is a $n \times n$ identity matrix. Using the above and (5.2.7) we find

$$(-\alpha + \alpha f'(0)\widehat{w}(k) - \lambda)(-1 - \lambda) + \alpha\beta = 0, \tag{5.2.9}$$

which can be solved for λ as,

$$\lambda(k) = \frac{-m(k) \pm \sqrt{m(k)^2 - 4n(k)}}{2}, \tag{5.2.10}$$

where

$$m(k) = 1 + \alpha(1 - f'(0)\widehat{w}(k)), \tag{5.2.11}$$

$$n(k) = \alpha(1 + \beta - f'(0)\widehat{w}(k)). \tag{5.2.12}$$

To compute the Turing and Turing-Hopf bifurcations we split λ into its real and imaginary parts, $\lambda = \mu + i\omega$. A *static* Turing bifurcation can be achieved when $\mu = 0$ and $\omega = 0$, and a *dynamic* Turing-Hopf bifurcation can occur when $\mu = 0$ and $\omega \neq 0$. A non-zero imaginary component of λ is required to generate oscillatory behaviour. The homogeneous steady state is stable if $\mathrm{Re}(\lambda) < 0$ for $\forall k \in \mathbb{R}$. To achieve Turing patterns the wave number must be non-zero, as a wave number of zero doesn't introduce any spatial patterning, and instead results in the formation of another homogeneous state, this is known as a bulk instability. At bifurcation there exists a value of k such that $\mathrm{Re}(\lambda) = 0$. This value is found by solving the following equation, which arises from the implicit function theorem,

$$F_k G_\omega - F_\omega G_k = 0, \tag{5.2.13}$$

where F and G are the real and imaginary parts of the characteristic equation (5.2.9), namely, $F = \mathrm{Re}(\mathcal{E})$, and $G = \mathrm{Im}(\mathcal{E})$. This condition states that bifurcations only

occurs when the eigenspectrum $\lambda(k)$ grazes the imaginary axis. Solving (5.2.13) for k gives us k_c, the critical wave number, for which a bifurcation occurs.

In the case of the 1D neural field model with adaptation (5.2.13) has a solution provided $\widehat{w}(k)$ has maxima for $k \neq 0$. The value of k at the maxima is the solution to (5.2.13). We will examine the system for a specific choice of Mexican hat type connectivity kernel, namely the balanced Wizard hat connectivity kernel,

$$w(x) = (1 - |x|)\mathrm{e}^{-|x|}. \tag{5.2.14}$$

The Fourier transform of this connectivity kernel (5.2.14) is given by

$$\widehat{w}(k) = \frac{4k^2}{(1+k^2)^2}, \tag{5.2.15}$$

which has maxima at $k = \pm 1$, hence $|k_c| = 1$. We will observe *static* Turing patterns in the case where $\lambda(k_c)$ is purely real. This occurs when $n(k_c) = 0$, and hence, $\lambda_+(k_c) = 0$ and $\lambda_-(k_c) = -m(k_c)$. As w is balanced, if $n(k_c) = 0$, $f'(0)\widehat{w}(k_c) = 1 + \beta$. An additional condition is that $\lambda_-(k_c) < 0$, i.e. $m(k_c) > 0$, and hence, $\alpha\beta < 1$. For a *dynamic* Turing-Hopf bifurcation $\lambda(k_c)$ must appear as a purely imaginary complex conjugate pair, hence $m(k_c) = 0$ and $n(k_c) > 0$. The first condition is met if $f'(0)\widehat{w}(k_c) = 1 + 1/\alpha$, and the second for $\alpha\beta > 1$. Figure 5.2.1 shows a bifurcation diagram in α and $f'(0)$, which shows the Turing (blue solid) and Turing-Hopf (red dashed) curves for a particular value of β. The two curves collide at $\alpha\beta = 1$, generating a *Takens-Bodagnov* bifurcation [22].

At bifurcation the pattern $\mathrm{e}^{\pm ik_c x}$ is excited. Beyond the bifurcation point, this pattern will grow in time, and there exists a range of $k \in (k_1, k_2)$ for which $\mathrm{Re}(\lambda(k)) > 0$. As we move away from bifurcation the linear approximation breaks down and the behaviour is dominated by the nonlinear terms. The approach described above can be easily generalised to two spatial dimensions, by replacing e^{ikx} with $\mathrm{e}^{i\mathbf{k}\cdot\mathbf{r}}$, where

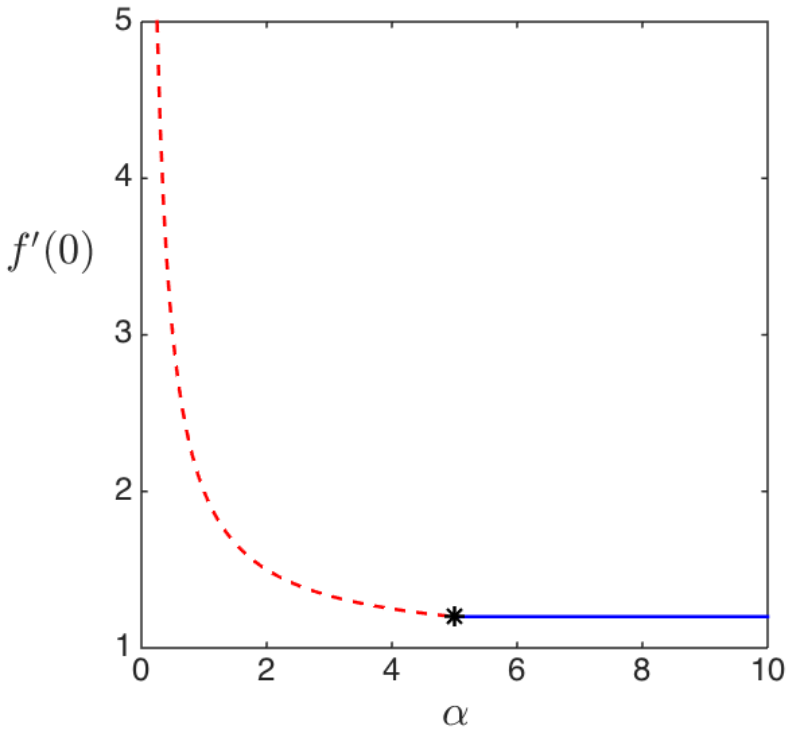

Figure 5.2.1. Turing bifurcation for 1D neural field model with adaptation: Bifurcation diagram in α and $f'(0)$, for the model described by (5.2.1)–(5.2.2), showing the Turing (blue solid) and Turing-Hopf (red dashed) bifurcation curves, for $\beta = 0.5$. The two curves meet at a *Takens-Bodagnov* bifurcation when $\alpha\beta = 1$ (black star).

$\mathbf{k} = [k_x, k_y]$, $\cdot$ represents the dot product, and the wave number is given by $k = |\mathbf{k}|$. As there are an infinite number of choices for k_x and k_y for a given k, it is common to restrict choices to doubly periodic solutions which can be expressed in terms of the basic symmetry groups of hexagon, square and rhombus [46].

5.3 Model description

We consider a globally coupled network of N θ-neurons, spatially distributed along a line of length L such that the jth neuron is at position $x_j = j\Delta x$, where $\Delta x = L/(N-1)$ is the spacing between neurons. The coupling between neuron i and neuron j depends solely upon the distance between the two neurons, $w_{ij} = w(|x_i - x_j|)$. The inclusion of space alters (3.1.9) and (3.1.10) in the following way,

$$\frac{\partial}{\partial t}\theta_j = 1 - \cos\theta_j + (1+\cos\theta_j)(\eta_j + g_j v_{\text{syn}}) - g_j \sin\theta_j, \tag{5.3.1}$$

$$Qg_j = \frac{2\kappa}{N}\sum_{i=1}^{N} w_{ij}\delta(\theta_i - \pi), \tag{5.3.2}$$

for $j = 1 \ldots N$, where $\theta_j \equiv \theta(x_j, t)$, $g_j \equiv g(x_j, t)$. As a reminder to the reader, η_i are the background drives, v_{syn} is the synaptic reversal potential, κ is the coupling strength, Q is the following differential operator,

$$Q = \left(1 + \frac{1}{\alpha}\frac{\partial}{\partial t}\right)^2, \tag{5.3.3}$$

and α^{-1} is the synaptic time scale.

5.3.1 Mean field limit

As seen in Chapter 3, taking the limit $N \to \infty$ allows us to describe the system in terms of the continuous probability distribution function $\rho(x, \eta, \theta, t)$, which now also

depends on x and satisfies the continuity equation:

$$\frac{\partial \rho}{\partial t} + \frac{\partial \rho v_\theta}{\partial \theta} = 0, \tag{5.3.4}$$

where v_θ is a given realisation of $\dot{\theta}$ (5.3.1) (remembering that η is a random variable),

$$v_\theta = \beta \mathrm{e}^{i\theta} + \gamma + \bar{\beta}\mathrm{e}^{-i\theta}, \tag{5.3.5}$$

and β and γ are unchanged from Chapter 3. The continuum limit of (5.3.2) now also includes an integral over space,

$$Qg = \frac{\kappa}{\pi} \sum_{m\in\mathbb{Z}} \int_{-\infty}^{\infty} \mathrm{d}y \int_0^{2\pi} \mathrm{d}\theta \int_{-\infty}^{\infty} \mathrm{d}\eta w(y-x)\mathrm{e}^{im(\theta-\pi)}. \tag{5.3.6}$$

The Ott-Antonsen (OA) ansatz [126] still holds for the spatially extended case, and allows us to write ρ as

$$\rho(x,\eta,\theta,t) = \frac{L(\eta)}{2\pi}\left\{1 + \sum_{n=1}^{\infty} a(x,\eta,t)^n \mathrm{e}^{in\theta} + \mathrm{cc}\right\}. \tag{5.3.7}$$

Substituting (5.3.1) into the continuity equation (5.3.4) we arrive at the same evolution equation for a,

$$\frac{\partial}{\partial t}a + ia^2\beta + ia\gamma + i\overline{\beta} = 0, \tag{5.3.8}$$

where a now also depends on x. Once again the background drive η is drawn from a Lorentzian distribution, given by (3.1.6), which allows us to perform contour integration to show that $z(x,t) = a(x,\eta_0 + i\Delta, t)$, where η_0 is the centre of the Lorentzian distribution and Δ is the full width at half maximum. This allows us to simplify the mean field dynamics of the synaptic conductance g to

$$Qg = \kappa \int w(y-x) f(z(y,t))\mathrm{d}y, \tag{5.3.9}$$

The dynamics of z are unchanged and given by

$$\partial z/\partial t = \mathcal{F}(z; \eta_0, \Delta) + \mathcal{G}(z, g; v_{\text{syn}}), \tag{5.3.10}$$

where z and g are now functions of space as well as time: $z \equiv z(x,t)$ and $g \equiv g(x,t)$, and $\mathcal{F}$ and $\mathcal{G}$ are given by (3.2.15) and (3.2.16) respectively.

5.4 Turing analysis

5.4.1 One spatial dimension

It is first interesting to consider a standard Turing instability analysis of our *next generation neural field* model. Given that standard neural field models support Turing instabilities for Mexican Hat type connectivity kernels, we shall choose the balanced Mexican hat connectivity kernel, $w(x) = (1 - |x|)\exp(-|x|)$. This connectivity kernel is often called a Wizard hat connectivity kernel. The balance condition ensures that at steady state $g(x,t) = g^* = 0$, for all x and t. We denote the corresponding value of $z(x,t)$ by z^*, which can be found by solving

$$\mathcal{F}(z^*; \eta_0, \Delta) = 0, \tag{5.4.1}$$

as $\mathcal{G}(z^*, 0; v_{\text{syn}}) = 0$ by definition. As Q is second order and z is complex the system is 4th order and it is useful to introduce the state variable, $u = [z, \bar{z}, K, g]^T$, where $K = (1 + \alpha^{-1}\partial/\partial t)g$, and the superscript T denotes transpose. The system of equation

is given as follows:

$$\frac{\partial z}{\partial t} = -i\frac{(z-1)^2}{2} + \frac{(z+1)^2}{2}(-\Delta + i\eta_0) + \left[iv_{\text{syn}}\frac{(z+1)^2}{2} - \frac{z^2+1}{2}\right]g, \tag{5.4.2}$$

$$\frac{\partial \bar{z}}{\partial t} = i\frac{(\bar{z}-1)^2}{2} + \frac{(\bar{z}+1)^2}{2}(-\Delta - i\eta_0) + \left[-iv_{\text{syn}}\frac{(\bar{z}+1)^2}{2} - \frac{\bar{z}^2+1}{2}\right]g, \tag{5.4.3}$$

$$\frac{\partial K}{\partial t} = \alpha\left(-K + \frac{\kappa}{\pi}\int w(y)f(z(y-x,t))dy\right), \tag{5.4.4}$$

$$\frac{\partial g}{\partial t} = \alpha\left(-g + K\right). \tag{5.4.5}$$

For convenience, in the following, we will define a and b as follows,

$$a = \frac{\partial z}{\partial t}(x,t); \qquad b = \frac{\partial \bar{z}}{\partial t}(x,t).$$

Note that $a = \bar{b}$.

We apply the following perturbation $u(x,t) = u^* + \delta u(x,t)$, where $\delta u(x,t) = \mathbf{A}e^{\lambda t}e^{ikx}$, and $\mathbf{A} \in \mathbb{R}^4$. As in §5.2, we exploit the fact that $w \otimes e^{ikx} = \widehat{w}(k)e^{ikx}$ to write

$$\frac{\partial}{\partial t}\delta u(x,t) = \mathcal{J}(k)\delta u(x,t), \tag{5.4.6}$$

where $\mathcal{J}$ is the following (k-dependent) Jacobian

$$\mathcal{J}(k) = \left.\begin{pmatrix} \dfrac{\partial a}{\partial z} & 0 & 0 & \dfrac{\partial a}{\partial g} \\ 0 & \dfrac{\partial b}{\partial \bar{z}} & 0 & \dfrac{\partial b}{\partial g} \\ \alpha\kappa\dfrac{\partial f}{\partial z}\widehat{w}(k) & \alpha\kappa\dfrac{\partial f}{\partial \bar{z}}\widehat{w}(k) & -\alpha & 0 \\ 0 & 0 & \alpha & -\alpha \end{pmatrix}\right|_{u^*}. \tag{5.4.7}$$

The terms in $\mathcal{J}(k)$ are given as follows,

$$\frac{\partial a}{\partial z} = -i(z-1) + (z+1)(-\Delta + i\eta_0) = -2\frac{z+1}{z-1}(-\Delta + i\eta_0), \tag{5.4.8}$$

$$\frac{\partial a}{\partial g} = iv_{\text{syn}}\frac{(z+1)^2}{2} - \frac{z^2+1}{2}, \tag{5.4.9}$$

$$\frac{\partial f}{\partial z} = \frac{1}{(1+z)^2}, \tag{5.4.10}$$

$$\widehat{w}(k) = \frac{4k^2}{(1+k^2)^2}. \tag{5.4.11}$$

where

$$\frac{\partial a}{\partial z} = \overline{\frac{\partial b}{\partial \bar{z}}}, \quad \frac{\partial a}{\partial g} = \overline{\frac{\partial b}{\partial g}}, \quad \frac{\partial f}{\partial z} = \overline{\frac{\partial f}{\partial \bar{z}}}. \tag{5.4.12}$$

As in the introduction to Turing analysis (§5.2), we must solve the characteristic equation $\mathcal{E}(\lambda, k) = 0$, where,

$$\mathcal{E}(\lambda, k) \equiv \det\left(\mathcal{J}(k) - \lambda(k)\mathrm{I}_4\right). \tag{5.4.13}$$

Using the above and (5.4.7) gives the following characteristic equation,

$$\left(\frac{\partial a}{\partial z} - \lambda\right)\left(\frac{\partial b}{\partial \bar{z}} - \lambda\right)(-\alpha - \lambda)^2 + \alpha^2\kappa\frac{\partial b}{\partial g}\frac{\partial f}{\partial \bar{z}}\widehat{w}(k)\left(\frac{\partial a}{\partial z} - \lambda\right) + \alpha^2\kappa\frac{\partial a}{\partial g}\frac{\partial f}{\partial z}\widehat{w}(k)\left(\frac{\partial b}{\partial \bar{z}} - \lambda\right) = 0. \tag{5.4.14}$$

Using (5.4.12) allows us to simplify (5.4.14) to,

$$\left|\frac{\partial a}{\partial z}\right|^2\left(\lambda^2 + 2\alpha\lambda + \alpha^2\right) - 2\mathrm{Re}\left(\frac{\partial a}{\partial z}\right)\left(\lambda^3 + 2\alpha\lambda^2 + \alpha^2\lambda\right) + \left(\lambda^4 + 2\alpha\lambda^3 + \alpha^2\lambda^2\right) + 2\alpha^2\kappa\left[\mathrm{Re}\left(\frac{\partial a}{\partial g}\frac{\partial b}{\partial \bar{z}}\frac{\partial f}{\partial z}\right) - \lambda\mathrm{Re}\left(\frac{\partial a}{\partial g}\frac{\partial f}{\partial z}\right)\right]\widehat{w}(k) = 0. \tag{5.4.15}$$

To compute (5.2.13) we must separate (5.4.15) into its real and imaginary components. To do so we must make use of the substitution $\lambda = \mu + i\omega$, which leads us to the following equation,

$$\left|\frac{\partial a}{\partial z}\right|^2 \left(\mu^2 - \omega^2 + 2i\mu\omega + 2\alpha(\mu + i\omega) + \alpha^2\right) - 2\mathrm{Re}\left(\frac{\partial a}{\partial z}\right)\left(\mu^3 - 3\mu\omega^2 + i(3\mu^2\omega - \omega^3) + 2\alpha(\mu^2 - \omega^2 + 2i\mu\omega) + \alpha^2(\mu + i\omega)\right) + \left(\mu^4 - 6\mu^2\omega^2 + \omega^4 + i(4\mu^3\omega - 4\mu\omega^3) + 2\alpha(\mu^3 - 3\mu\omega^2 + i(3\mu^2\omega - \omega^3)) + \alpha^2(\mu^2 - \omega^2 + 2i\mu\omega)\right) + 2\alpha^2\kappa\left[\mathrm{Re}\left(\frac{\partial a}{\partial g}\frac{\partial b}{\partial \bar{z}}\frac{\partial f}{\partial z}\right) - (\mu + i\omega)\mathrm{Re}\left(\frac{\partial a}{\partial g}\frac{\partial f}{\partial z}\right)\right]\widehat{w}(k) = 0. \tag{5.4.16}$$

It is now easy to separate (5.4.16) into its real and imaginary parts,

$$F \equiv \left|\frac{\partial a}{\partial z}\right|^2 \left(\mu^2 - \omega^2 + 2\alpha\mu\omega + \alpha^2\right) - 2\mathrm{Re}\left(\frac{\partial a}{\partial z}\right)\left(\mu^3 - 3\mu\omega^2 + 2\alpha(\mu^2 - \omega^2) + \alpha^2\mu\right) + \left(\mu^4 - 6\mu^2\omega^2 + \omega^4 + 2\alpha(\mu^3 - 3\mu\omega^2) + \alpha^2(\mu^2 - \omega^2)\right) + 2\alpha^2\kappa\mathrm{Re}\left(\frac{\partial a}{\partial g}\frac{\partial b}{\partial \bar{z}}\frac{\partial f}{\partial z} - \mu\frac{\partial a}{\partial g}\frac{\partial f}{\partial z}\right)\widehat{w}(k) = 0, \tag{5.4.17}$$

$$G \equiv \left|\frac{\partial a}{\partial z}\right|^2 (2\mu\omega + 2\alpha\omega) - 2\mathrm{Re}\left(\frac{\partial a}{\partial z}\right)\left(3\mu^2\omega - \omega^3 + 4\alpha\mu\omega + \alpha^2\omega\right) + \left(4\mu^3\omega - 4\mu\omega^3 + 2\alpha(3\mu^2\omega - \omega^3) + 2\alpha^2\mu\omega\right) - 2\alpha^2\kappa\omega\mathrm{Re}\left(\frac{\partial a}{\partial g}\frac{\partial f}{\partial z}\right)\widehat{w}(k) = 0. \tag{5.4.18}$$

In order to evaluate (5.2.13), we shall first differentiate F and G with respect to ω,

$$F_\omega = 2\left|\frac{\partial a}{\partial z}\right|^2 (-\omega + \alpha\mu) + 4\omega\mathrm{Re}\left(\frac{\partial a}{\partial z}\right)(+3\mu + 2\alpha) - 2\left(6\mu^2\omega - 2\omega^3 + 6\alpha\mu\omega + \alpha^2\omega\right), \tag{5.4.19}$$

$$G_\omega = 2\left|\frac{\partial a}{\partial z}\right|^2 (\mu + \alpha) - 2\mathrm{Re}\left(\frac{\partial a}{\partial z}\right)\left(3\mu^3 - 3\omega^2 + 4\alpha\mu + \alpha^2\right) + 2\left(2\mu^3 - 6\mu\omega^2 + 3\alpha(\mu^2 - \omega^2) + \alpha^2\mu\right) - 2\alpha^2\kappa\mathrm{Re}\left(\frac{\partial a}{\partial g}\frac{\partial f}{\partial z}\right)\widehat{w}(k). \tag{5.4.20}$$

When differentiating F and G with respect to k, we note that $\widehat{w}(k)$ is the only component of each that depends on k,

$$\begin{aligned}\frac{\mathrm{d}}{\mathrm{d}k}\widehat{w}(k) &= 4\frac{2k(1+k^2)^2 - 2(1+k^2)(2k)(k^2)}{(1+k^2)^4} = \frac{8k(1-k^4)}{(1+k^2)^4} \\ &= \frac{8k(1-k^2)}{(1+k^2)^3}.\end{aligned}$$

Hence,

$$F_k = 16\alpha^2\kappa\frac{k(1-k^2)}{(1+k^2)^3}\mathrm{Re}\left(\frac{\partial a}{\partial g}\frac{\partial b}{\partial \bar{z}}\frac{\partial f}{\partial z} - \mu\frac{\partial a}{\partial g}\frac{\partial f}{\partial z}\right) \tag{5.4.21}$$

$$G_k = -16\alpha^2\kappa\omega\frac{8k(1-k^2)}{(1+k^2)^3}\mathrm{Re}\left(\frac{\partial a}{\partial g}\frac{\partial f}{\partial z}\right). \tag{5.4.22}$$

The coefficients $|\partial a/\partial z|^2$, $\mathrm{Re}\,(\partial a/\partial z)$, $\mathrm{Re}\left(\frac{\partial a}{\partial g}\frac{\partial f}{\partial z}\right)$ and $\mathrm{Re}\left(\frac{\partial a}{\partial g}\frac{\partial b}{\partial \bar{z}}\frac{\partial f}{\partial z}\right)$ are computed in Appendix B. Interestingly, we find that

$$\mathrm{Re}\left(\frac{\partial a}{\partial g}\frac{\partial f}{\partial z}\right) = -\frac{1}{2}f(z), \tag{5.4.23}$$

which will be of use subsequently.

Turing instability

For a *static* Turing bifurcation $\mu = 0$ and $\omega = 0$, which yields the following characteristic equation

$$\left|\frac{\partial a}{\partial z}\right|^2 + 2\kappa\mathrm{Re}\left(\frac{\partial a}{\partial g}\frac{\partial b}{\partial \bar{z}}\frac{\partial f}{\partial z}\right)\widehat{w}(k) = 0, \tag{5.4.24}$$

and bifurcation equation

$$k(1-k^2)\left[\mathrm{Re}\left(\frac{\partial a}{\partial g}\frac{\partial b}{\partial \bar{z}}\frac{\partial f}{\partial z}\right)\left(\left|\frac{\partial a}{\partial z}\right|^2 - \alpha\mathrm{Re}\left(\frac{\partial a}{\partial z}\right) + \frac{1}{2}\alpha\kappa f(z)\widehat{w}(k)\right)\right] = 0. \tag{5.4.25}$$

Upon analysing this equation we found that the term inside the square brackets has no real roots and hence, $k(1-k^2)=0$. Since the wave number k must be non-zero to excite patterned Turing states, $|k_c|=1$, where k_c is the critical value of k, as described in §5.2. This implies that if we choose parameter values which satisfy (5.4.24) for $|k|=1$ and plot $\lambda(k)$ in the (μ,ω)-plane, the branch of solutions will graze the imaginary axis at $\omega=0$, corresponding to a static Turing bifurcation. Figure 5.4.1 shows the continuous spectrum $\lambda(k)$ at a static Turing bifurcation. It can be seen that the spectrum does indeed touch the imaginary axis at $\omega=0$.

Figure 5.4.2 shows a two parameter bifurcation diagram in the synaptic reversal potential v_{syn} and the mean background drive η_0, for a range of values for the coupling strength κ. The system is unstable to static Turing patterns in the parameter window enclosed by the curves. It can be seen that there are two critical values for η_0 if $v_{\text{syn}} \gtrsim 0$ and no Turing bifurcation if $v_{\text{syn}} \lesssim 0$. If we take the lower of the these two values of η_0 and begin to increase η_0, the branch of solutions (shown in Fig. 5.4.1) is pushed to the right in the (μ,ω)-plane, implying that $\text{Re}(\lambda)>0$ for a range of $k\in(k_1,k_2)$, and that the system is unstable and, hence, can exhibit static Turing patterns. If η_0 is increased further the branch of solutions tends back to the left in the (μ,ω)-plane, until we hit the second Turing bifurcation, resulting in a restoration of stability and a homogeneous steady state. For particular parameter sets, increasing η_0 may result in additional bifurcations occurring, namely a Turing-Hopf bifurcation. We will discuss this in the next subsection. For all values of η_0 there exists one critical value of v_{syn}. As v_{syn} is increased through this value we see the emergence of static Turing patterns. Increasing κ results in an increase in the angle made between the to sections of the bifurcation curve, and hence, a larger window of instability. Changing the heterogeneity of the background drive Δ has very little effect on the location and existence of the Turing bifurcations, and altering the synaptic time constant α has no effect, as it only scales λ.

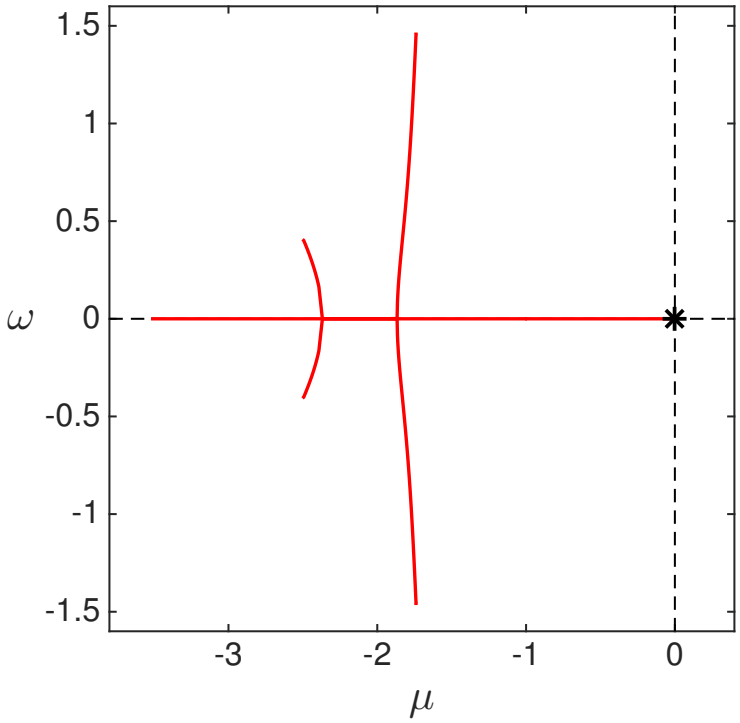

Figure 5.4.1. Static Turing bifurcation for next generation neural field model: Continuous spectrum of the system described by (5.4.2)–(5.4.5), at the static Turing bifurcation. This plot was computed by solving (5.4.24)–(5.4.25) to find the parameter values at which a Turing bifurcation occurs. Theses parameter values were then used to solve (5.4.14) for $\lambda(k) = \mu(k) + i\omega(k)$, which is plotted parametrically as a function of k. The solution branch can be seen to graze the imaginary axis at $\omega = 0$ (black star). Parameter values: $\eta_0 = -1.515$, $v_{\text{syn}} = 10$, $\Delta = 0.5$ $\alpha = 1$.

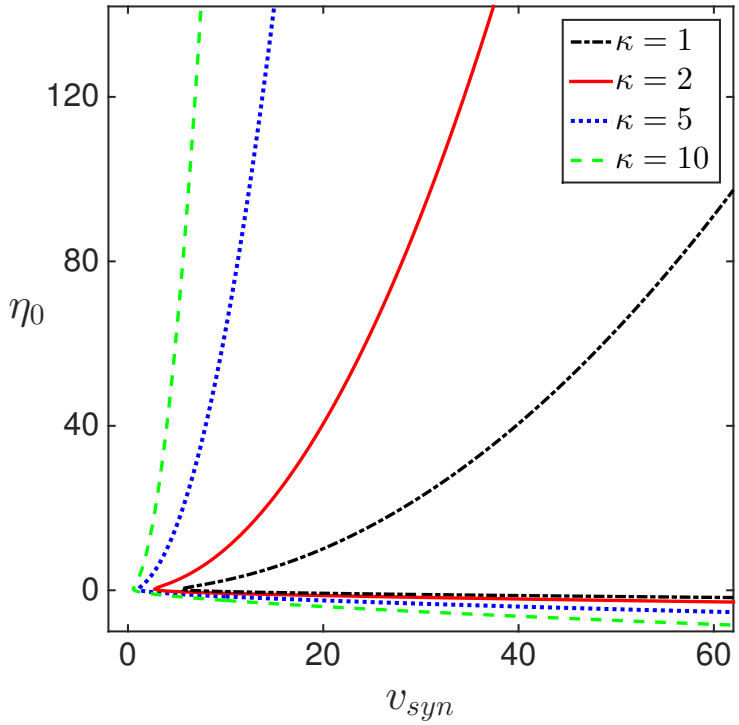

Figure 5.4.2. Static Turing bifurcation for next generation neural field model, given by (5.3.9)–(5.3.10)**:** Two parameter bifurcation diagram in synaptic reversal potential v_{syn} and the mean background drive η_0, showing the Turing curve for a number of different values of coupling strength κ. The system is unstable in the enclosed region. It can be seen that increasing κ increases the area of instability. Parameter values: $\Delta = 0.5$, $\alpha = 1$.

Turing-Hopf instability

As covered in §5.2, *dynamic* Turing-Hopf bifurcations occur when $\mu = 0$ and $\omega \neq 0$. Substituting $\mu = 0$ into (5.4.19), (5.4.20), (5.4.21) and (5.4.22) yields the following

$$\begin{aligned}
F_\omega &= -2\omega \left|\frac{\partial a}{\partial z}\right|^2 + 8\alpha\omega \mathrm{Re}\left(\frac{\partial a}{\partial z}\right) + 4\omega^3 - 2\alpha^2\omega, \\
G_\omega &= 2\alpha \left|\frac{\partial a}{\partial z}\right|^2 + 2\mathrm{Re}\left(\frac{\partial a}{\partial z}\right)\left(3\omega^2 - \alpha^2\right) - 6\alpha\omega^2 + \alpha f(z), \\
F_k &= 16\alpha^2\kappa \frac{k(1-k^2)}{(1+k^2)^3} \mathrm{Re}\left(\frac{\partial a}{\partial g}\frac{\partial b}{\partial \bar{z}}\frac{\partial f}{\partial z}\right), \\
G_k &= +8\alpha^2\kappa\omega \frac{k(1-k^2)}{(1+k^2)^3} f(z).
\end{aligned}$$

Hence, the condition for a Turing-Hopf bifurcation is,

$$\begin{aligned}
k(1-k^2)\Bigg[\omega^2 f(z)\left(\left|\frac{\partial a}{\partial z}\right|^2 + 4\alpha\mathrm{Re}\left(\frac{\partial a}{\partial z}\right) + 2\omega^2 - \alpha^2\right) - \mathrm{Re}\left(\frac{\partial a}{\partial g}\frac{\partial b}{\partial \bar{z}}\frac{\partial f}{\partial z}\right) \\
\times \left(\alpha\left|\frac{\partial a}{\partial z}\right|^2 + \mathrm{Re}\left(\frac{\partial a}{\partial z}\right)\left(3\omega^2 - \alpha^2\right) - 3\alpha\omega^2 + \frac{1}{2}\alpha^2\kappa f(z)\right)\widehat{w}(k)\Bigg] = 0,
\end{aligned} \tag{5.4.26}$$

with the characteristic equation (split into real and imaginary parts),

$$\left|\frac{\partial a}{\partial z}\right|^2\left(-\omega^2 + \alpha^2\right) + 4\alpha\omega^2\mathrm{Re}\left(\frac{\partial a}{\partial z}\right) + (\omega^4 - \alpha^2\omega^2) + 2\alpha^2\kappa\mathrm{Re}\left(\frac{\partial a}{\partial g}\frac{\partial b}{\partial \bar{z}}\frac{\partial f}{\partial z}\right)\widehat{w}(k) = 0, \tag{5.4.27}$$

$$\alpha\left|\frac{\partial a}{\partial z}\right|^2 + \mathrm{Re}\left(\frac{\partial a}{\partial z}\right)\left(\omega^2 - \alpha^2\right) - \alpha\omega^2 - \frac{1}{2}\alpha^2\kappa f(z)\widehat{w}(k) = 0. \tag{5.4.28}$$

Once again the term in the square brackets in (5.4.26) has no real roots, and hence, $|k_c| = 1$. Figure 5.4.3 shows the branch of solutions for a set of parameter values which satisfy (5.4.27) and (5.4.28), for $|k| = 1$. The branch of solutions $\lambda(k)$ grazes

the imaginary axis at $\omega = \pm 1.327$ (black stars), corresponding to a Turing-Hopf bifurcation.

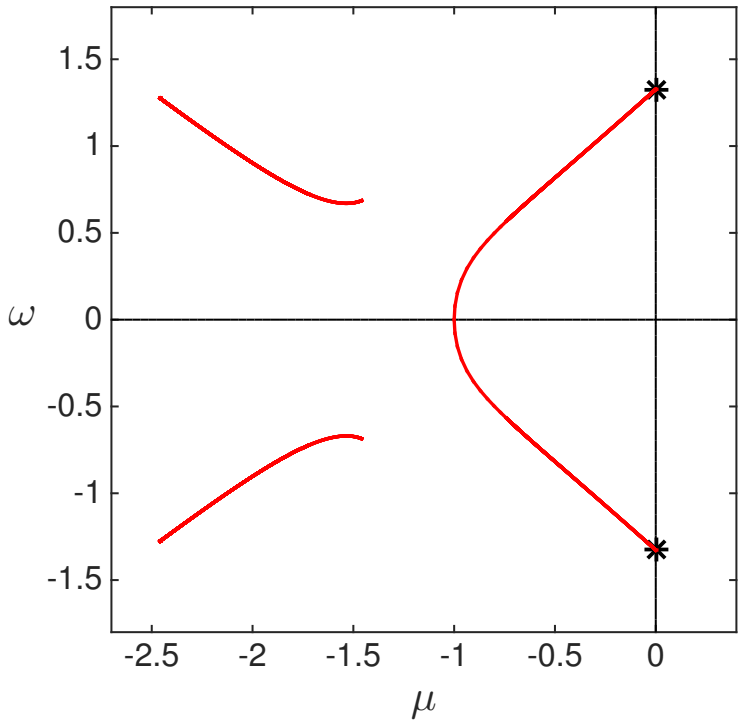

Figure 5.4.3. Turing-Hopf bifurcation for next generation neural field model: Continuous spectrum of the system described by (5.4.2)–(5.4.5), at the dynamic Turing bifurcation. This plot was computed by solving (5.4.26)–(5.4.28) to find a parameter set for which a Turing-Hopf bifurcation arises in the system. Using these parameter values, (5.4.14) was solved for $\lambda(k) = \mu(k) + i\omega(k)$, which is plotted parametrically as a function of k. The black stars represent the Turing-Hopf bifurcations which occur when $|k| = 1$ and $\omega = \pm 1.327$. Parameter values: $\eta_0 = -0.414$, $v_{\text{syn}} = -10$, $\Delta = 0.5$, $\alpha = 1$.

The Turing-Hopf curve is plotted as a function of synaptic reversal potential v_{syn} and average background drive η_0 in Fig. 5.4.4, for a range of different values of the synaptic time constant α. There is a noteworthy value of α where the system switches from having one critical value of η_0 for every value of v_{syn} to having two critical values for $v_{\text{syn}} \lesssim 0$ and the Turing-Hopf bifurcation not existing for $v_{\text{syn}} \gtrsim 0$. This value

depends on upon both Δ and κ. For the parameters chosen in Fig. 5.4.4 the bifurcation structure undergoes this switch for $\alpha = 1.585$. In both cases there exists one critical value of v_{syn} for every value of η_0 and the system displays *dynamic* Turing patterns, namely periodic travelling plane waves, as v_{syn} is decreased through this value. As was the case for the static Turing bifurcation curve, increasing κ increases the angle between the two sections of the bifurcation curve. Changing the heterogeneity of the background drive Δ has little effect on the location of the Turing-Hopf bifurcation.

The most exotic patterns occur when the Turing and Turing-Hopf bifurcations collide, due to the excitation of two different modes. As such, we choose values of Δ, κ and α for which this is possible. In particular we need α to be large enough that a Turing-Hopf bifurcation can occur for $v_{\text{syn}} > 0$. Figure 5.4.5 shows a bifurcation diagram in η_0 and v_{syn} for such a choice of parameter values, the blue curve represents the Turing-Hopf curve and the red the Turing curve. The system exhibits stationary patterns in the area to the right of the red curve and dynamic oscillatory patterns to the left of the blue curve. In the area where the two regions overlap we see more exotic patterns, which cannot be described by linear stability analysis. The insets show the behaviour of the synchrony R (where R is the magnitude of the Kuramoto order parameter z) near to the bifurcations. The details of the numerical scheme used to obtain these results is described in Appendix C.1. Here we simulated on a domain of length 50, with 600 grid points. Simulations were also done on finer meshes, and we can confirm that the results were unchanged.

Figure 5.4.6 shows a sample of the types of patterns that are seen in the system. As above, the numerical scheme is described in Appendix C.1. Here we simulated on a domain of length 40, with 600 grid points. The *static* Turing bumps are seen close to the Turing curve, but go unstable to different patterns further away from the curve. The *dynamic* Turing waves are seen close to the Turing-Hopf curve, and are stable even far away from this curve. The system can also support global breathers

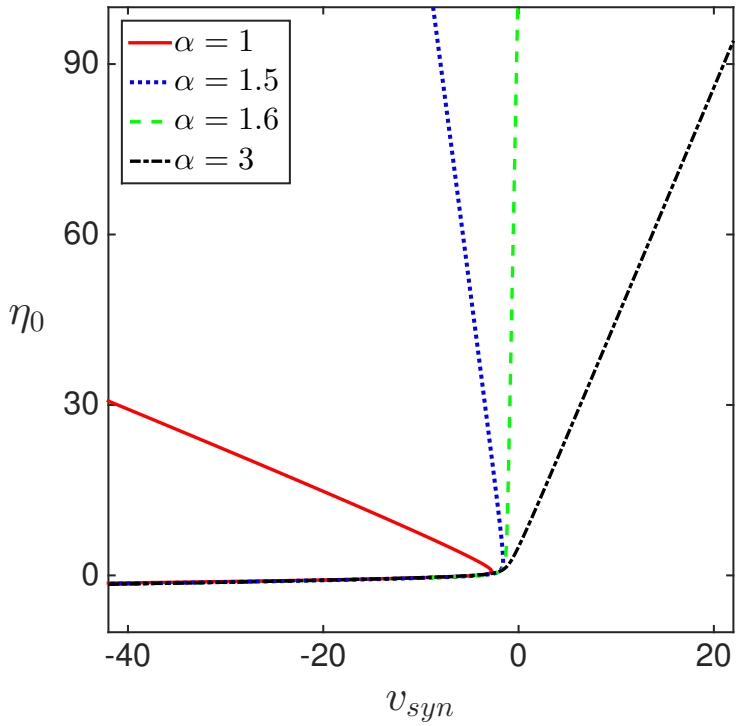

Figure 5.4.4. Turing-Hopf bifurcation for next generation neural field model: Two parameter bifurcation diagram in the synaptic reversal potential v_{syn} and the mean background drive η_0, for the system described by (5.4.2)–(5.4.5), showing the Turing-Hopf curve for a number of different values of α. The system is unstable in the enclosed region/area above the curve. It can be seen that increasing α through roughly 1.6 changes the bifurcation structure, such that the system has one Turing-Hopf point for every value of v_{syn}, rather than having two bifurcation points for $v_{\text{syn}} \lesssim 0$ and none for $v_{\text{syn}} \gtrsim 0$. Parameter values: $\Delta = 0.5$, $\kappa = 5$.

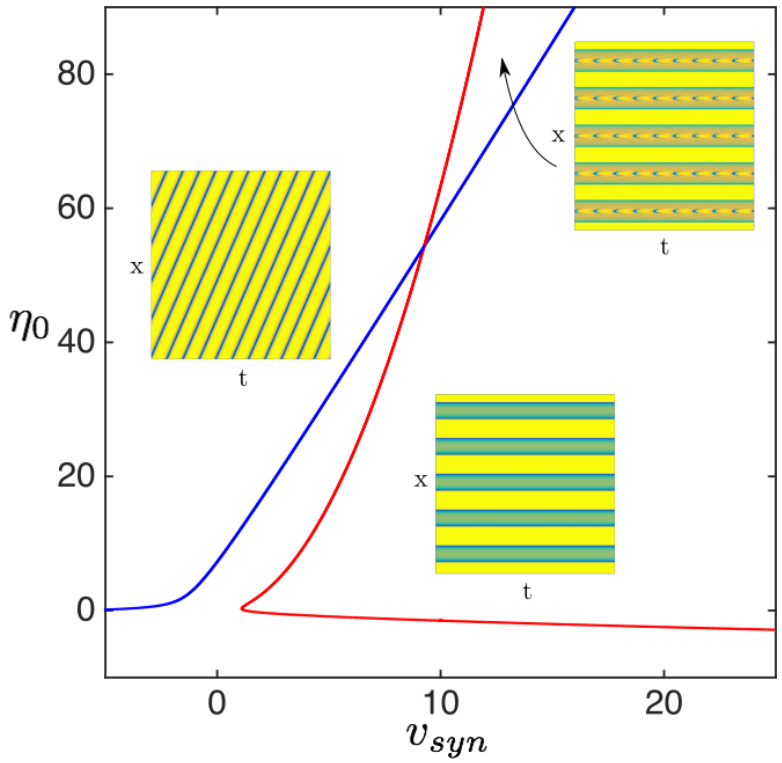

Figure 5.4.5. Turing analysis for next generation neural field model, given by (5.3.9)–(5.3.10)**:** Two parameter bifurcation diagram in the synaptic reversal potential v_{syn} and the average background drive η_0, showing the Turing curve (red) and the Turing-Hopf curve (blue). In the area to the left of the Turing curve we see stationary patterns and in the area to the right of the Turing-Hopf curve we see dynamic patterns. In the area where the two regions overlap we see more exotic patterens. The insets show the typical behaviour of R in each of the regions. Parameter values: $\Delta = 0.5$, $\kappa = 5$, $\alpha = 5$.

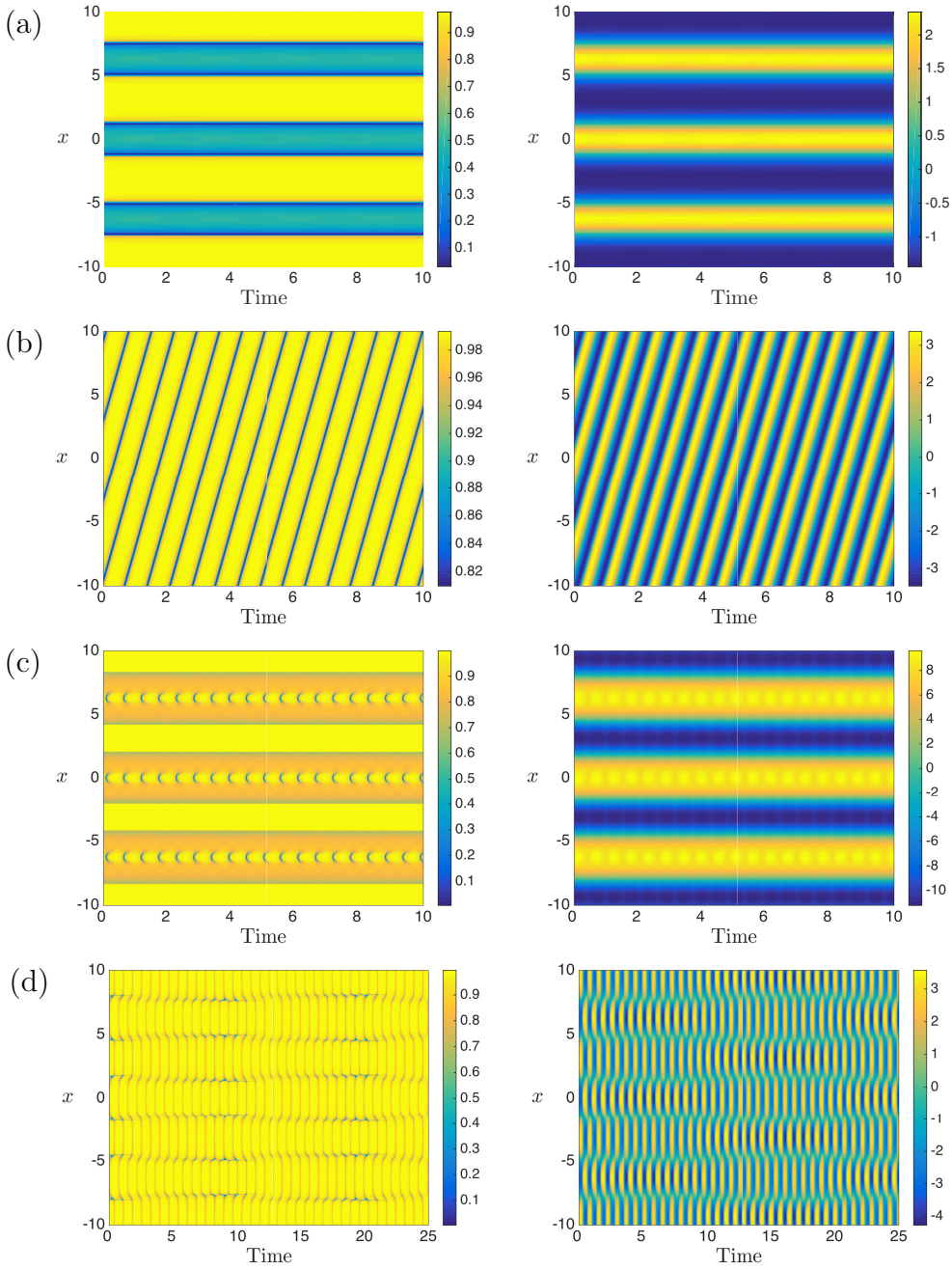

Figure 5.4.6. Zoo of patterns: Sample of the patterns that the system described by (5.3.9)–(5.3.10) can support. The left hand column shows the synchrony R and the right column shows the synaptic conductance g. (a) *Static* Turing bumps, $\eta_0 = 0$, $v_{\text{syn}} = 3$. (b) *Dynamic* Turing waves, $\eta_0 = 15$, $v_{\text{syn}} = -10$. (c) Structures within bumps, $\eta_0 = 60$, $v_{\text{syn}} = 10$. (d) Breathers, $\eta_0 = 15$, $v_{\text{syn}} = -10$. (Note change of timescale in (d).) Parameter values: $\Delta = 0.5$, $\kappa = 5$, $\alpha = 5$.

in this region. Breathers are bumps whose width oscillates in time. The breathers are shown in Fig. 5.4.6d and it can be seen that they are periodic in both space and time, with the amplitude of the breathers also oscillating in time. These states can exist for prolonged periods of time, but ultimately give way to the *dynamic* Turing waves. To obtain periodic travelling waves we applied perturbations of the form $\delta z = A_1(\cos x + i \sin x)$, $\delta g = \delta K = A_2 \cos x$. For the periodic breathing states, the perturbation to g and K was unchanged but $\delta z = A_1(\cos x + i \cos x)$. The more exotic patterns which have structure within the bumps are seen in a large parameter window, both inside the Turing-Hopf region and outside it. Both the Turing and Turing-Hopf bifurcations appear to be subcritical, based on observations from our numerical simulations. These patterns do not exist if we choose parameter values such that the Turing and Turing-Hopf regions do not overlap. Structures within bump solutions are not seen in standard neural field models. They are, however, commonly seen in networks of spiking neurons [107, 41], which suggests that this *next generation neural mass model* retains information about the underlying spiking model. Figure 5.4.7 shows the results for a simulation of 500 θ-neurons distributed on a ring of circumference 2π. It can be seen that a bump of oscillatory activity manifests in the system, a clear spatial order in the firing events cannot be seen, but the pattern of firing is not random.

5.4.2 Two spatial dimensions

It is trivial to extend the system to include a second spatial dimension. This is achieved by considering a network of θ-neurons on a two dimensional grid of length L_x and width L_y, instead of a one dimensional line of length L. The reduction follows the same procedure outlined in §5.3.1, and the reduced system is described by (5.4.2)–(5.4.5), under the replacement $x \to \mathbf{r}$ and $y \to \mathbf{r}'$, where $\mathbf{r} = [x, y]$ is a two dimensional vector.

Results from the 1D case described above would suggest that we should find Turing

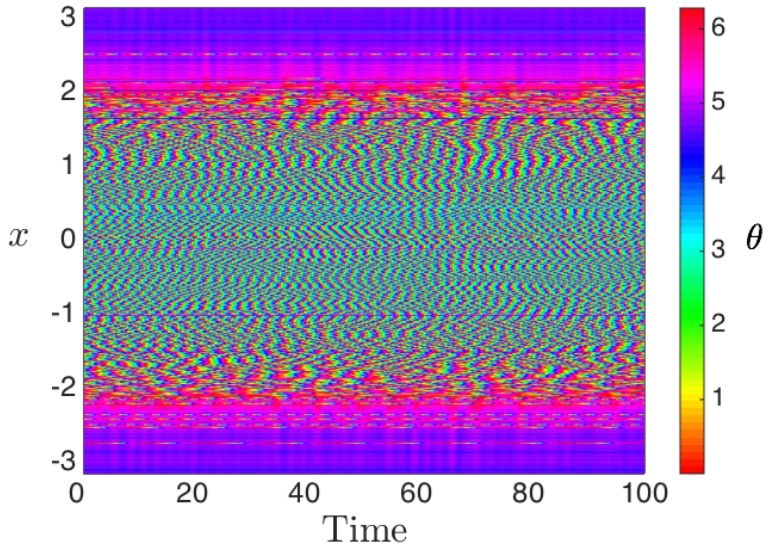

Figure 5.4.7. Bump attractor in simulation of 500 θ-neurons: Results for a simulation of 500 θ-neurons, spatially distributed on a ring with circumference 2π, showing the value of θ_i for $i = 1 \dots 500$, as a function of space and time. A bump of firing activity, centred around 0, can be clearly seen.

and Turing-Hopf bifurcations in the 2D case for $w(\mathbf{r}) = (1 - |\mathbf{r}|)\mathrm{e}^{-|\mathbf{r}|}$. As this kernel is not balanced in 2D and the 2D Turing analysis is simplest if we choose forms of $w(\mathbf{r})$, which allow us to make use of known formulae for Bessel functions, when computing the 2D Fourier transform of $w(\mathbf{r})$, we shall work with an alternative coupling kernel. This choice of kernel is given by $w(r) = E(r) - E(\beta r)/\gamma$ [127], where

$$E(r) = \frac{2}{3\pi}(K_0(r) - K_0(2r)), \tag{5.4.29}$$

and $K_\nu(x)$ is the modified Bessel function of the second kind of order ν. The properties of the modified Bessel function mean that this connectivity kernel has a 'nice' Fourier transform. This will allow us to easily evaluate the spatial convolution in the subsequent analysis. This kernel maintains the key properties of short range excitation and long range inhibition for $\beta < 1$ and $\gamma > 1$, and it is balanced for $\gamma = 1/\beta^2$. Figure 5.4.8 shows a plot of $w(\mathbf{r})$ for $\beta = 0.5$ and $\gamma = 4$. Introducing a two dimensional Fourier

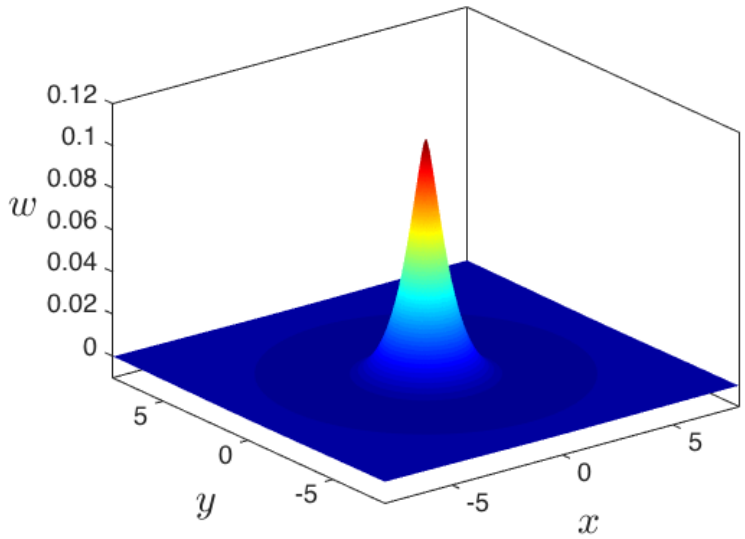

Figure 5.4.8. Two dimensional Mexican hat function: Plot of the connectivity kernel $w(\mathbf{r}) = E(\mathbf{r})) - E(\beta\mathbf{r})/\gamma$, for $\beta = 0.5$, $\gamma = 4$.

transform of the form

$$\widehat{\psi}(\mathbf{k}) = \int_{\mathbb{R}^2} \mathrm{e}^{i\mathbf{k}\cdot\mathbf{r}}\psi(\mathbf{r})\mathrm{d}\mathbf{r}, \tag{5.4.30}$$

and noting that the Hankel transform of $K_0(p\mathbf{r})$ is $H_p(k) = (k^2 + p^2)^{-1}$ we can compute the 2D Fourier transform of w,

$$\widehat{w}(k) = \frac{2}{3\pi}\left[H_1(k) - H_2(k) + \frac{H_{2\beta}(k)}{\gamma} - \frac{H_\beta(k)}{\gamma}\right]. \tag{5.4.31}$$

To simplify the calculations that follow, we shall once again let

$$a = \frac{\partial z}{\partial t}(\mathbf{r}, t); \quad b = \frac{\partial \bar{z}}{\partial t}(\mathbf{r}, t).$$

In this case perturbations take the form $u(\mathbf{r}, t) = \mathbf{A}\mathrm{e}^{\lambda t}\mathrm{e}^{i\mathbf{k}\cdot\mathbf{r}}$, where $\mathbf{k} = [k_x, k_y]$ and the wave number is given by $k = |\mathbf{k}|$. Applying a perturbation of this form gives

$$\frac{\partial}{\partial t}\delta u(\mathbf{r}, t) = \mathcal{J}(k)\delta u(\mathbf{r}, t), \tag{5.4.32}$$

where $\mathcal{J}(k)$ is the Jacobian matrix given by (5.4.7). The entries of (5.4.7) are given by (5.4.8)–(5.4.10), apart from $\widehat{w}(k)$ which is given by (5.4.31).

As before, we must solve the characteristic equation (5.2.9) and corresponding bifurcation condition (5.2.13). As $\widehat{w}(k)$ takes a different form, F_k and G_k need to be recomputed. Once again we note that the only part of F and G that depends on the wave number k is $\widehat{w}(k)$,

$$\frac{\mathrm{d}}{\mathrm{d}k}\widehat{w} = \frac{2}{3\pi}\left[\frac{\mathrm{d}H_1}{\mathrm{d}k} - \frac{\mathrm{d}H_2}{\mathrm{d}k} + \frac{1}{\gamma}\left(\frac{\mathrm{d}H_{2\beta}}{\mathrm{d}k} - \frac{\mathrm{d}H_\beta}{\mathrm{d}k}\right)\right], \tag{5.4.33}$$

and where

$$\frac{\mathrm{d}H_p}{\mathrm{d}k}(k) = \frac{-2k}{(p^2 + k^2)^2}. \tag{5.4.34}$$

Hence

$$F_k = 2\alpha^2\kappa\frac{\mathrm{d}\widehat{w}}{\mathrm{d}k}\left[\mathrm{Re}\left(\frac{\partial a}{\partial g}\frac{\partial b}{\partial \bar{z}}\frac{\partial f}{\partial z}\right)+\frac{1}{2}\mu f(z)\right], \tag{5.4.35}$$

$$G_k = \alpha^2\kappa\omega\frac{\mathrm{d}\widehat{w}}{\mathrm{d}k}f(z). \tag{5.4.36}$$

Turing instability

As before we observe a *static* bifurcation when $\mu = 0$ and $\omega = 0$, which yields the following set of equations

$$\left|\frac{\partial a}{\partial z}\right|^2 + 2\kappa\mathrm{Re}\left(\frac{\partial a}{\partial g}\frac{\partial b}{\partial \bar{z}}\frac{\partial f}{\partial z}\right)\widehat{w}(k) = 0, \tag{5.4.37}$$

$$\frac{\mathrm{d}\widehat{w}}{\mathrm{d}k}\left[\left|\frac{\partial a}{\partial z}\right|^2 - \alpha\mathrm{Re}\left(\frac{\partial a}{\partial z}\right)+\frac{1}{2}\alpha\kappa f(z)\widehat{w}(k)\right] = 0. \tag{5.4.38}$$

In this case, the term inside the square brackets can have real roots if

$$\left|\frac{\partial a}{\partial z}\right|^2 - \alpha\mathrm{Re}\left(\partial a/\partial z\right) < 0, \tag{5.4.39}$$

as $\alpha\kappa f(z)\widehat{w}(k)/2 > 0$, for $\forall k$. We were unable to find parameter values for which this inequality held, as the first term is always positive and the second term is always negative. The derivative of $\widehat{w}(k)$ has three real roots $0, \pm k^*$. Figure 5.4.9 shows a plot of k^* as a function of β, in the case that $\gamma = 1/\beta^2$. Again, one cannot excite patterns with the wavenumber $k = 0$. Hence, $|k_c| = k^*$. Remember that $k = |\mathbf{k}|$, so perturbations for which $\sqrt{k_x^2 + k_y^2} = k_c$ will excite Turing patterns, when the parameter values are chosen such that (5.4.37) is satisfied.

The continuous eigenspectrum $\lambda(k)$ is shown in Fig. 5.4.10. The black star corresponds to the static Turing bifurcation, which occurs at $k = 0.3863$. Increasing

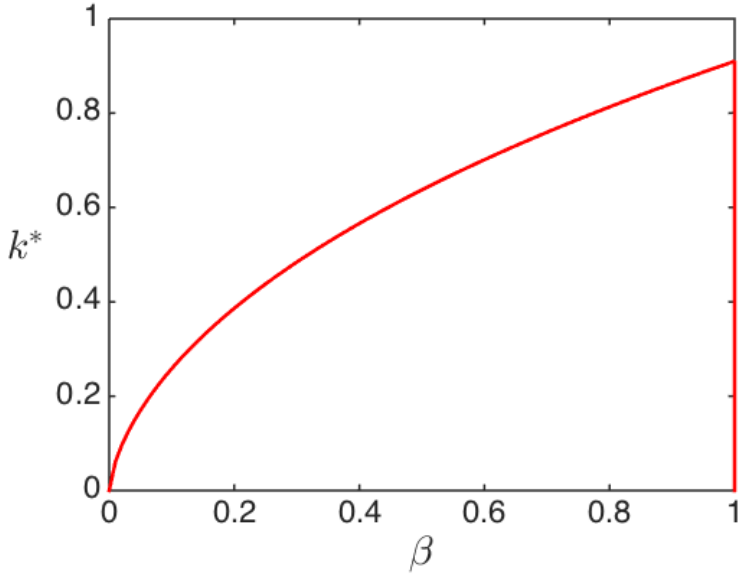

Figure 5.4.9. Critical k value as a function of β: Plot of the positive non-zero root of $\mathrm{d}\widehat{w}/\mathrm{d}k$ as a function of β, for a balanced kernel ($\gamma = 1/\beta^2$). Roots of $\mathrm{d}\widehat{w}/\mathrm{d}k$ occur as $[-k^*, 0, k^*]$.

the mean background drive η_0 would result in pushing the spectrum to the right in the (μ, ω)-plane, and hence, the system would go unstable to static Turing patterns. Figure 5.4.11 shows the Turing bifurcation curve as a function of the synaptic reversal potential v_{syn} and the average background drive η_0 for a range of different values of (a) the connectivity parameter β and (b) the coupling strength κ. It can be seen in Fig. 5.4.11a that increasing β decreases the area of instability. Note that the critical value of k changes with β, for $\beta = 0.1$ $k_c = 0.2585$, for $\beta = 0.2$ $k_c = 0.3863$, for $\beta = 0.5$ $k_c = 0.6373$ and for $\beta = 0.7$ $k_c = 0.7593$. In Fig. 5.4.11b we vary the values of κ, and fix $\beta = 0.2$. Here, increasing the value of κ increases the area in which we see static Turing patterns. As in the 1D case, altering the heterogeneity of the background drive Δ has little effect on the Turing bifurcation points and synaptic time constant α has no effect, as it simply scales λ.

Close to bifurcation the system can support a variety of different stationary

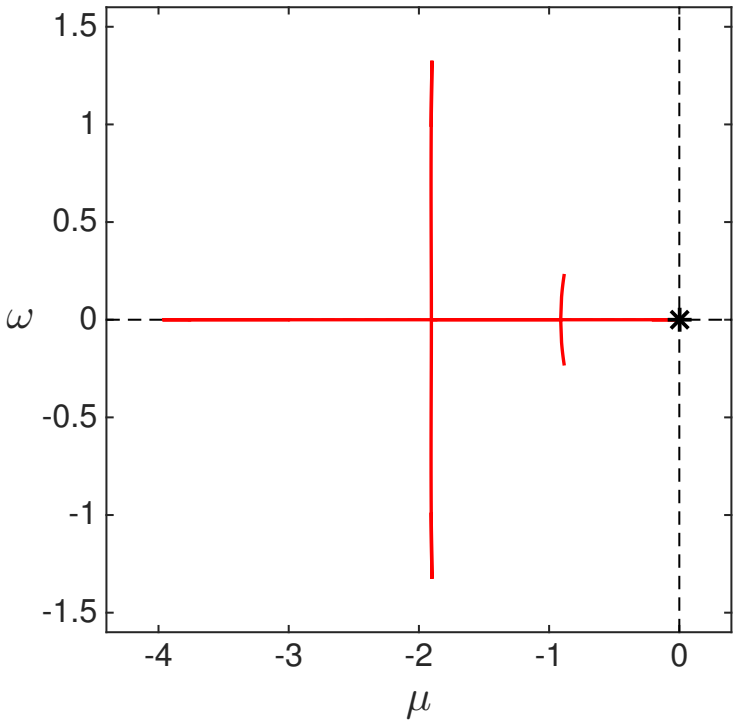

Figure 5.4.10. Static Turing bifurcation for next generation neural field model in 2D: Eigenspectrum of the system described by (5.4.2)–(5.4.5) with two spatial dimensions for parameter values which correspond to a Turing bifurcation. To obtain this plot we solved (5.4.37)–(5.4.39) for η_0 to find a parameter set for which a Turing bifurcation occurs. These parameter values were then used to solve (5.4.14) for $\lambda(k) = \mu(k) + i\omega(k)$, which is plotted parametrically as a function of k. The solution branch grazes the imaginary axis at $\omega = 0$ (black star), which corresponds to $k_c = 0.3863$. Parameter values: $\eta_0 = -0.1832$, $v_{\text{syn}} = 10$, $\Delta = 0.1$, $\kappa = 10$, $\alpha = 3$, $\beta = 0.2$.

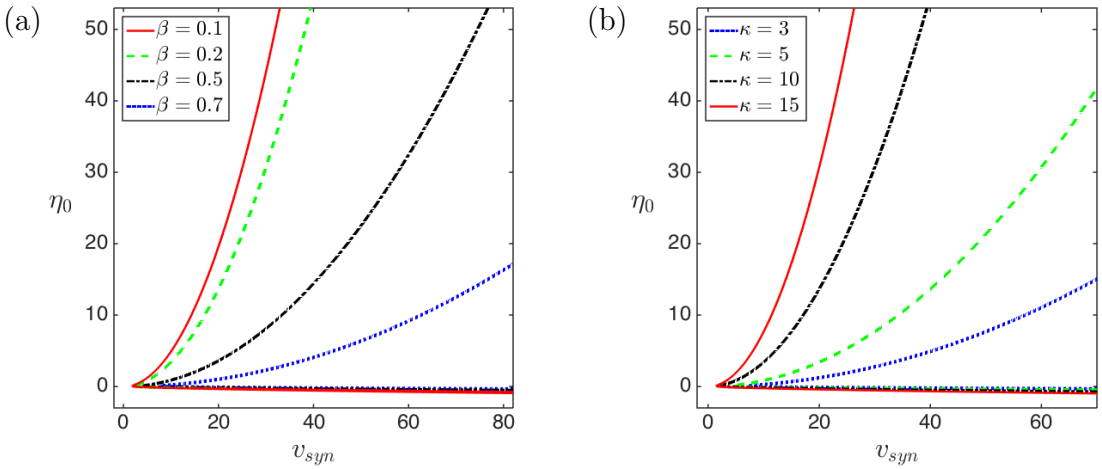

Figure 5.4.11. Static Turing bifurcation for next generation neural field model in 2D: Turing bifurcation curves, for the model describe by (5.3.9)–(5.3.10), plotted as functions of the synaptic reversal potential v_{syn} and the average background drive η_0 for a range of different values of (a) the connectivity parameter β and (b) the coupling strength κ. Increasing β can be seen to decrease the area of instability, while increasing κ increases the area of instability. Parameter values: $\Delta = 0.1$, $\kappa = 10$, $\alpha = 1$, $\beta = 0.2$.

patterns, such as Turing spots and stripes. Figure 5.4.12 shows a sample of these patterns. These simulations were run on a large square domain of width 80 with Neumann boundary conditions. The details of the numerical scheme used is described in Appendix C.2. As the numerical scheme is highly computationally extensive we were forced to simulated on a coarsely-grained lattice with 250×250 mesh points. A number of additional simulations were carried out on a finer lattice to confirm that the patterns observed were not merely due to the coarseness of the lattice. However, the spatial resolution was deemed satisfactory, by inspection. The different patterns are achieved by applying different spatial perturbations $\tilde{u}(x, y) = \mathrm{e}^{ik\mathbf{R}\cdot\mathbf{r}}$ to the steady state solution of the system close to the Turing bifurcation, where $\mathbf{R}$ are basis vectors for the basic symmetry groups of hexagon, square and rhombus. The three patterns shown below coexist in the same parameter space and appear (from our simulations) to all be stable.

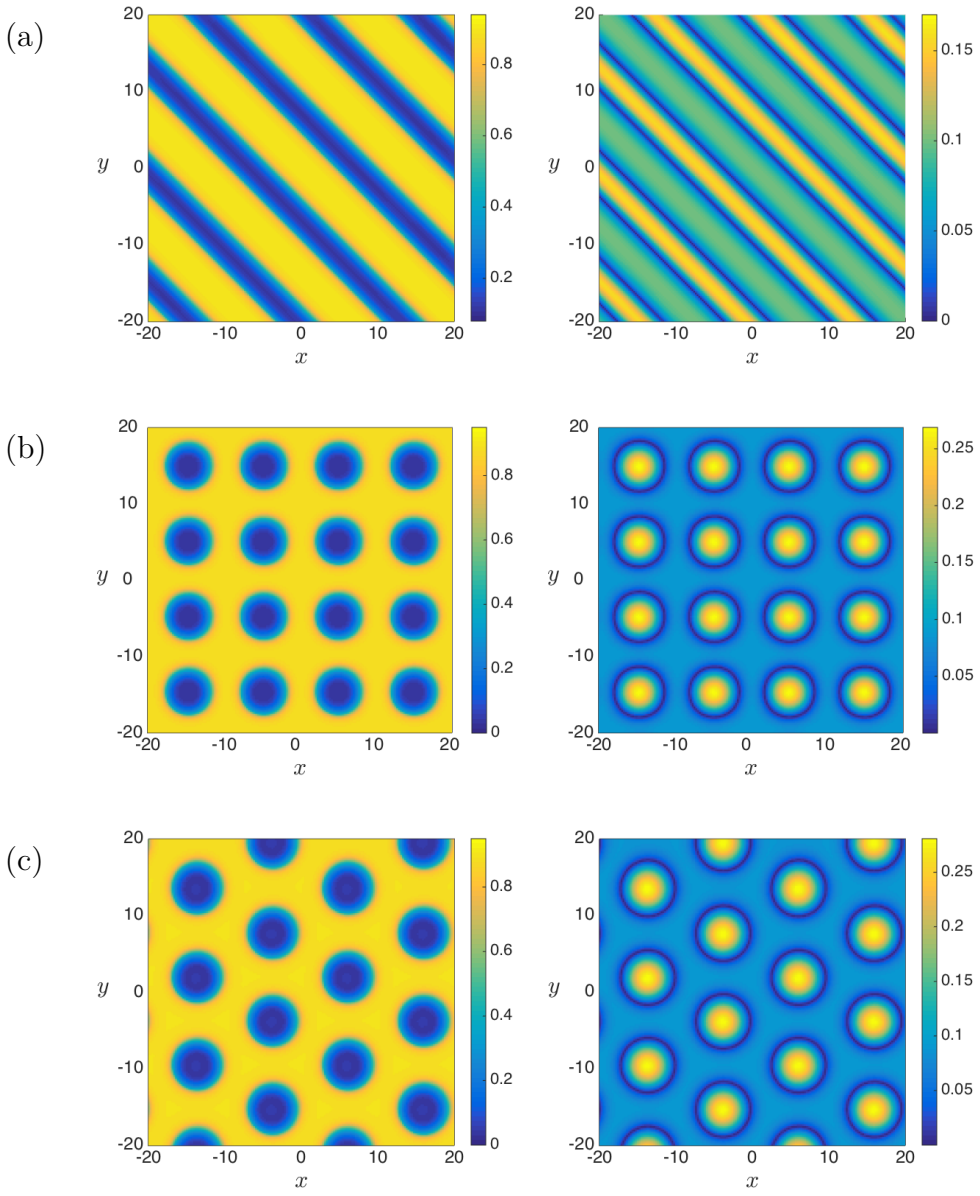

Figure 5.4.12. Stationary patterns for two spatial dimensions: Plots of the synchrony R (left) and synaptic conductance g (right) illustrating a number of different types of *static* Turing patterns that the system supports. The initial conditions are varied between the plots by applying different spatial perturbations $\tilde{u}(x, y)$ to the steady state solution. (a) Turing stripes $\tilde{u}(x, y) = A\cos(k_c(x + y)/\sqrt{2})$. (b) Turing spots (square lattice) $\tilde{u}(x, y) = A(\cos kx + \cos ky)$. (c) Turing spots (hexagonal lattice) $\tilde{u}(x, y) = A(\cos k_c x + \cos(k_c(x + \sqrt{3}y)/2) + \cos(k_c(x - \sqrt{3}y)/2))$. Parameter values: $\eta_0 = 0$, $v_{\text{syn}} = 4$, $\Delta = 0.1$, $\kappa = 3$, $\alpha = 1$, $\beta = 0.5$, $k_c = 0.6373$.

Turing-Hopf bifurcation

As in the case for one spatial dimension, we set $\mu = 0$, as *dynamic* Turing bifurcations occur when $\lambda = \pm i\omega$. This yields the following set of equations,

$$\frac{\mathrm{d}\widehat{w}}{\mathrm{d}k}\left[\omega^2 f(z)\left(\left|\frac{\partial a}{\partial z}\right|^2 + 4\alpha \mathrm{Re}\left(\frac{\partial a}{\partial z}\right) + 2\omega^2 - \alpha^2\right) - \mathrm{Re}\left(\frac{\partial a}{\partial G}\frac{\partial b}{\partial \bar{z}}\frac{\partial f}{\partial z}\right) \times \left(\alpha\left|\frac{\partial a}{\partial z}\right|^2 + \mathrm{Re}\left(\frac{\partial a}{\partial z}\right)\left(3\omega^2 - \alpha^2\right) - 3\alpha\omega^2 + \frac{1}{2}\alpha^2\kappa f(z)\right)\widehat{w}(k)\right] = 0, \tag{5.4.40}$$

$$\left|\frac{\partial a}{\partial z}\right|^2\left(-\omega^2 + \alpha^2\right) + 4\alpha\omega^2 \mathrm{Re}\left(\frac{\partial a}{\partial z}\right) + (\omega^4 - \alpha^2\omega^2) + 2\alpha^2\kappa \mathrm{Re}\left(\frac{\partial a}{\partial G}\frac{\partial b}{\partial \bar{z}}\frac{\partial f}{\partial z}\right)\widehat{w}(k) = 0, \tag{5.4.41}$$

$$\alpha\left|\frac{\partial a}{\partial z}\right|^2 + \mathrm{Re}\left(\frac{\partial a}{\partial z}\right)\left(\omega^2 - \alpha^2\right) - \alpha\omega^2 - \frac{1}{2}\alpha^2\kappa f(z)\widehat{w}(k) = 0. \tag{5.4.42}$$

Once again, we were unable to find any real roots for the term inside the square brackets in (5.4.40). Hence, as was the case for the Turing bifurcation k_c is determined by finding the roots of $\mathrm{d}\widehat{w}/\mathrm{d}k$, the reader is reminded that the positive non-zero root is shown as a function of β in Fig. 5.4.9. For $\beta = 0.2$, if we choose parameter values which satisfy (5.4.41) and (5.4.42), the system is unstable to *dynamic* Turing patterns for spatial perturbations of the form $\tilde{u}(x, y) = \mathbf{A}e^{i(k_x x + k_y y)}$, for $\sqrt{k_x^2 + k_y^2} = 0.3863$. The continuous eigenspectrum $\lambda(k)$ is shown in Fig. 5.4.13 at a Turing-Hopf bifurcation. The spectrum can be seen to touch the imaginary axis at $\omega \simeq 1.3$, corresponding to a *dynamic* Turing-Hopf bifurcation.

Figure 5.4.14 shows the Turing-Hopf bifurcation curve as a function of the synaptic reversal potential v_{syn} and the average background drive η_0, for a range of different values of (a) the connectivity parameter β and (b) the synaptic time constant α.

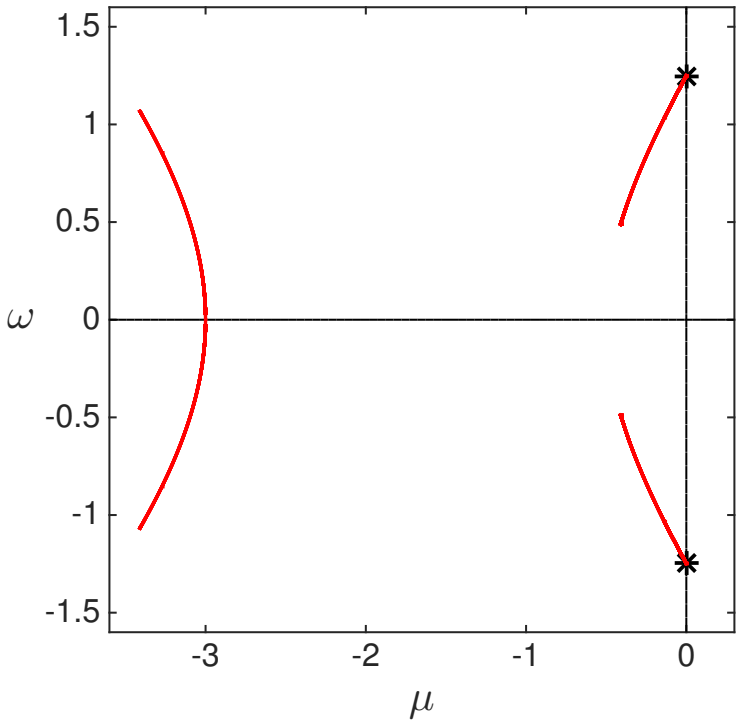

Figure 5.4.13. Turing-Hopf bifurcation for next generation neural field model in 2D: Eigenspectrum of the system, described by (5.4.2)–(5.4.5), in two spatial dimensions for parameter values which correspond to a Turing Hopf bifurcation. This plot was computed by solving (5.4.40)–(5.4.42) to find the parameter values for which the system undergoes a Turing-Hopf bifurcation. These parameter values were then used to solve (5.4.14) for $\lambda(k) = \mu(k) + i\omega(k)$, which is plotted parametrically as a function of k. The solution branch grazes the imaginary axis at $\omega = \pm 1.3$ (black star), when $k_c = 0.3863$. Parameter values: $\eta_0 = -0.1832$, $v_{\text{syn}} = 10$, $\Delta = 0.1$, $\kappa = 10$, $\alpha = 3$, $\beta = 0.2$.

We noted in the 1D case that there was a critical value of α for which the system switched from having a single Turing-Hopf bifurcation for every η_0 and v_{syn} to having two bifurcation points for $v_{\text{syn}} \lesssim 0$ and none for $v_{\text{syn}} \gtrsim 0$. This is also the case here. Figure 5.4.14a shows that increasing β causes the angle between the two sections of the Turing-Hopf curve to decrease and undergo this switch in behaviour at $\beta \simeq 0.48$. It can be seen in Fig. 5.4.14b that decreasing α has a similar effect, and the switch in behaviour happens at $\alpha \simeq 1.47$. In both plots the system is unstable to dynamic

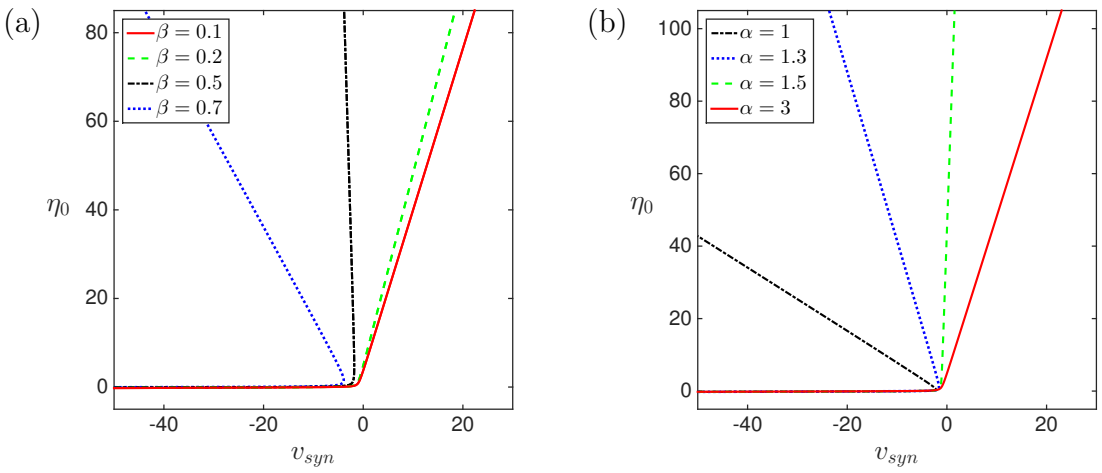

Figure 5.4.14. Turing-Hopf bifurcation curves for next generation neural field model in 2D: Turing-Hopf bifurcation curves, for the system described by (5.3.9)–(5.3.10) with two spatial dimension, plotted as functions of the synaptic reversal potential v_{syn} and the mean background drive η_0 for a range of different values of (a) the connectivity parameter β and (b) the synaptic time constant α. Increasing β reduces the angle between the two sections of the Turing-Hopf curve, increasing α has the opposite effect, increasing the angle and hence, increasing the are of instability. We observe *dynamic* Turing pattens to the left/of the bifurcation curves. Parameter values: $\Delta = 0.1$, $\kappa = 10$, $\alpha = 2$, $\beta = 0.2$.

Turing patterns (planar and radial waves) in the region above/to the right of the curves.

Near to the Turing-Hopf bifurcation the system supports standing and planar waves, which can be seen in Fig. 5.4.15. A perturbation of the form $\tilde{u}(x, y) = A(\cos(k_c(x + y)/\sqrt{2})$ initially induced standing waves, stationary waves in which

the amplitude oscillates in time. After some time the waves no longer oscillate in amplitude and move across the domain at a fixed speed, which is determined by the wave number k_c. These waves are known as planar waves. As in the 1D case, the

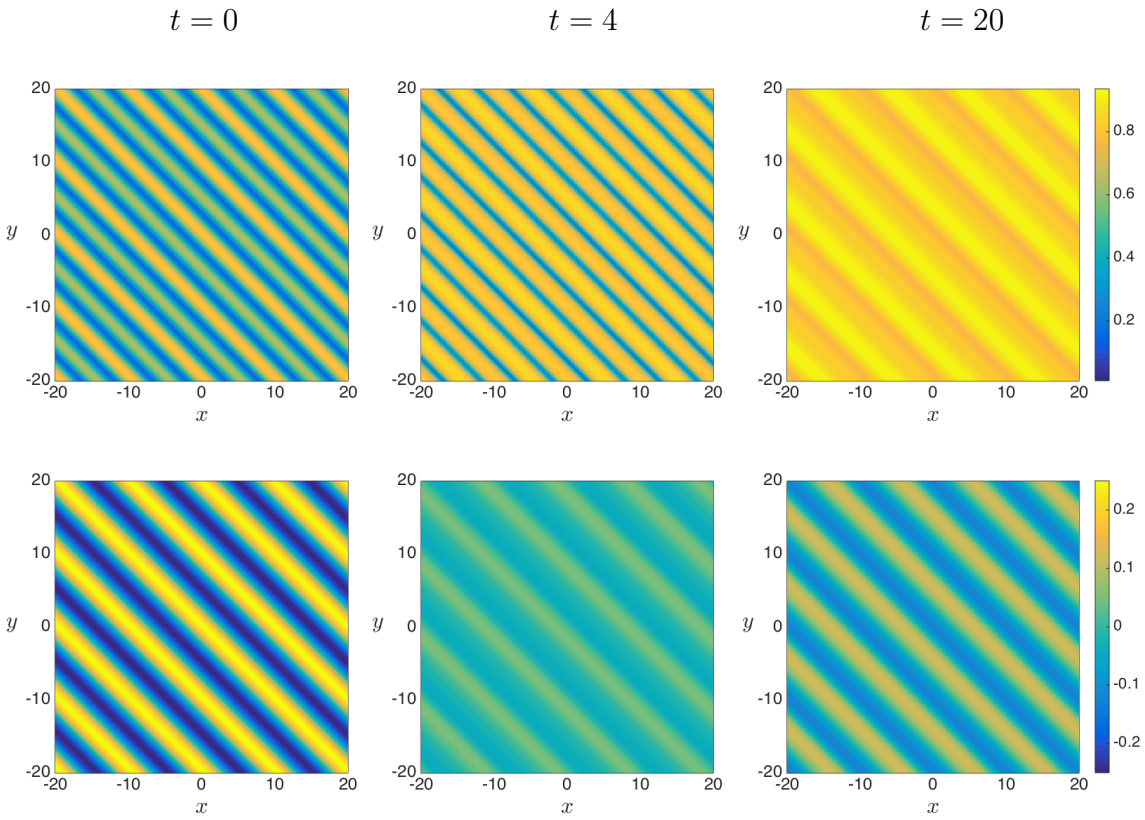

Figure 5.4.15. Planar waves in two dimensions: Plots of the synchrony R (top row) and synaptic conductance g (bottom row) for a number of time points, showing the evolution of planar waves in the two dimensional system, for a spatial perturbation of the form $\tilde{u}(x, y) = A(\cos(k_c(x + y)/\sqrt{2})$. The perturbation initially induces standing waves. These waves then transition into planar waves which move across the domain at a fixed speed. Parameter values: $\eta_0 = 0$, $v_{\text{syn}} = -10$, $\Delta = 0.1$, $\kappa = 3$, $\alpha = 3$, $\beta = 0.5$, $k_c = 0.6373$.

system can supports breathers, whose amplitude and width oscillate in time. If the system is perturbed with a hexagonal pattern, we see the emergence of breathers on a hexagonal lattice, this is shown in Fig. 5.4.16. Breathers can also develop on a square lattice, when the system is perturbed with a square pattern.

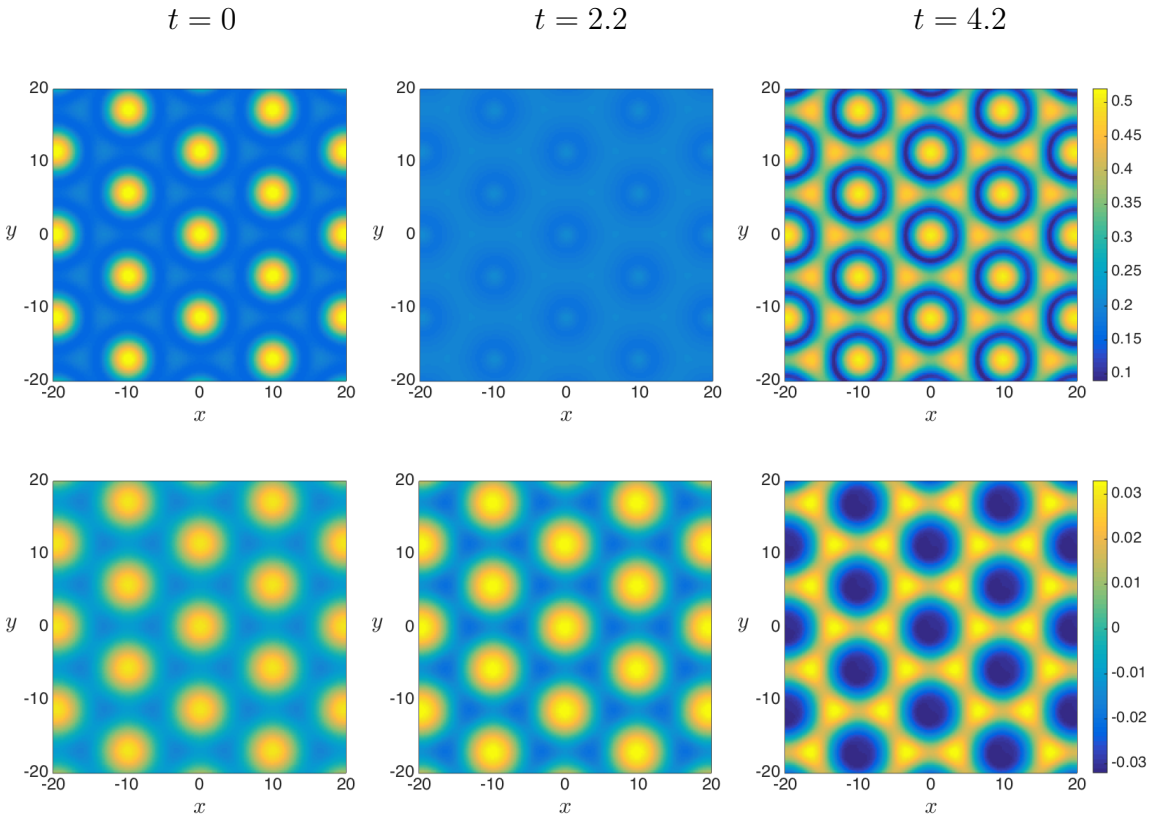

Figure 5.4.16. Breathers in two dimensions: Snapshots of the synchrony R (top) and synaptic conductance g (bottom) at a number of time points, depiciting breathers on a two dimensional domain. The steady state solution is perturbed with the hexagonal pattern $\tilde{u}(x, y) = A(\cos k_c x + \cos(k_c(x + \sqrt{3}y)/2) + \cos(k_c(x - \sqrt{3}y)/2))$. These patterns only exist for a finite amount of time before transitioning into the solutions shown in Fig. 5.4.17. Parameter values: $\eta_0 = 0$, $v_{\text{syn}} = -10$, $\Delta = 0.1$, $\kappa = 3$, $\alpha = 3$, $\beta = 0.5$, $k_c = 0.6373$.

Unlike in the 1D case these breathing states transition to standing waves, rather than periodic travelling waves, which are shown in Fig. 5.4.17. The breathers shown in Fig. 5.4.16 only exist for a finite amount of time before transitioning to these standing waves. The hexagonal structure of the spots remains constant as the positive and negative conductance states alternate, i.e the spots, which had a positive synaptic conductance, switch to a negative value of synaptic conductance and the surrounding area does the opposite. This solution could be formed by an interaction of a left- and right-travelling wave. We will discuss possible further analysis of this in Chapter 7. The patterns shown in Fig. 5.4.15, 5.4.16 and 5.4.17 all exist in the same parameter

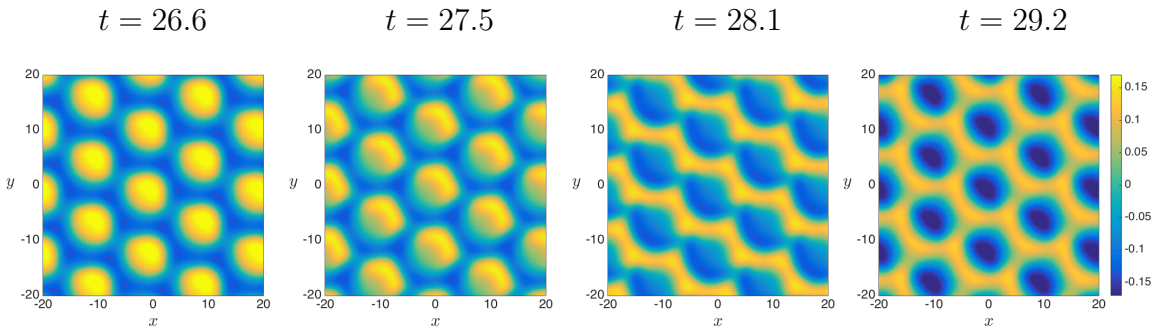

Figure 5.4.17. Standing waves in two dimensions: Two dimensional plots of the synaptic conductance g at different time points, showing the evolution of two dimensional standing waves. These *dynamic* patterns manifest in the system when it is perturbed with a hexagonal pattern (as in Fig. 5.4.16) and allowed to evolve for a sufficient amount of time. At $t = 26.6$, the spots have a positive value of g, and as the system evolves this positive activity state becomes a negative activity state. Parameter values: $\eta_0 = 0$, $v_{\text{syn}} = -10$, $\Delta = 0.1$, $\kappa = 3$, $\alpha = 3$, $\beta = 0.5$, $k_c = 0.6373$.

window, and the planar waves and standing waves appear (from numerical simulation) to both be stable. Appendix C.2 describes the numerical scheme used to create these plots, the domain size and number of mesh points was chosen to be the same as in §5.4.1.

As in §5.4.1 we wish to explore the behaviour of the system when both the Turing and Turing-Hopf bifurcations coincide. Figure 5.4.18 shows a two parameter bifurcation

diagram in synaptic reversal potential v_{syn} and mean background driveη_0 where the other parameters are chosen such that the Turing and Turing-Hopf bifurcations curves collide. If we compare this diagram to Fig. 5.4.5, we see that the point at which the two curves collide occurs for a larger value of v_{syn} and η_0 for the system with two spatial dimensions. If we chose a set of parameter values that put the system in the

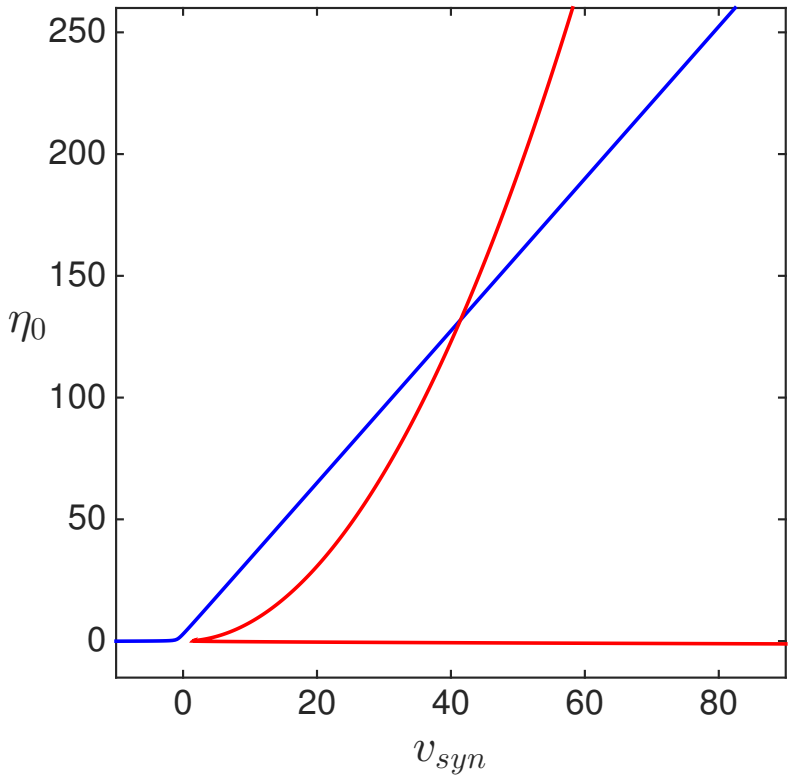

Figure 5.4.18. Turing and Turing-Hopf bifurcations in 2D: Bifurcation diagram for the system given by (5.4.2)–(5.4.5) with two spatial dimension, in the synaptic reversal potential v_{syn} and the mean background drive η_0 showing the Turing (red) and Turing-Hopf (blue) bifurcations curves. The system supports *static* Turing patterns to the right of the Turing curve and *dynamic* Turing waves in the region to the left of the Turing-Hopf curve. In the area where the system can supports both *static* and *dynamic* patterns we observe more exotic patterns that cannot be explained using linear stabilty analysis. Parameter values: $\Delta = 0.1$, $\kappa = 15$, $\alpha = 2$, $\beta = 0.2$.

vicinity of both the Turing and Turing-Hopf bifurcations we observe two dimensional

versions of the patterns seen in the 1D case. Figure 5.4.19 shows the evolution of these patterns on the two dimensional hexagonal lattice. Radial waves develop in the centre of the spots and propagate out to the edge of the spots. This production of radial waves is periodic. As in the one dimensional patterns, the structure inside the spots is only seen in the order parameter z and not in the synaptic conductance g. The amplitude of the synaptic current g performs small oscillation which are not visible here. If we perturb the system with a square pattern, we see the same behaviour. The only difference is that the spots are distributed on a square lattice rather than a hexagonal one. Alternatively, if we perturb the system with a striped pattern, a stripe of activity is generated in the centre of the high activity stripes, which splits and propagates away from the centre of the stripe. As the wavelength k_c was shorter in this simulation we chose a larger domain size of 100, to minimise the edge effects. The number of mesh points and numerical scheme were unchanged from the previous simulations.

5.5 Discussion

In this chapter we outlined how to spatially extend the model presented in Chapter 3. This was achieved by spatially distributing our network of θ-neurons on a line and including a synaptic weighting function that depended upon the distance between two neurons. As shown in §5.3.1, the OA ansatz still holds and we arrive at our *next generation neural field model*, which takes the form of a generalised neural field model. The population firing rate depends upon the within-population synchrony, which is now a function of space and time. This allows us to track the evolution of synchrony within patterns and waves.

Our new model is first analysed in one spatial dimension, using Turing instability analysis. It was found that the model supports patterns typically seen in standard

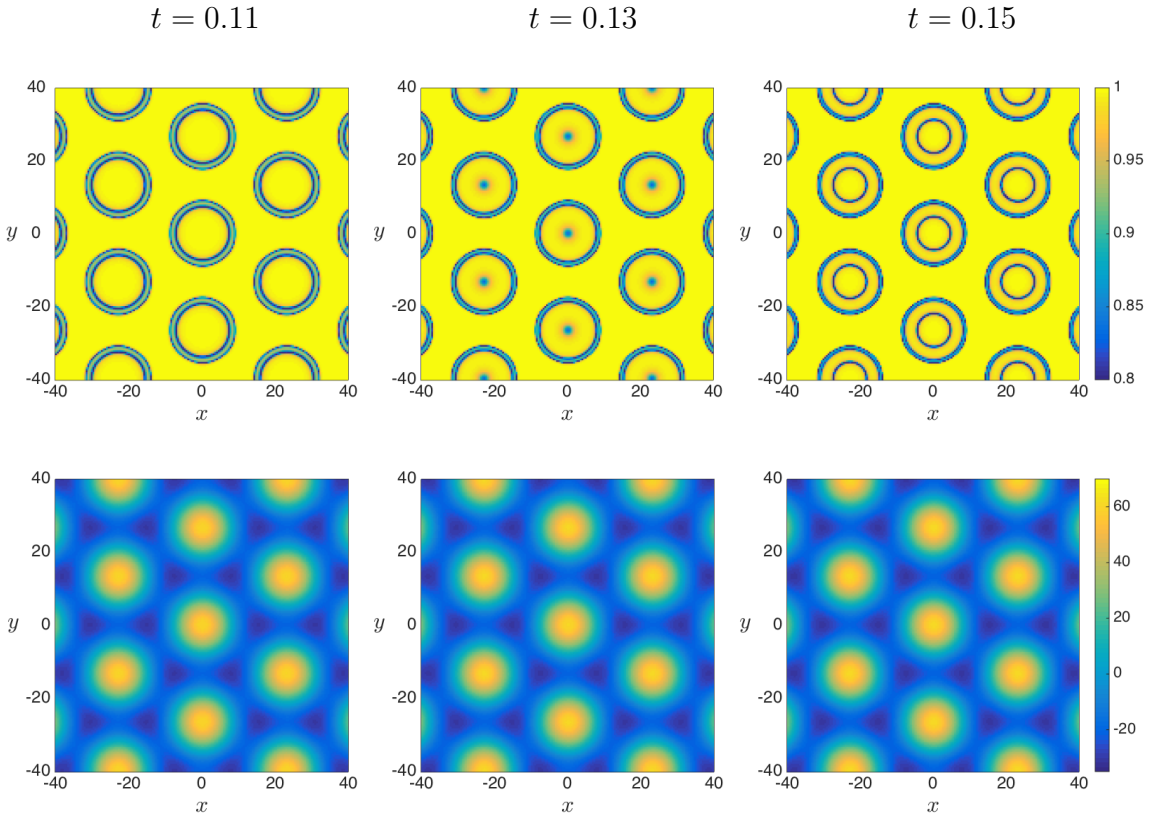

Figure 5.4.19. Dynamic Turing bumps in two spatial dimensions: Two dimensional surface plots of the synchrony R (top) and synaptic conductance g (bottom) at a series of time points, showing spots on a two dimensional hexagonal lattice in the region of parameter space that the Turing and Turing-Hopf bifurcations collide. Radial waves can be seen emanating from the centre of the spots for a prolonged period of time, which then breaks down and a oscillating structre appears in the bumps. Parameter values: $\eta_0 = 130$, $v_{\text{syn}} = 40$, $\Delta = 0.1$, $\kappa = 15$, $\alpha = 2$, $\beta = 0.2$, $k_c = 0.386$.

neural field models, such as stationary periodic patterns, planar waves and breathers. More interestingly, the model also supported states not commonly seen in standard neural field models. We discovered periodic solutions in which there was an oscillating structure inside the bumps. These exotic patterns are more typically seen in networks of spiking models, which led us to the conclusion that our reduced model preserves some notion of the underlying spiking behaviour.

Including a second spatial dimension, once again provided us with a wide range of global patterns, some of which can been seen in standard neural field models and some of which which cannot. In particular, we observed standing waves in the system with two spatial dimensions, which were not seen in the system with one spatial dimension. We also observe the periodic states in which there is an oscillating structure within the bumps, as seen in the 1D system.

As Turing instability analysis is a linear analysis, it can only describe the system arbitrarily close to bifurcation. Traditionally, when analysing neural field equations, one would perform a weakly nonlinear analysis to describe the behaviour of the system as it is moved away from bifurcation. As such an analysis is only valid close to bifurcation, and our system is highly nonlinear, we will instead use numerical analysis techniques to explore the behaviour of the system away from bifurcation. Using numerical analysis allows us to explore the behaviour of the system more thoroughly. This analysis is carried out in Chapter 6.

Chapter 6

Next generation neural fields II: Numerical analysis of patterned states

In Chapter 5 we described the derivation of our *next generation neural field model*, and carried out a Turing instability analysis, in both one and two spatial dimensions. It was stated that as we move away from bifurcation the linear approximation breaks down and that the behaviour is dominated by the nonlinear terms. It is customary to consider a weakly nonlinear analysis to describe the behaviour of the system away from bifurcation. However, as our model is highly nonlinear, we opt for a numerical analysis when considering the system away from bifurcation. Using numerical machinery developed by Daniele Avitabile [10], we can continue global Turing patterns, as well as localised states. In this chapter we will only consider parameter continuations for the system in one spatial dimension.

In the field of theoretical neuroscience, the analysis of waves and patterns in standard neural field theories has contributed to many biological advances. A variety of neurological disorders such as epilepsy and spreading depression during migraine

episodes are characterized by spatially localized oscillations and waves propagating across the surface of the brain. As biological systems are not confined to operate near bifurcation points, it is important to analyse the system away from these points to gain a full understanding of the behaviour of the system. Unlike typical neural field models, we cannot use the Heaviside approximation to make further analytical progress since the firing rate is now a fixed real valued function of the Kuramoto order parameter. As such, we must use numerical techniques to analyse the system away from bifurcation. Numerical analysis is particularly important for analysing travelling fronts, solutions which connect two fixed points of the system. Travelling fronts connecting high activity states to low activity states or high blood oxygen states to low blood oxygen states are commonly observed in human brain recordings [4, 39]. In particular, such fronts are seen during strokes, epilepsy and migraines [151, 19].

This chapter begins with an overview of the set up of our system and a brief introduction to Avitabile's numerical continuation software, describing how we can apply it to our model. We first consider the static Turing patterns to verify the analytical calculations, which were carried out in Chapter 5. Using numerical methods we can also examine the behaviour of these solutions away from bifurcation. In §6.2.2, we consider periodic travelling waves and calculate dispersion curves for these travelling waves. The final section concerns itself with the continuation of local states, and in particular travelling fronts.

6.1 Overview of the numerical problem

We are faced with the challenge of constructing solutions and numerically analysing them for the system,

$$\left(1+\frac{1}{\alpha}\frac{\partial}{\partial t}\right)^2 g = \kappa\int_{-\infty}^{\infty} \mathrm{d}y w(y-x) f(z(y,t)) \tag{6.1.1}$$

$$\frac{\partial z}{\partial t}(x,t) = \mathcal{F}(z(x,t);\eta_0,\Delta) + \mathcal{G}(z(x,t),g(x,t);v_{\mathrm{syn}}), \tag{6.1.2}$$

where f, $\mathcal{F}$ and $\mathcal{G}$ given by (3.2.12), (3.2.15) and (3.2.16) respectively. As the analysis in Chapter 5 was carried out on the infinite domain, we will (unless otherwise stated) use Neumann boundary conditions on a suitably large domain in order to imitate the infinite domain. For computational convenience we transform the system to an equivalent partial differential equation (PDE) system, using Fourier transforms to expose spatial derivatives. This step is required to numerically evaluate the spatial convolution in (6.1.1) on the infinite domain. We could employ MATLAB's built-in fast Fourier transform algorithm to compute the integral, if the problem were posed on a ring with periodic boundary conditions, but unfortunately that is not the case here. We shall define ϕ as the spatial convolution in (6.1.1),

$$\phi(x,t) = \int_{-\infty}^{\infty} \mathrm{d}y w(y-x) f(z(y,t)). \tag{6.1.3}$$

For now we will assume the synaptic kernel $w(x) = (1-|x|)\mathrm{e}^{-|x|}$. Introducing a two dimensional Fourier transform of the form

$$\psi(x,t) = \frac{1}{(2\pi)^2}\int_{-\infty}^{\infty}\mathrm{d}k\int_{-\infty}^{\infty} d\lambda \mathrm{e}^{i(kx+\lambda t)}\widehat{\psi}(k,\lambda), \tag{6.1.4}$$

and assuming that the Fourier transform of f exists allows us to express (6.1.3) as

$$\widehat{\phi}(k,\lambda) = \widehat{w}(k)\widehat{f}(z(k,\lambda)), \tag{6.1.5}$$

where $\widehat{w}$ is the one dimensional Fourier transform of w given by (5.4.11) and $\widehat{f}$ is the two dimensional Fourier transform of f. Upon cross multiplication of the denominator of $\widehat{w}(k)$ and application of the inverse Fourier transformation [45], we arrive at the following equation

$$(1-\partial_{xx})^2\phi(x,t) = -4f(z(x,t)). \tag{6.1.6}$$

Hence, the system of equations can be written as,

$$(1-\partial_{xx})^2\left(1+\frac{1}{\alpha}\partial_t\right)^2 g = -4\kappa\partial_{xx}f(z), \tag{6.1.7}$$

$$\partial_t z = \mathcal{F}(z;\eta_0,\Delta) + \mathcal{G}(z,g;v_{\text{syn}}), \tag{6.1.8}$$

where f, $\mathcal{F}$ and $\mathcal{G}$ are given by (3.2.12), (3.2.15) and (3.2.16), respectively.

The Turing analysis in Chapter 5 exposed the existence of periodic travelling waves. To analyse these waves numerically it is convenient to transform to the travelling wave frame $\xi = x - ct$, where c is the speed of the wave. This allows us to construct the travelling wave (TW) solutions as stationary profiles in this reference frame. As in Chapter 5 we will define a state vector $u = [z_R, z_I, K, g]^T$, where $z_R = \text{Re}(z)$, $z_I = \text{Im}(z)$ and $K = (1+\alpha^{-1}\partial/\partial t)g$. As the numerical machinery used here does not support complex variables, we separate z into its real and imaginary components rather than using $\bar{z}$ as our additional variable. First we let $u(x,t) \to U(x-ct) \equiv U(\xi)$, where $U(\xi) = [Z_R(\xi), Z_I(\xi), \tilde{K}(\xi), \tilde{g}(\xi)]^T$. Substituting this into (6.1.7) and (6.1.8)

gives the following set of TW ODEs,

$$\left(1-\frac{\mathrm{d}^2}{\mathrm{d}\xi^2}\right)^2\left(1-\frac{c}{\alpha}\frac{\mathrm{d}}{\mathrm{d}\xi}\right)^2\tilde{g}=-4\kappa\frac{\mathrm{d}^2}{\mathrm{d}\xi^2}f(Z), \tag{6.1.9}$$

$$-c\frac{\mathrm{d}}{\mathrm{d}\xi}Z=\mathcal{F}(Z;\eta_0,\Delta)+\mathcal{G}(Z,\tilde{g};v_{\mathrm{syn}}). \tag{6.1.10}$$

This system of equations can be continued numerically with c as a variable, provided we include an additional phase condition,

$$\Psi(\widehat{U},U)=\int \mathrm{d}\xi\frac{\mathrm{d}\widehat{U}}{\mathrm{d}\xi}(\xi)(U(\xi)-\widehat{U}(\xi))=0, \tag{6.1.11}$$

where $\widehat{U}(\xi)$ is a suitable reference solution, such as the initial wave profile found from simulations. This condition minimises the difference between the solution $U(\xi)$ and the reference solution $\widehat{U}(\xi)$.

For convenience, we shall write the system defined by (6.1.7) and (6.1.8) as,

$$\mathcal{M}\partial_t u(x,t)=F(u(x,t)), \tag{6.1.12}$$

where $\mathcal{M}$ is the mass matrix operator

$$\mathcal{M}=\begin{pmatrix}1&0&0&0\\0&1&0&0\\0&0&(1-\partial_{xx})^2&0\\0&0&0&1\end{pmatrix}. \tag{6.1.13}$$

This set of equations will be used when performing parameter continuations of the stationary Turing patterns. In the travelling wave coordinates (6.1.12) becomes,

$$-c\mathcal{M}\frac{\mathrm{d}}{\mathrm{d}\xi}U=F(U), \tag{6.1.14}$$

where $\mathcal{M}$ is given by (6.1.13) under the replacement $\partial_{xx} \to \mathrm{d}^2/\mathrm{d}\xi^2$. We will use this system of TW equations when examining the dynamic Turing waves.

Discretising the system into N points, on a line of length L, transforms the operators $\mathrm{d}/\mathrm{d}\xi$ and $\mathrm{d}^2/\mathrm{d}\xi^2$ into $N \times N$ matrices denoted by **Dx** and **Dxx**, respectively. We choose to use central finite differences with a second order of accuracy, and as such define **Dx** and **Dxx** as,

$$\sum_j \mathbf{Dx}_{i,j} v_j = \frac{-v_{i-1} + v_{i+1}}{2\Delta x}, \tag{6.1.15}$$

$$\sum_j \mathbf{Dxx}_{i,j} v_j = \frac{v_{i-1} - 2v_i + v_{i+1}}{\Delta x^2}, \tag{6.1.16}$$

where $\Delta x = L/(N-1)$. Enforcing Neumann boundary conditions imposes the following

$$\mathbf{Dx}(1,j) = \mathbf{Dx}(j,1) = 0, \qquad \forall j = 1 \ldots N, \tag{6.1.17}$$

$$\mathbf{Dxx}(1,2) = \mathbf{Dxx}(N,N-1) = \frac{2}{\Delta x^2}. \tag{6.1.18}$$

The matrix operator $\mathcal{M}$ becomes a $4N \times 4N$ matrix **M**,

$$\mathbf{M} = \begin{pmatrix} \mathrm{I}_N & 0 & 0 & 0 \\ 0 & \mathrm{I}_N & 0 & 0 \\ 0 & 0 & (1 - \mathbf{Dxx})^2 & 0 \\ 0 & 0 & 0 & \mathrm{I}_N \end{pmatrix}. \tag{6.1.19}$$

The discretisation of (6.1.11) is given as

$$\Psi(\widehat{U}, U) = \Delta x \sum_j (\mathbf{D}\widehat{U})_j^T (U_j - \widehat{U}_j) = 0, \tag{6.1.20}$$

where

$$\mathbf{D} = \begin{pmatrix} \mathbf{Dx} & 0 & 0 & 0 \\ 0 & \mathbf{Dx} & 0 & 0 \\ 0 & 0 & \mathbf{Dx} & 0 \\ 0 & 0 & 0 & \mathbf{Dx} \end{pmatrix}. \tag{6.1.21}$$

The continuation software employs the Newton generalised minimal residual method (Newton-GMRES) to iteratively solve the system

$$c\mathbf{MDx}U + F(U) = 0, \qquad \Psi(\widehat{U}, U) = 0,$$

for (U, c).

To calculate the stability of the patterns in the TW frame we linearise around the TW solution $U(x - ct)$,

$$u(x,t) = U(x - ct) + \epsilon \mathrm{e}^{\lambda t}\tilde{U}(x - ct) + \mathcal{O}(\epsilon^2). \tag{6.1.22}$$

Substituting this into (6.1.12) (and neglecting higher order terms) gives

$$\mathcal{M}\partial_t \left[U(x - ct) + \epsilon \mathrm{e}^{\lambda t}\tilde{U}(x - ct)\right] = F(U(x - ct)) + \epsilon \mathrm{e}^{\lambda t}F'(U(x - ct))\tilde{U}(x - ct). \tag{6.1.23}$$

Transforming to the co-moving frame (ξ, t) and noting that $\mathcal{M}\partial_t U = F(U)$ (from (6.1.14)), we find that

$$\mathcal{M}\left[\lambda \mathrm{e}^{\lambda t}\tilde{U}(\xi) - c\mathrm{e}^{\lambda t}\frac{\mathrm{d}}{\mathrm{d}\xi}\tilde{U}(\xi)\right] = \mathrm{e}^{\lambda t}F'(U(\xi))\tilde{U}(\xi), \tag{6.1.24}$$

which allows us to write

$$\lambda\mathcal{M}\psi(\xi) = \left[c\mathcal{M}\frac{\mathrm{d}}{\mathrm{d}\xi} + F'(U(\xi))\right]\psi(\xi). \tag{6.1.25}$$

In the discretised system this equation takes the form,

$$\lambda \mathbf{M}\psi(\xi) = [c\mathbf{MDx} + F'(U(\xi))]\,\psi(\xi). \tag{6.1.26}$$

The continuation software estimates the stability of the the TW solution by computing the eigenvalues of $c\mathbf{MDx} + F'(U)$ at each point along the continuation branch.

6.2 Continuation of global patterns

6.2.1 Static Turing patterns

We will first numerically continue the stationary patterns seen in Chapter 5 to verify the results and examine the behaviour of these solutions away from bifurcation. As these patterns are static we do not require the transformation to the travelling wave frame, and we can instead continue steady state solutions of (6.1.8) and (6.1.7). Discretising the system into 1000 points on a domain of length 16π allows us to continue these stationary patterns. Figure 6.2.1 shows a one parameter continuation in the mean background drive, η_0. Solid (dashed) lines represent stable (unstable) states. The bump solution bifurcates off the homogeneous steady state ($g^* = 0$) at $\eta_0 = -0.89$ and $\eta_0 = 15.8$; these values matches the values found for the Turing bifurcations in Chapter 5. It is clear to see that these patterned Turing states exist for $\eta_0 < -0.89$ and $\eta_0 > 15.8$, confirming that the Turing bifurcations are indeed subcritical (at least for the parameter values chosen here). Figure 6.2.1 illustrates that the static Turing pattern is stable for a wide range of values of η_0. Increasing the synaptic reversal potential v_{syn} was found to increase this range even further. If v_{syn} is decreased through zero the patterned state no longer exists for any value of η_0, which is to be expected from Fig. 5.4.2.

A selection of solution states were chosen from the branch shown in Fig. 6.2.1 and

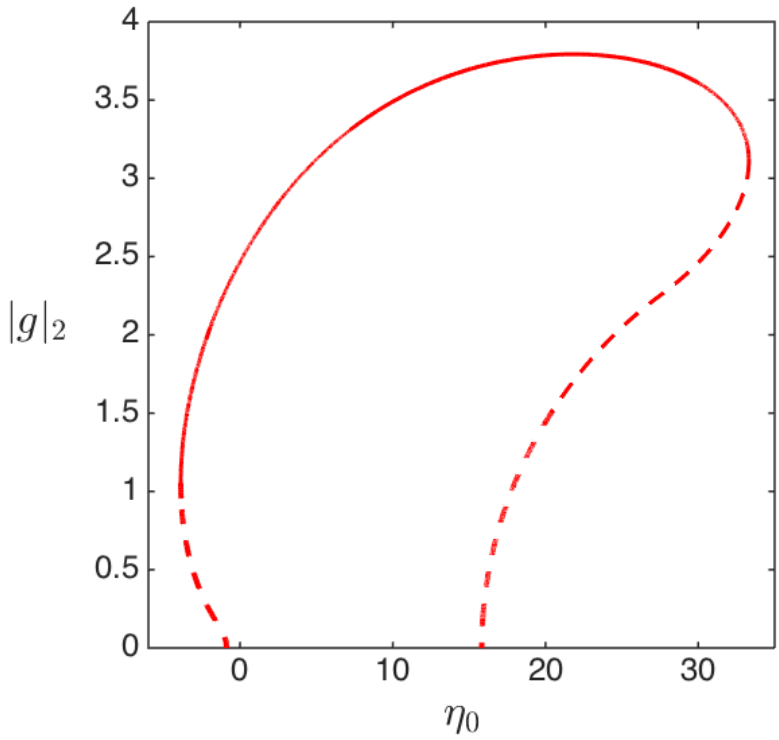

Figure 6.2.1. Continuation of the spatially periodic Turing pattern: Bifurcation diagram in the mean background drive η_0 of a global patterned state, which is a stationary solution of the system described by (6.1.7)–(6.1.8). Solid (dashed) lines represent stable (unstable) patterned states. The patterned solution bifurcates off the homogeneous steady steady ($g^* = 0$) at Turing bifurcations at $\eta_0 = -0.89$ and $\eta_0 = 15.8$. Parameter values: $v_{\text{syn}} = 5$, $\Delta = 0.5$, $\kappa = 5$, $\alpha = 1$.

the synchrony R and synaptic conductance g at each of these points are displayed in Fig. 6.2.2. Figure 6.2.2a shows the solution along the unstable branch at $\eta_0 = -2$. It can be seen that when the activity is high (larger $|g|$) there is low synchrony, and when the activity is low, there is high synchrony. Figure 6.2.2b shows the solution along the stable branch at $\eta_0 = 0$. The low activity state still has a lower value of synchrony. However, it is not as low as in Fig. 6.2.2a. Figure 6.2.2c shows another stable solution, this time for $\eta_0 = 30$. For this solution state there appears to have been a switch in the behaviour; the synaptic conductance g is now predominately negative rather than positive. A possible explanation for this is the system switches from being dominated by excitation to being dominated by inhibition. However, we do not explore this further.

6.2.2 Dynamic Turing patterns

It is now interesting to examine the periodic waves found in the vicinity of the Turing-Hopf bifurcation. As these waves are periodic it is convenient to switch to periodic boundary conditions. For periodic boundary conditions **Dx** and **Dxx** are given by (6.1.15) and (6.1.16), respectively, with the following boundary constraints,

$$\mathbf{Dx}(1, N) = -\mathbf{Dx}(N, 1) = -\frac{1}{\Delta x} \tag{6.2.1}$$

$$\mathbf{Dxx}(1, N) = \mathbf{Dx}(N, 1) = \frac{1}{\Delta x}. \tag{6.2.2}$$

By enforcing periodic boundary conditions we fix the spatial period of the wave, to the length of the domain. Altering the domain size allows us to examine the relationship between this period p and the wave speed c. Note that the domain size may also be integer multiples of the spatial period. We will not focus on that case here. Figure 6.2.3 shows the evolution of a periodic wave on a domain of length π, 2π and 4π, respectively. Examining the gradient of the waves we can see that the waves travel

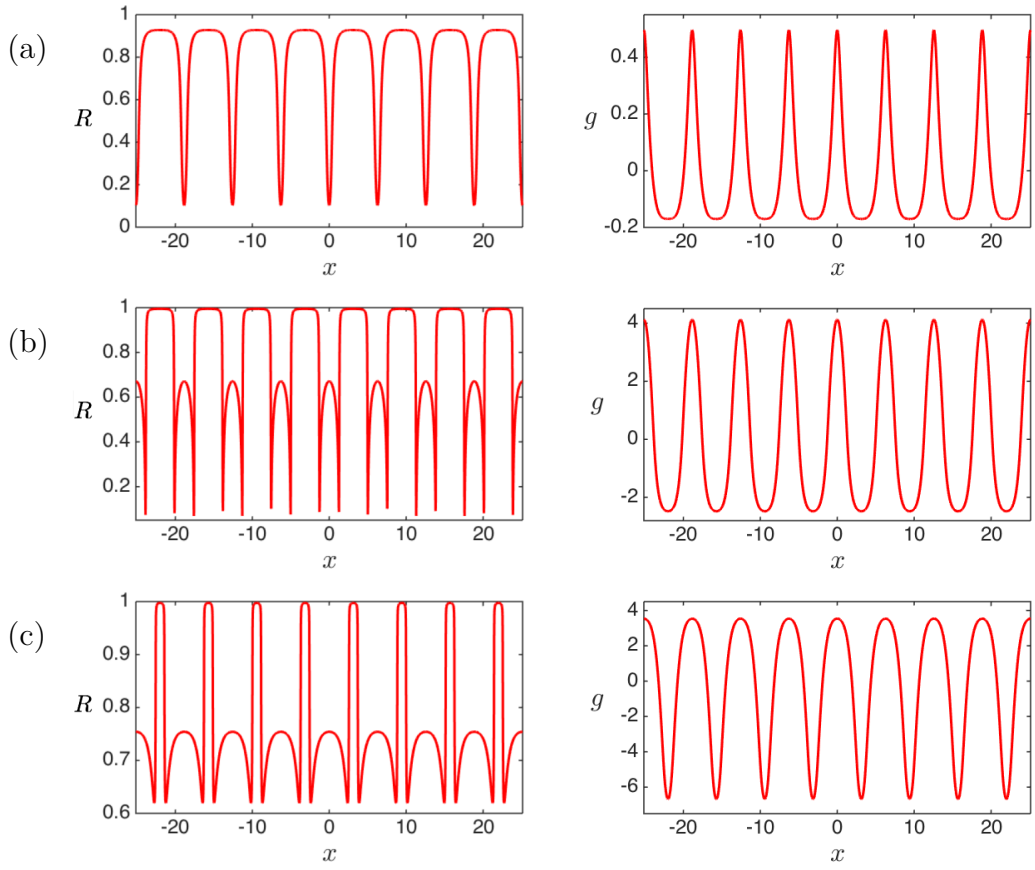

Figure 6.2.2. Global patterns away from bifurcation: Plots showing the behaviour of the synchrony R (left) (where R is the magnitude of the Kuramoto order parameter z) and the synaptic conductance g (right) at different points along the continuation branch shown in Fig. 6.2.1. (a) Unstable branch at $\eta_0 = -2$. (b) Stable branch at $\eta_0 = 0$. (c) Stable branch at $\eta_0 = 30$. Parameter values: $v_{\text{syn}} = 5$, $\Delta = 0.5$, $\kappa = 5$, $\alpha = 1$.

faster on the larger domains. Near a Turing-Hopf bifurcation the speed of the wave is given as ω/k, hence, the smaller the wave number the faster the waves will travel. It is also interesting to note that the amplitude of the waves is greatest for the domain of length 2π. In Chapter 5 we found that at bifurcation the system was unstable to perturbations of the form $e^{ik_c x}$, where $|k_c| = 1$, hence, the spatial period of these patterns is 2π. As such, the periodic patterns found here, on the domain of length 2π, correspond to the Turing waves found in Chapter 5. These simulations were carried out using the numerical scheme described in Appendix C.1, for 400 grid points.

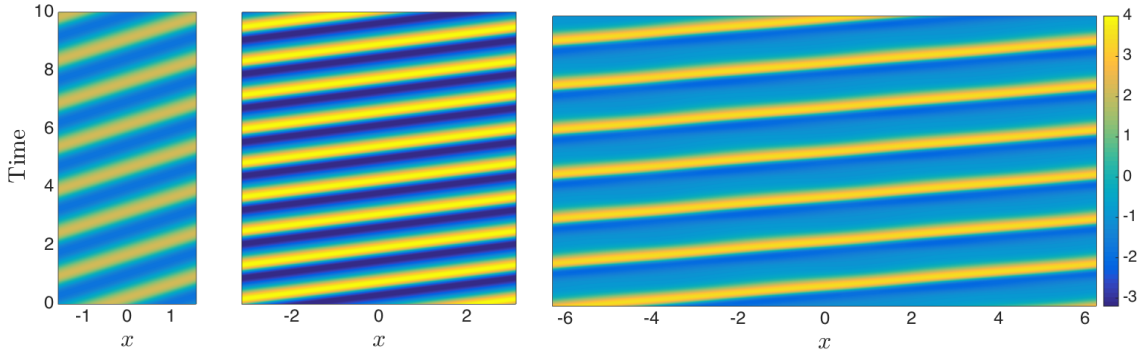

Figure 6.2.3. Periodic waves on domains of different lengths: Surface plots showing the evolution of the synaptic conductance g for the system given by (6.1.7)–(6.1.8), on domains of different sizes with periodic boundary conditions. It can be seen that the waves travel faster on the larger domains. Parameter values: $\eta = 0$, $v_{\text{syn}} = -5$, $\Delta = 0.5$, $\kappa = 5$, $\alpha = 5$.

We carried out a one parameter continuation of the average background drive η_0 for each of these waves, by numerically continuing (6.1.9) and (6.1.10), where the domain was discretised into 400 spatial points. Figure 6.2.4 shows (a) the wave speed c and (b) the 2-norm of the synaptic conductance g as a function of η_0. The solid (dashed) lines correspond to stable (unstable) patterned states, and the stars represent the point at which the system goes unstable to the spatially patterned states. The red curve represents the domain of length π, the blue line shows the values for the domain of length 2π and the green line corresponds to the system with a domain of

length 4π. It can be seen that these waves emerge from the homogeneous steady state ($g^* = 0$) with a non-zero wave speed, at different values of η_0. The value for which periodic waves emerge when the domain size is 2π corresponds to the Turing-Hopf bifurcation found in Chapter 5, as the wave number for this wave solution corresponds to the most unstable wave number $|k_c| = 1$. For the simulations on the domain of size π and 4π the wave numbers are $k = 2$ and $k = 0.5$, respectively. It can be seen that homogeneous steady state goes unstable to these patterns at a larger value of η_0.

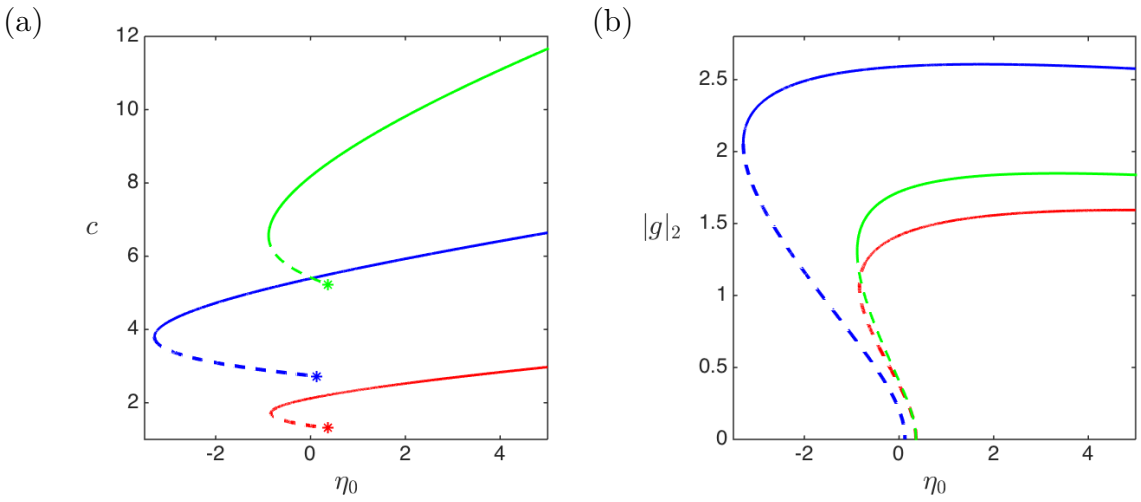

Figure 6.2.4. Continuation in η_0 for periodic waves: One parameter bifurcation diagram in the mean background drive η_0 of the stationary wave solution of the system defined by (6.1.9)–(6.1.10). The continuation is shown as a function of (a) the speed of the wave and (b) the 2-norm of the synaptic conductance g as a function of η_0 for a domain of size π (red), 2π (blue) and 4π (green). The stars indicate the point at which the system goes unstable to patterns in each case. Solid (dashed) lines represent stable (unstable) patterned states. Parameter values: $v_{\text{syn}} = -5$, $\Delta = 0.5$, $\kappa = 5$, $\alpha = 1$.

To fully explore the relationship between the wave speed c and the spatial period p, it is convenient to normalise the system such that the domain size is 1 and p becomes

a model parameter. This leads to the following system of equations:

$$\left(p^2 - \frac{\mathrm{d}^2}{\mathrm{d}\xi^2}\right)^2 \left(p - \frac{c}{\alpha}\frac{\mathrm{d}}{\mathrm{d}\xi}\right)^2 \tilde{g} = -4p^4\kappa\frac{\mathrm{d}^2}{\mathrm{d}\xi^2}f(Z), \tag{6.2.3}$$

$$-c\partial_\xi Z = p(\mathcal{F}(Z;\eta_0,\Delta) + \mathcal{G}(Z,\tilde{g};v_{\mathrm{syn}})). \tag{6.2.4}$$

Finding solutions to these equations and continuing them in p allows us to compute dispersion curves for the system, as shown in Fig. 6.2.5. We can see that periodic waves, such as those shown in Fig. 6.2.5, only exist for a finite range of spatial periods. For every value of p there exists two wave solutions with different speed, one of which is stable (solid) and one of which is unstable (dashed), as expected from examining Fig. 6.2.4a. Stability was computed numerically as described in §6.1. If we increase the mean background drive η_0 the dispersion curve is no longer a closed loop and the system has one stable speed for every value of spatial period.

6.3 Continuation of local patterns

In this section we will focus on travelling fronts, localised patterns which connect two fixed points of the system. Hence, in order for the system to support these local patterns it must have at least two steady states, which is not possible with a balanced connectivity kernel. As such, we opt for a change in coupling kernel and choose the unbalanced normalised exponentially decaying function, $w(x) = \exp(-|x|)/2$. The Fourier transform of $w(x)$ is given as $\widehat{w}(k) = 1/(1+k^2)$. Using the methods described in §6.1, we can transform to an equivalent PDE system, which gives

$$(1 - \partial_{xx})\left(1 + \frac{1}{\alpha}\partial_t\right)^2 g = \kappa f(z), \tag{6.3.1}$$

$$\partial_t z = \mathcal{F}(z;\eta_0,\Delta) + \mathcal{G}(z,g;v_{\mathrm{syn}}), \tag{6.3.2}$$

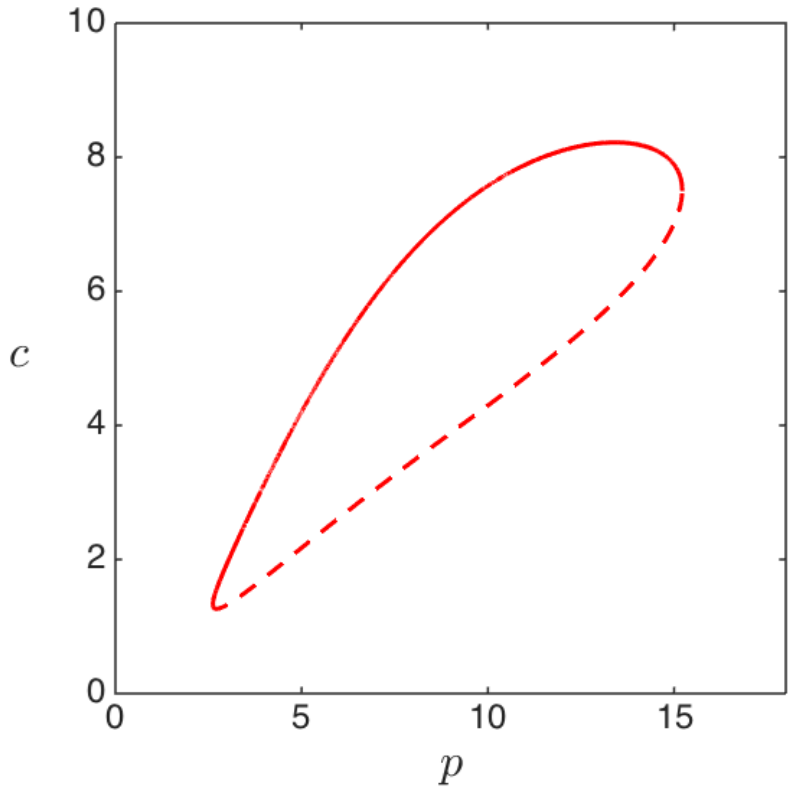

Figure 6.2.5. Dispersion curve for periodic travelling waves: One parameter continuation for the system described by (6.2.3)–(6.2.4), showing the relationship between wave speed c and the spatial period p of the periodic travelling waves. Solid (dashed) lines show stable (unstable) solutions. We can see that for the chosen parameter values the periodic waves only exist for a finite range of periods. Parameter values: $\eta_0 = 0$, $v_{\text{syn}} = -5$, $\Delta = 0.5$, $\kappa = 5$, $\alpha = 1$.

where f, $\mathcal{F}$ and $\mathcal{G}$ are given by (3.2.12), (3.2.15) and (3.2.16), respectively. Once again, we use Neumann boundary conditions on a suitably large domain.

Before analysing the travelling wave solutions we first examine the spatially clamped system. At steady state,

$$g^* = 4\kappa f(z), \tag{6.3.3}$$

$$\mathcal{F}(z^*; \eta_0, \Delta) + \mathcal{G}(z^*, g^*; v_{\text{syn}}) = 0, \tag{6.3.4}$$

where we have used the fact that $\int \mathrm{d}y w(y) = 1$. The solutions to these equations were found numerically and continued in the synaptic reversal potential v_{syn} and the mean background drive η_0 using XPPAUT [66]. Figure 6.3.1 shows a two parameter bifurcation diagram in v_{syn} and η_0. The system has three fixed points in the region enclosed by the saddle-node curves (red). Hence, we will look for travelling fronts in this region of parameter space. Increasing the synaptic time constant α introduces a Hopf bifurcation in this region, which may lead to interesting oscillating fronts, which connect nodes to periodic orbits or periodic orbits to other periodic orbits. However, as the numerical machinery considered here only allows for the continuation of solutions which are stationary in the travelling wave frame we will not consider them further here. These states are discussed briefly in Chapter 7.

Figure 6.3.2 shows a typical wave profile, which connects a high activity state to a low activity state. At steady state the synaptic conductance g is directly proportional to the firing rate. As such, we shall refer to the high (low) activity state as the state with a large (small) value of synaptic conductance g. Interestingly, we see ripples in the wake of the front, which may indicate that the solution connects a node to a focus. To examine this further we plotted the solution in the phase space $[\mathrm{Re}(z), \mathrm{Im(z)}, g]$, see Fig. 6.3.3. This illustrates that it is indeed a node-focus connection. The focus is the high activity state and the node the low activity state.

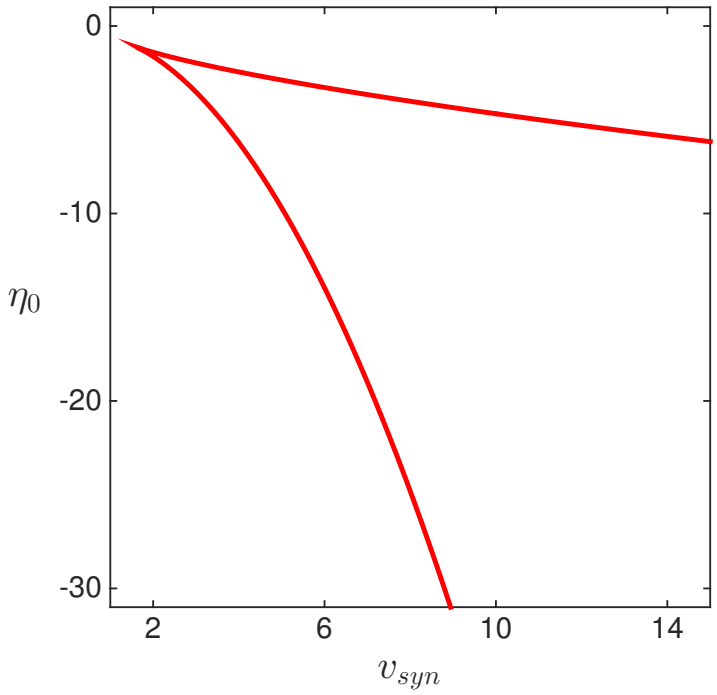

Figure 6.3.1. Spatially clamped system with exponential kernel: Two parameter bifurcation diagram of the steady state solutions of (6.3.3)–(6.3.4) in the synaptic reversal potential v_{syn} and the mean background drive η_0, showing the saddle node curve. In the area enclosed by the saddle node curve there are 3 fixed points, there is one fixed point elsewhere. Parameter values: $\Delta = 0.5$, $\kappa = 5$, $\alpha = 1$.

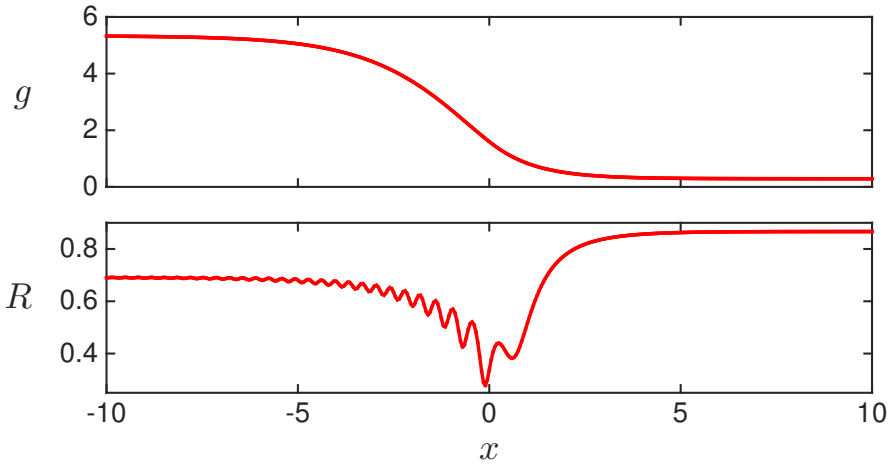

Figure 6.3.2. Profile of the travelling wave solution: Profile of the travelling wave solution showing the synaptic conductance g and the synchrony R, from a simulation of (6.3.1)–(6.3.2). Parameter values: $\eta_0 = -3$, $v_{\text{syn}} = 4$, $\Delta = 0.5$, $\kappa = 5$, $\alpha = 1$.

Before numerically continuing the travelling wave solution we simulated (6.3.1) and (6.3.2) for a range of different parameter sets. Figure 6.3.4 shows the evolution of the travelling front for a number of different values for the mean background drive η_0. One can clearly observe that increasing η_0 results in a faster wave speed. Examining the left hand column of Fig. 6.3.4 reveals that the ripples seen in the wake of the front, as shown in Fig. 6.3.2, become more prominent and long-lived as η_0 is increased. The numerical scheme used to produce these plots is described in Appendix C.3. Here we used 1000 mesh points on a domain of length 60. As the front never reaches the edge of the domain in the period of time we are interested in the simulated behaviour is not affected by edge effects.

To continue the travelling front solution we once again transform to the travelling

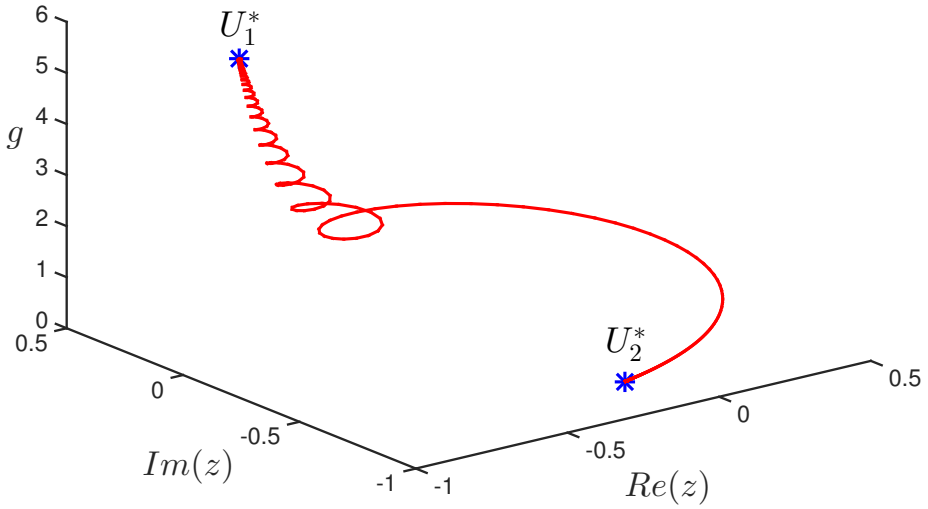

Figure 6.3.3. Phase portrait of the travelling wave solution: Three dimensional phase space plot of the travelling wave solution, corresponding to the front shown in Fig. 6.3.2, showing the connection between the two fixed points; high activity state U_1^* and the low activity state U_2^*. Parameter values as in Fig. 6.3.2.

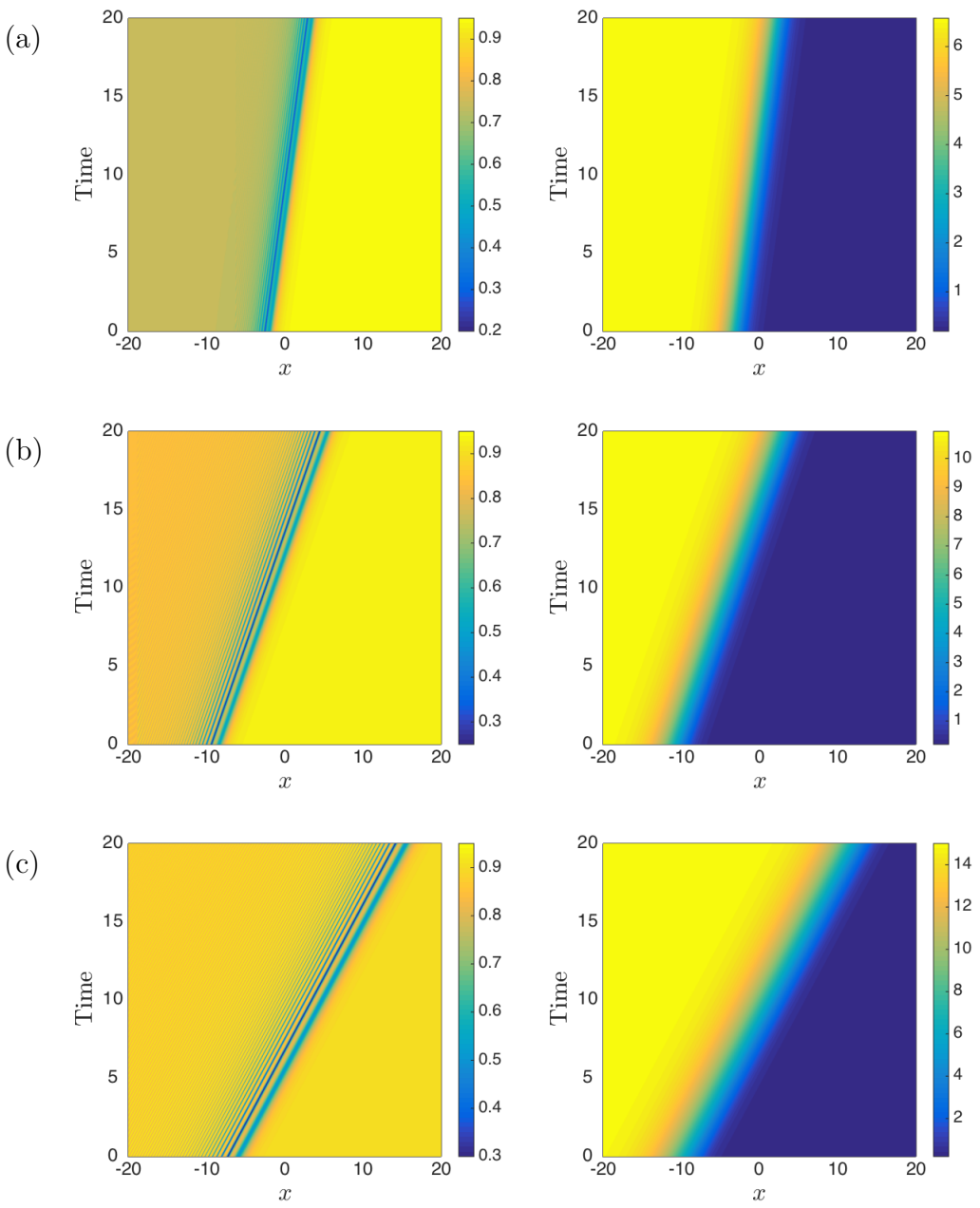

Figure 6.3.4. Simulations of a travelling front in (6.3.1)–(6.3.2)**:** Surface plots showing the front moving across the domain, for a number of different value of the mean background drive η_0: (a) $\eta_0 = 4$, (b) $\eta_0 = 7.5$, (c) $\eta_0 = 10$. The left hand column shows the synchrony R (where R is the magnitude of the Kuramoto order parameter z) and the right column shows the synaptic conductance g. It can be seen that increasing η_0 increases the speed at which the wave propagates across the domain. Also noteworthy is that increasing η_0 increases the prominence of the ripples in the wake of the front. Parameter values: $v_{\text{syn}} = -5$, $\Delta = 0.5$, $\kappa = 5$, $\alpha = 5$.

wave frame $u(x,t) \to U(x-ct) \equiv U(\xi)$,

$$\left(1 - \frac{\mathrm{d}^2}{\mathrm{d}\xi^2}\right)\left(1 - \frac{c}{\alpha}\frac{\mathrm{d}}{\mathrm{d}\xi}\right)^2 \tilde{g} = \kappa f(Z), \tag{6.3.5}$$

$$-c\frac{\mathrm{d}}{\mathrm{d}\xi}Z = \mathcal{F}(Z;\eta_0,\Delta) + \mathcal{G}(Z,\tilde{g};v_{\mathrm{syn}}). \tag{6.3.6}$$

The wave profile in Fig. 6.3.2 was numerically continued in the average background drive η_0 to create the bifurcation diagram shown in Fig. 6.3.5 (red). The mirror image of the wave profile was also continued; this accounts for the second solution set (blue). Note that the two solutions sets are symmetric. The solid (dashed) lines correspond to stable (unstable) solutions. The same solution was also continued in v_{syn} (the synaptic reversal potential), which can be seen in Fig. 6.3.6. As in Fig. 6.3.5, the blue curve represents the mirror image of the solution represented by the red curve.

An examination of Fig. 6.3.5 demonstrates that for every value of η_0 there are 6 possible values for c. However only 3 of these are unique, as moving at speed c_1 in the case where the excited state is on the left is the same as moving at speed $-c_1$ in the case where the excited state is on the right. This is also the case for the continuation of v_{syn} in Fig. 6.3.6 Of the 3 unique values of c, one is stable and two are unstable. We note that there are ripples in the wake of the stable branch solutions and the solutions for the upper of the two unstable branches, but not for the lower of the two unstable branches. To examine this further we explored the eigenstructure of the homogeneous steady states for each of the values of c. Figure 6.3.7 shows the eigenvalues, $\lambda = \omega + i\nu$ of both fixed points for each of the possible values of c, as well as the profile of R, where the high activity state is on the left. The key difference between the cases where we see ripples and the case in which we do not is that there is only one stable eigenvalue in the case without ripples and it is purely real. However, in the other case the unstable eigenvalues are complex and real. The reduction in $|\nu|$ between $c = 0.3594$ and $c = 0.9470$ cases likely accounts for the reduction in the

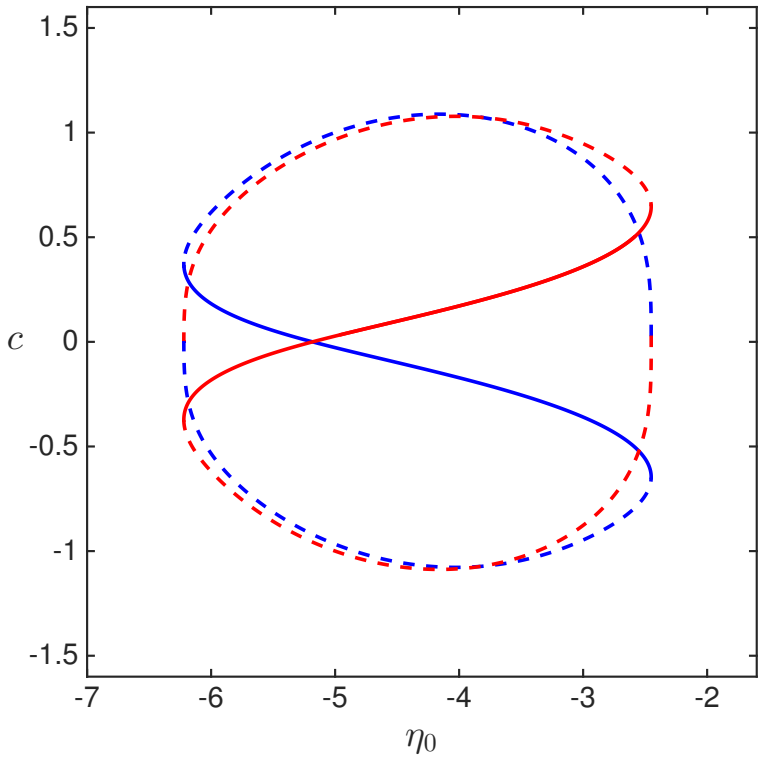

Figure 6.3.5. Continuation in η_0 of the travelling wave solution: Bifurcation diagram in the mean background drive η_0, showing the wave speed c as a function of η_0. This plot was calculated by continuing stationary solutions of (6.3.5)–(6.3.6). Solid lines represent stable branches and dashed lines unstable branches. Red lines have a profile similar to that in Fig. 6.3.2 (excited state on the left) and the blue lines represent the mirror image of that state. Parameter values: $v_{\text{syn}} = 4$, $\Delta = 0.5$, $\kappa = 5$, $\alpha = 1$.

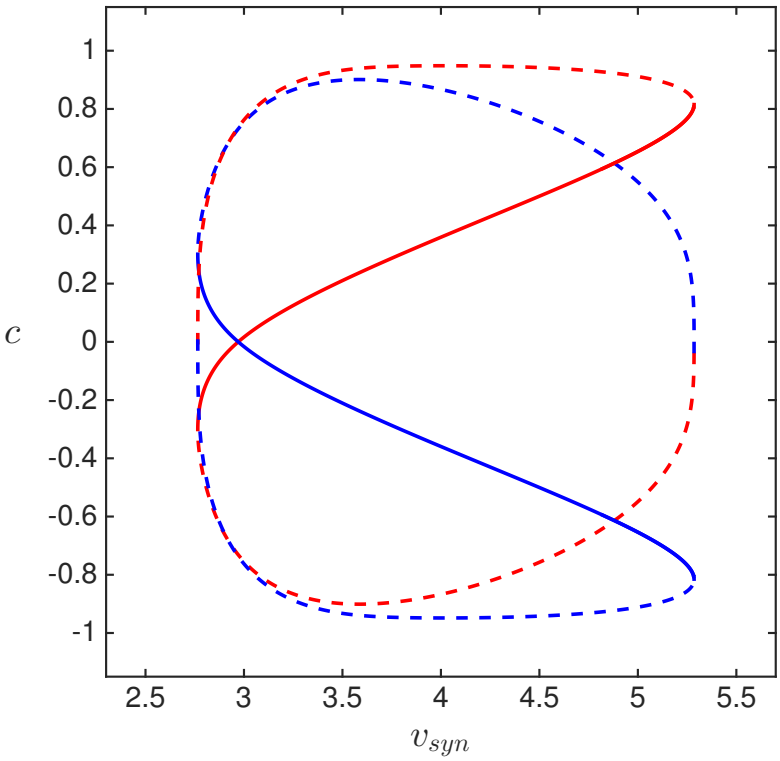

Figure 6.3.6. Continuation in $v_{\mathbf{syn}}$ of the travelling wave solution: Bifurcation diagram for the model prescribed by (6.3.5)–(6.3.6), demonstrating how the synaptic reversal potential v_{syn} influences the wave speed c. Solid lines represent stable branches and dashed lines unstable branches. As in Fig. 6.3.5 the red curve corresponds to solutions which have profile similar to that shown in Fig. 6.3.2 and the blue curve represent the mirror image of that state. Parameter values: $\eta_0 = -3$, $\Delta = 0.5$, $\kappa = 5$, $\alpha = 1$.

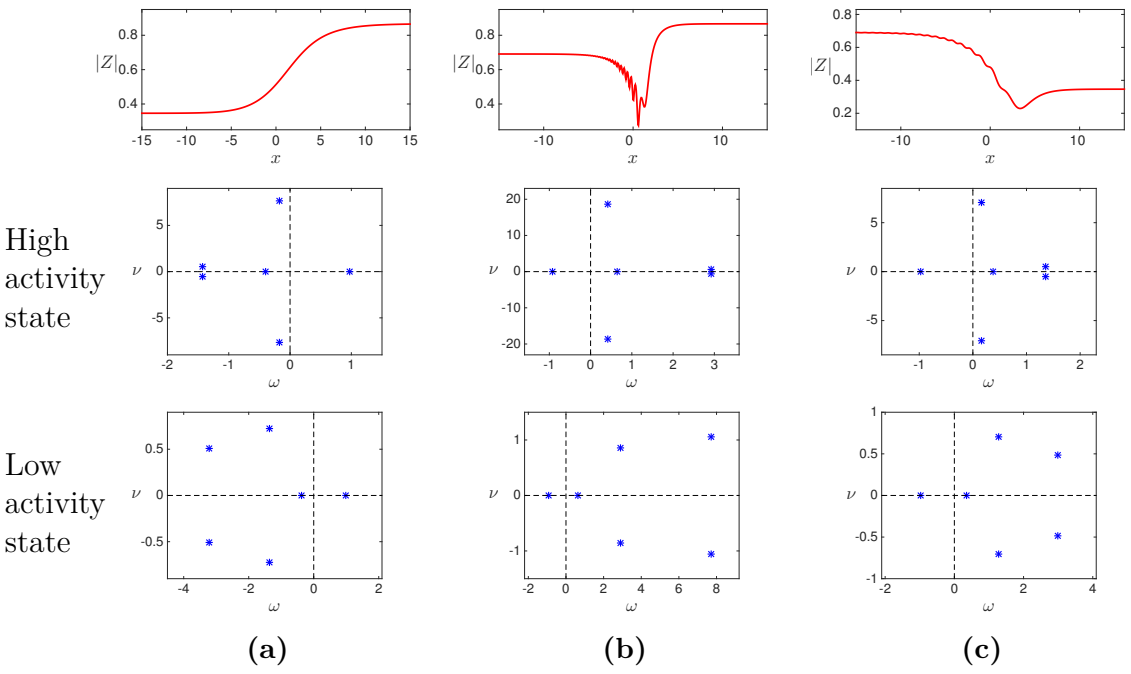

Figure 6.3.7. Eigenstructure of fixed points in system with exponential kernel: Wave profile and eigenvalues, $\lambda = \omega + i\nu$, of both of the fixed points, for the 3 possible values of c. These calculations were carried out for the system described by (6.3.5)–(6.3.6). a) $c = -0.8769$, b) $c = 0.3594$, c) $c = 0.9470$. Parameter values: $\eta_0 = -3$, $v_{\text{syn}} = 4$, $\Delta = 0.5$, $\kappa = 5$, $\alpha = 1$.

amplitude of the ripples.

6.4 Discussion

This chapter was a natural extension of the work presented in Chapter 5. Here we used numerical techniques to analyse the spatio-temporal patterns presented in the previous chapter. As the population firing rate in our model is a fixed derived function, we cannot make use of the convenient Heaviside approximation, which allows for the stability of spatial patterns to be examined away from bifurcation in standard neural field models. As such, we use numerical analysis to examine the system away from bifurcation, which allows us to explore the behaviour of the system more thoroughly. We began this chapter with an overview of the numerical machinery that was used to carry out the subsequent analysis. The analysis of the spatially periodic states confirmed that the Turing bifurcations found in Chapter 5 were subcritical.

Making a switch to periodic boundary conditions enabled us to explore the behaviour of the periodic travelling waves away from bifurcation. We found an isolated closed dispersion curve in §6.2.2, with one stable and one unstable branch. Interestingly, these periodic travelling waves can achieve high wave speeds, which could be interesting for further study. Further explorations may lead to the discovery of more branches of the dispersion curve. Another interesting extension would be to extend machinery described in §6.1 to continue periodic solutions, like the ones seen in Chapter 5 when the Turing and Turing Hopf bifurcations collide.

Making a switch to an alternative coupling kernel, in §6.3, allowed us to analyse local patterns, in particular, travelling fronts. At the beginning of the chapter, we outlined the biological significance of such solutions and stated the importance of developing numerical techniques to examine these solutions. In particular, Aquino *et al.* [7] discovered blood oxygen level dependent (BOLD) waves propagating across the

cortex at speeds of roughly 2–12 mms^{-1}. Discrepancies in BOLD waves are believed to play an important role in the generation of strokes [151]. In our model, we discovered travelling front solutions which connected a node to a focus in phase space, allowing for ripples to form in the wake of the front. We briefly mentioned the existence of fronts which connected nodes to periodic orbit, which would make for an interesting further study, and are discussed in more detail in the next and final chapter. Further analysis of these waves would be required to understand their role in neurological disorders such as stoke and epilepsy. It is also important to note that this analysis was carried out for a system spatially extended in one spatial dimension. The cortical surface is a two dimensional object and as such, a further analysis of our next generation neural fields model in two spatial dimensions would be needed to make real biological links.

Chapter 7

Discussion

To conclude this thesis we now look back on the main results presented here and also look to the future to explore possible extensions of this work.

7.1 Recapitulation of thesis

The goal of this thesis was to develop a new modelling approach to aid in the understanding of brain imaging experiments. The key requirement of this new approach was that it must be able to describe within population synchrony in the mean field limit.

After a brief overview of the thesis, we began with an introduction to neuronal dynamics and discussed the prevalence of oscillations in human EEG/MEG studies. Also in Chapter 2, we reviewed the use of MEG for measuring brain activity. The focus of this chapter then shifted to mathematical modelling of brain dynamics. We reviewed the use of both single neuron models and mean field type models in theoretical neuroscience, which set the scene for the development of our *next generation neural mass model*.

We began Chapter 3 with a discussion of the shortcomings of standard neural mass

modelling, paying particular attention to their inability to describe synchronisation phenomena. We then introduced our *next generation neural mass model* which makes use of the OA ansatz to reduce a network of θ-neurons to an equivalent low dimensional system. We found that the inclusion of a realistic form of synaptic coupling leads to a mean field model which takes the form of generalised neural mass model, where the firing rate function is now a derived quantity that implicitly depends on the within population synchrony. A bifurcation analysis of the single population model demonstrated that the system supports oscillations for a wide window of parameter space, unlike a standard neural mass model that cannot support oscillations without the presence of delays or a second population. Including a second population and creating an excitatory-inhibitory pair provided us with a rich bifurcation structure. In particular, the two population system was found to support torus, isola and period doubling bifurcations.

Chapter 4 began with an introduction to the beta rhythm, and discussed movement-induced changes of this brain rhythm: movement-related beta decrease (MRBD) and post movement beta rebound (PMBR). We presented experimental results which illustrated the key features of MRBD and PMBR for a median nerve stimulation protocol. Using the single population model we showed that the reduced model could support both MRBD and PMBR. As the single population model failed to reproduce PMBR of the desired length, we introduced a second identical population to test the theory that the ipsilateral hemisphere plays an important role in the generation of PMBR. The two hemisphere model provided both a stronger and longer PMBR.

Given that neural mass models are themselves the building blocks of neural field models, we construct a neural field model using similar techniques to those presented in Chapter 3 to reduce a spatially distributed network of θ-neurons to arrive at our *next generation neural field model*. We carried out a Turing instability analysis in both one and two spatial dimensions, and found a range of different patterned state,

including static Turing patterns, global periodic breathers, dynamic Turing waves, and most interestingly globally periodic bumps states in which there exists a structure inside the bump. These exotic states have not be seen in standard neural mass models. They are, however, typically seen in large networks or spiking neurons, which implies that our reduced model retains some knowledge of the underlying spiking network. These patterned states were found in the region or parameter space where the Turing and Turing-Hopf bifurcations collided. Importantly, as the two bifurcations were found for a fixed critical wave number k_c this is a real intersection of the two curves, rather than crossing at different values of k_c.

The work presented in Chapter 5 nicely set the scene for Chapter 6, where we used numerical techniques to analyse the full nonlinear system. In this chapter we used numerical machinery developed by Avitabile [10] to verify the analytical results and explore the behaviour of these global patterns away from bifurcation. The final section of Chapter 6 focused on numerically continuing travelling fronts, solutions which connect two fixed points of the system. These connections were found to be connect a node to a focus, which resulted in ripples forming in the wake of the front.

Upon reflection, we realised that the inclusion of shunts in our next generation neural field model was biologically unrealistic. A more biologically realistic model is presented in [34], and the analysis undertaken in Chapter 5 and 6 is redone for this model.

7.2 Future work

This work raised a lot of interesting questions and provided many potential projects for the future. Given the model's ability to track within population synchronisation and its success in explaining beta rebound, we strongly advocate its subsequent use in future population-level modelling approaches for understanding *in vivo* brain activity

states. ERD and ERS are commonly observed phenomena in electrophysiological brain recording, which cannot be explained using standard neural mass modelling approaches. Here, we have presented a mechanistic model which can both reproduced and explain these phenomena. The model points to a strong link between within population synchronisation and observed spectral power.

There is plenty of scope for extending the model to include more biologically relevant features. One possible extension to the model would be to include a variety of different synaptic receptors. We have assumed that PMBR and MRBD are mediated by the same type of synaptic receptor. However, Hall *et al.* suggest that MRBD is a GABA-A mediated process, whilst PMBR appears to be generated by a non-GABA-A receptor mediated process [78]. A further model that distinguishes between receptors, may offer important insights into motor processes, and can be readily accomplished within the framework that we have presented here. Laing *et al.* has shown that it is possible to extend the work presented here to include gap junction coupling [109]. It is well known that gap junctions play an important role in the generation of neural rhythms, both functional [85, 16] and pathological [162, 61]. Other potentially interesting features include action potential generation, dendritic processing, and stochasticity. In particular, Lai *et al.* demonstrated that the OA ansatz can be extended to perform a mean-field reduction for Kuramoto networks in the presence of noise [106], and this approach could also be used to treat QIF and θ-neuron networks.

One of the major downfalls of our model is the assumption of all-to-all coupling, albeit a reasonable assumption when considering small densely connected areas for cortex. Recent work by Chandra *et al.* has shown that it is possible to apply the OA reduction to a not fully connected network of θ-neurons. The cost of such an extension is a more complicated system of reduced equations, where there are as many equations as node degrees [38]. They find that for networks with scale free degree distributions the nodes with different node degrees admit a large variation of behaviour, which is

not possible in networks with all-to-all connectivity as they all have the same node degree.

As the OA ansatz assumes a unimodal distribution, it can only describe unimodal states and as such cannot describe cluster states. Cluster states, characterised by the formation of multiple synchronised groups, frequently occur in nature. For example, networks of neuronal, photochemical, and electrochemical oscillators tend to synchronise in clusters [69, 155, 101]. Implementing minor adjustments to the OA ansatz, allowed Skardal *et al.* to extend the ansatz to describe cluster states [149]. Their insight was to define an order parameter for each of the cluster states; the first order parameter describes the degree of synchronisation in the entire population, the second describes the degree of two cluster synchronisation and so on. The paper focused on a two-cluster state for a network of Kuramoto oscillators, but could easily be extended to describe multi-cluster states in a network of θ-neurons.

More generally, there is a pressing need to develop new reductive techniques to handle alternative single neuron models, such as those of Izhikevich type [88]. For phase oscillator single neuron models this is intrinsically linked to the mathematical challenge of generalising the OA approach, whilst for more general conductance based neurons one might appeal to the McKean-Vlasov-Fokker-Planck approach of Baladron *et al.* [12]. Indeed, we would like to think of the work presented here as a first example of a next generation neural mass model and that there will be others to follow. By maintaining some notion of within population synchrony it provides a link between the microscopic and macroscopic brain scales, but only for a specific choice of single neuron model. We hope that for a general single neuron model this mathematical step is not as elusive as originally thought.

Even without extending the model, or developing more general formulations, there are still a plethora of questions that we did not have time to answer. Of particular utility would be an understanding of the response to periodic forcing, as this would

be a precursor to understanding patterns of phase-locking, clustering, chaos, and the multiplicity of attractors expected at the network level. Unpublished work by colleagues at the SPMIC points to PMBR being suppressed if the median nerve is stimulated again within 0.5 second of the first stimulation. The PMBR after the second stimulations is no longer or larger in magnitude than the response from a single stimulation. Understanding the model's response to periodic forcing may allow us to better understand this phenomenon.

The desire to understand large scale brain dynamics as observed using EEG, MEG and fMRI has prompted the increasing use of computational models [23]. Many of these approaches, such as exemplified by the Virtual Brain project [142], make use of networks of interconnected neural mass models. The Virtual Brain project is an open source platform for simulating large networks of neural mass models, using anatomical connectivity matrices. The aim of this software, used by both theoreticians and clinicians, is to better understand neurological and psychiatric disorders and develop individual treatment plans for patients suffering from these disorders [21]. Given that we understand the dynamics of our model in the absence of additional neural masses, an interesting study would be to place our next generation neural mass (either a single or two population system) on each node of a network described by an anatomical connectivity matrix. Assuming a weakly coupled regime would allow one to compute and track bifurcations of the entire network model.

In Chapter 4, we stated that schizophrenia patients do not have as strong of a PMBR as healthy controls. It has also been shown that the severity of the disease can be directly linked to this reduction in PMBR [140]. As such, a further study in which we explore which parameters strengthen or weaken the PMRB in the model would be compelling. However, as schizophrenia affects the entire brain rather than a small area of cortex, I believe it would be more beneficial to do a large network study as described in the previous paragraph, using anatomical connectivity matrices

from both patients and health controls. One could then assess if strengthening or weakening certain connections restored the strong PMBR.

In the two population analysis, described in Chapter 3, we discovered a parameter window for which high amplitude and low amplitude oscillations coexisted. In Chapter 2 we discussed the success of the Jansen Rit model in epilepsy modelling as it had this feature of coexisting periodic orbits. Hence, our model may be an ideal candidate for modelling epilepsy. We did not explore this potential application of the model, but feel it would prove another interesting project.

We used our next generation neural mass model to describe both MRBD and PMRB in Chapter 4. We also saw an increase in high beta/gamma activity in our model when the drive was switched on, which we stated was seen in real data, but in a slightly more frontal area of motor cortex. To test this theory one could use our next generation neural field model and examine where the increases in firing activity occur. Another intriguing test for our neural field model would be to see if it could reproduce the spread of MRBD and PMBR across the cortex to the ipsilateral hemisphere.

When analysing neural field models, it is customary to perform a weakly nonlinear analysis; however, we favoured a numerical analysis here. Using weakly nonlinear analysis to construct amplitude equations to describe the behaviour of the system as we move away from bifurcation would be another interesting project. In particular, should we wish to explore the transition from the periodic breathers to the standing waves, as seen in the 2D case in Chapter 5, the amplitude equations may allow us to do this. Beyond a Turing-Hopf a left- and right-travelling wave may interact to form a standing wave, if so then the condition for finding this would be tractable using weakly nonlinear analysis.

In Chapter 6 we pointed to the existence of fronts that connect periodic orbits to nodes/focuses, for the spatially extended model with an exponential coupling kernel. Figure 7.2.1 shows a numerical simulation of such a front, illustrating how (a) the

synaptic conductance g and (b) the synchrony R evolve in this case. The machinery used here doesn't allow for the continuation of these solutions, known as defects. The analysis of defects is still an open problem. Close examination of Fig. 7.2.1 reveals that there are two fronts in this connection between a node and limit cycle, which appear to be moving at different speed. Even more interesting, would be the analysis of fronts which connect two periodic orbits of different amplitudes. The spreading of such a wave across the cortex could be viewed as the spreading of an epileptic seizure.

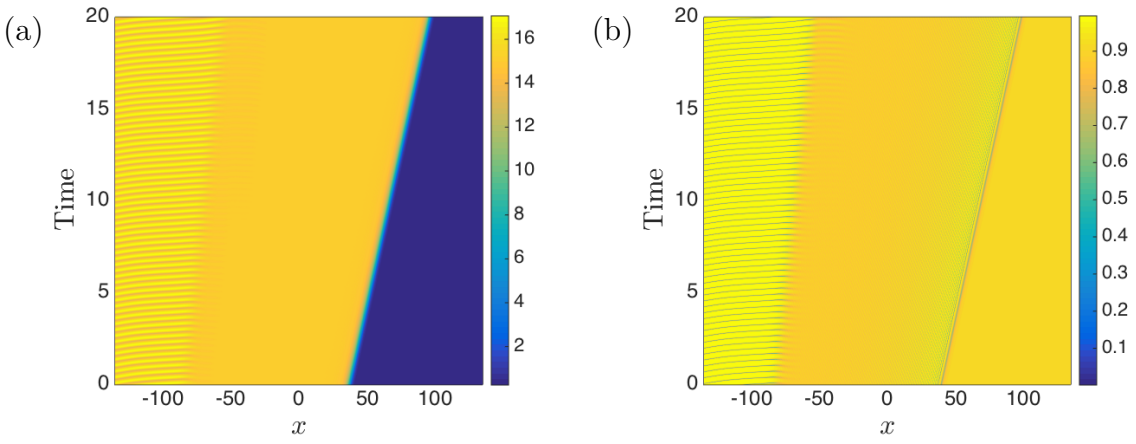

Figure 7.2.1. Travelling wave connecting a periodic orbit to a node: Surface plots showing the evolution of (a) the synaptic conductance g and (b) the synchrony R for a front which connects an oscillatory state to a fixed point state. This type of behaviour was discovered in the model defined by (6.3.1)–(6.3.2).

Another numerical challenge would be to continue the periodic patterns seen in Chapter 5 when the Turing and Turing-Hopf bifurcations collide. These patterns have both a spatial and a temporal period, which would require extending the machinery described in Chapter 6 to continue both a spatial and a temporal pattern. This has been achieved by Avitabile in his PhD thesis for the Brusselator model [9].

As the cortical surface is a two dimensional system, a natural extension to the

work presented in Chapter 6, would be to extend the numerical analysis to explore the behaviour of the system in two spatial dimensions. We would be unable to transform to an equivalent PDE framework as we did in the 1D case as the 2D Fourier transform of the coupling kernel in this case is not easily separable. A more achievable approach would be to use MATLAB's built in fast fourier transform algorithm to compute the spatial convolution. This would however, restrict us to analysing the system on the periodic domain.

The formulation of neural field models has not changed much since the seminal work of Wilson and Cowan, Nunez and Amari, and although the work presented in this thesis is a departure from this formulation, further deviation is still required. To fully understand the brain and neural computation, we must build models which can incorporate biological features, such as white matter tracts. The relationship between structure and function is a major research focus in the neuroimaging community [134], discrepancies in structural/functional connectivity are frequently used as biomarkers for mental health and disease, see [125] for a review on the structural changes seen in schizophrenia. Neural field models which also include grey matter tracts modelled on individual human connectivity matrices could prove beneficial in understanding these discrepancies. Such advancements would require accompanying advancements in the mathematical theory, which may be achieved by exploiting and extending techniques from differential geometry, uncertainty quantification, scientific computation, nonlinear dynamics and stochastic optimal control to achieve this.

To conclude, this thesis answered a number of important research questions but also presented an extensive collection of new questions, both mathematical and biological. The main mathematical challenge lies in generalising the OA ansatz and developing new reductive techniques. The clinical questions we discussed include, can this model explain the reduced PMBR seen in schizophrenia patients and will the spatially extended model help us understand the spread of both MRBD and PMBR across the

cortex? It is our belief that the model can support the reduced PMBR in schizophrenia patients and that it will be possible to use the spatially extended model to further explore the spread of MRBD and PMBR over the cortical surface.

Appendix A

Numerical scheme for large scale simulations

In this appendix we briefly discuss the numerical scheme used for the large scale network simulations, from Chapter 3.

A.1 Quadratic integrate-and-fire network

The system we wish to simulate is

$$\frac{\mathrm{d}}{\mathrm{d}t}v_i = \eta_i + v_i^2 + I_i, \qquad i = 1, \ldots, N, \tag{A.1.1}$$

where

$$I_i = g(t)(v_{\mathrm{syn}} - v_i), \tag{A.1.2}$$

and g evolves as follows

$$\left(1 + \frac{1}{\alpha}\frac{\mathrm{d}}{\mathrm{d}t}\right)^2 g(t) = \frac{\kappa}{N}\sum_{j=1}^{N}\sum_{m\in\mathbb{Z}}\delta(t - T_j^m), \tag{A.1.3}$$

where the parameters are described in Chapter 3. First, we introduce the variable K,

$$K = \left(1 + \frac{1}{\alpha}\frac{\mathrm{d}}{\mathrm{d}t}\right) g, \tag{A.1.4}$$

to write (A.1.3) as

$$\frac{\mathrm{d}g}{\mathrm{d}t} = \alpha\left(-g + K\right), \tag{A.1.5}$$

$$\frac{\mathrm{d}K}{\mathrm{d}t} = \alpha\left(-K + \frac{\kappa}{N}\sum_{j=1}^{N}\sum_{m\in\mathbb{Z}}\delta(t - T_j^m)\right). \tag{A.1.6}$$

As the coupling is all-to-all, g and K are the same for every neuron so we can use one equation to describe g and K for every neuron, making the system of order $N + 2$.

We must make use of MATLAB's event detection algorithm to evolve the system. Including the options

```
1 options = odeset('Events',@spike,'OutputSel',1,'Refine',refine);
```

in MATLAB's ODE solvers halts the simulations at conditions defined in the function 'spike', see below.

```
1 function [value,isterminal,direction] = spike(t,y,N,p)
2 % t = time, y = [v(1:N),g,K], N = number of neurons,
3 % p = parameters vector
4 v = y(1:N);
5 v_th = 100;
6 value = [v-v_th] ;              % Detect threshold crossing
7 isterminal = [ones(N,1)];       % Stop the integration
8 direction = [ones(N,1)];        % Only increases through v_th
9 end
```

The inclusion of line 7 in the above code means that the algorithm only detects events in which the voltage v is increased though v_{th}. When an event is detected the ODE

solver stops, the label of the neuron that crossed threshold is outputted, along with the spike timing and the evaluation of the each variables up to that point. Inserting a *for* or a *while* loop around the ODE solver allows the simulation to run for a predetermined number of spikes or amount of time. Before returning to the beginning of the loop the voltage of the neuron that crossed the threshold v_{th}, must be reset to v_{reset}. As the δ-function in (A.1.6) is non-zero when the neuron spikes (voltage crosses threshold), we add $\alpha\kappa/N$ to the variable K.

```
1    y(T_s,N+2)=y(T_s,N+2)+alpha*(kappa/N);        % T_s = spike time
2    y(T_s,b) = -100;
```

We must also accumulate the output at each iteration, otherwise the output of the ODE solver gets overwritten at each iteration.

A.2 θ-NEURON NETWORK

When we transform to the θ-neuron framework, the dynamics are described as follows

$$\frac{\mathrm{d}}{\mathrm{d}t}\theta_i = (1-\cos\theta_i) + (1+\cos\theta_i)(\eta_i + g(t)v_{\text{syn}}) - g(t)\sin\theta_i, \tag{A.2.1}$$

$$\frac{\mathrm{d}g}{\mathrm{d}t} = \alpha\left(-g+K\right), \tag{A.2.2}$$

$$\frac{\mathrm{d}K}{\mathrm{d}t} = \alpha\left(-K + 2\frac{\kappa}{N}\sum_{j=1}^{N}\sum_{m\in\mathbb{Z}}\delta(\theta-\pi)\right). \tag{A.2.3}$$

As above, the system is of order $N+2$.

To evolve the system we once again make use of MATLAB's event detection algorithms. The event detection function, for the θ-neuron network, is given below.

```
1 function [value,isterminal,direction] = spike(t,y,N,p)
2 % t = time, y = [theta(1:N),g,K], N = number of neurons,
3 % p = parameters vector
```

```
4 theta = y(1:N);
5 value = [theta-pi] ;              % Detect when phases crosses pi
6 isterminal = [ones(N,1)];         % Stop the integration
7 direction = [ones(N,1)];          % Only increases through pi
8 end
```

For the θ-neuron network we do not need to reset the phase variable θ. However, we still need to account for the effect of the spike on the other neurons in the population by adding $2\alpha\kappa/N$ to the K variable.

```
1   y(T_s,N+2)=y(T_s,N+2)+2*alpha*(kappa/N);      % T_s = spike time
```

As above, we concatenate the output after event detection and then perform another iteration until the maximum number of events or amount of time is reached.

Appendix B

Calculating coefficients for Turing analysis

In this appendix we compute the coefficients required for the Turing analysis in Chapter 5. Note that each of the coefficients is evaluated at steady state, hence, $g = 0$.

$$
\begin{aligned}
\left|\frac{\partial a}{\partial z}\right|^2 &= 4\frac{z+1}{z-1}\frac{\bar{z}+1}{\bar{z}-1}(-\Delta + i\eta_0)(-\Delta - i\eta_0) \\
&= 4\frac{|z|^2 + 2\mathrm{Re}(z) + 1}{|z|^2 - 2\mathrm{Re}(z) + 1}(\Delta^2 + \eta_0^2) \\
\mathrm{Re}\left(\frac{\partial a}{\partial z}\right) &= \mathrm{Re}\left(-2\frac{z+1}{z-1}\frac{\bar{z}-1}{\bar{z}-1}\right)(-\Delta + i\eta_0) \\
&= \mathrm{Re}\left(-2\frac{|z|^2 - 2i\mathrm{Im}(z) - 1}{|z|^2 - 2\mathrm{Re}(z) + 1}\right)(-\Delta + i\eta_0) \\
&= -2\frac{|(z|^2 - 1)\Delta + 2\mathrm{Im}(z)\eta_0}{|z|^2 - 2\mathrm{Re}(z) + 1} \\
\mathrm{Re}\left(\frac{\partial a}{\partial g}\frac{\partial c}{\partial z}\right) &= \mathrm{Re}\left[\left(iv_{\mathrm{syn}}\frac{(z+1)^2}{2} - \frac{z^2-1}{2}\right)\left(\frac{4\alpha\kappa}{\pi}\frac{1}{(1+z)^2}\frac{k^2}{(1+k^2)^2}\right)\right] \\
&= \mathrm{Re}\left[-\frac{2\alpha\kappa}{\pi}\frac{k^2}{(1+k^2)^2}\left(iv_{\mathrm{syn}} - \frac{z^2-1}{(z+1)^2}\right)\right]
\end{aligned}
$$

$$
\begin{aligned}
&= \mathrm{Re}\left[\frac{2\alpha\kappa}{\pi}\frac{k^2}{(1+k^2)^2}\frac{z-1}{z+1}\frac{\bar{z}+1}{\bar{z}+1}\right] \\
&= \mathrm{Re}\left[\frac{2\alpha\kappa}{\pi}\frac{k^2}{(1+k^2)^2}\frac{|z|^2+2i\mathrm{Im}(z)-1}{|z|^2+2\mathrm{Re}(z)+1}\right] \\
&= \frac{2\alpha\kappa}{\pi}\frac{k^2}{(1+k^2)^2}\frac{|z|^2-1}{|z|^2+2\mathrm{Re}(z)+1}
\end{aligned}
$$

$$
\begin{aligned}
\mathrm{Re}\left(\frac{\partial a}{\partial g}\ \frac{\partial b}{\partial \bar{z}}\frac{\partial c}{\partial z}\right) &= \mathrm{Re}\left[\left(iv_{\mathrm{syn}}\frac{(z+1)^2}{2}-\frac{z^2-1}{2}\right)\left(-2\frac{\bar{z}+1}{\bar{z}-1}(-\Delta-i\eta_0)\right)\right. \\
&\qquad\left.\times\left(\frac{4\alpha\kappa}{\pi}\frac{1}{(1+z)^2}\frac{k^2}{(1+k^2)^2}\right)\right] \\
&= \mathrm{Re}\left[-\frac{4\alpha\kappa}{\pi}\frac{k^2}{(1+k^2)^2}(-\Delta-i\eta_0)\frac{\bar{z}+1}{\bar{z}-1}\left(iv_{\mathrm{syn}}-\frac{z^2-1}{(z+1)^2}\right)\right] \\
&= \mathrm{Re}\left[\frac{4\alpha\kappa}{\pi}\frac{k^2}{(1+k^2)^2}(\Delta+i\eta_0)\left(iv_{\mathrm{syn}}\frac{\bar{z}+1}{\bar{z}-1}-\frac{z-1}{z+1}\frac{\bar{z}+1}{\bar{z}-1}\right)\right] \\
&= \mathrm{Re}\left[\frac{4\alpha\kappa}{\pi}\frac{k^2}{(1+k^2)^2}(\Delta+i\eta_0)\left(iv_{\mathrm{syn}}\frac{\bar{z}+1}{\bar{z}-1}\frac{z-1}{z-1}-\frac{|z|^2+2i\mathrm{Im}(z)-1}{|z|^2-2i\mathrm{Im}(z)-1}\right)\right] \\
&= \mathrm{Re}\left[\frac{4\alpha\kappa}{\pi}\frac{k^2}{(1+k^2)^2}(\Delta+i\eta_0)\left(iv_{\mathrm{syn}}\frac{|z|^2+2i\mathrm{Im}(z)-1}{|z|^2-2i\mathrm{Re}(z)-1}\right.\right. \\
&\qquad\left.\left.-\frac{|z|^2-1+2i\mathrm{Im}(z)}{|z|^2-1-2i\mathrm{Im}(z)}\frac{|z|^2-1+2i\mathrm{Im}(z)}{|z|^2-1+2i\mathrm{Im}(z)}\right)\right] \\
&= \mathrm{Re}\left[\frac{4\alpha\kappa}{\pi}\frac{k^2}{(1+k^2)^2}(\Delta+i\eta_0)\left(iv_{\mathrm{syn}}\frac{|z|^2+2i\mathrm{Im}(z)-1}{|z|^2-2i\mathrm{Re}(z)-1}\right.\right. \\
&\qquad\left.\left.-\frac{(|z|^2-1)^2-4\mathrm{Im}(z)^2+4i\mathrm{Im}(z)(|z|^2-1)}{(|z|^2-1)^2+4\mathrm{Im}(z)^2}\right)\right] \\
&= -\frac{4\alpha\kappa}{\pi}\frac{k^2}{(1+k^2)^2}\left[-2\Delta v_{\mathrm{syn}}\frac{\mathrm{Im}(z)}{|z|^2-2i\mathrm{Re}(z)-1}-\eta_0 v_{\mathrm{syn}}\frac{|z|^2-1}{|z|^2-2i\mathrm{Re}(z)-1}\right. \\
&\qquad\left.-\Delta\frac{(|z|^2-1)^2-4\mathrm{Im}(z)^2}{(|z|^2-1)^2+4\mathrm{Im}(z)^2}+4\eta_0\frac{4i\mathrm{Im}(z)(|z|^2-1)}{(|z|^2-1)^2+4\mathrm{Im}(z)^2}\right]
\end{aligned}
$$

Appendix C

Numerical scheme for the spatially distributed system

In this appendix we briefly discuss the numerical scheme used to simulate our next generation neural field model in both one and two spatial dimensions.

C.1 One spatial dimension - Mexican hat type kernel

The system is described by the following set of PDEs,

$$\frac{\partial z}{\partial t} = -i\frac{(z-1)^2}{2} + \frac{(z+1)^2}{2}(-\Delta + i\eta_0) + \left[iv_{syn}\frac{(z+1)^2}{2} - \frac{z^2+1}{2}\right]g, \tag{C.1.1}$$

$$\left(1 + \frac{1}{\alpha}\frac{\partial}{\partial t}\right)^2 g = \kappa \int w(y-x)f(z(y,t))\mathrm{d}y. \tag{C.1.2}$$

As in Appendix A, we introduce the variable K,

$$K = \left(1 + \frac{1}{\alpha}\frac{\partial}{\partial t}\right)g, \tag{C.1.3}$$

which allows us to write (C.1.2) as

$$\frac{\partial K}{\partial t}(x,t) = \alpha\left(-K(x,t) + \kappa\left[w \otimes f(z)\right](x,t)\right), \tag{C.1.4}$$

$$\frac{\partial g}{\partial t}(x,t) = \alpha\left(-g(x,t) + K(x,t)\right), \tag{C.1.5}$$

where $\otimes$ represents the spatial convolution. Given MATLAB's capabilities to evolve complex-valued differential equations we do not separate (C.1.1) into its real and imaginary components.

Introducing the Fourier transform as described by (5.2.6), allows us to write,

$$\left[w \otimes f(z)\right](x,t) = \widehat{w}(k)\widehat{f}(z(k,t)), \tag{C.1.6}$$

where $\widehat{w}$ and $\widehat{f}$ are the Fourier transforms of w and f, respectively. The Fourier transform of w is given in Chapter 5 by (5.2.15). Using cross multiplication and the inverse Fourier transform, we may write (C.1.4) as,

$$\left(1 - \frac{\partial^2}{\partial x^2}\right)^2 \frac{\partial K}{\partial t}(x,t) = \alpha\left(-K(x,t) - 4\kappa\frac{\partial}{\partial x}f(z(x,t))\right). \tag{C.1.7}$$

The system was simulated on a line of length $2L$, running from $-L$ to L and discretised into N spatial points. The size of the domain was chosen to be suitably large ($L > 50$) and Neumann boundary conditions were used, in order to mimic in the infinite domain. The spatial derivatives ∂_{xx} were computed using central finite differences with second order accuracy, such that

$$\partial_{xx} \to \mathbf{Dxx}, \tag{C.1.8}$$

where $\mathbf{Dxx}$ is a $N \times N$ matrix. The system can be easily simulated using MATLAB

ode solvers as

$$\mathcal{M}\frac{\mathrm{d}\mathbf{U}}{\mathrm{d}t} = F(\mathbf{U}), \tag{C.1.9}$$

where $\mathbf{U} = [\mathbf{z}, \mathbf{K}, \mathbf{g}]$, and $\mathcal{M}$ is the mass matrix,

$$\mathcal{M} = \begin{pmatrix} I_N & 0 & 0 \\ 0 & (1 - \mathbf{Dxx})^2 & 0 \\ 0 & 0 & I_N \end{pmatrix}. \tag{C.1.10}$$

C.2 Two spatial dimensions - Mexican hat type kernel

The 2D system was simulated on a square lattice, with spatial dimensions $2L \times 2L$ and $N \times N$ mesh points. As in the 1D case we chose a suitably large domain ($L > 40$) and Neumann boundary conditions in order to imitate the infinite domain. Unfortunately, the Fourier transform of the connectivity kernel used in this case is not easily separable, hence, we cannot transform to an equivalent PDE system as we did in the 1D case. Instead we are forced to use matrix multiplication to compute the integral,

$$\int w(\mathbf{r}' - \mathbf{r}) f(z(\mathbf{r}', t))\mathrm{d}\mathbf{r}' \to \sum_{m}^{N^2}\sum_{n}^{N^2} \rho_{mn} W(m, n) f(Z(n)), \tag{C.2.1}$$

where ρ_{mn} is a weighting factor, $Z = [z(x_1, y_1), z(x_2, y_1), \ldots, z(x_N, y_1), z(x_1, y_2), \ldots, z(x_N, y_N)]^T$ and W is the following $N^2 \times N^2$ matrix,

$$W = w \begin{pmatrix} \sqrt{a_{ij}^2 + b_{11}^2} & \sqrt{a_{ij}^2 + b_{12}^2} & \ldots & \sqrt{a_{ij}^2 + b_{1N}^2} \\ \sqrt{a_{ij}^2 + b_{21}^2} & \sqrt{a_{ij}^2 + b_{22}^2} & \ldots & \sqrt{a_{ij}^2 + b_{2N}^2} \\ \vdots & \vdots & \ddots & \vdots \\ \sqrt{a_{ij}^2 + b_{N1}^2} & \sqrt{a_{ij}^2 + b_{N2}^2} & \ldots & \sqrt{a_{ij}^2 + b_{NN}^2} \end{pmatrix}, \tag{C.2.2}$$

where $a_{ij} = x_i - x_j$ and $b_{ij} = J_N(y_i - y_j)$ for $i, j = 1 \dots N$ and J a $N \times N$ matrix of ones. To impose Neumann boundary conditions the weighting factors ρ_{mn} were selected as follows,

$$\rho_{mn} = \begin{cases} 0.5 & \text{if } m = 1 \text{ or } n = 1 \\ 1 & \text{else.} \end{cases} \tag{C.2.3}$$

The system can now easily be simulated using MATLAB's ode solvers, albeit extremely computationally expensive. For future work we would recommend using periodic boundary conditions, so that one can exploit MATLAB's built in fast Fourier transform algorithms.

C.3 One spatial dimension - exponential kernel

The system is described by (C.1.1) and (C.1.2), where $w(x) = \mathrm{e}^{-|x|}/2$. The manipulations follow a similar form to those described in Appendix C.1, the only difference is that the Fourier transform of w is given as follows,

$$\widehat{w}(k) = \frac{1}{1 + k^2}. \tag{C.3.1}$$

Hence, upon cross multiplication and inverse Fourier transform of (C.1.6) we arrive at the following PDE to describe the evolution of K,

$$\left(1 - \frac{\partial^2}{\partial x^2}\right) \frac{\partial K}{\partial t}(x,t) = \alpha \left(-K(x,t) + \kappa f(z(x,t))\right). \tag{C.3.2}$$

The discretisation follows the same steps as outlined in Appendix C.1, and the

system is described by (C.1.9), where $\mathcal{M}$ is given as,

$$\mathcal{M} = \begin{pmatrix} I_N & 0 & 0 \\ 0 & (1 - \mathbf{Dxx}) & 0 \\ 0 & 0 & I_N \end{pmatrix}. \tag{C.3.3}$$

Bibliography

[1] URL `http://www.engr.sjsu.edu/rkwok/squid.htm`.

[2] M. Alegre, A. Labarga, I. G. Gurtubay, J. Iriarte, A. Malanda, and J. Artieda. Beta electroencephalograph changes during passive movements: sensory afferences contribute to beta event-related desynchronization in humans. *Neuroscience Letters*, 331(1):29–32, 2002.

[3] M. Alegre, I. Alvarez-Gerriko, M. Valencia, J. Iriarte, and J. Artieda. Oscillatory changes related to the forced termination of a movement. *Clinical Neurophysiology*, 119(2):290–300, 2008.

[4] D. M. Alexander, A. R. Nikolaev, P. Jurica, M. Zvyagintsev, K. Mathiak, and C. van Leeuwen. Global Neuromagnetic Cortical Fields Have Non-Zero Velocity. *PLOS ONE*, 11(3):e0148413, 2016.

[5] S. Amari. Homogeneous nets of neuron-like elements. *Biological Cybernetics*, 17: 211–220, 1975.

[6] S. Amari. Dynamics of Pattern Formation in Lateral-Inhibition Type Neural Fields. *Biological Cybernetics*, 27:77–87, 1977.

[7] K. M. Aquino, M. M. Schira, P. A. Robinson, P. M. Drysdale, and M. Breakspear. Hemodynamic Traveling Waves in Human Visual Cortex. *PLoS Computational Biology*, 8(3):e1002435, 2012.

[8] P. Ashwin, S. Coombes, and R. Nicks. Mathematical frameworks for oscillatory network dynamics in neuroscience. *Journal of Mathematical Neuroscience*, 6(2): 1–92, 2016.

[9] D. Avitabile. *Computation of planar patterns and their stability*. PhD thesis, University of Surrey, 2008.

[10] D. Avitabile. Numerical computation of coherent structures in spatially-extended neural networks. Tutorial at Second International Conference on Mathematical Neuroscience, Antibes Juan-les-Pins, 2016.

[11] D. Avitabile and H. Schmidt. Snakes and ladders in an inhomogeneous neural field model. *Physica D: Nonlinear Phenomena*, 294:24–36, 2015.

[12] J. Baladron, D. Fasoli, O. Faugeras, and J. Touboul. Mean field description of and propagation of chaos in networks of Hodgkin-Huxley and FitzHugh-Nagumo neurons. *Journal of Mathematical Neuroscience*, 2(10), 2012.

[13] J. Bardeen, L. N. Cooper, and J. R. Schrieffer. Microscopic Theory of Superconductivity. *Physical Review*, 106(1):162–164, 1957.

[14] R. Ben-Yishai, R. L. Bar-Or, and H. Sompolinsky. Theory of orientation tuning in visual cortex. *Proceedings of the National Academy of Sciences of the United States of America*, 92(9):3844–8, 1995.

[15] J. Benda and A. V. M. Herz. A Universal Model for Spike-Frequency Adaptation. *Neural Computation*, 15(11):2523–2564, 2003.

[16] M. V. L. Bennett and R. S. Zukin. Electrical coupling and neuronal synchronization in the Mammalian brain. *Neuron*, 41(4):495–511, 2004.

[17] H. Berger. Über das Elektroenzenkephalogram des Menschen. *Archiv für Psychiatrie und Nervenkrankheiten*, 87:527–70, 1929.

[18] H. Berger. Über das Elektroenzenkephalogram des Menschen. *Archiv für Psychiatrie und Nervenkrankheiten*, 94:16–60, 1931.

[19] M. Berger, E.-J. Speckmann, H. Pape, and A. Gorji. Spreading Depression Enhances Human Neocortical Excitability in vitro. *Cephalalgia*, 28(5): 558–562, 2008.

[20] R. L. Beurle. Properties of a Mass of Cells Capable of Regenerating Pulses. *Philosophical Transactions of the Royal Society B: Biological Sciences*, 240(669), 1956.

[21] B. S. Bhattacharya and F. N. Chowdhury, editors. *Validating Neuro-Computational Models of Neurological and Psychiatric Disorders*. Springer, 2015.

[22] R. Bogdanov. Bifurcations of the limit cycle of a family of plane vector fields. *Trudy Semin. Petrovskogo*, 2:23–35, 1976.

[23] I. Bojak and M. Breakspear. Neuroimaging , Neural Population Models for. In R. Jaeger, D. Jung, editor, *Encyclopedia of Computational Neuroscience*. Springer, 2014.

[24] C. Börgers and N. Kopell. Synchronization in networks of excitatory and inhibitory neurons with sparse, random connectivity. *Neural Computation*, 15: 509–538, 2003.

[25] C. Börgers and N. Kopell. Effects of Noisy Drive on Rhythms in Networks of Excitatory and Inhibitory Neurons. *Neural Computation*, 17(3):557–608, 2005.

[26] P. C. Bressloff. Traveling fronts and wave propagation failure in an inhomogeneous neural network. *Physica D: Nonlinear Phenomena*, 155(1):83–100, 2001.

[27] P. C. Bressloff and S. Coombes. Physics of the Extended Neuron. *International Journal of Modern Physics B*, 11(20):2343–2392, 1997.

[28] P. C. Bressloff and M. A. Webber. Neural field model of binocular rivalry waves. *Journal of computational neuroscience*, 32(2):233–52, 2012.

[29] P. C. Bressloff, J. D. Cowan, M. Golubitsky, P. J. Thomas, and M. C. Wiener. Geometric visual hallucinations, Euclidean symmetry and the functional architecture of striate cortex. *Philosophical transactions of the Royal Society of London. Series B, Biological sciences*, 356(1407):299–330, 2001.

[30] M. Brookes and K. Singh. Methods in mind. *Physics World*, pages 39–44, 2013.

[31] M. J. Brookes, J. Vrba, S. E. Robinson, C. M. Stevenson, A. M. Peters, G. R. Barnes, A. Hillebrand, and P. G. Morris. Optimising experimental design for MEG beamformer imaging. *NeuroImage*, 39(4):1788–802, 2008.

[32] M. J. Brookes, J. R. Wood, C. M. Stevenson, J. M. Zumer, T. P. White, P. F. Liddle, and P. G. Morris. Changes in brain network activity during working memory tasks: a magnetoencephalography study. *NeuroImage*, 55(4):1804–15, 2011.

[33] M. J. Brookes, E. B. Liddle, J. R. Hale, M. W. Woolrich, H. Luckhoo, P. F. Liddle, and P. G. Morris. Task induced modulation of neural oscillations in electrophysiological brain networks. *NeuroImage*, 63(4):1918–30, 2012.

[34] A. Byrne, D. Avitabile, and S. Coombes. A next generation neural
eld model: The evolution of synchrony within patterns and waves. *Physical Review E*, submitted, 2017.

[35] A. Byrne, M. J. Brookes, and S. Coombes. A mean field model for movement

induced changes in the β rhythm. *Journal of Computational Neuroscience*, to appear, 2017.

[36] J. Cannon, M. M. McCarthy, S. Lee, J. Lee, C. Börgers, M. a. Whittington, and N. Kopell. Neurosystems: brain rhythms and cognitive processing. *The European Journal of Neuroscience*, 39(5):705–19, 2014.

[37] F. Cassim, C. A. C. Monaca, W. Szurhaj, J.-l. Bourriez, L. Defebvre, P. Derambure, and J.-d. Guieu. Does post-movement beta synchronization reflect an idling motor cortex? *Neuroreport*, 12(17):3859–3863, 2001.

[38] S. Chandra, D. Hathcock, K. Crain, T. M. Antonsen, M. Girvan, and E. Ott. Modeling the Network Dynamics of Pulse-Coupled Neurons. 2017.

[39] G. Chapuisat and R. Joly. Asymptotic profiles for a travelling front solution of a biological equation Asymptotic profiles for a travelling front solution of a biological equation. Mathematical Models and Methods in. *Applied Sciences, World Scientific Publishing*, 21(10):2155–2177, 2011.

[40] D. O. Cheyne. MEG studies of sensorimotor rhythms: a review. *Experimental neurology*, 245:27–39, 2013.

[41] C. C. Chow and S. Coombes. Existence and Wandering of Bumps in a Spiking Neural Network Model. *SIAM Journal on Applied Dynamical Systems*, 5(4): 552–574, 2006.

[42] D. Cohen. Magnetoencephalography: evidence of magnetic fields produced by alpha-rhythm currents. *Science*, 161(3843):784–6, 1968.

[43] D. Cohen. Magnetoencephalography: detection of the brain's electrical activity with a superconducting magnetometer. *Science*, 175(4022):664–6, 1972.

[44] J. A. Connor and C. F. Stevens. Prediction of repetitive firing behaviour from voltage clamp data on an isolated neurone soma. *The Journal of Physiology*, 213(1):31–53, 1971.

[45] S. Coombes. Dynamics of synaptically coupled integrate-and-fire-or-burst neurons. *Physical Review E*, 67(4):041910, 2003.

[46] S. Coombes. Waves, bumps, and patterns in neural field theories. *Biological Cybernetics*, 93(2):91–108, 2005.

[47] S. Coombes. Large-scale neural dynamics: simple and complex. *NeuroImage*, 52 (3):731–9, 2010.

[48] S. Coombes and A. Byrne. *Lecture Notes Nonlinear Dynamics in Computational Neuroscience: from Physics and Biology to ICT*, chapter Next generation neural mass models. PoliTO. Springer, 2017.

[49] S. Coombes and C. R. Laing. Pulsating fronts in periodically modulated neural field models. *Physical Review E*, 83(1):011912, 2011.

[50] S. Coombes and M. R. Owen. Bumps, Breathers, and Waves in a Neural Network with Spike Frequency Adaptation. *Physical Review Letters*, 94(14):148102, 2005.

[51] S. Coombes, G. Lord, and M. Owen. Waves and bumps in neuronal networks with axo-dendritic synaptic interactions. *Physica D: Nonlinear Phenomena*, 178 (3):219–241, 2003.

[52] S. Coombes, P. beim Graben, R. Potthast, and J. Wright, editors. *Neural Fields: Theory and Applications*. Springer, 2014.

[53] L. N. Cooper. Bound Electron Pairs in a Degenerate Fermi Gas. *Physical Review*, 104(4):1189–1190, 1956.

[54] R. Curtu and B. Ermentrout. Pattern Formation in a Network of Excitatory and Inhibitory Cells with Adaptation. *SIAM Journal on Applied Dynamical Systems*, 3(3):191–231, 2004.

[55] L. da F. Costa and T. J. Velte. Automatic characterization and classification of ganglion cells from the salamander retina. *The Journal of Comparative Neurology*, 404(1):33–51, 1999.

[56] M. P. Dafilis, F. Frascoli, P. J. Cadusch, and D. T. J. Liley. Chaos and generalised multistability in a mesoscopic model of the electroencephalogram. *Physica D*, 238:1056–1060, 2009.

[57] N. J. Davis, S. P. Tomlinson, and H. M. Morgan. The role of β-frequency neural oscillations in motor control. *The Journal of Neuroscience*, 32(2):403–4, 2012.

[58] G. Deco, V. K. Jirsa, and A. R. McIntosh. Emerging concepts for the dynamical organization of resting-state activity in the brain. *Nature Reviews Neuroscience*, 12:43–56, 2011.

[59] A. Destexhe and T. J. Sejnowski. The Wilson-Cowan model, 36 years later. *Biological Cybernetics*, 101(1):1–2, 2009.

[60] T. H. Donner and M. Siegel. A framework for local cortical oscillation patterns. *Trends in Cognitive Sciences*, 15(5):191–199, 2011.

[61] F. E. Dudek. Gap Junctions and Fast Oscillations: A Role in Seizures and Epileptogenesis? *Epilepsy currents*, 2(4):133–136, 2002.

[62] A. K. Engel and P. Fries. Beta-band oscillations–signalling the status quo? *Current Opinion in Neurobiology*, 20(2):156–65, 2010.

[63] B. Ermentrout. Type I membranes, phase resetting curves, and synchrony. *Neural Computation*, 8(5):979–1001, 1996.

[64] B. Ermentrout. Neural networks as spatio-temporal pattern-forming systems. *Reports on Progress in Physics*, 61(4):353–430, 1998.

[65] B. Ermentrout and D. H. D. H. Terman. *Mathematical foundations of neuroscience*. Springer, 2010.

[66] G. B. Ermentrout. *Simulating, Analyzing, and Animating Dynamical Systems: A Guide To Xppaut for Researchers and Students*. Society of Industrial & Applied Mathematics, 2002.

[67] G. B. Ermentrout and J. D. Cowan. A Mathematical Theory of Visual Hallucination Patterns. 34:137–150, 1979.

[68] G. B. Ermentrout and N. Kopell. Parabolic Bursting in an Excitable System Coupled with a Slow Oscillation. *SIAM Journal on Applied Mathematics*, 46(2): 233–253, 1986.

[69] G. B. Ermentrout and N. Kopell. Multiple pulse interactions and averaging in systems of coupled neural oscillators. *Journal of Mathematical Biology*, 29(3): 195–217, 1991.

[70] K. H. Finley. On the occurrence of rapid frequency potential changes in the human electroencephalogram. *American Journal of Psychiatry*, 101(2):194–200, 1944.

[71] R. F. Fox. Stochastic versions of the Hodgkin-Huxley equations. *Biophysical Journal*, 72(5):2068–74, 1997.

[72] W. J. Freeman. Tutorial on neurobiology: From single neurons to brain chaos. *International Journal of Bifurcation and Chaos*, 2:451–482, 1992.

[73] A. Fry, K. J. Mullinger, G. C. O'Neill, E. L. Barratt, P. G. Morris, M. Bauer, J. P. Folland, and M. J. Brookes. Modulation of post-movement beta rebound

by contraction force and rate of force development. *Human Brain Mapping*, 37 (7):2493–2511, 2016.

[74] W. Gaetz, M. Macdonald, D. Cheyne, and O. C. Snead. Neuromagnetic imaging of movement-related cortical oscillations in children and adults: age predicts post-movement beta rebound. *NeuroImage*, 51(2):792–807, 2010.

[75] W. Gaetz, J. C. Edgar, D. J. Wang, and T. P. L. Roberts. Relating MEG measured motor cortical oscillations to resting γ-aminobutyric acid (GABA) concentration. *NeuroImage*, 55(2):616–21, 2011.

[76] M. Gola, M. Magnuski, I. Szumska, and A. Wróbel. EEG beta band activity is related to attention and attentional deficits in the visual performance of elderly subjects. *International Journal of Psychophysiology*, 89(3):334–341, 2013.

[77] J. Gross, J. Kujala, M. Hamalainen, L. Timmermann, A. Schnitzler, and R. Salmelin. Dynamic imaging of coherent sources: Studying neural interactions in the human brain. *Proceedings of the National Academy of Sciences of the United States of America*, 98(2):694–9, 2001.

[78] S. D. Hall, I. M. Stanford, N. Yamawaki, C. J. McAllister, K. C. Rönnqvist, G. L. Woodhall, and P. L. Furlong. The role of GABAergic modulation in motor function related neuronal network activity. *NeuroImage*, 56:1506–1510, 2011.

[79] S. D. Hall, E. J. Prokic, C. McAllister, K. C. Ronnqvist, A. C. Williams, N. Yamawaki, C. Witton, G. L. Woodhall, and I. M. Stanford. Gaba-mediated changes in inter-hemispheric beta frequency activity in early-stage parkinson's disease. *Neuroscience*, 281:68–76, 2014.

[80] D. Hill and G. Parr. *Electroencephalography a symposium on its various aspects*. Macdonald, 1950.

[81] A. Hillebrand, K. D. Singh, I. E. Holliday, P. L. Furlong, and G. R. Barnes. A new approach to neuroimaging with magnetoencephalography. *Human Brain Mapping*, 25(2):199–211, 2005.

[82] J. F. Hipp, D. J. Hawellek, M. Corbetta, M. Siegel, and A. K. Engel. Large-scale cortical correlation structure of spontaneous oscillatory activity. *Nature neuroscience*, 15(6):884–90, 2012.

[83] A. L. Hodgkin. The local electric changes associated with repetitive action in a non-medullated axon. 107(2):165–81, 1948.

[84] A. L. Hodgkin and A. F. Huxley. A Quantitative Description of Membrane Current and its Application to Conduction and Excitation in Nerve. *The Journal of physiology*, 117(4):500–544, 1952.

[85] S. G. Hormuzdi, M. A. Filippov, G. Mitropoulou, H. Monyer, and R. Bruzzone. Electrical synapses: a dynamic signaling system that shapes the activity of neuronal networks. *Biochimica et biophysica acta*, 1662(1-2):113–37, 2004.

[86] M. X. Huang, J. C. Mosher, and R. M. Leahy. A sensor-weighted overlapping-sphere head model and exhaustive head model comparison for MEG. *Physics in medicine and biology*, 44(2):423–40, 1999.

[87] A. Hutt, M. Bestehorn, and T. Wennekers. Pattern formation in intracortical neuronal fields. *Network*, 14(2):351–68, 2003.

[88] E. Izhikevich. Simple model of spiking neurons. *IEEE Transactions on Neural Networks*, 14(6):1569–1572, 2003.

[89] B. H. Jansen and V. G. Rit. Electroencephalogram and visual evoked potential generation in a mathematical model of coupled cortical columns. *Biological Cybernetics*, 73:357–366, 1995.

[90] H. Jasper and W. Penfield. Electrocorticograms in man: Effect of voluntary movement upon the electrical activity of the precentral gyrus. *European Archives of Psychiatry and Clinical Neuroscience*, 183(1):163–174, 1949.

[91] H. H. Jasper and H. L. Andrews. Human brain rhythms. I. Recording techniques and preliminary results. *Journal of General Physiology*, 14:98–126, 1936.

[92] H. H. Jasper and H. L. Andrews. Brain Potentials and Voluntary Muscle Activity in Man. *Journal of Neurophysiology*, 1(2):87–100, 1938.

[93] A. Jeewajee, C. Barry, V. Douchamps, D. Manson, C. Lever, and N. Burgess. Theta phase precession of grid and place cell firing in open environments. *Philosophical transactions of the Royal Society of London. Series B, Biological sciences*, 369(1635):20120532, 2014.

[94] O. Jensen, P. Goel, N. Kopell, M. Pohja, R. Hari, and B. Ermentrout. On the human sensorimotor-cortex beta rhythm: Sources and modeling. *NeuroImage*, 26(2):347–355, 2005.

[95] V. K. Jirsa and H. Haken. A derivation of a macroscopic field theory of the brain from the quasi-microscopic neural dynamics. *Physica D*, 99:503–526, 1997.

[96] V. K. Jirsa and J. A. S. Kelso. Spatiotemporal pattern formation in neural systems with heterogeneous connection topologies. *Phys. Rev. E*, 62:8462âĂŞ8465, 2000.

[97] M. T. Jurkiewicz, W. C. Gaetz, A. C. Bostan, and D. Cheyne. Post-movement beta rebound is generated in motor cortex: evidence from neuromagnetic recordings. *NeuroImage*, 32(3):1281–9, 2006.

[98] B. r. E. Kilavik, M. Zaepffel, A. Brovelli, W. A. MacKay, and A. Riehle. The

ups and downs of β oscillations in sensorimotor cortex. *Experimental neurology*, 245:15–26, 2013.

[99] Z. P. Kilpatrick and P. C. Bressloff. Stability of bumps in piecewise smooth neural fields with nonlinear adaptation. *Physica D*, 239:1048–1060, 2010.

[100] K. Kim, S. Begus, H. Xia, S.-K. Lee, V. Jazbinsek, Z. Trontelj, and M. V. Romalis. Multi-channel atomic magnetometer for magnetoencephalography: a configuration study. *NeuroImage*, 89:143–51, 2014.

[101] I. Z. Kiss, Y. Zhai, and J. L. Hudson. Emerging Coherence in a Population of Chemical Oscillators. *Science*, 296(5573), 2002.

[102] N. Kopell, G. B. Ermentrout, M. a. Whittington, and R. D. Traub. Gamma rhythms and beta rhythms have different synchronization properties. *Proceedings of the National Academy of Sciences of the United States of America*, 97(4): 1867–1872, 2000.

[103] S. M. Korogod and I. B. Kulagina. Geometry-induced features of current transfer in neuronal dendrites with tonically activated conductances. *Biological Cybernetics*, 79(3):231–240, 1998.

[104] Y. Kuramoto. Self-entrainment of a population of coupled nonlinear oscillators. In H. Araki, editor, *International Symposium on Mathematical Problems in Theoretical Physics*, volume 39, page 420. 1975.

[105] Y. Kuramoto. Collective synchronization of pulse-coupled oscillators and excitable units. *Physica D*, 50:15–30, 1991.

[106] Y. M. Lai and M. A. Porter. Noise-induced synchronization, desynchronization, and clustering in globally coupled nonidentical oscillators. *Physical Review E*, 88:012905, 2013.

[107] C. Laing and C. C. Chow. Stationary bumps in networks of spiking neurons. *Neural Computation*, 13:1473–1494, 2001.

[108] C. Laing and S. Coombes. The importance of different timings of excitatory and inhibitory pathways in neural field models. *Network: Computation in Neural Systems*, 17(2):151–172, 2006.

[109] C. R. Laing. Exact neural fields incorporating gap junctions. *SIAM Journal on Applied Dynamical Systems*, page to appear, 2015.

[110] C. R. Laing. *Computational Models of Brain and Behavior*, chapter Phase oscillator network models of brain dynamics. Wiley-Blackwell, 2016.

[111] C. R. Laing and C. C. Chow. A Spiking Neuron Model for Binocular Rivalry. *Journal of Computational Neuroscience*, 12:39–53, 2002.

[112] P. E. Latham, B. J. Richmond, P. G. Nelson, and S. Nirenberg. Intrinsic Dynamics in Neuronal Networks . I . Theory. *Journal of Neurophysiology*, 83: 808–827, 2000.

[113] E. B. Liddle, D. Price, L. Palaniyappan, M. J. Brookes, S. E. Robson, E. L. Hall, P. G. Morris, and P. F. Liddle. Abnormal salience signaling in schizophrenia: The role of integrative beta oscillations. *Human brain mapping*, 2016.

[114] D. T. J. Liley, P. J. Cadusch, and M. P. Dafilis. A spatially continuous mean field theory of electrocortical activity. *Network (Bristol, England)*, 13(1):67–113, 2002.

[115] A. S. H. Z. L. H. Lopes da Silva, F H. Hoeks. Model of brain rhythmic activity. *Kybernetik*, (15):27–37, 1974.

[116] F. H. Lopes da Silva, A. van Rotterdam, P. Barts, E. van Heusden, and W. Burr. Models of neuronal populations: the basic mechanisms of rhythmicity. *Progress in Brain Research*, 45:281–308, 1976.

[117] T. B. Luke and E. Barreto. Complete Classification of the Macroscopic Behavior of a Heterogeneous Network of Theta Neurons. *Neural Computation*, 25:3207–3234, 2013.

[118] P. K. Maini. Using mathematical models to help understand biological pattern formation. *Comptes Rendus Biologies*, 327(3):225–234, 2004.

[119] P. Maquet, C. Degueldre, G. Delfiore, J. Aerts, J.-M. Peters, A. Luxen, and G. Franck. Functional Neuroanatomy of Human Slow Wave Sleep. *The Journal of Neuroscience*, 17(8):2807–2812, 1997.

[120] H. Markram, E. Muller, S. Ramaswamy, M. W. Reimann, M. Abdellah, C. A. Sanchez, A. Ailamaki, L. Alonso-Nanclares, N. Antille, S. Arsever, G. A. A. Kahou, T. K. Berger, A. Bilgili, N. Buncic, A. Chalimourda, G. Chindemi, J.-D. Courcol, F. Delalondre, V. Delattre, S. Druckmann, R. Dumusc, J. Dynes, S. Eilemann, E. Gal, M. E. Gevaert, J.-P. Ghobril, A. Gidon, J. W. Graham, A. Gupta, V. Haenel, E. Hay, T. Heinis, J. B. Hernando, M. Hines, L. Kanari, D. Keller, J. Kenyon, G. Khazen, Y. Kim, J. G. King, Z. Kisvarday, P. Kumbhar, S. Lasserre, J.-V. Le Bé, B. R. Magalhães, A. Merchán-Pérez, J. Meystre, B. R. Morrice, J. Muller, A. Muñoz-Céspedes, S. Muralidhar, K. Muthurasa, D. Nachbaur, T. H. Newton, M. Nolte, A. Ovcharenko, J. Palacios, L. Pastor, R. Perin, R. Ranjan, I. Riachi, J.-R. Rodríguez, J. L. Riquelme, C. Rössert, K. Sfyrakis, Y. Shi, J. C. Shillcock, G. Silberberg, R. Silva, F. Tauheed, M. Telefont, M. Toledo-Rodriguez, T. Tränkler, W. Van Geit, J. V. Díaz, R. Walker, Y. Wang, S. M. Zaninetta, J. DeFelipe, S. L. Hill, I. Segev, and F. Schürmann.

Reconstruction and Simulation of Neocortical Microcircuitry. *Cell*, 163(2): 456–492, 2015.

[121] A. Mary, M. Bourguignon, V. Wens, M. Op de Beeck, R. Leproult, X. De Tiège, and P. Peigneux. Aging reduces experience-induced sensorimotor plasticity. A magnetoencephalographic study. *NeuroImage*, 104:59–68, 2015.

[122] E. Montbrió, D. Pazó, and A. Roxin. Macroscopic description for networks of spiking neurons. *Physica Review X*, 5:021028, 2015.

[123] R. Moran, D. A. Pinotsis, and K. Friston. Neural masses and fields in dynamic causal modeling. *Frontiers in Computational Neuroscience*, 7(57):1–12, 2013.

[124] S. D. Muthukumaraswamy, J. F. M. Myers, S. J. Wilson, D. J. Nutt, K. Hamandi, A. Lingford-Hughes, and K. D. Singh. Elevating endogenous GABA levels with GAT-1 blockade modulates evoked but not induced responses in human visual cortex. *Neuropsychopharmacology*, 38(6):1105–12, 2013.

[125] K. L. Narr and A. M. Leaver. Connectome and schizophrenia. *Current Opinion in Psychiatry*, 28(3):229–235, 2015.

[126] E. Ott and T. M. Antonsen. Low dimensional behavior of large systems of globally coupled oscillators. *Chaos*, 18(3):037113, 2008.

[127] M. R. Owen, C. R. Laing, and S. Coombes. Bumps and rings in a two-dimensional neural field: splitting and rotational instabilities. *New Journal of Physics*, 9 (37807), 2007.

[128] G. Pfurtscheller. Central beta rhythm during sensorimotor activities in man. *Electroencephalography and clinical neurophysiology*, 51(3):253–64, 1981.

[129] G. Pfurtscheller and A. Berghold. Patterns of cortical activation during planning of voluntary movement. *Electroencephalography and clinical neurophysiology*, 72 (3):250–8, 1989.

[130] G. Pfurtscheller and F. H. Lopes da Silva. Event-related EEG/MEG synchronization and desynchronization: basic principles. *Clinical Neurophysiology*, 110 (11):1842–1857, 1999.

[131] G. Pfurtscheller and T. Solis-Escalante. Could the beta rebound in the EEG be suitable to realize a "brain switch"? *Clinical Neurophysiology*, 120(1):24–9, 2009.

[132] G. Pfurtscheller, A. Stancák, and C. Neuper. Event-related synchronization (ERS) in the alpha band–an electrophysiological correlate of cortical idling: a review. *International Journal of Psychophysiology*, 24(1-2):39–46, 1996.

[133] G. Pfurtscheller, C. Neuper, C. Brunner, and F. L. da Silva. Beta rebound after different types of motor imagery in man. *Neuroscience letters*, 378(3):156–9, 2005.

[134] A.-C. Philippe, M. Clerc, T. Papadopoulo, and R. Deriche. A nested cortex parcellation combining analysis of MEG forward problem and diffusion MRI tractography. In *2012 9th IEEE International Symposium on Biomedical Imaging (ISBI)*, pages 518–521. IEEE, 2012.

[135] D. J. Pinto and G. B. Ermentrout. Spatially Structured Activity in Synaptically Coupled Neuronal Networks: I. Traveling Fronts and Pulses. *SIAM Journal on Applied Mathematics*, 62(1):206–225, 2001.

[136] A. Riehle and E. Vaadia. *Motor Cortex in Voluntary Movements: A Distributed System for Distributed Functions*. CRC Press, 2004.

[137] J. Rinzel. Electrical excitability of cells, theory and experiment: Review of the Hodgkin-Huxley foundation and an update. *Bulletin of Mathematical Biology*, 52(1-2):3–23, 1990.

[138] J. Rinzel and B. Ermentrout. Analysis of neural excitability and oscillations. In C. Koch and I. Segev, editors, *Methods in Neuronal Modelling: From synapses to Networks*. MIT Press, 1989.

[139] S. E. Robinson and J. Vrba. Functional neuroimaging by synthetic aperture magnetometry (SAM). In Y. T, K. M, K. S, K. H, and N. N, editors, *Recent Advances in Biomagnetism*, pages 302–305. Tohoku University Press, 1998.

[140] S. E. Robson, M. J. Brookes, E. L. Hall, L. Palaniyappan, J. Kumar, M. Skelton, N. G. Christodoulou, A. Qureshi, F. Jan, M. Z. Katshu, E. B. Liddle, P. F. Liddle, and P. G. Morris. Abnormal visuomotor processing in schizophrenia. *NeuroImage: Clinical*, 2015.

[141] R. Salmelin and R. Hari. Spatiotemporal characteristics of sensorimotor neuromagnetic rhythms related to thumb movement. *Neuroscience*, 60(2):537–550, 1994.

[142] P. Sanz-Leon, S. A. Knock, A. Spiegler, and V. K. Jirsa. Mathematical framework for large-scale brain network modeling in The Virtual Brain. *NeuroImage*, 111: 385–430, 2015.

[143] J. Sarvas. Basic mathematical and electromagnetic concepts of the biomagnetic inverse problem. *Physics in Medicine and Biology*, 32:11–22, 1987.

[144] A. Schnitzler, S. Salenius, R. Salmelin, V. Jousmäki, and R. Hari. Involvement of primary motor cortex in motor imagery: a neuromagnetic study. *NeuroImage*, 6(3):201–8, 1997.

[145] P. D. Schwindt and C. N. Johnson. Atomic Magnetometer for Human Magnetoencephalograpy. Technical report, Sandia National Laboratories, 2010.

[146] K. Sekihara, S. Nagarajan, D. Poeppel, A. Marantz, and Y. Miyashita. Reconstructing spatio-temporal activities of neural sources using an MEG vector beamformer technique. *IEEE Transactions on Biomedical Engineering*, 48(7): 760–771, 2001.

[147] D. Senkowski, D. Talsma, C. S. Herrmann, and M. G. Woldorff. Multisensory processing and oscillatory gamma responses: effects of spatial selective attention. *Experimental brain research*, 166(3-4):411–26, 2005.

[148] D. Sheng, S. Li, N. Dural, and M. V. Romalis. Subfemtotesla Scalar Atomic Magnetometry Using Multipass Cells. *Physical Review Letters*, 110(16):160802, 2013.

[149] P. S. Skardal, E. Ott, and J. G. Restrepo. Cluster synchrony in systems of coupled phase oscillators with higher-order coupling. *Physical Review E*, 84: 036208, 2011.

[150] T. Solis-Escalante, G. R. Müller-Putz, G. Pfurtscheller, and C. Neuper. Cue-induced beta rebound during withholding of overt and covert foot movement. *Clinical Neurophysiology*, 123(6):1182–90, 2012.

[151] G. G. Somjen, P. G. Aitken, M. Balestrino, O. Herreras, and K. Kawasaki. Spreading depression-like depolarization and selective vulnerability of neurons. A brief review. *Stroke*, 21:179–83, 1990.

[152] R. C. Sotero, N. J. Trujillo-Barreto, Y. Iturria-Medina, F. Carbonell, and J. C. Jimenez. Realistically coupled neural mass models can generate EEG rhythms. *Neural Computation*, 19:478–512, 2007.

[153] A. Spiegler, T. R. Knösche, K. Schwab, J. Haueisen, and F. M. Atay. Modeling brain resonance phenomena using a neural mass model. *PLoS Computational Biology*, 7(12):e1002298, 2011.

[154] C. M. Stevenson, M. J. Brookes, and P. G. Morris. β-Band correlates of the fMRI BOLD response. *Human brain mapping*, 32(2):182–97, 2011.

[155] A. F. Taylor, P. Kapetanopoulos, B. J. Whitaker, R. Toth, L. Bull, and M. R. Tinsley. Clusters and Switchers in Globally Coupled Photochemical Oscillators. *Physical Review Letters*, 100(21):214101, 2008.

[156] L. Timmermann and E. Florin. Parkinson's disease and pathological oscillatory activity: is the beta band the bad guy? - New lessons learned from low-frequency deep brain stimulation. *Experimental neurology*, 233(1):123–5, 2012.

[157] A. M. Turing. The Chemical Basis of Morphogenesis. *Philosophical Transactions of the Royal Society of London B: Biological Sciences*, 237(641), 1952.

[158] P. Valdes-Sosa, J. M. Sanchez-Bornot, R. C. Sotero, Y. Iturria-Medina, Y. Aleman-Gomez, J. Bosch-Bayard, F. Carbonell, and T. Ozaki. Model driven EEG/fMRI fusion of brain oscillations. *Human Brain Mapping*, 30:2701–21, 2009.

[159] W. van Drongelen, M. Yuchtman, B. D. Van Veen, and A. C. van Huffelen. A spatial filtering technique to detect and localize multiple sources in the brain. *Brain Topography*, 9(1):39–49, 1996.

[160] B. Van Veen and K. Buckley. Beamforming: a versatile approach to spatial filtering. *IEEE ASSP Magazine*, 5(2):4–24, 1988.

[161] B. D. Van Veen, W. van Drongelen, M. Yuchtman, and A. Suzuki. Localization

of brain electrical activity via linearly constrained minimum variance spatial filtering. *IEEE transactions on bio-medical engineering*, 44(9):867–80, 1997.

[162] J. L. P. Velazquez and P. L. Carlen. Gap junctions, synchrony and seizures. *Trends in neurosciences*, 23(2):68–74, 2000.

[163] J. Vrba and S. E. Robinson. Signal processing in magnetoencephalography. *Methods*, 25(2):249–71, 2001.

[164] X. J. Wang. Neurophysiological and Computational Principles of Cortical Rhythms in Cognition. *Physiological Reviews*, 90(3):1195–1268, 2010.

[165] H. R. Wilson and J. D. Cowan. Excitatory and inhibitory interactions in localized populations of model neurons. *Biophysical Journal*, 12(1):1–24, 1972.

[166] H. R. Wilson and J. D. Cowan. A mathematical theory of the functional dynamics of cortical and thalamic nervous tissue. *Biological Cybernetics*, 13(2): 55–80, 1973.

[167] K. Wimmer, D. Q. Nykamp, C. Constantinidis, and A. Compte. Bump attractor dynamics in prefrontal cortex explains behavioral precision in spatial working memory. *Nature Neuroscience*, 17(3):431–439, 2014.

[168] M. Zaepffel, R. Trachel, B. E. Kilavik, and T. Brochier. Modulations of EEG Beta Power during Planning and Execution of Grasping Movements. *PLoS ONE*, 8(3):e60060, 2013.

[169] L. H. Zetterberg, L. Kristiansson, and K. Mossberg. Performance of a model for a local neuron population. *Biological Cybernetics*, 31:15–26, 1978.

[170] K. Zhang. Representation of spatial orientation by the intrinsic dynamics of the head-direction cell ensemble: a theory. *Journal of Neuroscience*, 16(6), 1996.

[171] J. E. Zimmerman, P. Thiene, and J. T. Harding. Design and Operation of Stable rf-Biased Superconducting Point-Contact Quantum Devices, and a Note on the Properties of Perfectly Clean Metal Contacts. *Journal of Applied Physics*, 41(4): 1572, 1970.